

AD-A261 165



DOCUMENTATION PAGE

Form Approved
OMB No. 0704-0188

(2)

Notation is estimated to average 1 hour per response, including the time for reviewing instructions, searching existing data sources, gathering and reviewing the collection of information, sending comments regarding this burden estimate or any other aspect of this reducing this burden to Washington Headquarters Services, Directorate for Information Operations and Reports, 1215 Jefferson Ave., and to the Office of Management and Budget, Paperwork Reduction Project (0704-0188), Washington, DC 20503.

1. AGENCY USE ONLY (Leave blank)		2. REPORT DATE 12/31/92		3. REPORT TYPE AND DATES COVERED FINAL TECH. RPT: 11/1/89 to 10/31/92	
4. TITLE AND SUBTITLE (U) Fundamental Studies of Droplet Interactions in Dense Sprays (U)				5. FUNDING NUMBERS PE - 61102F PR - 2308 SA - BS G - AFOSR 90-0064	
6. AUTHOR(S) Professor W.A. Sirignano, Principal Investigator Professor S.E. Elghobashi, Dr. I. Kim, Dr. C.H. Chiang					
7. PERFORMING ORGANIZATION NAME(S) AND ADDRESS(ES) Department of Mechanical and Aerospace Engineering University of California, Irvine Irvine, CA 92717				8. PERFORMING ORGANIZATION REPORT NUMBER AFOSR-TR- 93 0073	
9. SPONSORING/MONITORING AGENCY NAME(S) AND ADDRESS(ES) AFOSR/NA 110 Duncan Avenue, Suite B115 Bolling AFB DC 20332-0001				10. SPONSORING/MONITORING 93-04642 136p	
11. SUPPLEMENTARY NOTES					
12a. DISTRIBUTION/AVAILABILITY STATEMENT Approved for public release; distribution is unlimited				12b. DISTRIBUTION CODE	
13. ABSTRACT (Maximum 200 words) The research addressed interactions amongst droplets in a dense spray. The effects of neighboring droplets, that were a few droplet diameters away, on a vaporizing droplet were examined by theoretical and computational analyses for two basic configurations: (1) the axisymmetric convective situation where two or three droplets moved in tandem and (2) the fully three-dimensional convective situation where droplets moved side-by-side. Droplets in the wake of other droplets experienced a reduction in drag force, transport rates, and vaporization rate, sometimes causing collisions. Sufficiently close droplets moving side-by-side, approximately in parallel, experienced a repulsive lift force and an increased drag force. Vaporizing liquid oxygen droplets in a hydrogen gas environment were studied at both subcritical and supercritical pressures considering the variable liquid density with the associated droplet swelling during heating and the dependence of the local critical state upon local composition. Droplet surface conditions could be subcritical even if pressures were supercritical for pure oxygen due to diffusing hydrogen. The critical surface regressed towards the droplet surface as the droplet heated. Engineering correlations for the drag coefficients, Nusselt numbers, and Sherwood numbers for hydrocarbon fuel droplets in dense sprays were obtained.					
14. SUBJECT TERMS Dense Sprays, Droplet Interactions, Droplet Spray, Fuel Spray and Droplet Heating and Vaporization, Oxygen Droplet Heating and Vaporization, Supercritical Droplet Behavior				15. NUMBER OF PAGES 134	
				16. PRICE CODE	
17. SECURITY CLASSIFICATION OF REPORT Unclassified	18. SECURITY CLASSIFICATION OF THIS PAGE Unclassified	19. SECURITY CLASSIFICATION OF ABSTRACT Unclassified	20. LIMITATION OF ABSTRACT UL		

00 1 3 1 000

Final Technical Report

**Fundamental Studies of Droplet Interactions
in Dense Sprays**

AFOSR - 90 - 0064

November 1, 1989 to October 31, 1992

Prepared by :

Professor W. A. Sirignano, Principal Investigator

Professor S. E. Elghobashi

Dr. I. Kim

Dr. C. H. Chiang

Accession For	
NTIS	CRA&I
DTIC	TAB
Unannounced	
Justification	
By	
Distribution /	
Availability Codes	
Dist	Avail and / or Special
A-1	

THIS REPORT IS UNCLASSIFIED

Department of Mechanical and Aerospace Engineering
University of California, Irvine, California

Submitted to: Dr. J. Tishkoff, Program Manager

December 31, 1992

Table of Contents

Abstract	1
Nomenclature	2
1. Introduction	4
2. Three-dimensional flow over two spheres placed side by side	5
2.1 Problem statement and numerical solution	5
2.2 Results and discussion	6
3. Three-dimensional flow computation for two interacting, moving droplets	12
3.1 Problem statement	12
3.2 Results and discussion	13
4. Three-dimensional flow computation for two interacting, vaporizing, moving droplets	15
5. Axisymmetric interactive fuel droplet calculations	17
6. LOX vaporization at subcritical conditions	19
7. LOX vaporization at near-critical or supercritical conditions	20
Acknowledgement	24
References	25
Professional Personnel	27
Publications	27
Presentation	28
Interactions	30
Addenda	

Abstract

The research addressed interactions amongst droplets in a dense spray. The effects of neighboring droplets, that were a few droplet diameters away, on a vaporizing droplet were examined by theoretical and computational analyses for two basic configurations: (1) the axisymmetric convective situation where two or three droplets moved in tandem and (2) the fully three-dimensional convective situation where droplets moved side-by-side. Droplets in the wake of other droplets experienced a reduction in drag force, transport rates, and vaporization rate, sometimes causing collisions. Sufficiently close droplets moving side-by-side, approximately in parallel, experienced a repulsive lift force and an increased drag force. Vaporizing liquid oxygen droplets in a hydrogen gas environment were studied at both subcritical and supercritical pressures considering the variable liquid density with the associated droplet swelling during heating and the dependence of the local critical state upon local composition. Droplet surface conditions could be subcritical even if pressures were supercritical for pure oxygen due to diffusing hydrogen. The critical surface regressed towards the droplet surface as the droplet heated. Engineering correlations for the drag coefficients, Nusselt numbers, and Sherwood numbers for hydrocarbon fuel droplets in dense sprays were obtained.

Nomenclature

a_o	initial droplet radius
a_t	instantaneous droplet radius
d_o	initial distance between droplet centers normalized initial droplet diameter
d_t	instantaneous distance between droplet centers normalized initial droplet diameter
D'_∞	dimensional mass diffusivity at infinity
D_{ij}	binary diffusion coefficient
f	fugacity
h'	dimensional film heat transfer coefficient
h'_m	dimensional film mass transfer coefficient
$\Delta \overline{H}_v$	enthalpy of vaporization
k'_∞	dimensional thermal conductivity at infinity
k	thermal conductivity of the gas phase
\dot{m}_v	mass vaporization rate on the droplet surface
$Y_{f,av}$	average mass fraction on the droplet surface
i, j, k	unit vectors in x, y, and z direction, respectively
l_t	instantaneous droplet position in y direction
N_1, N_2, N_3	numbers of grid points in ξ, η, ζ directions
ν'_∞	dimensional kinematic viscosity at infinity
P	pressure
r	radial direction
Re	initial Reynolds number based on initial droplet diameter, $U'_{d,o} 2a_o / \nu'_\infty$
Re_t	instantaneous Reynolds number, $U'_{d,t} 2a_t / \nu'_\infty$
T	temperature
t	dimensionless time normalized by $a_o / U'_{d,o}$
$U'_{d,o}$	initial dimensional droplet velocity
$U'_{d,t}$	instantaneous dimensional droplet velocity, $\sqrt{V_{\infty,t}^2 + U_{\infty,t}^2}$
$U'_{\infty,t}$	instantaneous dimensional droplet velocity in x-direction
$V'_{\infty,t}$	instantaneous dimensional droplet velocity in y-direction
x, y, z	Cartesian coordinates
x	mole fraction
Y	mass fraction

Greek symbols

ρ	dimensionless gas density normalized by ρ'_∞
ρ'_∞	dimensional gas density at infinity
θ	angular direction
ξ, η, ζ	nonorthogonal generalized coordinates

τ	viscous stress tensor
ψ_{ps}	pseudo-stream function
ϕ	fugacity coefficient

Superscript
' dimensional quantity

Subscript
o initial quantity
l liquid phase

1. Introduction

Practical combustors with direct injection of liquid fuel have regions of large concentration of droplets, which we will call dense sprays. In such regions, the effect of neighboring droplets modifies the ambient conditions in the flow near any given droplet. As a consequence, the drag coefficient, lift coefficient, moment coefficient, Nusselt number, Sherwood number, and vaporization rates are different from those of an isolated droplet at the same Reynolds number and transfer number. Also, the droplet trajectories, droplet lifetime, and local gas-phase mixture ratios can be significantly affected by the differences in transport processes and the modified flow field due to neighboring droplets. In many practical situations, including liquid rocket engines, turbojet engines, and ramjet engines, droplet heating and vaporization can be a rate-controlling phenomena. Therefore, the modifications in the droplet behavior due to dense spray effects can have important consequences.

The geometrical configurations of droplets in a real region of large concentration are complex and subject to uncertainty. Droplet arrays as discussed by Sirignano [1], although artificial, can provide information on droplets interaction and give a detailed analysis of the problem. The principal investigator and his co-workers [2-7] performed research on axisymmetric configurations of interacting particles (or droplets) in the wake of another particles (or droplets). The major new goal of this project is the study of three-dimensional interactions between droplets.

Three tasks has been performed step by step to attack the three-dimensional interactions between droplets. First, we investigated incompressible, isothermal, three-dimensional flow over two identical (solid or liquid) spheres which were *held fixed relative to each other* in the transverse direction against the uniform stream at Reynolds number $O(100)$. We determined the effects of three-dimensional interactions on the lift, moment, and drag coefficients as a function of the dimensionless distance between the two spheres and Reynolds number. Some novel phenomena in the near wake were discovered as the gap between the two spheres decreases. Our results are also compared with available experimental and numerical data. This study will be discussed briefly in Section 2. Details are provided in Reference 9 which is attached as an addendum to this report.

Secondly, we studied interactions of two identical droplets which are injected and then move side by side into an initially quiescent, incompressible, isothermal fluid medium. The droplets decelerate due to the drag and change their direction of motion due to the lift. By placing the origin of a noninertial reference frame at the center of mass of the two droplets, the Navier-Stokes equations include a noninertial term which is evaluated from Newton's second law for the droplet motion. This study will be discussed briefly in Section 3. Details are provided in Reference 18 which is attached as an addendum to this report.

In the third task, we extended the above studies by considering three-dimensional

interactions between two identical n-octane droplets injected into a high-temperature and high-pressure environment which is typically encountered in practical combustors. The droplets are cold initially and are subsequently vaporizing due to the high temperature. The energy equation, the species equation, and the equation of state, in addition to the Navier-Stokes equations, are solved simultaneously in the gas phase to account for vaporization of the droplets and temperature distribution in the domain. In addition, nonlinear coupled interface boundary conditions between the gas and liquid phases are imposed simultaneously. This study will be discussed in detail in Section 4. We expect to submit a manuscript for journal publication on this subject in the near future.

In addition to the above three-dimensional calculations, three tasks which make use of advanced axisymmetrical models have been conducted in this program, namely: (1) axisymmetric interactive fuel droplet calculations, (2) LOX vaporization at subcritical conditions, (3) LOX vaporization at near-critical or supercritical conditions.

The first task investigates fuel droplets moving in tandem by axisymmetric calculations. This research addresses the interaction of three vaporizing droplets moving collinearly which represents a model of an injected stream of fuel droplets. The purposes of this study are to study the wake effect of the lead droplet on the downstream droplets and to examine the effects of initial spacing on the total system. Some technical discussion will be given in Section 5. More details are available in our journal publication [7]. This publication is attached as an addendum to this report.

In another task, vaporizing liquid oxygen droplets are studied including axisymmetric interactions amongst fuel and oxygen droplets. Vaporization of LOX droplets in convective hydrogen environment over a wide range of pressure has been investigated. Current emphasis is placed on the understanding of supercritical LOX vaporization where many complex transport phenomena, such as the vanishing of the gas/liquid interface, diffusion of gas vapor into droplet, and real gas effects, become very important in determining the droplet vaporization rate.

Progress has occurred in the study of vaporization of an isolated LOX droplet in a convective hydrogen environment at subcritical conditions. This study will be discussed in Section 6. A copy of the preprint describing this research is attached as an addendum to this report. Modifications of this low pressure model to consider near-critical or supercritical conditions have been made in order to fulfill this task. The details are presented in Section 7.

2. Three-dimensional flow over two spheres placed side by side

2.1 Problem statement and numerical solution

We consider a steady, three-dimensional, incompressible, laminar flow of a Newtonian fluid past two identical (solid or liquid) spheres held fixed, with the line connecting the

sphere centers normal to a uniform stream, as shown in Figure 1; d_o denotes the distance, normalized by the sphere radius, from the sphere center to the x-y symmetry plane between the two spheres. Far upstream, the flow is uniform with constant velocity $U_\infty \mathbf{i}$ parallel to the x-axis. Two symmetry planes are noted in Figure 1: the x-z plane containing the centers of the two spheres and the x-y plane located at $z = -d_o$ midway between the sphere centers.

The governing equations and boundary conditions, coordinate system, computational grid, and numerical method are discussed in detail in the addendum to this report.

The dimensional drag, lift, and moment coefficients are evaluated from

$$F'_D = \int_S -p' \mathbf{n} \cdot \mathbf{i} dS' + \int_S \mathbf{n} \cdot \boldsymbol{\tau}' \cdot \mathbf{i} dS', \quad (1)$$

$$F'_L = \int_S -p' \mathbf{n} \cdot \mathbf{k} dS' + \int_S \mathbf{n} \cdot \boldsymbol{\tau}' \cdot \mathbf{k} dS', \quad (2)$$

$$\mathbf{M}' = \int_S \mathbf{r}' \times \boldsymbol{\tau}' dS', \quad (3)$$

where S' denotes the surface of the sphere, \mathbf{n} is the outward unit normal vector at the surface, \mathbf{r}' is the position vector from the center of the sphere, and $\boldsymbol{\tau}'$ is the viscous stress tensor. The lift force is assumed positive when it is directed toward the positive z-axis. Due to symmetry, only the y-component of the moment is non-zero and is assumed positive in counter-clockwise direction.

Nondimensional coefficients of drag, lift, and moment are defined respectively as

$$C_D = \frac{F'_D}{\frac{1}{2} \rho' U_\infty'^2 \pi a_o'^2} \quad (4)$$

$$C_L = \frac{F'_L}{\frac{1}{2} \rho' U_\infty'^2 \pi a_o'^2} \quad (5)$$

$$C_M = \frac{\mathbf{M}' \cdot \mathbf{j}}{\frac{1}{2} \rho' U_\infty'^2 \pi a_o'^3} \quad (6)$$

2.2 Results and discussion

We first tested the three-dimensional code by solving the flow generated by an impulsively started solid sphere in a quiescent fluid at two Reynolds numbers: 50 and 100. The time-dependent solution converges asymptotically to a steady-state which is in excellent

agreement with available experimental data and correlations as shown in Tables 1, 2, 3, and 4. Tables 1 and 3 list the drag coefficients as a function of the computational grid density at Reynolds numbers 50 and 100 respectively, and compare them with the data of Roos & Willmarth [10] and also with the correlations of Clift *et al.* [11]. Tables 2 and 4 show the pressures at the front and rear stagnation points and the separation angle measured from the front stagnation point as a function of grid density at Reynolds number 50 and 100, in comparison with the data of Taneda [12] and also with the correlations of Clift *et al.* [11]. Although the solution in these test cases are axisymmetric, none of the three velocity components in our formulation becomes identically zero. Therefore, the three-dimensional solution scheme is fully exercised here. The calculations were performed for three different grids, $(N_1 \times N_2 \times N_3) = (20 \times 21 \times 21)$, $(30 \times 31 \times 31)$, and $(40 \times 41 \times 41)$, in a computational domain with an outer boundary located at 21 sphere radii from the sphere center. The dimensionless times needed to reach steady state for Reynolds number 50 and 100 are 9 and 15, respectively. The results for interactions of two solid spheres will be presented and discussed first and, then, those for two liquid spheres will be discussed shortly thereafter in the remainder of the section.

In order to illustrate better the fluid motion, we consider the flow field in the x-z plane of symmetry, which is defined as the *principal plane*, where the narrowest path between the two spheres occurs; hence the strongest interactions between them occur there. We first describe the main flow features that emerged from our results, then we examine the results in detail.

Figure 2(a) displays a sketch of actual streamlines around a single solid or liquid sphere in the principal plane at Reynolds number 100. As expected, two identical counter-rotating vortices (corresponding to a single vortex ring) exist in the wake, and the downstream stagnation point is located on the axis of symmetry. Line I-II connecting the front and rear stagnation points in the standard axisymmetric flow over a single sphere will be used as a reference line. We refer to the region above the line I-II as the 'top' or 'upper' region and that below the line as the 'bottom' or 'lower' region.

Figure 2(b) displays a sketch of actual streamlines around one of the two spheres in the principal plane at Reynolds number 100. The two spheres are separated by a distance $d_o = 2$. Due to the *blockage* of the flow in the gap between the two spheres, the streamlines diverge away from the x-y symmetry plane (located at $z = -d_o$) as they approach the front stagnation region. Thus, the stagnation streamline of the single sphere case (I-S₁ in Figure 2(a)) no longer intersects the sphere, and another streamline closer to the symmetry plane meets the sphere to form the new front stagnation streamline at point P. As a consequence, the fluid particles move faster in the lower left region around the sphere than in the upper left region, and this causes the pressure in the lower left region to be lower than that in the upper left region. The resulting pressure difference between the upper and lower left regions is higher than that between the bottom of the sphere and the narrow path. This pressure imbalance, which will be discussed later in detail, causes

repulsion of the two spheres. The contribution of shear stress differences to the repulsion will be discussed later in this section.

Figure 2(b) shows an interesting streamline pattern in the wake region. Two counter-rotating eddies exist in the wake but their configuration is quite different from that for axisymmetric flow. The lower eddy is formed by the fluid separating on the lower portion of the sphere as in the case of axisymmetric flow. The upper eddy is not formed by the fluid separating on the upper portion of the sphere, but rather by the fluid turning around the lower eddy and being entrained by the upper flow. This upper eddy is detached from the sphere. A portion of the fluid moving around the bottom of the sphere passes between the detached upper eddy and the sphere. The streamline A-B encompassing the upper eddy intersects itself, and the intersection point, C, designated as the downstream stagnation point, is shifted toward the x-y symmetry plane. Both eddies are smaller than those of the axisymmetric flow. These new features can be explained as follows. The pressure above the upper wake is less than that below the lower wake due to the increased acceleration of the fluid in the narrow path between the two spheres. Thus, the fluid particles turning around the lower eddy are pushed into the upper region of the wake. The pressure distribution around the sphere will be discussed further.

Figure 2(c) shows a sketch of the actual streamline pattern at Reynolds number 100 for the case of $d_o = 1.5$. The shifting of the front stagnation streamline and stagnation point toward the x-y symmetry plane are more obvious here than in the previous case of $d_o = 2$. The significant difference is in the wake region where both the upper eddy and downstream stagnation point vanish. Fluid particles separating on the upper portion of the sphere move downstream without returning (streamline D-E). On the other hand, fluid particles turning around the lower eddy move into the upper region of the wake until they reach near the upper separation point, D, and then move downstream in an S-shaped path (streamline F-G) without returning to form an eddy. The lower eddy shrinks as the two spheres are closer, and the pressure difference between the top and bottom of the wake is larger.

It is interesting to examine the changes in the separation region at the sphere surface for the cases of $d_o = 2$ and 1.5. More specifically, we examine the behavior of the circle of intersection of the wake and the sphere. Our results show that the circle is slightly shifted toward the x-y symmetry plane due to the decreased pressure in the gap region with respect to that in the wake lower region. This shifting produces separation angles at the top, middle, and bottom of the sphere with values of 123.1° , 126.5° , and 126.2° , respectively, for the case of $d_o = 1.5$, where the angles are measured from the front stagnation point of the axisymmetric flow case. This is in contrast with an angle of 125.7° at all positions in the single sphere case.

A stream function ψ cannot be defined and calculated from the velocity in the principal plane due to the existence of a divergence associated with the third component of velocity. Nevertheless, for descriptive purposes only, it is convenient to use the algorithm

$$\psi_{ps}(r, \theta_o) = \psi_{ps}(r_o, \theta_o) + \int_{r_o}^r -u_\theta dr \quad (7)$$

to present approximations to the streamline pattern. It is understood that since a true streamfunction does not exist, the pseudo-streamfunction, ψ_{ps} , is dependent upon the integration path. The above algorithm specifically involves only radial integration; u_θ can be recovered by differentiation of this function, but u_r cannot be recovered. The streamlines presented in Figures 2(a), 2(b), and 2(c) were based on this algorithm.

Phenomena in the wake similar to those described above have been found in a few previous studies. Rosfjord [13] obtained results similar to those in Figures 2(b) and 2(c) in his experimental and numerical studies of the recirculating flow region between two-dimensional, parallel, separated jets. He found that for velocity ratios between two jets equal to 1.11 and 1.25 (upper to lower), two eddies exist near the injector face, but the upper eddy is detached from the injector face, and a portion of the fluid originating at the lower jet is entrained by the upper jet, passing between the detached upper eddy and the injector face. He also reported that for a velocity ratio of 1.4, only the lower eddy existed and a complete entrainment of the weaker jet was observed. In particular, the flow S-shaped loop near the stronger jet was clearly indicated. Recently, Dandy & Dwyer [14] also found a similar flow pattern in their numerical study of steady, uniform shear flow past a single solid sphere.

In order to facilitate the visualization of the three-dimensional character of the flow in the wake region discussed above, we present the pathlines of selected fluid particles in the addendum.

In the following discussion, we classify the proximity of the two spheres into three regimes: *close*, *intermediate*, and *far-separated*, depending on the values of d_o and Re . Figures 3 and 4 pertain to flows around solid spheres, while Figures 5, 6, 7, and 8 relate to flows around liquid spheres.

Figures 3(a), 3(b), and 3(c) show the total lift coefficient and the lift coefficients due to viscous and pressure contributions, respectively, as a function of d_o at Reynolds numbers 50, 100, and 150. The total lift coefficient, Figure 3(a), is positive when the two spheres are close ($d_o < 7.9$ for $Re = 50$, $d_o < 4$ for $Re = 100$, and $d_o < 3.4$ for $Re = 150$). That is, the two spheres repel each other, and the repulsion is stronger the closer they are. Our results show that both the viscous and pressure contributions have an important effect on the repelling force, but the pressure contribution is more dominant when $Re \geq 100$ (compare Figures 3(b) and 3(c)). On the other hand, the total lift coefficient is negative and relatively small – that is, the two spheres attract each other weakly – at intermediate separation distances ($7.9 < d_o < 21$ for $Re = 50$, $4 < d_o < 21$ for $Re = 100$, and $3.4 < d_o < 21$ for $Re = 150$). At these distances, the pressure is the main contributor to the attraction force at all Reynolds numbers. The smaller the Reynolds number, the

smaller the pressure effect, the weaker the attraction, and the narrower the region of attraction is. When $d_o \geq 21$, however, the lift vanishes, and the two spheres have no interactions at any Reynolds numbers.

As discussed earlier, when the two spheres are in close proximity, the front stagnation point is shifted toward the x-y symmetry plane, and the fluid particles accelerate faster in the lower left region than they accelerate in the upper left region of the sphere. This difference in acceleration results in a net negative pressure gradient normal to and away from the x-y symmetry plane, contributing to the repulsion between the two spheres. The shear stress is also higher in the lower left region than in the upper left region. Furthermore, the shear force in the lower left region, due to its inclination with the x-axis, contributes to both the lift (parallel to the z-axis) and drag (parallel to the x-axis), whereas the shear force at the top of the sphere contributes mainly to the drag. Therefore, both the pressure and shear forces contribute to a positive lift force (i.e. the two spheres repel each other) when the two spheres are close.

On the other hand, when the two spheres are in the intermediate separation regime, the velocity vector distributions show that the front stagnation streamline is almost straight, and thus the flow in the lower left is not affected by the presence of the other sphere. Nevertheless, the gap between the two spheres causes the flow to accelerate slightly faster on the top of the sphere than on the bottom, and as a result, the average pressure in the lower region is slightly higher than that in the narrow gap. Thus, the two spheres attract each other weakly, and the attraction force is mainly due to the pressure distribution. The shear force, nearly parallel to the x-axis at the top of the sphere, contributes mainly to the drag but not to the lift.

Figure 4 shows the drag coefficient as a function of the dimensionless distance at Reynolds numbers 50, 100, and 150. The drag increases with decreasing d_o when d_o is less than 4 for all Reynolds numbers. It increases slightly with increasing d_o , at intermediate separation distances, and eventually tends to that of a single sphere when $d_o \geq 21$. The drag increases as the two spheres get close because the shear stress on the sphere is increased and the pressure distribution is changed due to the flow acceleration on the lower left region as well as in the gap between them. Results for the moment coefficient are provided in the addendum.

In the analysis of the flow field past two liquid spheres, we use a viscosity ratio (internal to external fluid) of 25 and density ratio of 300. These values are typical of a liquid-hydrocarbon fuel in a high-temperature, high-pressure surrounding gas generally encountered in gas turbine combustors (Raju & Sirignano [5]).

As in the solid sphere case, we examine the flow field for two liquid spheres in the x-z plane of symmetry, the *principal plane*, where the narrowest path between liquid spheres is encountered. The streamlines discussed earlier in Figures 2(a), 2(b), and 2(c) can also represent typical streamlines in the external flow of liquid spheres. However, there are differences from the solid sphere case. First, the angle, measured from $\theta = 0$, at which

separation occurs on the sphere surface is much higher than that of the solid sphere. Secondly, a closer examination of the velocity vector plot (Figures 5(a) and 6(a)) in the wake region indicates that the separating streamline, instead of being nearly normal to the sphere surface, now curves closer to the sphere surface producing a "squashed" recirculation zone. The length of the recirculating eddy is also slightly smaller than that of the solid sphere.

Figures 5(a) and 5(b) show the velocity vector fields of the external and internal flows, respectively, in the principal plane at Reynolds number 100 where the two spheres are separated by a distance $d_o = 2$. A secondary eddy in the liquid-sphere stern region is evident in both the upper and lower regions in the principal plane, but the eddy centers in both regions are asymmetrical with respect to the $z = 0$ plane. Also, these eddies are concomitant with the occurrence of the eddies in both regions in the external flow. Figures 6(a) and 6(b) show the velocity vector fields of the external and internal flows in the principal plane at Reynolds number 100 for the case of $d_o = 1.5$. The secondary internal eddy in the liquid-sphere stern region exists only in the lower region, and the secondary eddy in the upper region no longer exists. The vanishing secondary internal eddy in the upper region is accompanied by the disappearance of the recirculating eddy in the upper region in the external flow.

Calculations of the lift, moment, and drag coefficients were performed for dimensionless distances from the liquid sphere center to the symmetry plane between two liquid spheres in the range $1.5 \leq d_o \leq 25$, for a viscosity ratio (internal to external fluid) of 25 and density ratio of 300 at Reynolds numbers 50, 100, and 150. Figures 7 and 8 show the coefficients of total lift and drag as a function of dimensionless distance at Reynolds numbers 50, 100, and 150. The coefficients of total lift, moment, and drag are slightly smaller in absolute value than those of the solid spheres at both the repelling and attraction separation distances and at all Reynolds numbers. The lower coefficients of the liquid sphere are attributed to the surface motion of the liquid sphere which reduces the velocity gradient and friction force. A smaller drag coefficient for the liquid sphere in axisymmetric flow has been also found in earlier calculations (Clift *et al.* [11]).

We did not perform calculations for Reynolds number higher than 150, because it is known that the wake becomes unstable at a Reynolds number in the range of 130-220 for a single sphere (Taneda [12]; Goldburg & Florsheim [15]; Willmarth & Roos [10]; Nakamura [16]; Kim & Pearlstein [17]) and our present goal is to obtain steady-state solutions. For the solution of a flow including the three-dimensional unsteady wake, a complete computational domain (i.e. encompassing the two spheres without a symmetry plane) and periodic boundary conditions in ζ -direction will be necessary.

3. Three-dimensional flow computation for two interacting, moving droplets

3.1 Problem statement

We consider an unsteady, three-dimensional, incompressible, laminar flow generated by two identical (spherical) droplets injected into initially quiescent constant property Newtonian fluid. The droplets move side by side in the same plane as shown in Figure 9, where d_t denotes the instantaneous distance, normalized by the droplet radius, from the droplet center to the y-z symmetry plane between the two droplets. We neglect the net gravity force acting on the droplet and also assume that the Weber number is small enough that the droplet remains spherical. We choose the origin of a non-rotating noninertial reference frame at the center of mass of the two droplets and the angle of initial droplet motion $\alpha_0 = 0$. Far upstream, the flow is uniform and has an instantaneous velocity $V_{\infty,t} \mathbf{j}$ parallel to the y-axis. It is noted that there are two symmetry planes in Figure 9. One is the x-y plane in which the centers of the two droplets lie, and the other is the y-z plane which is midway between the droplet centers.

As shown in Figure 9, we utilize three coordinate systems in our formulation, the Cartesian coordinates (x,y,z) for the gas phase whose origin is at the center of mass of the two droplets, the Cartesian coordinates (x_l, y_l, z_l) for the liquid phase whose origin is at the droplet center, and also the nonorthogonal generalized coordinates (ξ, η, ζ) . ξ is the radial, η is the angular, and ζ is the azimuthal direction. Due to symmetry of the geometry, the physical domain is chosen as one quarter of an ellipsoid-like space.

Details about the coordinate system, governing equations and boundary conditions, and the numerical method are provided in Reference 18 which is an addendum to this report.

The drag, lift, and moment coefficients are evaluated in dimensional form as follows.

$$F'_D = \int_S -p' \mathbf{n} \cdot \mathbf{e}_D dS' + \int_S \mathbf{n} \cdot \boldsymbol{\tau}' \cdot \mathbf{e}_D dS' \quad (8)$$

$$F'_L = \int_S -p' \mathbf{n} \cdot \mathbf{e}_L dS' + \int_S \mathbf{n} \cdot \boldsymbol{\tau}' \cdot \mathbf{e}_L dS' \quad (9)$$

$$M' = \int_S \mathbf{r}' \times \boldsymbol{\tau}' dS', \quad (10)$$

where $\mathbf{e}_D \equiv (-\sin\alpha_l \mathbf{i} + \cos\alpha_l \mathbf{j})$, $\mathbf{e}_L \equiv (\cos\alpha_l \mathbf{i} + \sin\alpha_l \mathbf{j})$, S' denotes the surface of the droplet, \mathbf{n} is the outward unit normal vector at the surface, \mathbf{r}' is the position vector from the center of the droplet, and $\boldsymbol{\tau}'$ is the viscous stress tensor.

The repelling force is assumed positive. Due to the geometrical symmetry, only the z-component of moment exists, and counter-clockwise direction is assumed positive.

The non-dimensional coefficients of drag, lift, and moment are defined respectively as

$$C_D = \frac{F'_D}{\frac{1}{2}\rho'U_{d,t}'^2\pi a_o'^2} \quad (11)$$

$$C_L = \frac{F'_L}{\frac{1}{2}\rho'U_{d,t}'^2\pi a_o'^2} \quad (12)$$

$$C_M = \frac{\mathbf{M}' \cdot \mathbf{k}}{\frac{1}{2}\rho'U_{d,t}'^2\pi a_o'^3} \quad (13)$$

The moving droplets change their directions due to the interactions with the surrounding fluid. However, in order to insure its accuracy, the computational grid must satisfy the condition that the lift and torque are zero for a single droplet moving in any direction.

3.2 Results and discussion

We first tested the three-dimensional code by solving the steady axisymmetric flow past a single droplet at Reynolds number 100. Since the code developed solves for three Cartesian components of velocity in the transformed grid, an axisymmetric test calculation still exercises the fully three-dimensional aspects of the code.

Here, we discuss the flow generated by an impulsively started single droplet into an initially quiescent fluid using the three-dimensional solution procedure for viscosity ratio of 25 and a density ratio of 300 (liquid to gas) at Reynolds number 100. The time-dependent solution converges asymptotically to the steady-state results. Table 5 lists the drag coefficients (C_{DP} and C_{DV} are respectively the pressure and viscous parts of C_D) as a function of the computational grid density which are in good agreement with the correlation of Rivkind & Ryskin [19]. Table 6 shows two angles measured from the front stagnation point where θ_{1s} is the angle at which the surface vorticity changes its sign and θ_{2s} is the angle at which the surface velocity is zero.

The calculations were performed for three different grids, $N_1 \times N_2 \times N_3$ and $N_{1l} \times N_{2l} \times N_{3l} = 20 \times 11 \times 32$ and $10 \times 11 \times 32$, $30 \times 15 \times 48$ and $15 \times 15 \times 48$, and $40 \times 21 \times 64$ and $20 \times 21 \times 64$, in a computational domain having an outer boundary located at 21 droplet radii from the droplet center. The solutions from the three different grids were stable and smooth, and each takes dimensionless times of 20 to reach steady state.

Tables 5 and 6 show that the results of the $30 \times 15 \times 48$ grid differ by only 0.8 % in the drag coefficient and 0.7 % in the separation angle from those of the $40 \times 21 \times 64$ grid. Thus, for computational economy (a long time period is needed for our time-dependent solution of the moving droplets), we selected the medium size grid $30 \times 15 \times 48$ for the external flow and $15 \times 15 \times 48$ in the liquid phase for the remaining calculations.

For the interaction of two moving droplets, calculations were performed for initial dimensionless distance $d_o = 2$ and 9 at initial Reynolds number 100 for the time period $0 \leq t \leq 250$. This period is about one quarter of the lifetime for a vaporizing droplet injected into a combustor, and so major changes in transport processes and flow field would be expected to occur. The viscosity and density ratios (liquid to gas) for the droplet is 25 and 300, respectively, which are typical of a liquid-hydrocarbon fuel in a high-temperature, high-pressure surrounding gas generally encountered in gas turbine combustors.

Figure 10(a) shows the trajectory of one droplet for $d_o = 2$, where the numbers on the line denote the dimensionless time measured from injection. The final location of the droplet at $t = 250$ is $(d_t, l_t) = (2.505, 212.6)$. Now, since the final location of a single droplet at $t = 250$ in the case of no drag and lift forces acting on it would be $(d_t, l_t) = (2, 250)$, the figure indicates that the two droplets are repelling each other as well as decelerating, and the change of distance (normalized by droplet radius) is much higher (37.4 vs. 0.505) due to the drag than due to the lift force. Figure 10(b) shows the trajectory of one droplet for $d_o = 9$. The final location of the droplet at $t = 250$ is $(d_t, l_t) = (8.968, 213.1)$. The theoretical final location of a single droplet at $t = 250$ in the case of no drag and lift forces would be $(d_t, l_t) = (9, 250)$; therefore, Figure 10(b) indicates that the two droplets are weakly attracting each other as well as decelerating, and the change of distance is much higher due to the drag than due to the lift force.

Figure 11 shows the lift coefficients of the droplet for $d_o = 2$ and 9 as a function of the instantaneous Reynolds number, where the repelling force is taken as positive. The lift coefficient for $d_o = 2$ is positive during the time period $0 \leq t \leq 250$, and becomes gradually smaller in time because the distance between the droplets is increasing and their directions of motion are changing due to the repelling force. On the other hand, the lift coefficient for $d_o = 9$ is negative during that time period but slowly goes towards zero. The change of the distance between the two droplets for $d_o = 9$ case is negligibly small as shown in Figure 10(b). Thus, this result also indicates that the lift coefficient slowly approaches zero when Reynolds number decreases with the fixed dimensionless distance 9. The figure also shows that rapid change occurs initially due to an impulsive start of the droplets and the quasi-steady state occurs when $t \geq 30$.

Figure 12 shows the drag coefficients of the droplet for $d_o = 2$ and 9 as a function of instantaneous Reynolds number. The drag coefficient for $d_o = 2$ is higher than that for $d_o = 9$. In earlier time, the difference is greater but becomes gradually smaller as time increases. The reason is that the droplets for $d_o = 2$ are repelling each other and

the distance between them is increasing, and so the drag becomes gradually smaller. The drag coefficient for $d_o = 9$ is almost identical to that for a single droplet (slightly higher than for a single droplet when $t \geq 30$). We found in Section 2 that for the fixed spheres and $d_o \geq 4$, the drag coefficient is almost identical to that of a single sphere. Figure 12 also shows large drag coefficient initially which indicates that large shear stress and pressure occur initially due to impulsive start.

The moment coefficients are discussed in the addendum. That paper also discusses the sudden drop in the speed at the moment of droplet injection and the monotonic decrease with time following injection. The speed for $d_o = 2$ is lower than $d_o = 9$ due to the larger drag of $d_o = 2$.

4. Three-dimensional flow computation for two interacting, vaporizing, moving droplets.

We consider an unsteady, three-dimensional, variable property, laminar flow generated by two identical (spherical) droplets injected into an initially quiescent, high-temperature, high-pressure air environment. Then, the droplets move side by side in the same plane as shown in Figure 9. The coordinate system is exactly same as that used in Section 3.

Since our goal is to study the flow interaction with the two droplets, we present the equations for the gas and liquid phases. The governing equations in both phases and the boundary conditions are nondimensionalized using the initial droplet radius a'_o as the characteristic length, the initial droplet velocity $U'_{d,o}$ as the characteristic velocity, and the initial air temperature $T'_{\infty,o}$ as the characteristic temperature. The properties in the gas phase are normalized by those at infinity, and the properties in the liquid phase are normalized by initial droplet properties.

Gas phase

$$\frac{\partial \rho}{\partial t} + \nabla \cdot (\rho \mathbf{V}) = 0, \quad (14)$$

$$\rho \frac{d\mathbf{V}_s}{dt} + \frac{\partial \rho \mathbf{V}}{\partial t} + \nabla \cdot (\rho \mathbf{V} \mathbf{V}) = -\nabla p + \frac{2}{Re} \nabla \cdot \boldsymbol{\tau}, \quad (15)$$

$$\begin{aligned} C_p \left(\frac{\partial \rho T}{\partial t} + \nabla \cdot (\rho \mathbf{V} T) \right) + (h_f - h_a) \left(\frac{\partial \rho Y_f}{\partial t} + \nabla \cdot (\rho \mathbf{V} Y_f) \right) \\ = \frac{2}{Re Pr} \nabla \cdot (k \nabla T) + \frac{2}{Re Sc} \nabla \cdot ((h_f - h_a) \rho D \nabla Y_f), \end{aligned} \quad (16)$$

$$\frac{\partial \rho Y_f}{\partial t} + \nabla \cdot (\rho \mathbf{V} Y_f) = \frac{2}{ReSc} \nabla \cdot (\rho D \nabla Y_f), \quad (17)$$

where \mathbf{V}_s is the velocity of the center of mass of the two droplets, $\boldsymbol{\tau}$ is the deviatoric stress tensor, h_f and h_a are the enthalpies of fuel vapor and air, respectively, Y_f is the fuel mass fraction, and D is the diffusivity.

Liquid phase

$$\nabla \cdot \mathbf{V}_l = 0, \quad (18)$$

$$\frac{d\mathbf{V}_d}{dt} + \frac{\partial \mathbf{V}_l}{\partial t} + \nabla \cdot (\mathbf{V}_l \mathbf{V}_l) = -\nabla p_l + \frac{2}{Re_l} \nabla \cdot \boldsymbol{\tau}_l, \quad (19)$$

$$C_{pl} \left(\frac{\partial T_l}{\partial t} + \nabla \cdot (\mathbf{V}_l T_l) \right) = \frac{2}{Re_l Pr_l} \nabla \cdot (k_l \nabla T_l), \quad (20)$$

where \mathbf{V}_d is the droplet velocity and the subscript l denotes the liquid phase.

The governing equations are transformed to the generalized coordinates (ξ, η, ζ) , which allow for any three-dimensional body of arbitrary shape. The numerical integration of the equations is performed using a computational cubic mesh with equal spacing ($\delta\xi = \delta\eta = \delta\zeta = 1$). The conditions at the interface were derived from principle of continuity, conservation, and thermodynamic equilibrium. The overall behavior of droplet vaporization is strongly dependent on the evaluation of local properties at the interface where complex nonlinear transport phenomena take place. A quasi-linearization method was adopted to evaluate iteratively the nonlinear terms in the interface conditions. Kim *et al.* [20] will provide details of the boundary and interface conditions.

The code we have developed will take a large amount of cpu hours on a Cray Y-MP due to the integration for a long time period to capture an unsteady behavior of droplets and three-dimensionality of the problem. To check our numerical algorithm, we solved the flow generated by a *single* cold n-octane fuel droplet suddenly injected into a hot and high pressure gas stream by using a coarse grid ($20 \times 11 \times 32$ in the gas phase and $12 \times 11 \times 32$ in the liquid phase). The values of the physical parameters used are given in Table 7.

Figure 13 shows the history of the drag coefficients for a single vaporizing droplet during the time period $0 \leq t \leq 250$. It is shown that a large drag coefficient is found initially which indicates that large values of shear stress and pressure occur initially due to the impulsive start. During the initial relaxation period, the drag coefficient falls rapidly. Subsequently, the drag coefficient decreases slowly due to the blowing effect on the droplet surface despite a reduction in the Reynolds number.

Figure 14 shows the average Nusselt number as a function of dimensionless time. The average Nusselt number is defined as follows.

$$\begin{aligned}
Nu_{av} &= \frac{2a'_i h'}{k'_\infty} \\
&= \frac{1}{2\pi a_i (T_\infty - T_{s,av})} \int_S k(\nabla T) \cdot \mathbf{n} dS,
\end{aligned} \tag{21}$$

where ' denotes dimensional quantity and k is the thermal conductivity of the gas phase normalized by the thermal conductivity at infinity. Figure 14 shows that the Nusselt number is decreasing with time. The Nusselt number is the dimensionless rate of the heat transfer, and the decrease of the Nusselt number is mainly attributed to the reduction of the Reynolds number due to the droplet deceleration under the action of the drag.

Figure 15 show the average Sherwood number as a function of dimensionless time. The average Sherwood number is defined in dimensional form as follows.

$$\begin{aligned}
Sh_{av} &= \frac{2a'_i h'_m}{\rho'_\infty D'_\infty} \\
&= \frac{1}{2\pi a_i (Y_{f\infty} - Y_{f,s,av})} \int_S \rho D(\nabla Y_f) \cdot \mathbf{n} dS,
\end{aligned} \tag{22}$$

where ' denotes dimensional quantity and D is the mass diffusivity of the gas phase normalized by the mass diffusivity at infinity. Figure 15 shows that the Sherwood number is decreasing with time. The Sherwood number is the dimensionless rate of the mass transfer, and the decrease of the Sherwood number is mainly attributed to the reduction of the Reynolds number.

5. Axisymmetric interactive fuel droplet calculations

This axisymmetrical calculation considers the effects of variable thermophysical properties, transient heating and internal circulation of liquid, deceleration of the flow due to the drag of the droplet, boundary-layer blowing, and moving interface due to surface regression as well as relative droplet motion. Details of the analysis are provided in Reference [7] which is included as an addendum to this report. The results are compared with those of an isolated droplet [21] as well as those of the two-droplet system [6] to investigate the effect of the presence of the third droplet. The interaction effects from the downstream or upstream droplet are identified. Then the behavior of trailing droplets, which follow the first two or three droplets, can be estimated from the results of the first two or three droplets on account of the nearly periodical nature of linear droplet arrangements.

The variations of trajectory with time and drag coefficients vs. instantaneous Reynolds number for the cases of different initial spacings are illustrated in Figure 16. D12 is the

time-dependent nondimensional center-to-center spacing between the first two droplets and D_{23} is the corresponding spacing between the second and third droplets. Results of Case 1 with large initial spacing ($D_{12}=D_{23}=12$) indicate that the drag coefficient is smaller for the second droplet than for the lead droplet and still smaller for the third droplet. The drag coefficient of each droplet is reduced from the isolated droplet value. The major decrease in drag occurs in the first two droplets. In Case 2, the drag coefficients of the lead and the second droplets are significantly reduced (comparing curves 7 and 10, and 8 and 11, respectively) due to the strong interactions when the first two droplets are spaced only two diameters away. Similar trends occur for the downstream droplet pairs of Case 3 (comparing curves 8 and 14, and 9 and 15, respectively). The third droplet in Case 2 has a higher drag coefficient than that of the second droplet since the second droplet is better shielded by the droplet before it. The D_{23} thus increases with time. Also, note that the drag coefficient of the third droplet, which is spaced far away from the second droplet, seems to be approximately independent of D_{12} as indicated in curves 9 and 12. However, it strongly depends upon D_{23} as illustrated in curves 9, 12 and 15.

Results for the cases of sufficiently large spacing (above approximately 6 droplet diameters) show that the flow field of each droplet is qualitatively similar to that of an isolated droplet, although the transport rates are reduced along the downstream direction due to the cascade effect of the wake. The major drops in transport rates occur in the first two droplets. For the cases of small droplet spacings (less than approximately 3 droplet diameters), the flow field of downstream droplets can be significantly altered due to the interaction effects from the upstream droplets. Usually, the second droplet has the lowest drag coefficient since it interacts with both neighboring droplets. However, the difference in transport rates between the second and the third droplets is not significant since both droplets are fully protected by the wake of the first droplet. The effect of D_{23} on the behavior of the first droplet is insignificant. However, depending upon the values of D_{12} as well as D_{23} , the effect of D_{23} on the behavior of the second droplet may become significant. The general qualitative conclusions drawn from the two-droplet study [6] can be applied to two neighboring droplets in the three-droplet analysis. The correlations for heat transfer and droplet dynamics have been developed and are applicable in a one-dimensional droplet spray calculation.

In addition to the general qualitative conclusions drawn from the two-droplet study, we have further obtained the following conclusions:

(1) Results for the cases of sufficiently large spacing (above approximately 6 droplet diameters) show that the flow field of each droplet is qualitatively similar to the field of an isolated droplet, although the transport rates are reduced along the downstream direction due to the cascade effect of the wake.

(2) For the cases of small droplet spacings (less than approximately 3 droplet diameters), the flow field of downstream droplets can be significantly altered due to the interaction effects from the upstream droplets.

(3) The major drop in transport rates occur in the first two droplets. Usually, the recirculating wake from the lead droplet has dissipated a significant portion of the momentum and energy upstream of the second droplet. As a result, the further reduction in transport rates from the second to the third droplet becomes very limited.

(4) Usually, the second droplet has the lowest drag coefficient since it interacts with both neighboring droplets. However, the difference in transport rates between the second and the third droplets is not significant.

(5) The effect of D_{23} on the behavior of the first droplet is insignificant. However, depending upon the values of D_{12} as well as D_{23} , the effect of D_{23} on the behavior of the second droplet is not negligible.

(6) The correlations for heat transfer and droplet dynamics have been developed [7] and are applicable to droplet spray calculation.

6. LOX vaporization at subcritical conditions

The second task involves the axisymmetric calculation of an isolated LOX (liquid oxygen) droplet. A detailed analysis of LOX droplet heating and vaporization and the mixing of the oxygen and fuel vapors in a high temperature, low pressure (10 – 20 atm), convective environment has been conducted. This problem features very complex property calculations along with very high transfer number ($\approx O(100)$) and high density ratio. The variation of liquid-phase density with temperature is significant. The LOX may experience the thermal expansion during the transient heating and the surface moving velocity cannot be neglected. In order to account carefully for unsteadiness due to density variation, the variable liquid-density with primitive variables (V_r, V_z, p_l and ρ_l) are employed. Note that in previous codes [21,6], the liquid-phase momentum equations are formulated by a stream function-vorticity approach. The modifications of the code to adapt the primitive variables for the liquid phase as well as to employ more accurate interface conditions have been developed.

The general considerations include : the effects of variable thermophysical properties, real gas behavior, transient heating and internal circulation of liquid, deceleration of the flow due to the drag of the droplet, boundary-layer blowing, and moving interface. An implicit finite-difference scheme has been developed to solve the complete set of Navier-Stokes, energy, and species equations. Some preliminary results have been presented in Chiang and Sirignano [22]. The results are presented for the low pressure case. The interesting phenomena due to the large surface blowing and surface boiling are examined.

We have learned in all calculations that the LOX droplet surface very quickly reaches the boiling temperature, which is about 120 K for the case of 10 atms ambient pressure. However, the droplet core remains cold since the conductivity is low and, at the early time, the circulation strength is not strong enough to convect much energy. All the available

heat transfer from the gas phase is used to heat the surface and is also utilized for the latent heat of vaporization. The surface boiling persists throughout the droplet lifetime. The very rich and cold oxygen vapor surrounding the droplet is depicted in Figure 17. The large gradient occurs at the front stagnant region as we expect. The LOX droplet would require much of energy for the heat of vaporization rather than for the heating the internal fluid. As a result, the transient droplet heating is responsible for the unsteady thermal behavior of the LOX droplet. The high surface blowing velocity has a significant effect on the flow structure and modifies the flow separation angle and wake length, etc. The drag coefficient, Nusselt and Sherwood numbers are reduced to values below their corresponding stagnant values. A copy of the preprint [22] describing this research is attached as an addendum to this report.

7. LOX vaporization at near-critical or supercritical conditions

Most rocket engine combustors are operated in the very high pressure domain where LOX droplets may vaporize at near or even super-critical conditions. Hence, the current objective of this task is concentrated on an understanding of fundamental transport processes underlying high pressure LOX droplet vaporization.

The extension of the present low pressure model to cover the pressure range from the subcritical region to the supercritical region is currently underway. The solubility of the fuel vapor in the liquid phase makes a multicomponent droplet formulation necessary. Also, a new technique is needed to compute mass fraction and thermophysical properties at gas/liquid phase equilibrium and to account for the droplet regression rate due to vaporization as well as phase change across the critical surface, with continuous density and temperature gradients at the surface.

Several modifications associated with physical behavior have been conducted to extend the previous low pressure LOX droplet vaporizing model to deal with the ambient pressure in the range from the near-critical region to the supercritical region. They are summarized below.

1. A comprehensive calculation of variations of thermophysical properties with respect to temperature for each species component is performed. The high pressure correction, the mixing rules to evaluate the thermodynamic properties, and the quantum gas behavior of hydrogen vapor are considered. The gas-phase and liquid-phase properties tables have been constructed in order to evaluate the thermodynamic properties efficiently by a two-variable linear interpolation.

2. The real gas effect in the high pressure case is taken into account by incorporating a compressibility factor in the gas-phase equation of state. A modified Redlich-Kwong equation of state with the mixing rules of Chueh and Prausnitz are employed. The enthalpy of vaporization is derived from the equation of state by using the fugacity equation.

Since the swelling effect of the LOX vaporization is significant, a primitive variable approach is formulated to analyze the internal motion and thermal and mass transport within the droplet.

3. The solubility of the fuel vapor in the liquid phase has been considered by a multicomponent formulation. The principle of equal temperature, pressure, and fugacity of both phases for phase equilibria is used to compute the surface mass fraction of species for gas and liquid. A brief description of the new phase equilibrium conditions at the droplet interface is given below.

Thermodynamic equilibrium of a mixture gives

$$T^\ell = T^g, \quad P^\ell = P^g, \quad f_i^\ell = f_i^g \quad (23)$$

which ultimately presents the following system of equations to be solved:

$$\begin{aligned} x_{O_2}^\ell \times \phi_{O_2}^\ell(x_{O_2}^\ell, x_{H_2}^\ell, T, P) &= x_{O_2}^g \times \phi_{O_2}^g(x_{O_2}^g, x_{H_2}^g, T, P) \\ x_{H_2}^\ell \times \phi_{H_2}^\ell(x_{O_2}^\ell, x_{H_2}^\ell, T, P) &= x_{H_2}^g \times \phi_{H_2}^g(x_{O_2}^g, x_{H_2}^g, T, P) \end{aligned} \quad (24)$$

$$(25)$$

A phase equilibrium diagram and enthalpy of vaporization from this analysis is given in Figure 18.

The single-component interface equations are replaced by the following interface equations for a multicomponent fluid.

Conservation of species:

$$\left[\dot{m}_v Y_i - \rho D_{ij} \frac{\partial}{\partial r} Y_i \right]_{r+} = \left[\dot{m}_v Y_i - \rho D_{ij} \frac{\partial}{\partial r} Y_i \right]_{r-} \quad (26)$$

Conservation of energy:

$$\begin{aligned} -k \frac{\partial}{\partial r} T \Big|_{r-} &= k \frac{\partial}{\partial r} T \Big|_{r+} + \left[\dot{m}_v Y_{O_2} - \rho D_{ij} \frac{\partial}{\partial r} Y_{O_2} \right]_{r+} (\Delta \bar{H}_{v,O_2} - \Delta \bar{H}_{v,H_2}) \\ &+ \dot{m}_v \Delta \bar{H}_{v,H_2} \end{aligned} \quad (27)$$

where $\dot{m}_v = \rho(V - \dot{r})_{r+}$

4. A new technique is being tested to locate the gas/liquid interface and to compute the regression rate due to vaporization as well as phase change across the critical surface, with continuous density and temperature gradients at the surface.

A calculation is performed to study vaporization behavior before the droplet reaches the critical mixing state. The changes of properties at the interface occur very rapidly during the droplet vaporization. Diffusion length scales are reduced at the elevated pressure. The transport rates are faster than those in the low pressure case; hence, the droplet lifetime is shorter. As a result, a very small time step is mandatory to ensure accuracy. Figure 19 indicates that radius increases with time due to the swelling effect of droplet as well as the condensation of vapor. The reduced enthalpy of vaporization also contributes to the fast vaporization of the droplet. The enthalpy of vaporization shown in Figure 20 is significantly reduced from the conventional "latent heat". A remarkable condensation of gas-phase vapor occurs at the early droplet lifetime. The vaporization begins as the surface temperature increases.

Figure 21 presents the variations of compressibility factors (averaged around the azimuthal direction) for the gas and liquid phases at the interface. When the two compressibilities are equal, the critical mixing state is reached. The apparent trend of two phases merging into one continuous phase is shown. Since the critical mixing state highly depends on temperature and mass fraction, the droplet surface at different locations will reach the critical mixing state at different times. The diffusivity for the liquid phase is, in general, two orders-of-magnitude less than that of the gas phase; as a result, most of the diffusing vapors are concentrated in the boundary-layer region at the interface.

Various kinds of approaches and numerical schemes and algorithms are under examination to address the following difficulties occurring during the computation.

1. The surface temperature rises very quickly for the high pressure case. Since the liquid-vapor equilibrium conditions require a separate iterative-scheme to solve for surface mass fraction and temperature, we have temporarily de-coupled the momentum equations from the energy and species conditions and solved them sequentially. We found that the present method tends to overestimate the blowing velocity at the early droplet time. A relaxation factor is hence applied to decrease artificially the vaporization rate during the early period.

2. An appropriate numerical boundary condition at the droplet center must be developed for the present cylindrical-coordinate velocity formulation and spherical-grid system. Otherwise, local errors occur.

3. Some information about thermophysical properties at the critical state is still being sought.

4. The entire calculation has been very time-consuming. Especially, computation of the compressibility factor (which requires an iterative procedure to solve a cubic polynomial) utilizes a large portion of computing time. We are pursuing alternative strategies (i.e. by a linear interpolation method to fetch the values from existing tables; however, it would require huge memory storages) for simplification of this part of the calculation.

Currently, we have advanced our high-pressure LOX model to deal with the vaporization at supercritical conditions. The major difficulties in the calculation are : 1) the

formulation of boundary conditions, especially to trace the location of the "droplet interface", 2) the property calculation of the "gas/liquid puff" at the interface. Basically, we have developed two modelling approaches, which are currently undergoing investigation, to handle the interface conditions. Here, we briefly describe our strategies step-by-step to make calculations at supercritical conditions.

(1) Determine the critical mixing temperature with respect to various pressure levels. The Redlich-Kwong equation of state with the mixing rules of Chueh and Prausnitz is employed for vapor-liquid equilibria calculation for H_2/O_2 system. The critical mixing temperature is determined when the compressibilities (or mass fractions of a component) at both phases reach the same value. Figure 22 demonstrates that the critical mixing temperature and oxygen mass fraction at the interface reduce, while compressibility increases as pressure increases.

(2) The droplet "pseudo-interface location" is determined by the critical mixing temperature. Note that the pseudo-interface will slightly deviate from its original spherical shape due to the convective effects in both gas and liquid phases. In calculating the vaporization rate, it is still assumed that the droplet remains spherical (by the use of an averaged radius).

(3) The first approach assumes that there is no gas/liquid interface. The flowfield is continuous from the gas phase to the liquid phase and the problem is solved as a single-phase problem. The solutions strongly depend on the property evaluation at the interface.

(4) Since there is limited availability of the critical point thermo-physical properties data in the literature, we assume that all thermo-physical properties are also continuous from the liquid to the gas phase. The consideration of singular behavior of some thermo-physical properties is excluded in the present study. A second-order linear interpolation scheme is employed to obtain the values at critical mixing state. However, we have learned that the direct calculation of density using this approach will lead to a failure in the calculation of vaporization rate. Hence, the density is obtained from compressibility relations. The variation of mass with respect to time is shown in Figure 23. After an early condensing period, the droplet reaches the critical mixing state and the evaporation rate increases dramatically beyond the critical point.

(5) Another modelling approach assumes that there exists a spherical "pseudo-interface." The gas and liquid phase equations are solved separately, and the solutions are matched at the interface. In this approach, constant-temperature (at its critical mixing state) and constant-mass-fraction interface conditions are employed. The shear (or normal) stress conditions are applied even though the surface tension vanishes at the interface. We still suffered some numerical difficulties in this approach and the preliminary numerical results are not comparable to the existing data.

In parallel to the high-pressure LOX calculation, we are modifying the previous program for the interactive hydrocarbon-fuel droplet to take LOX or hydrogen droplet va-

porization into account. The modifications include: (1) a primitive variables approach for the liquid phase, (2) thermodynamics property evaluations for oxygen and hydrogen fuel, and (3) more accurate formulation of the interface to include droplet surface expansion.

We currently are addressing several technical difficulties listed below:

1. There is a need for a suitable initial variable profile to start the calculation. The pressure field (and mass residual sum) between two droplets could destroy the solutions since a large magnitude of vaporization occurs if droplets suddenly encounter an inappropriate temperature profile at the beginning of the simulation.

2. The computation will be very costly. The whole primitive variables calculation for a vaporizing LOX or hydrogen droplet requires a very small time step to guarantee a converged solution at the droplet interface. In addition, the grid generation routine requires more iterations to keep track of the rapidly recessing droplet surface.

We will modify the current computational model to improve the numerical stability problem. Also, a simple formulation of droplet vaporization may be constructed in order to conserve our very limited CRAY Y-MP hours. More detailed thermophysical property information for a hydrogen droplet is currently being compiled.

Acknowledgement

We would like to thank Mr. Lyle Wiedeman and Dr. Allen Schiano in the Office of Academic Computing of UCI for their assistance in using a three-dimensional graphic package Application Visualization System (AVS). The support of the Pittsburgh Supercomputing Center and the San Diego Supercomputer Center under a block grant of the Office of Academic Computing of UCI are gratefully acknowledged.

References

1. Sirignano, W. A., 1983, Fuel droplet vaporization and spray combustion. *Prog. Energy and Comb. Sci.* 291-322.
2. Patnaik, G., 1986, A numerical solution of droplet vaporization with convection. Ph.D. Dissertation, Carnegie-Mellon University.
3. Tal(thau), R., Lee, D. N. & Sirignano, W. A., 1983, Hydrodynamics and heat transfer in sphere assemblages - cylindrical cell models. *Int. J. Heat Mass Transfer* **26**, No. 9, 1265-1273.
4. Tal(thau), R., Lee, D. N. & Sirignano, W. A., 1984, Heat and momentum transfer around a pair of spheres in viscous flow. *Int. J. Heat Mass Transfer* **27**, No. 11, 1253-1262.
5. Raju, M. S. & Sirignano, W. A., 1990, Interaction between two vaporizing droplets in an intermediate-Reynolds-number flow. *Phys. Fluids A*, **2**(10), 1780-1796.
6. Chiang, C. H. & Sirignano, W. A., 1993a, Numerical analysis of interacting, convecting, vaporizing fuel droplets with variable properties. *Int. J. Heat Mass Transfer*, in press.
7. Chiang, C. H. & Sirignano, W. A., 1993b, Axisymmetric calculations of three-droplet interactions. *Atomization and Sprays*, in press.
8. Anderson, D. A., Tannehill, J. C. & Pletcher, R. H., 1984, *Computational Fluid Mechanics and Heat Transfer*. Hemisphere Publishing.
9. Kim, I., Elghobashi S. & Sirignano, W. A., 1993, Three-dimensional flow over two spheres placed side by side. *J. Fluid Mech.* **246**, 465-488.
10. Roos, F. W. & Willmarth, W. W., 1971, Some experimental results on sphere and disk drag. *AIAA J.* **9**, 285-291.
11. Clift, R., Grace, J. R. & Weber, M. E., 1978, *Bubbles, Drops, and Particles*. Academic Press, New York.
12. Taneda, S., 1956, Experimental investigation of the wake behind a sphere at low Reynolds number. *J. Phys. Soc. Japan* **11** 1104-1108.
13. Rosfjord, T. J., 1974, Experimental and theoretical investigations of the recirculating flow region between two-dimensional, parallel, separated jets. Ph.D. Dissertation, Princeton University.

14. Dandy, D. S. & Dwyer, H. A., 1990, A sphere in shear flow a finite Reynolds number: effect of shear on particle lift, drag, and heat transfer. *J. Fluid Mech.* **216**, 381-410.
15. Goldburg, A. & Florsheim, B. H., 1966, Transition and Strouhal number for the incompressible wake of various bodies. *Phys. Fluids* **9**, 45-50.
16. Nakamura I., 1976, Steady wake behind a sphere. *Phys. Fluids* **19**, 5-8.
17. Kim, I. & Pearlstein, A. J., 1990, Stability of the flow past a sphere. *J. Fluid Mech.* **211**, 73-93.
18. Kim, I., Elghobashi S. & Sirignano, W. A., 1992, Three-dimensional flow computation for two interacting, moving droplets. AIAA preprint 92-0343.
19. Rivkind V. Y. & Ryskin, G., 1976, Flow structure in motion of a spherical drop in a fluid medium at intermediate Reynolds numbers. *Fluid Dyn.* **11**, 5-12.
20. Kim, I., Elghobashi S. & Sirignano, W. A., 1993, Three-dimensional flow computation for two interacting, vaporizing, moving droplets with variable properties. to be presented at AIAA 24th Fluid Dynamics Conference, Orlando, Florida.
21. Chiang, C. H., Raju, M. S. & Sirignano, W. A., 1992, Numerical analysis of convecting, vaporizing fuel droplet with variable properties. *Int. J. Heat Mass Transfer*, **35**, No. 5, pp. 1307-1324.
22. Chiang, C. H. & Sirignano, W. A., 1991, Axisymmetric vaporizing oxygen droplet computations. AIAA preprint 91-0281, presented at the *AIAA 29th Aerospace Sciences Meeting*, Reno, Nevada.

Professional Personnel

W. A. Sirignano, Professor, Principal investigator.

S. E. Elghobashi, Professor.

I. Kim, Postdoctoral research associate, Ph. D. January 1990 – present.

C. H. Chiang, Postdoctoral research associate, Ph. D. September 1990 – present,
Ph. D. candidate prior to September 1990.

Dissertation Title: Isolated and interacting, vaporizing fuel droplets: field calculation with variable properties.

Publications

The following papers and one book article have resulted at least partially from the research performed under this research program.

1. Raju, M. S. & Sirignano, W. A., 1990, Interaction between two vaporizing droplets in an intermediate-Reynolds-number flow. *Phys. Fluids A*, **2**(10), 1780-1796.
2. Chiang, C. H. & Sirignano, W. A., 1991, Axisymmetric vaporizing oxygen droplet computations. AIAA preprint 91-0281, presented at the *AIAA 29th Aerospace Sciences Meeting*, Reno, Nevada.
3. Sirignano, W. A., Chiang, C. H., Kim, I. & Elghobashi, S. E., 1991, Aerodynamic interactions amongst neighboring droplets, presented at the 4th international Symposium on Computational Fluid Dynamics.
4. Sirignano, W. A., 1991, Computational challenges in spray combustion, presented at the U. S. - Japan Heat Transfer Seminar.
5. Delplanque, J. P., Chiang, C. H. & Sirignano, W. A., 1991, Numerical simulation and modelling of LOX droplet vaporization at supercritical conditions, presented at the 28th JANNAF Combustion Meeting.
6. Kim, I., Elghobashi S. & Sirignano, W. A., 1991, Three-dimensional flow interactions between two neighboring spheres, presented at the *44th Annual Meeting of the Division of Fluid Dynamics of the American Physical Society*, Scottsdale, Arizona.
7. Kim, I., Elghobashi S. & Sirignano, W. A., 1992, Three-dimensional flow computation for two interacting, moving droplets. AIAA preprint 92-0343, presented at the *AIAA 30th Aerospace Sciences Meeting*, Reno, Nevada.

8. Chiang, C. H., Raju, M. S. & Sirignano, W. A., 1992, Numerical analysis of convecting, vaporizing fuel droplet with variable properties. *Int. J. Heat Mass Transfer*, **35**, No. 5, pp. 1307-1324.
9. Sirignano, W. A., 1993, Computational spray combustion, in Numerical Modelling in Combustion, (Chung, T. J. ed.), Hemisphere Publication. in press.
10. Chiang, C. H. & Sirignano, W. A., 1993a, Numerical analysis of interacting, convecting, vaporizing fuel droplets with variable properties. *Int. J. Heat Mass Transfer*, in press. Also see Preprint No. 90-0357, AIAA 28th Aerospace Sciences Meeting.
11. Chiang, C. H. & Sirignano, W. A., 1993b, Axisymmetric calculations of three-droplet interactions. *Atomization and Sprays*, in press. Also presented at the *Fifth international ICLASS Conference on Liquid Atomization and Spray Systems*.
12. Kim, I., Elghobashi S. & Sirignano, W. A., 1993, Three-dimensional flow over two spheres placed side by side. *J. Fluid Mech.* **246**, 465-488.
13. Kim, I., Elghobashi S. & Sirignano, W. A., 1993, Three-dimensional flow computation for two interacting, vaporizing, moving droplets with variable properties. to be presented at the *AIAA 24th Fluid Dynamics Conference*, Orlando, Florida.
14. Sirignano, W. A., 1993, Fluid dynamics of sprays (invited Freeman Scholar paper). *J. Fluids Engineering*, in press.
15. Sirignano, W. A., Delplanque, J. P. & Chiang, C. H., 1993, Liquid propellant droplet vaporization, Driving mechanism for rocket combustion instability, to be presented at the *First International Symposium on Liquid Rocket Combustion Instability*.

Presentations

1. Chiang, C. H., "Numerical analysis of interacting, convecting, vaporizing fuel droplets with variable properties," presented at the AIAA 28th Aerospace Sciences Meeting, Reno, Nevada, Jan. 1990.
2. Sirignano, W. A., "Combustion instability computational analysis," presented at the JANNAF Workshop on Numerical Methods in Combustion Instability, Orlando, FL, Feb. 1990.
3. Sirignano, W. A., "Fundamental studies of droplet interactions in dense sprays," presented at the AFOSR Contractors' Meeting, Atlanta, GA, June 1990.

4. Sirignano, W. A., "Heat and mass transfer in liquid-gas spray systems," presented at the ASME Winter Annual Meeting, Dallas, TX, Nov. 1990.
5. Chiang, C. H., "Axisymmetric vaporizing oxygen droplet computations," presented at the AIAA 29th Aerospace Sciences Meeting, Reno, Nevada, Jan. 1991.
6. Sirignano, W. A., "Interacting LOX droplets in dense sprays," presented at the AFOSR Contractors' Meeting, Boulder, CO, June 1991.
7. Sirignano, W. A., "Aerodynamic interactions amongst neighboring droplets," presented at the 4th international Symposium on Computational Fluid Dynamics, UC Davis, CA, Sep. 1991.
8. Sirignano, W. A., "Computational challenges in spray combustion," presented at the U. S. - Japan Heat Transfer Seminar, Oiso, Japan, Oct. 1991.
9. Sirignano, W. A., "Numerical simulation and modelling of LOX droplet vaporization at supercritical conditions," presented at the 28th JANNAF Combustion Meeting, Brooks Air Force Base, San Antonio, TX, Oct. 1991.
10. Sirignano, W. A., "Axisymmetric calculations of three-droplet interactions," presented at the Fifth international ICLASS Conference on Liquid Atomization and Spray Systems, Gaithersburg, MD, July 1991.
11. Kim, I., "Three-dimensional flow interactions between two neighboring spheres," presented at the 44th Annual Meeting of the Division of Fluid Dynamics of the American Physical Society, Scottsdale, Arizona, Nov. 1991.
12. Kim, I., "Three-dimensional flow computation for two interacting, moving droplets," presented at the AIAA 30th Aerospace Sciences Meeting, Reno, Nevada, Jan. 1992.
13. Sirignano, W. A., "Recent Advances in fuel droplet and spray theory," UC San Diego, CA, Jan. 1992.
14. Sirignano, W. A., "Recent Advances in fuel droplet and spray theory," University of Southern California, CA, March 1992.
15. Sirignano, W. A., "Fundamentals of spray combustion," *AFOSR Propulsion Contractors Meeting*, LaJolla, CA, June 1992.
16. Sirignano, W. A., "Fluid dynamics of sprays (invited Freeman Scholar paper)," presented at the ASME Winter Annual Meeting, Anaheim, CA, Nov. 1992.

17. Kim, I., "Three-dimensional flow computation for two interacting, vaporizing, moving droplets with variable properties," to be presented at the AIAA 24th Fluid Dynamics Conference, Orlando, Florida, July 1993.

Interactions

Many of the papers listed under publications were presented as conference papers. Even journal papers usually were presented in a precursor form. We have participated in AFOSR Contractors Meetings and Workshops as requested by the sponsor. W. A. Sirignano has served in several advisory or consultant roles with NASA, the National Research Council, and major government contractors. In particular, he has served as: Member, NASA Space Science and Application Advisory Committee; Member, National Research Council Space Studies Board and Chairman, Committee on Microgravity Research; Consultant, United Technologies Research Center; Consultant, Allison Gas Turbine Division of General Motors; Consultant, Sandia National Laboratories; Member, USRA Science Council for Microgravity Science and Applications. Dr. Sirignano has been involved in other research programs funded by AFWAL, AFAL, and ONR that have some relationship to the research performed in this program. Various invited seminars, invited papers or articles, and honors have resulted for the principal investigator based, at least partially, on this AFOSR research. Examples are the 1992 ASME Freeman Scholar Award, which involves a special ASME lecture and journal article, the 1992 AIAA Combustion and Propellants Award, upgrade to Fellow of the AAAS, and the 1991 AIAA Pendray Aerospace Literature Award.

$N_1 \times N_2 \times N_3$	C_{DP}	C_{DV}	C_D	C_D^*
$20 \times 21 \times 21$	0.706	0.951	1.657	
$30 \times 31 \times 31$	0.683	0.934	1.617	
$40 \times 41 \times 41$	0.676	0.929	1.605	1.58

Table 1. Drag coefficients as a function of grid density at $Re = 50$, where * denotes the data from Roos & Willmarth (1971) and also Clift *et al.* (1978).

$N_1 \times N_2 \times N_3$	P_{of}	P_{or}	θ_s	θ_s^*
$20 \times 21 \times 21$	0.611	-0.1088	136.53	
$30 \times 31 \times 31$	0.606	-0.0982	138.10	
$40 \times 41 \times 41$	0.604	-0.0954	138.63	139.3

Table 2. Pressure at the front and rear stagnation points and the separation angle measured from the front stagnation point as a function of grid density at $Re = 50$, where * denotes the data from Clift *et al.* (1978).

$N_1 \times N_2 \times N_3$	C_{DP}	C_{DV}	C_D	C_D^*
$20 \times 21 \times 21$	0.555	0.593	1.148	
$30 \times 31 \times 31$	0.532	0.582	1.114	
$40 \times 41 \times 41$	0.524	0.581	1.105	1.09

Table 3. Drag coefficients as a function of grid density at $Re = 100$, where * denotes the data from Roos & Willmarth (1971) and also Clift *et al.* (1978).

$N_1 \times N_2 \times N_3$	P_{of}	P_{or}	θ_s	θ_s^*
$20 \times 21 \times 21$	0.555	-0.0924	124.24	
$30 \times 31 \times 31$	0.555	-0.0819	125.74	
$40 \times 41 \times 41$	0.554	-0.0789	126.25	126.5

Table 4. Pressure at the front and rear stagnation points and the separation angle measured from the front stagnation point as a function of grid density at $Re = 100$, where * denotes the data from Taneda (1956) and Clift *et al.* (1978).

Gas	Liquid				
$N_1 \times N_2 \times N_3$	$N_{1l} \times N_{2l} \times N_{3l}$	C_{DP}	C_{DV}	C_D	C_D^*
$20 \times 11 \times 32$	$10 \times 11 \times 32$	0.542	0.586	1.128	
$30 \times 15 \times 48$	$15 \times 15 \times 48$	0.520	0.573	1.092	
$40 \times 21 \times 64$	$20 \times 21 \times 64$	0.511	0.571	1.081	1.08

Table 5. Drag coefficients as a function of grid density at $Re = 100$, where * denotes the data from the correlation. of Rivkind & Ryskin (1976)

Gas	Liquid		
$N_1 \times N_2 \times N_3$	$N_{1l} \times N_{2l} \times N_{3l}$	θ_{1s}	θ_{2s}
$20 \times 11 \times 32$	$10 \times 11 \times 32$	126.81	146.50
$30 \times 15 \times 48$	$15 \times 15 \times 48$	127.70	150.13
$40 \times 21 \times 64$	$20 \times 21 \times 64$	127.74	151.20

Table 6. Angles at which the surface vorticity changes its sign and the surface velocity is zero as a function of grid density at $Re = 100$, where the angles are measured from the front stagnation point.

Parameter	Value
Initial Reynolds number in gas phase	100
Relative velocity of droplet, m/s	25
Free stream temperature, K	1250
Combustor pressure, atm	10
Prandtl number in gas phase	0.74
Prandtl number in liquid phase	8.53
Schmidt number in gas phase	2.33
Molecular weight of oxidizer, kg/kmol	29.0
Molecular weight of fuel (n-octane), kg/kmol	114.2
Droplet initial temperature, K	300
Viscosity ratio (liquid to gas)	10.5
Density ratio (liquid to gas)	247.9
Specific heat ratio (liquid to gas)	1.89
Latent heat, cal/g	72.5

Table 7. Physical parameters used in the calculation

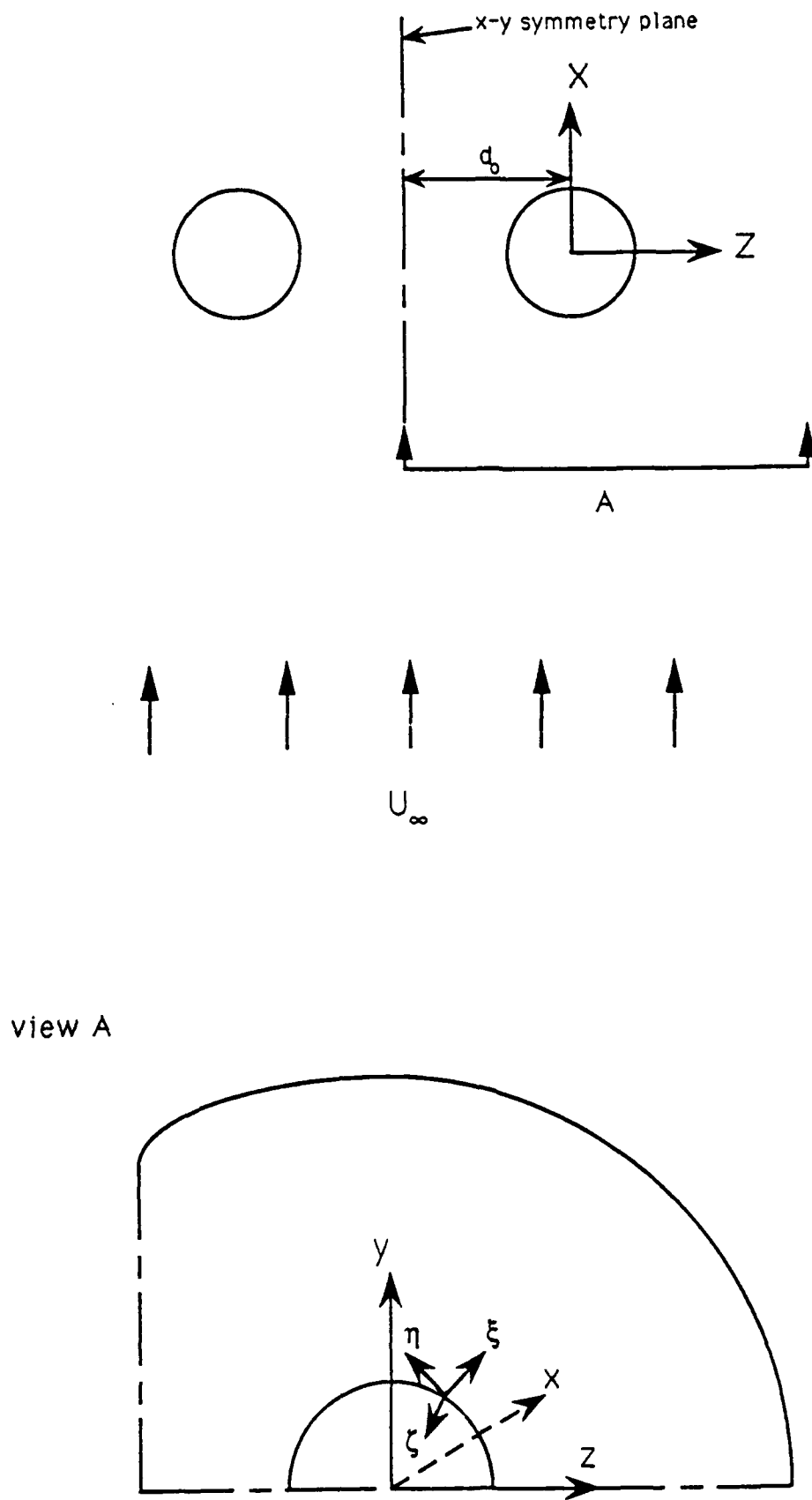


Figure 1. Flow geometry and coordinates

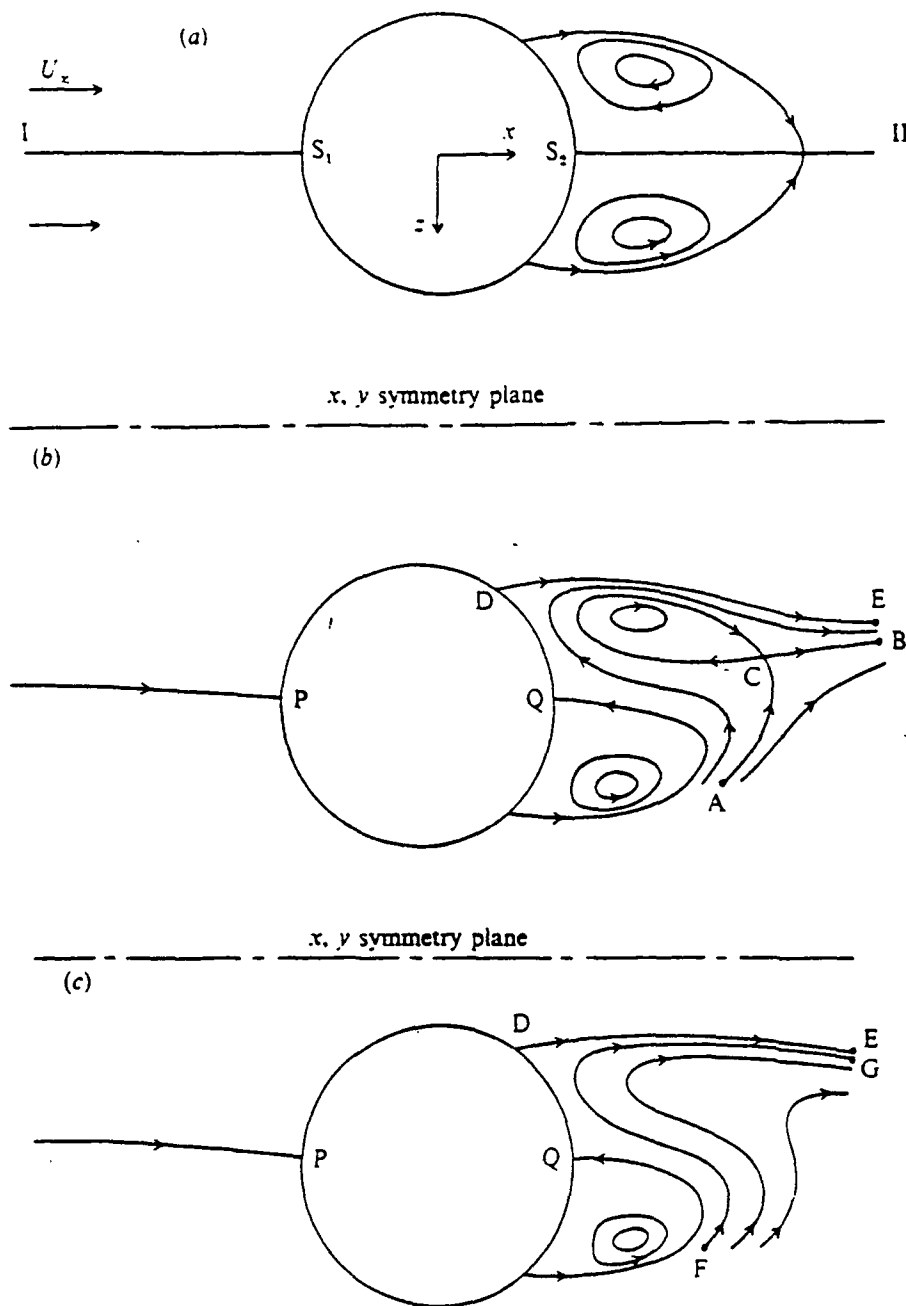


Figure 2. Sketch of typical streamlines over one of the two solid spheres in the principal plane (x-z plane) at $Re = 100$ for (a) axisymmetric flow; (b) $d_o = 2$; (c) $d_o = 1.5$.

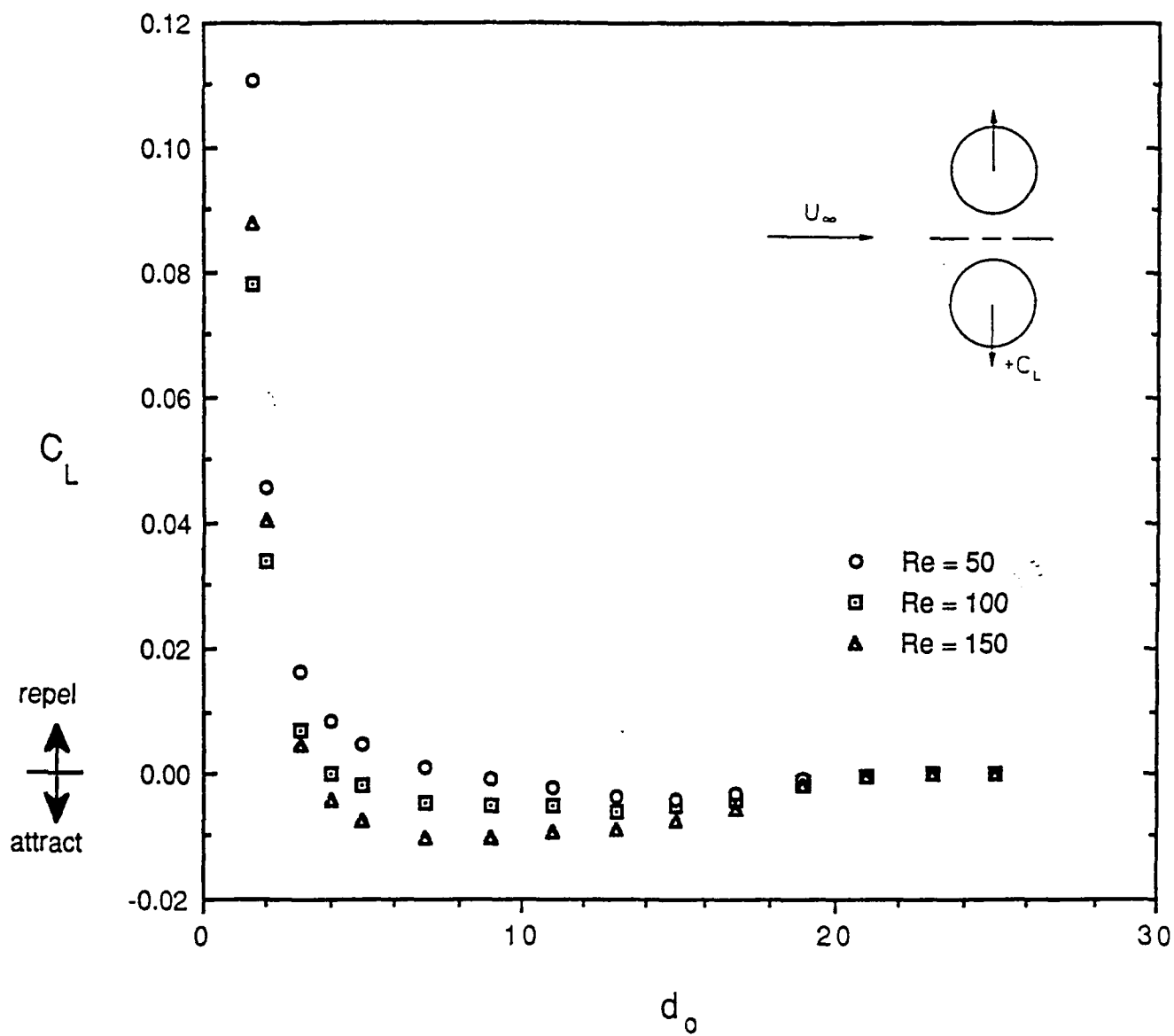


Figure 3(a) Total lift coefficient of the solid sphere as a function of d_o at $Re = 50, 100$, and 150

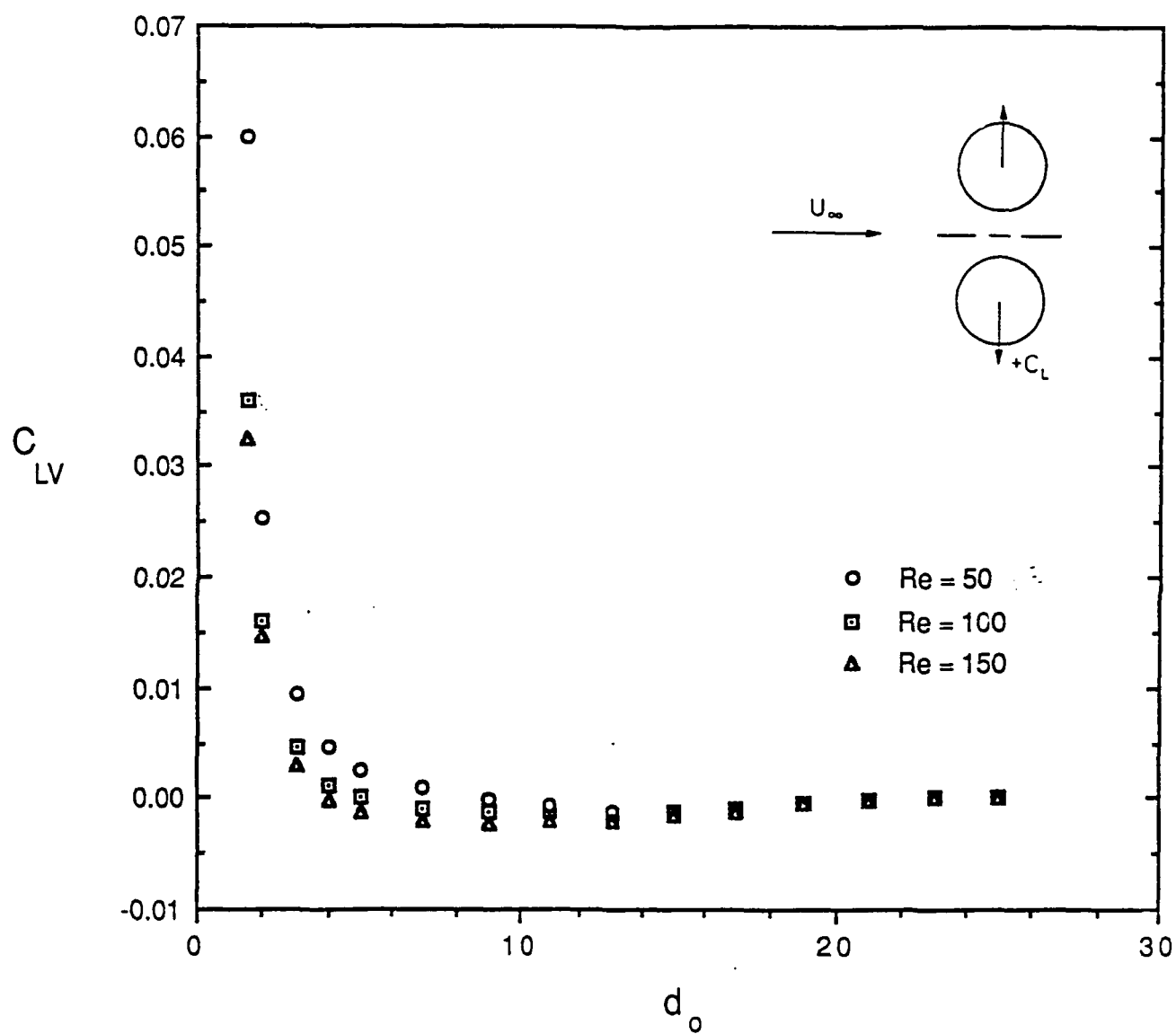


Figure 3(b) Viscous contribution to the lift coefficient of the solid sphere as a function of d_o at $Re = 50, 100$, and 150

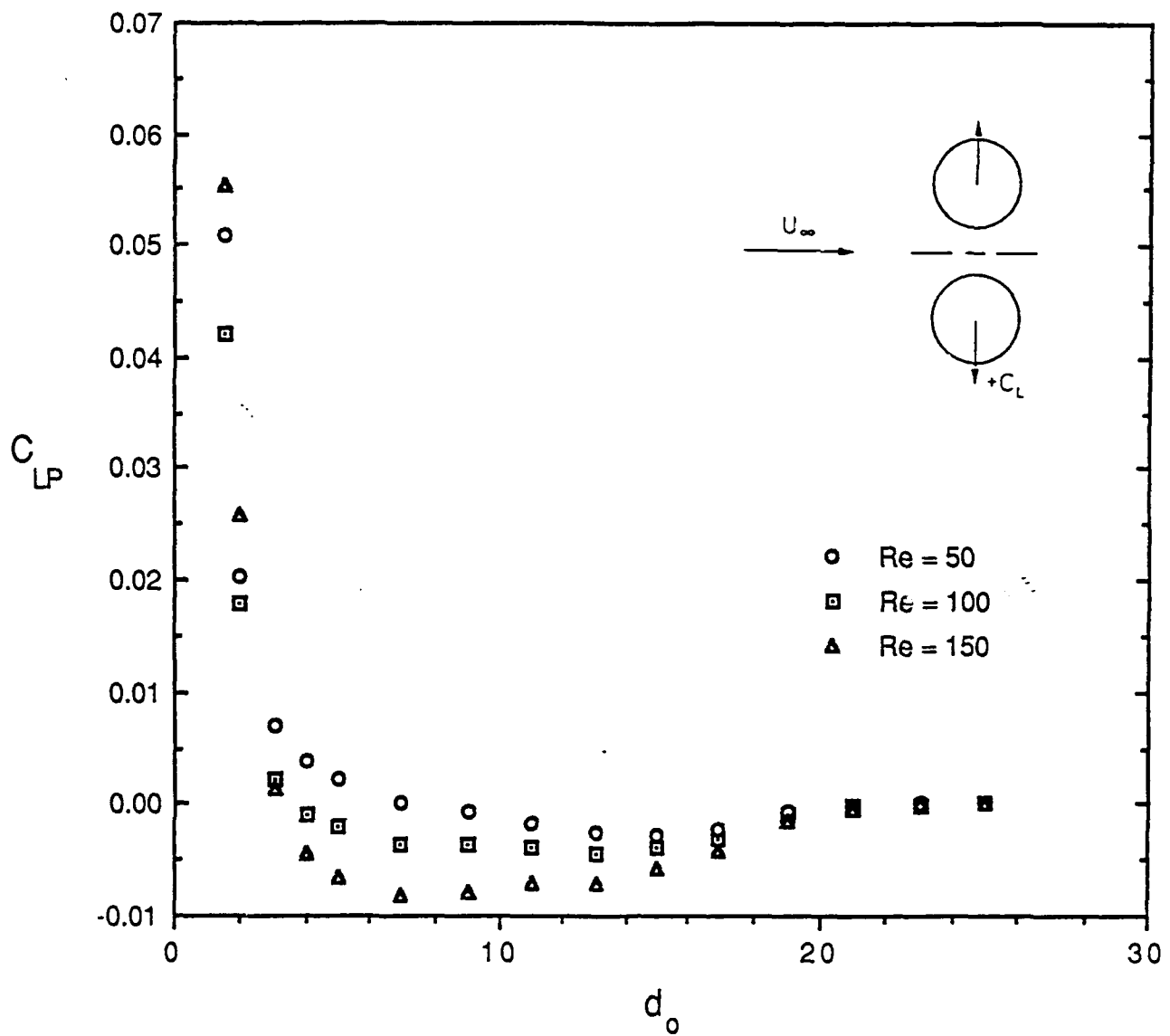


Figure 3(c) Pressure contribution to the lift coefficient of the solid sphere as a function of d_o at $Re = 50, 100$, and 150

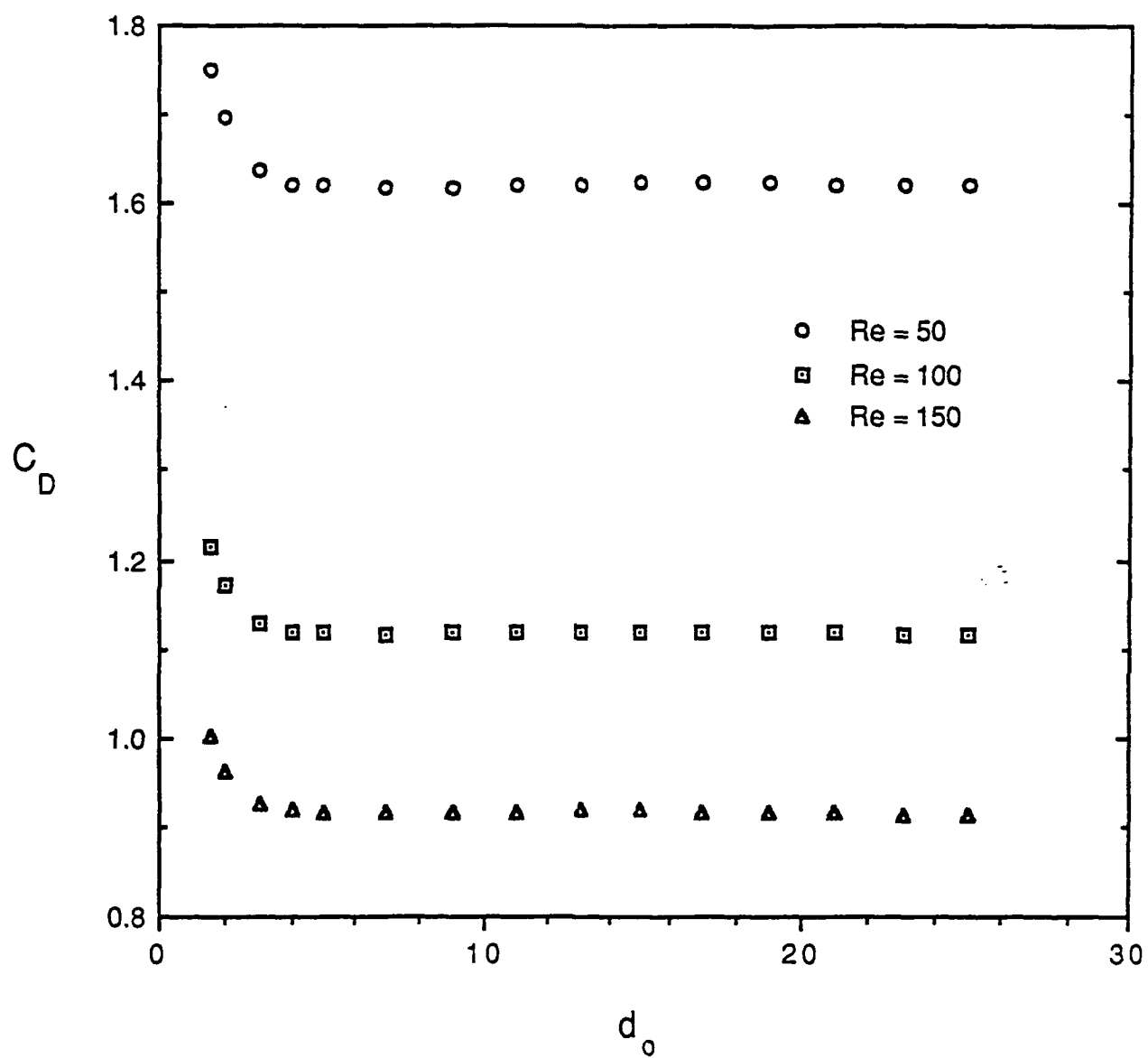
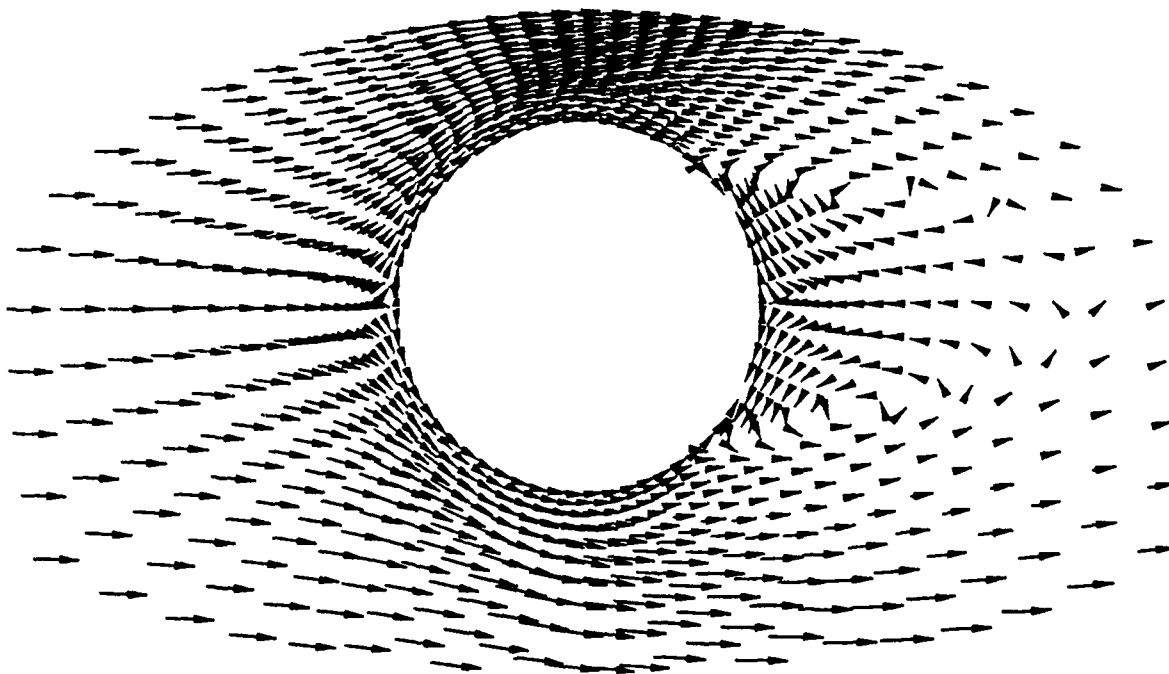


Figure 4. Drag coefficient of the solid sphere as a function of d_o at $Re = 50, 100$, and 150 .

(a)



(b)

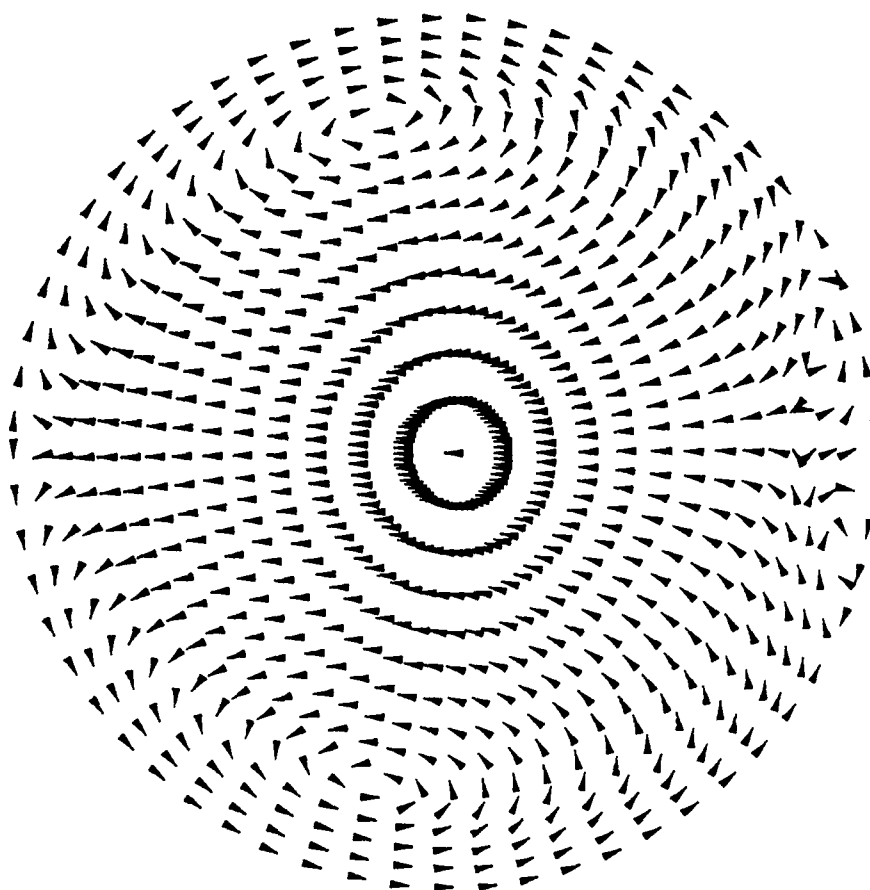
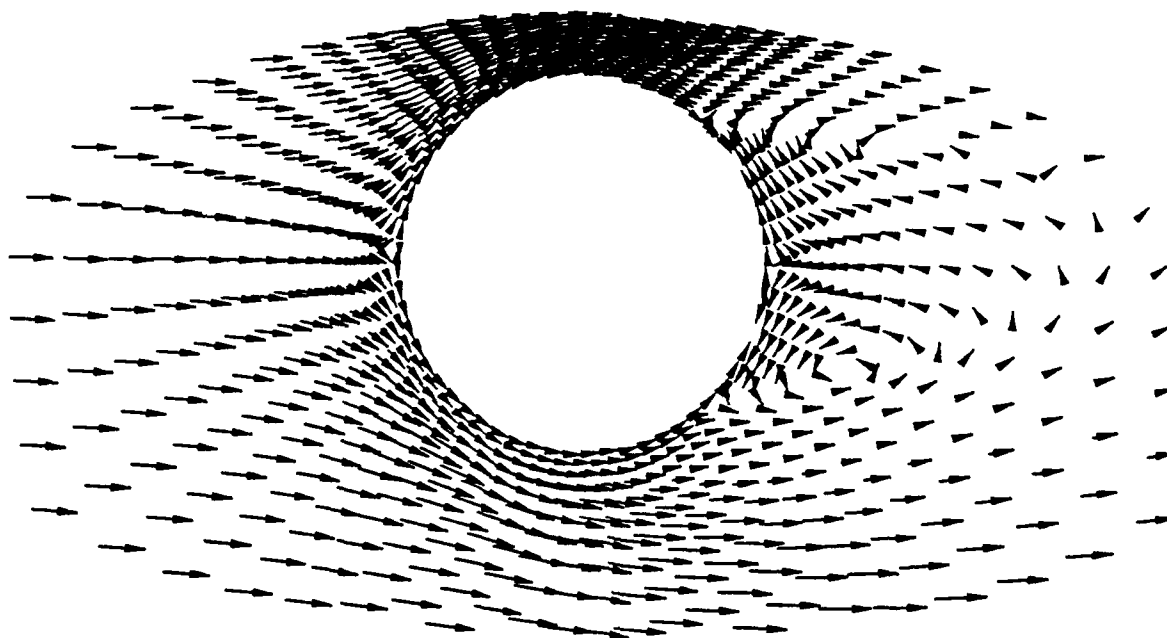


Figure 5. Velocity vector fields in the principal plane for a liquid sphere at $Re = 100$ for $d_o = 2$: (a) external flow; (b) internal flow

(a)



(b)

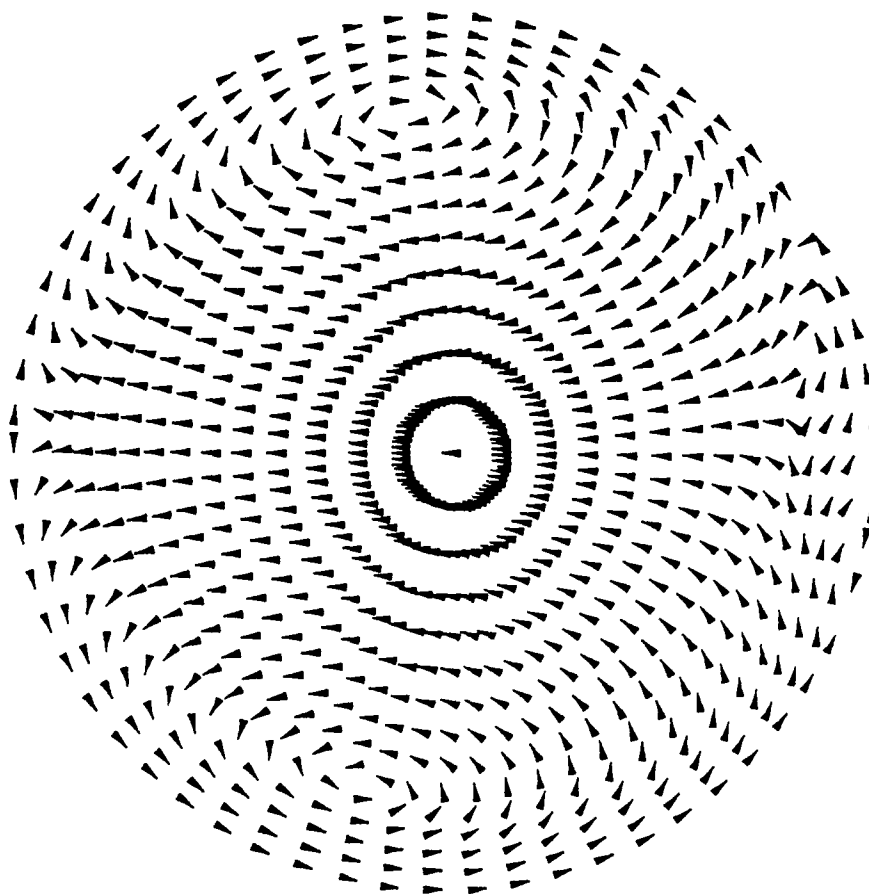


Figure 6. Velocity vector fields in the principal plane for a liquid sphere at $Re = 100$ for $d_o = 1.5$: (a) external flow; (b) internal flow

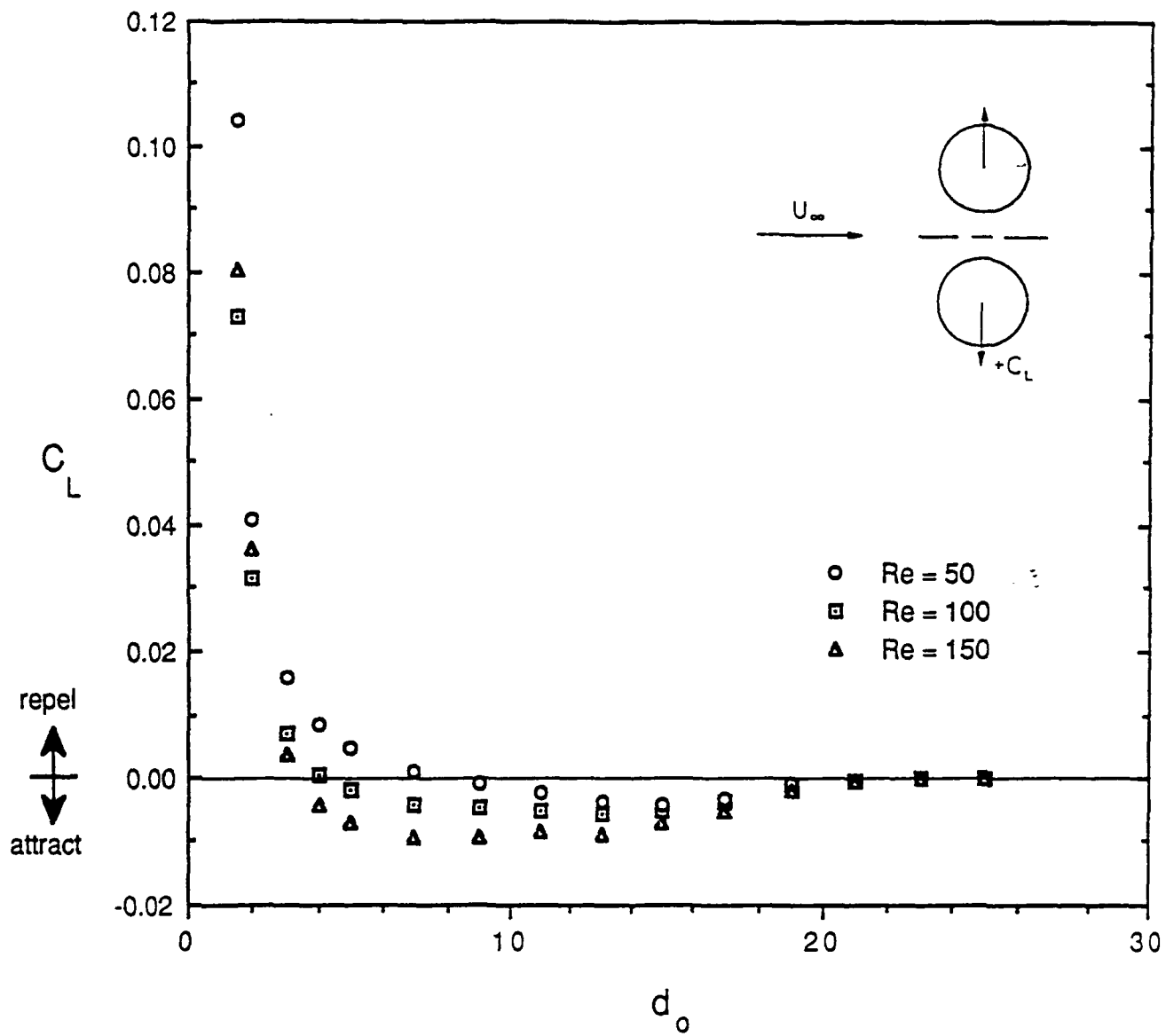


Figure 7. Total lift coefficients of the liquid sphere as a function of d_o at $Re = 50, 100$, and 150

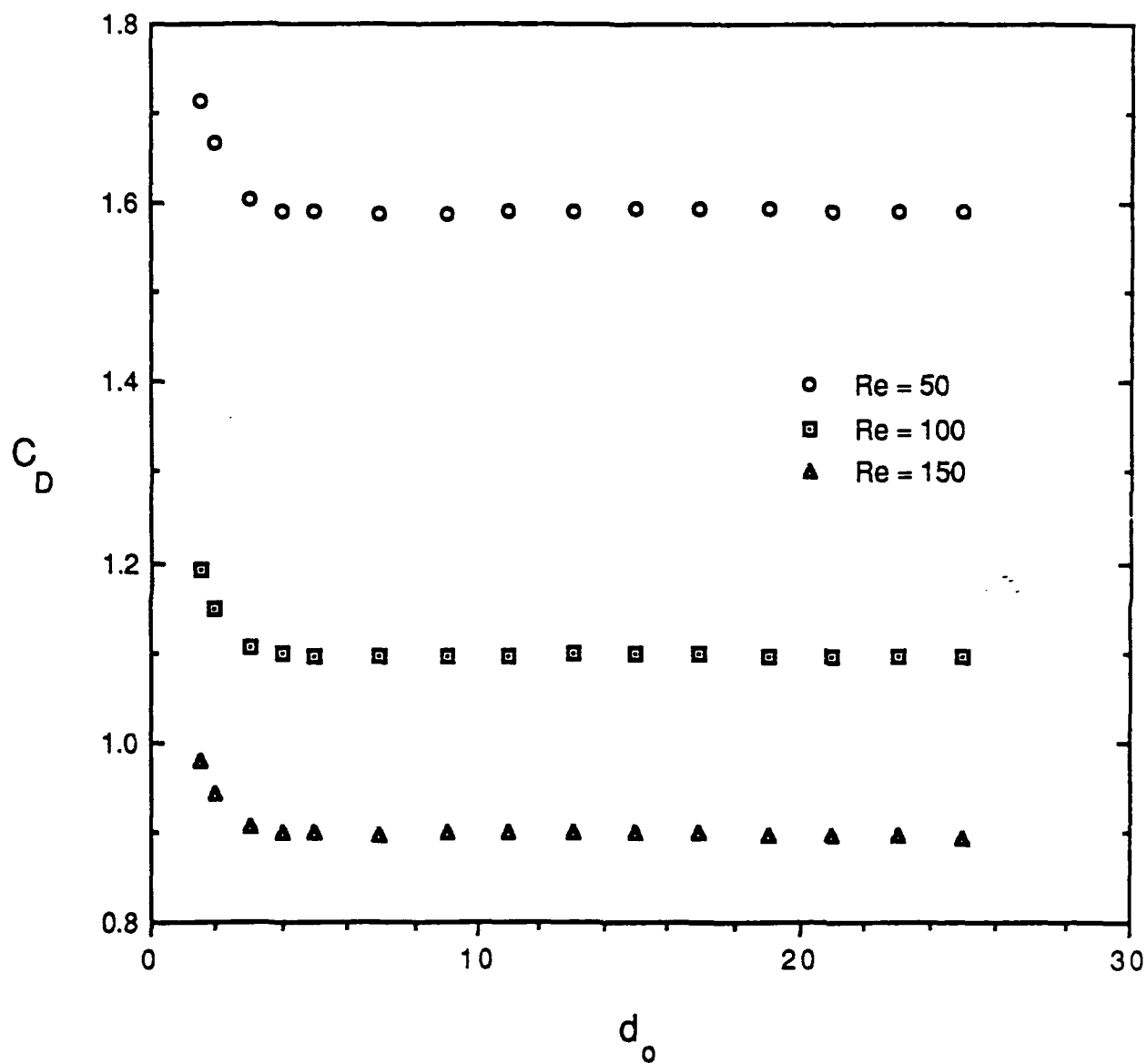
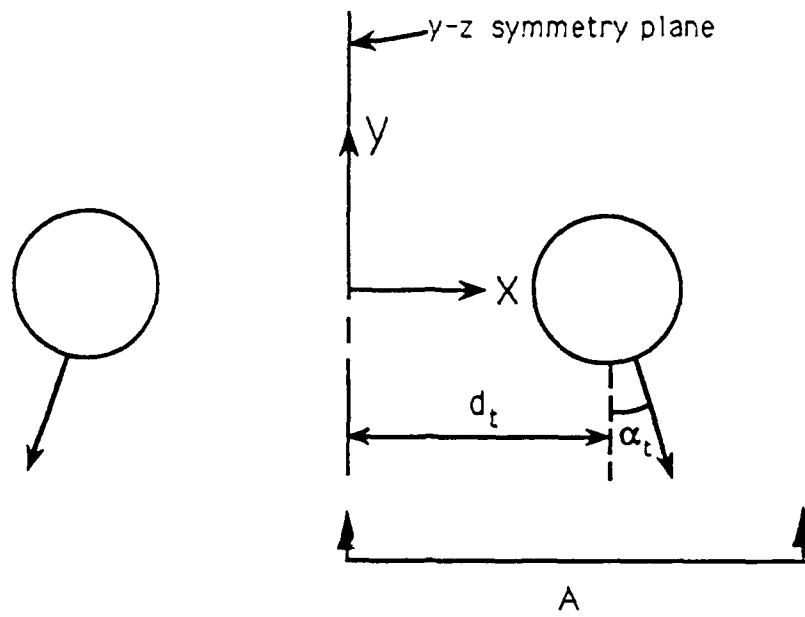


Figure 8. Drag coefficient of the liquid sphere as a function of d_o at $Re = 50, 100$, and 150 .



view A

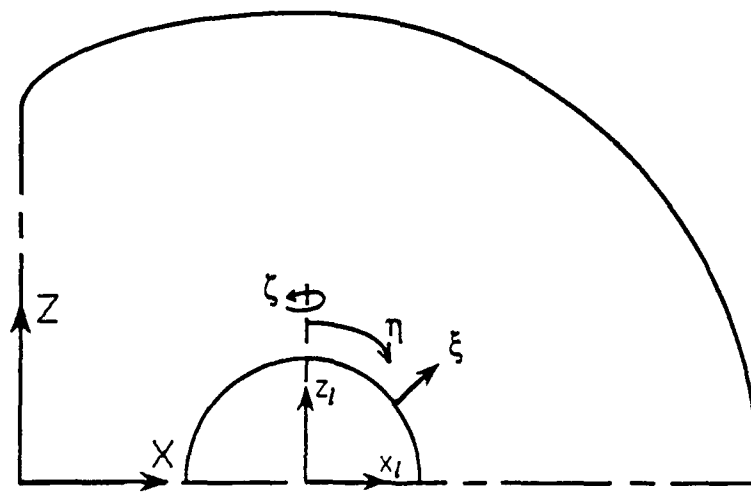
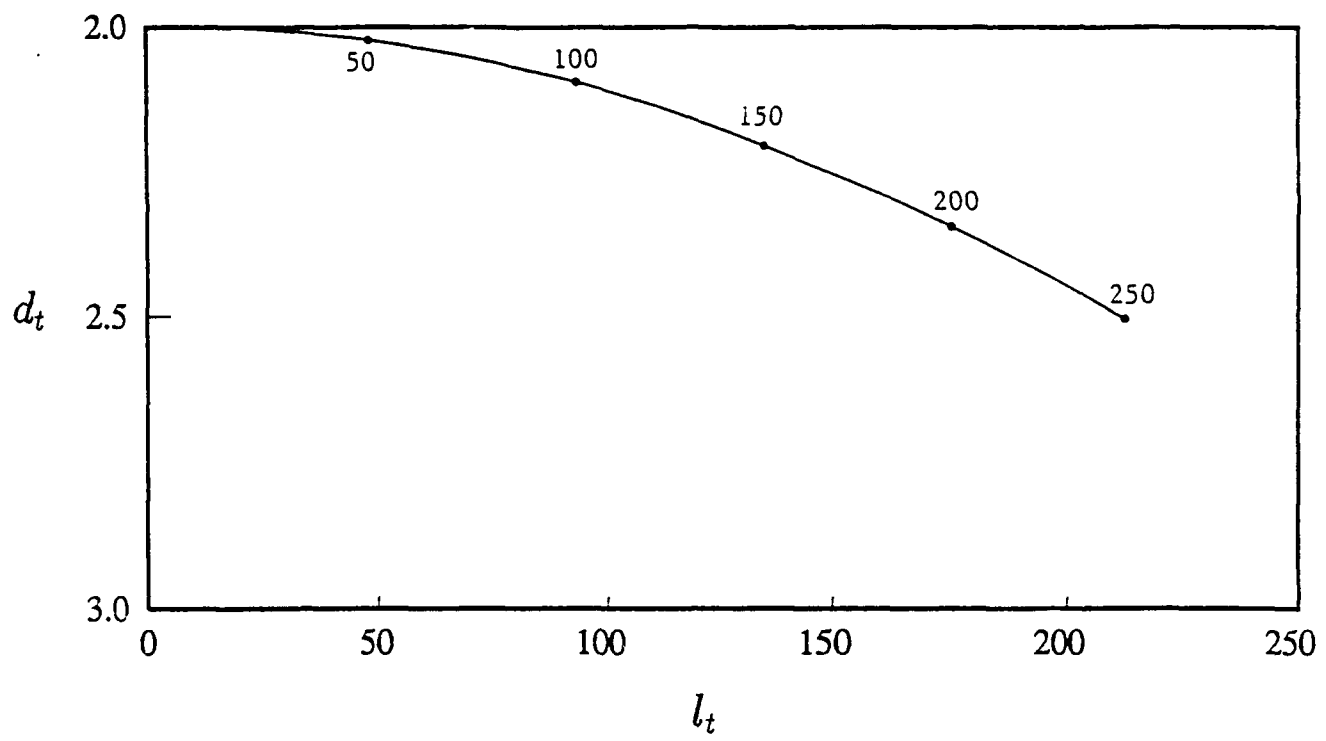


Figure 9. Flow geometry and coordinates

$d_o = 2$



$d_o = 9$

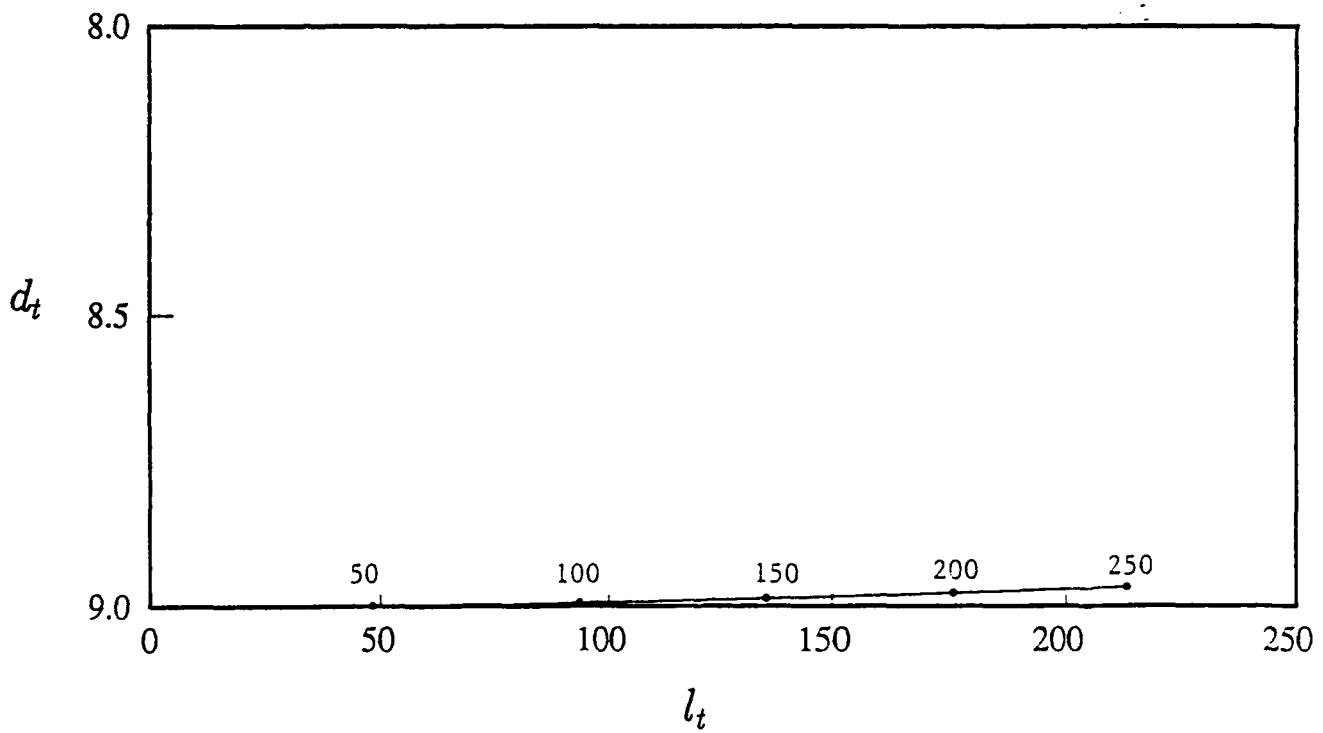


Figure 10. Trajectory of one droplet for (a) $d_o = 2$ and (b) $d_o = 9$.

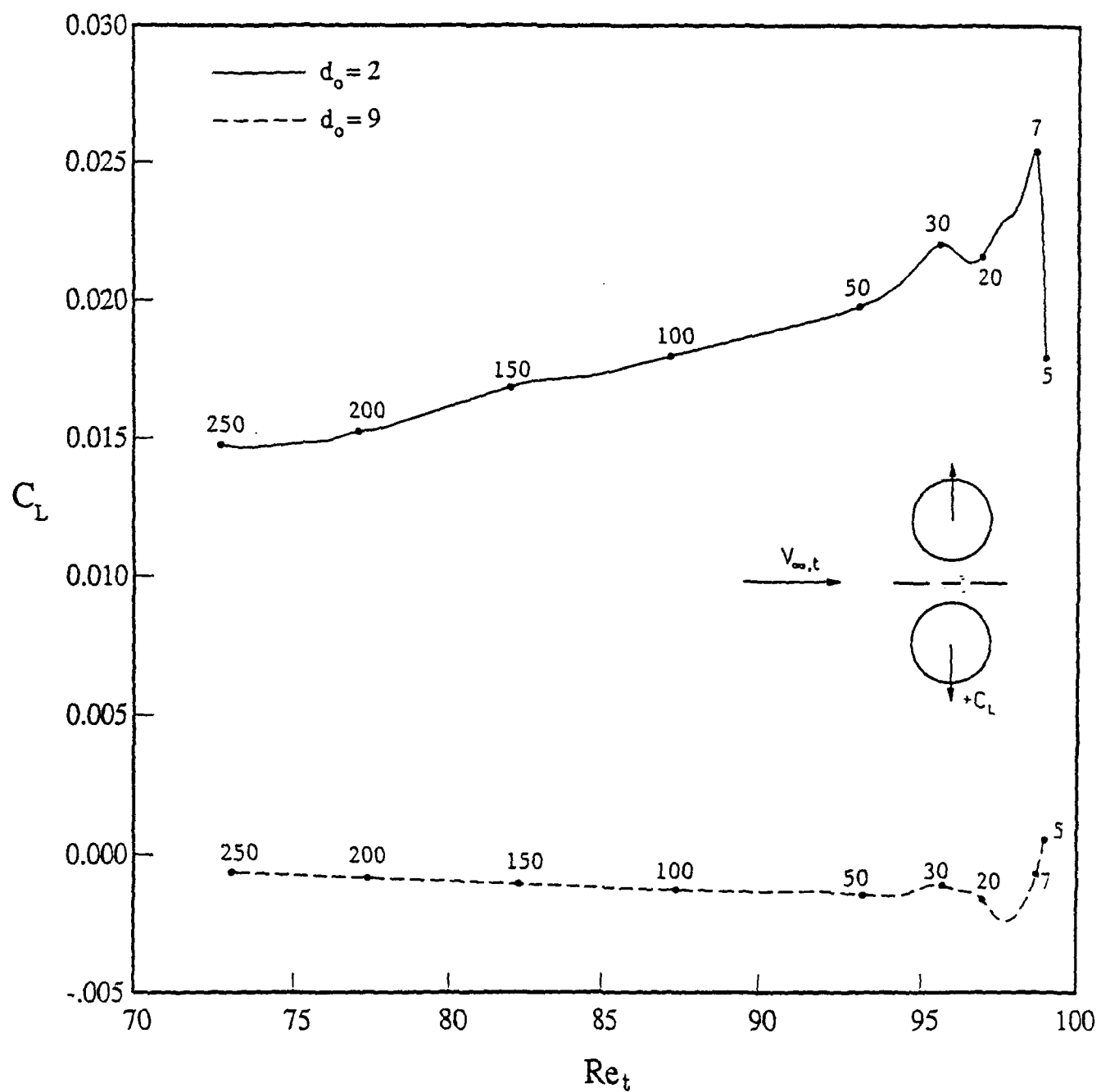


Figure 11. Lift coefficients as a function of instantaneous Reynolds number for $d_o = 2$ and 9 , where the numbers on the curves denote the dimensionless time.

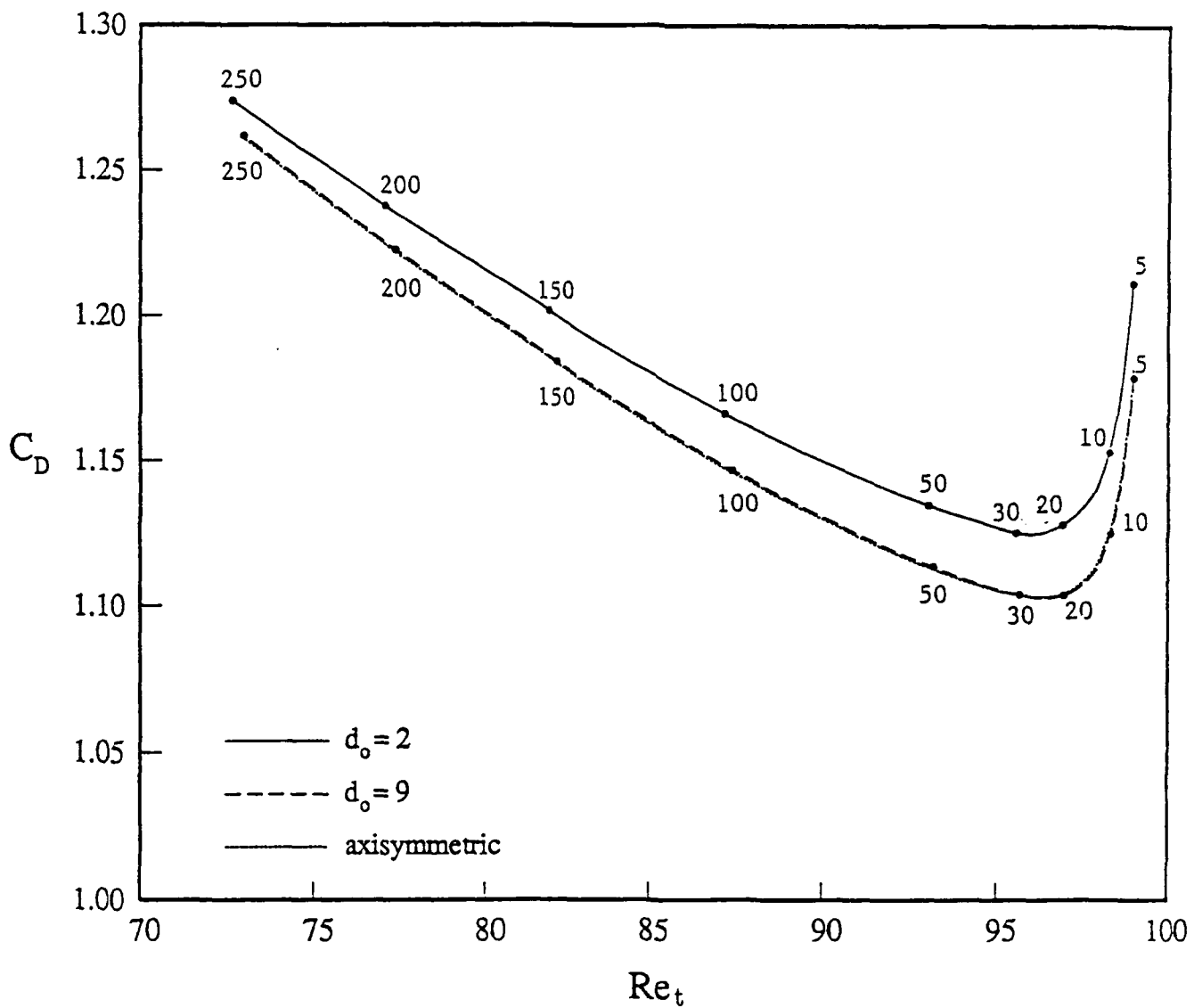


Figure 12. Drag coefficients as a function of instantaneous Reynolds number for $d_o = 2$ and 9, where the numbers on the curves denote the dimensionless time.

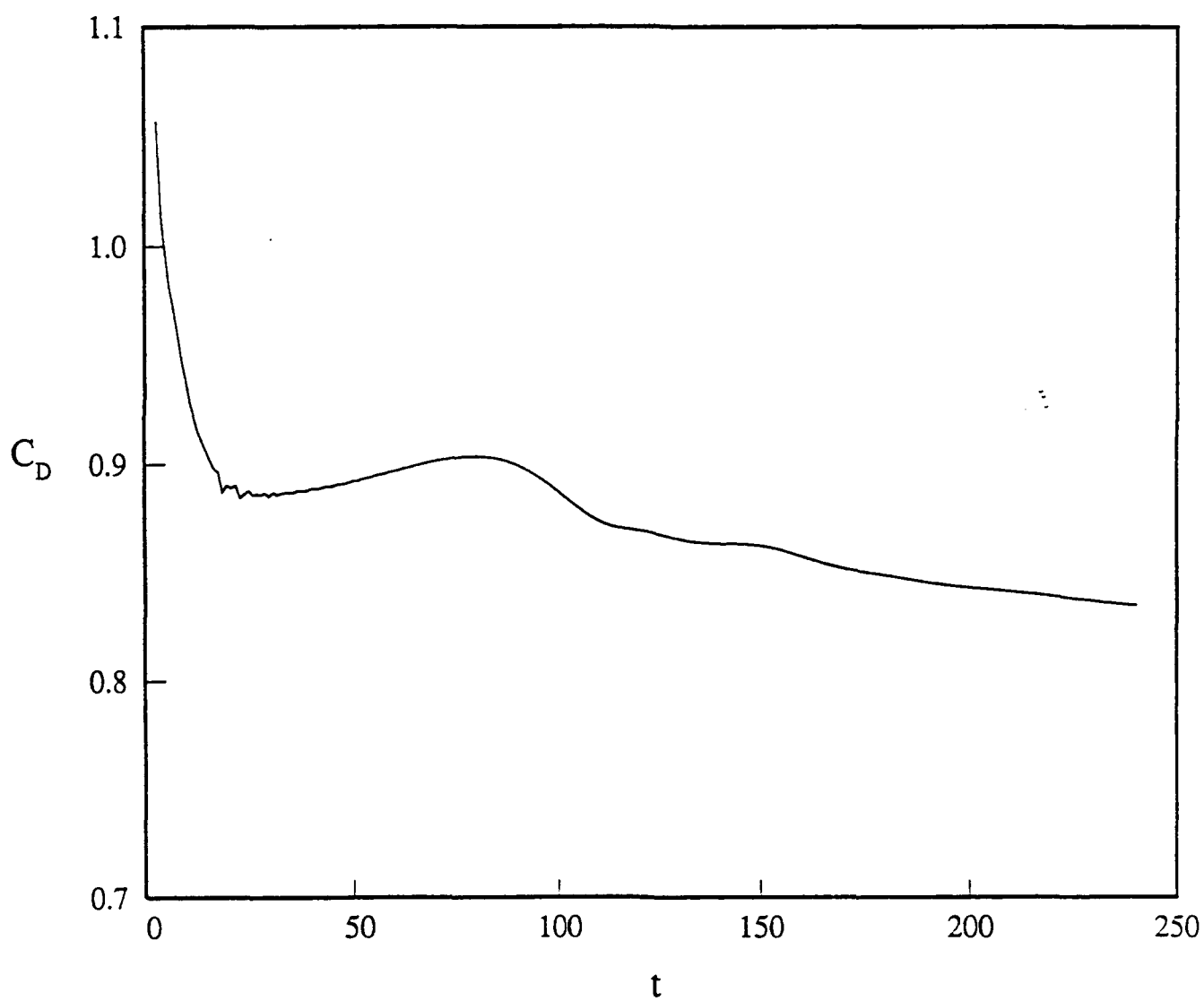


Figure 13. Drag coefficient as a function of dimensionless time.

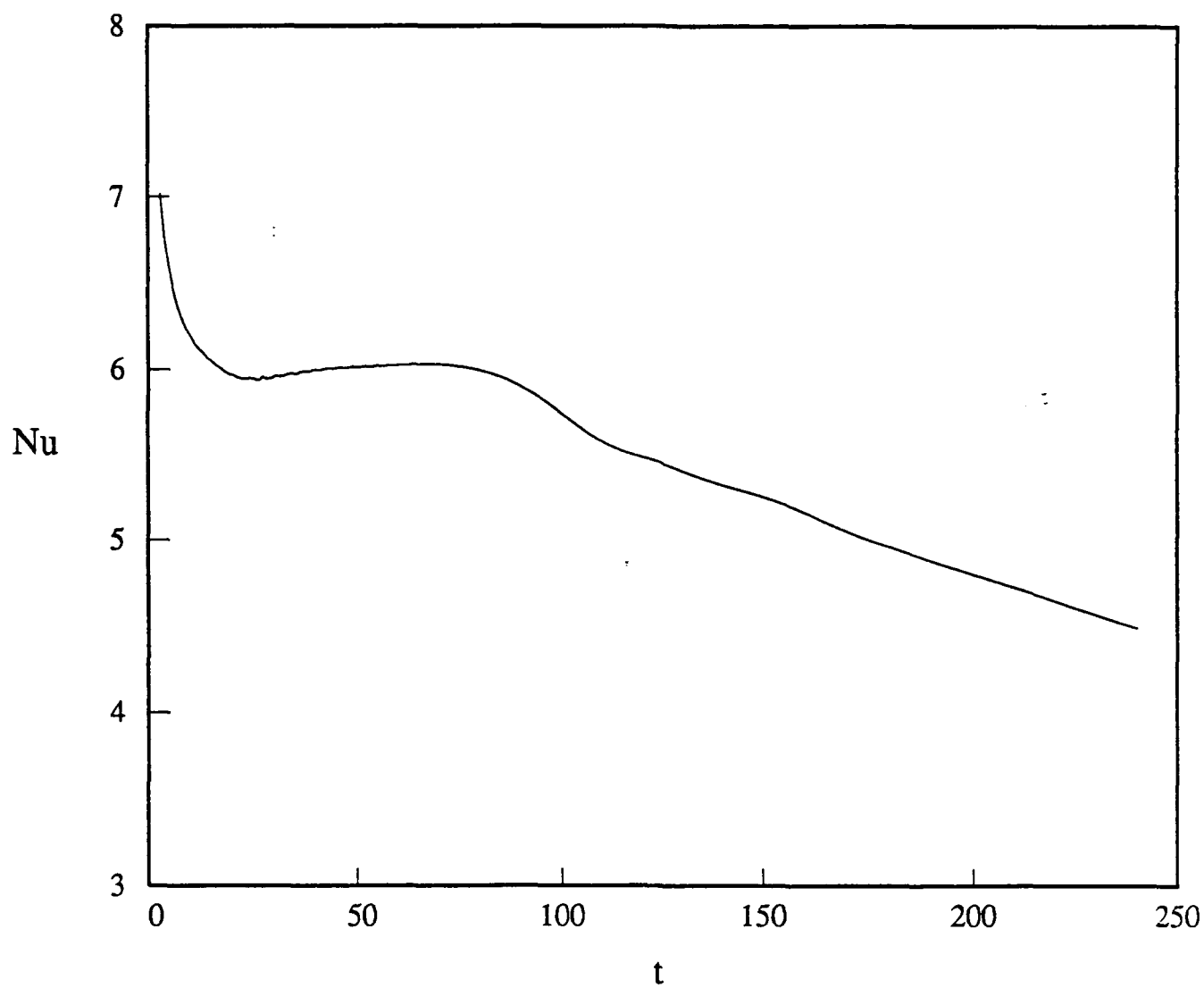


Figure 14. Nusselt number as a function of dimensionless time.

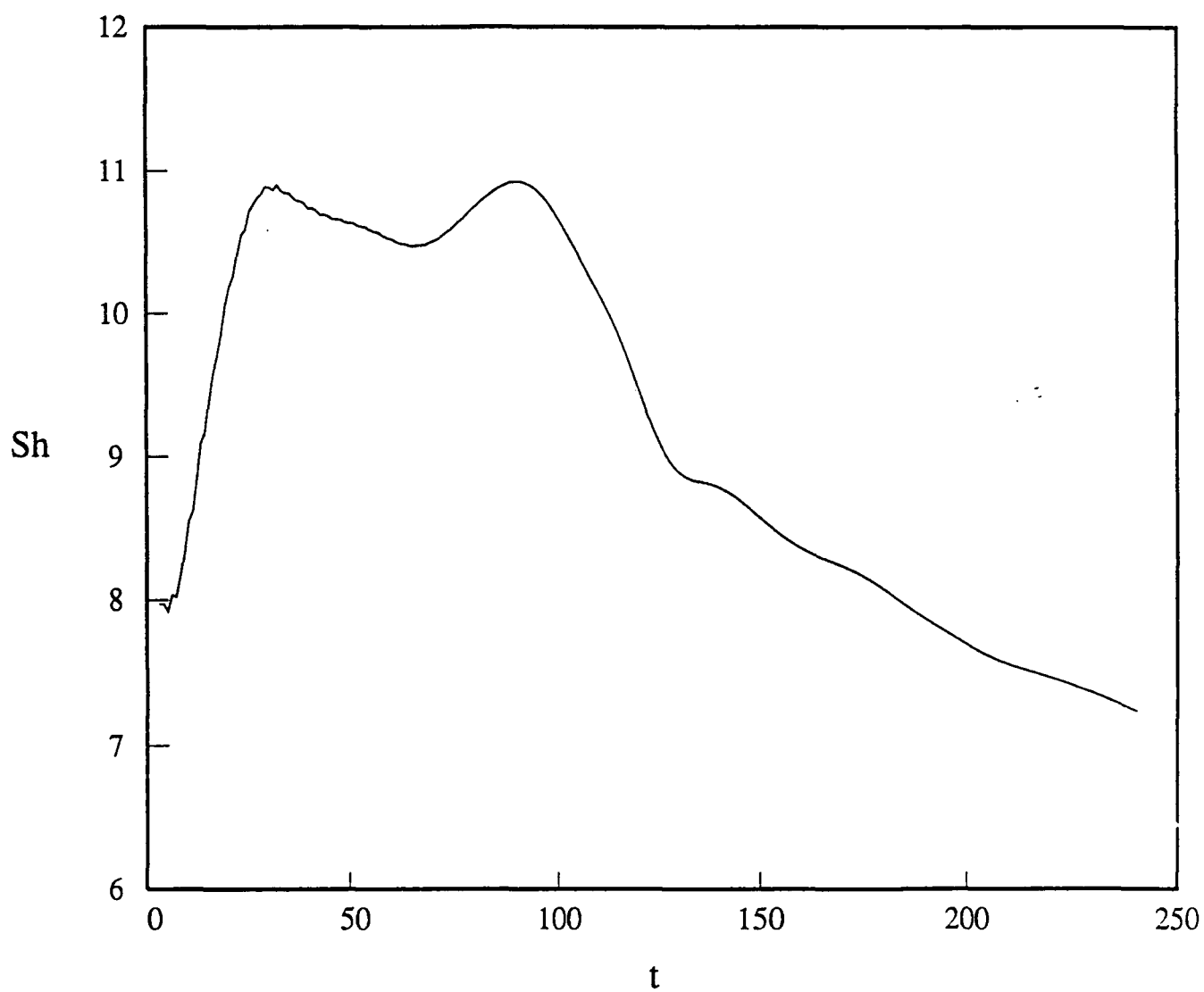


Figure 15. Sherwood number as a function of dimensionless time.

Legends:

Case 1: Initial $R_1 = 1, R_2 = 1, R_3 = 1, D_{12}=12, D_{23}=12, Re=100$

Case 2: Initial $R_1 = 1, R_2 = 1, R_3 = 1, D_{12}=4, D_{23}=12, Re=100$

Case 3: Initial $R_1 = 1, R_2 = 1, R_3 = 1, D_{12}=12, D_{23}=4, Re=100$

1. D_{12} , Case 1; 2. D_{23} , Case 1; 3. D_{12} , Case 2;

4. D_{23} , Case 2; 5. D_{12} , Case 3; 6. D_{23} , Case 3;

7. C_D for the Lead Droplet, Case 1; 8. C_D for the Second Droplet, Case 1;

9. C_D for the Third Droplet, Case 1; 10. C_D for the Lead Droplet, Case 2;

11. C_D for the Second Droplet, Case 2; 12. C_D for the Third Droplet, Case 2;

13. C_D for the Lead Droplet, Case 3; 14. C_D for the Second Droplet, Case 3;

15. C_D for the Third Droplet, Case 3; 16. C_D for an Isolated Droplet;

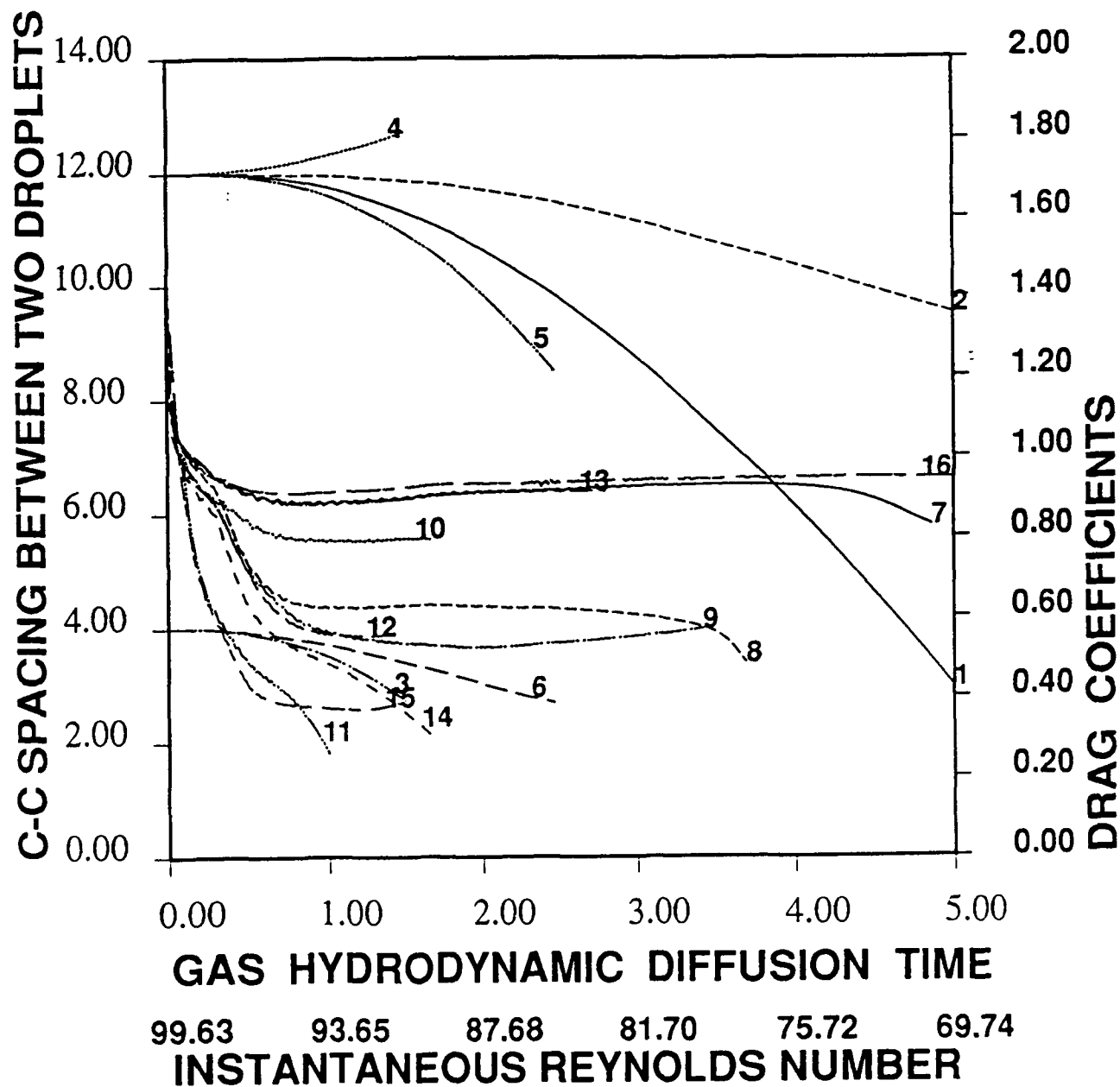


Figure 16. Time variation of droplet drag coefficients and droplet spacings for the cases of large initial droplet spacings.

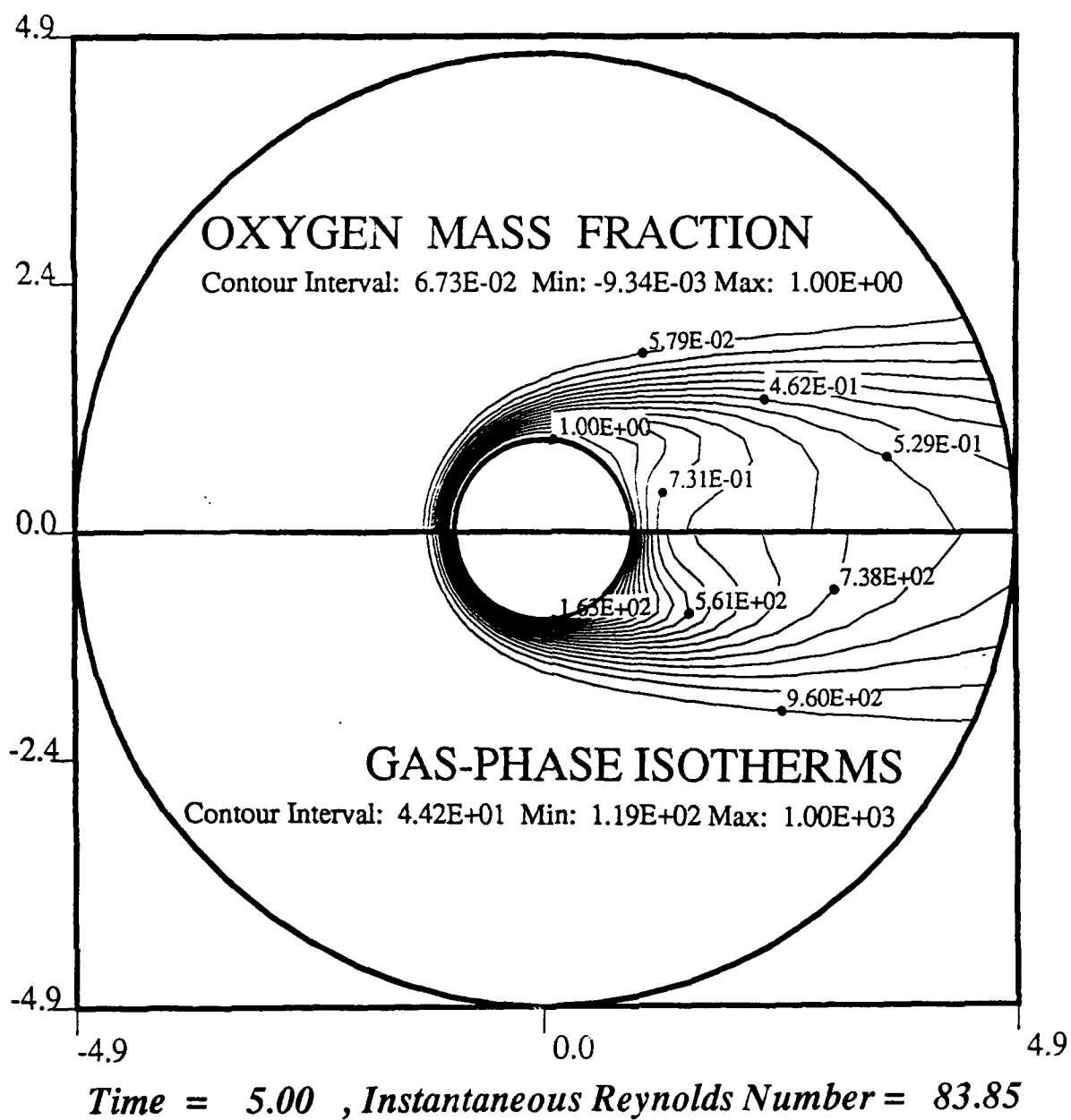


Figure 17. Oxygen mass-fraction contours and isotherms.

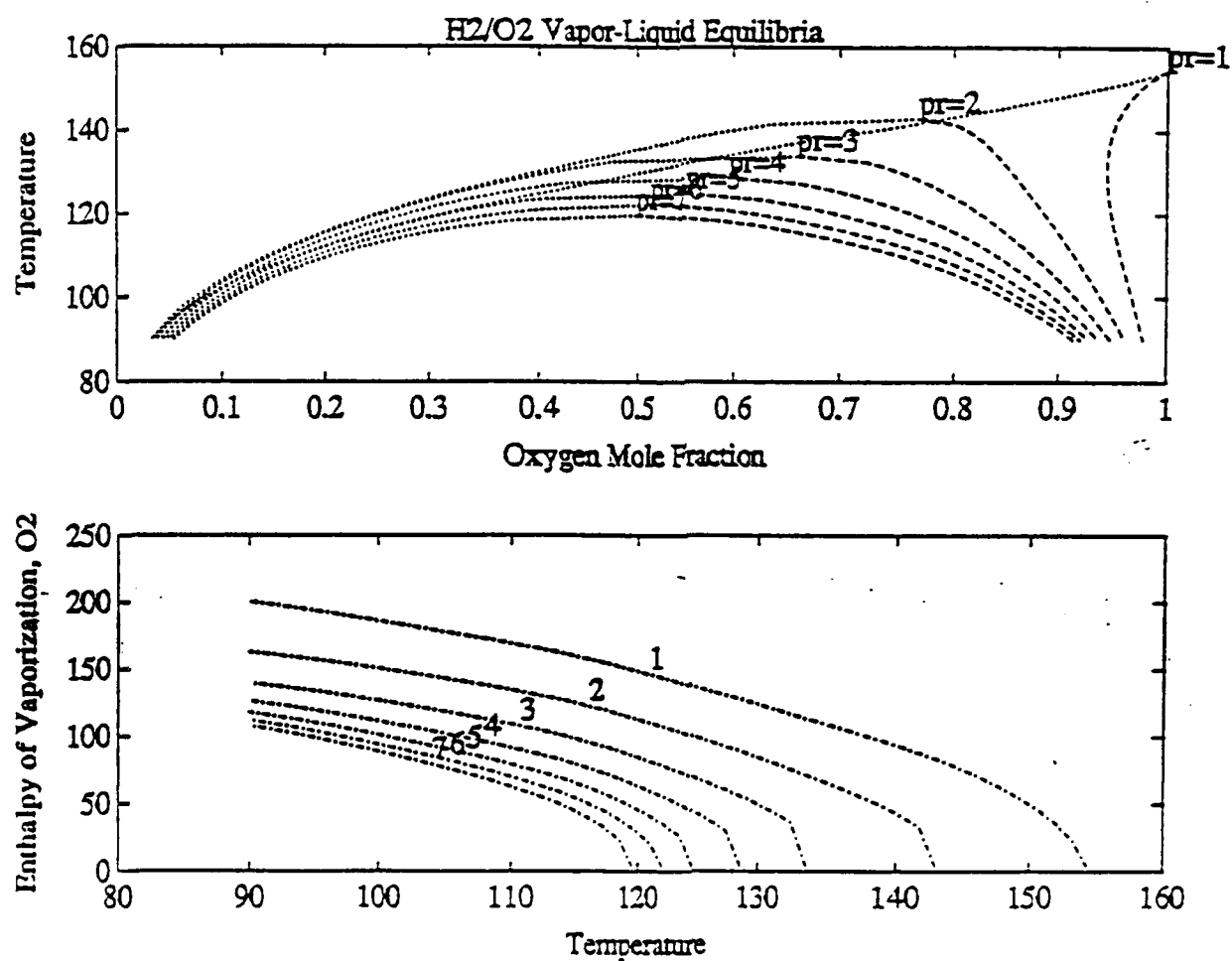


Figure 18. Hydrogen/Oxygen vapor-liquid equilibria and enthalpy of vaporization for liquid oxygen at different reduced pressures.

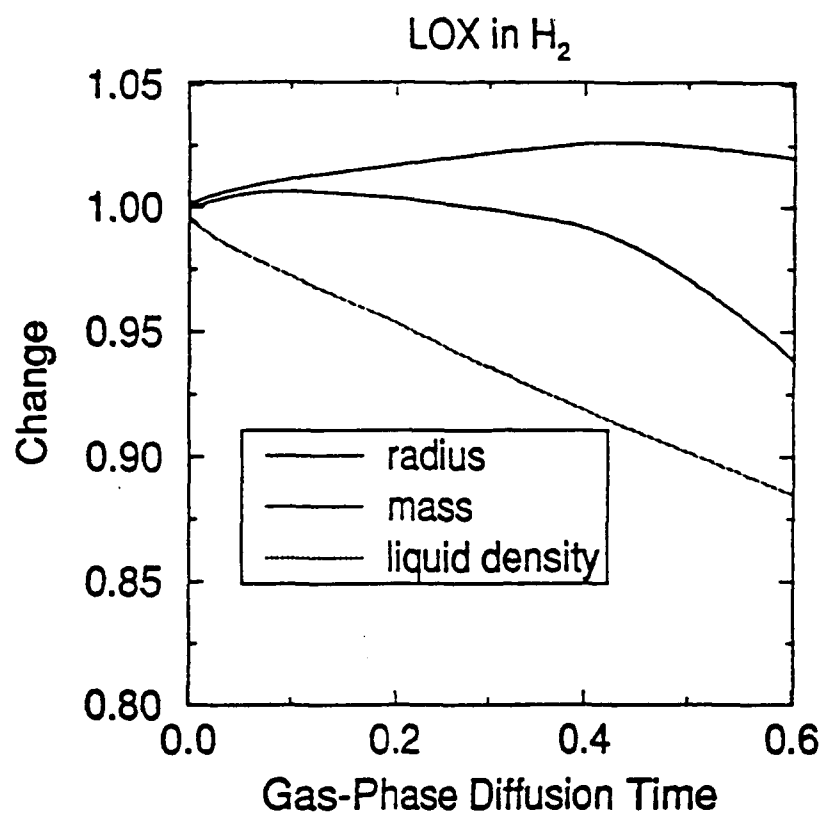


Figure 19. Time variations of droplet radius, mass and liquid density.

Enthalpy of Vaporization

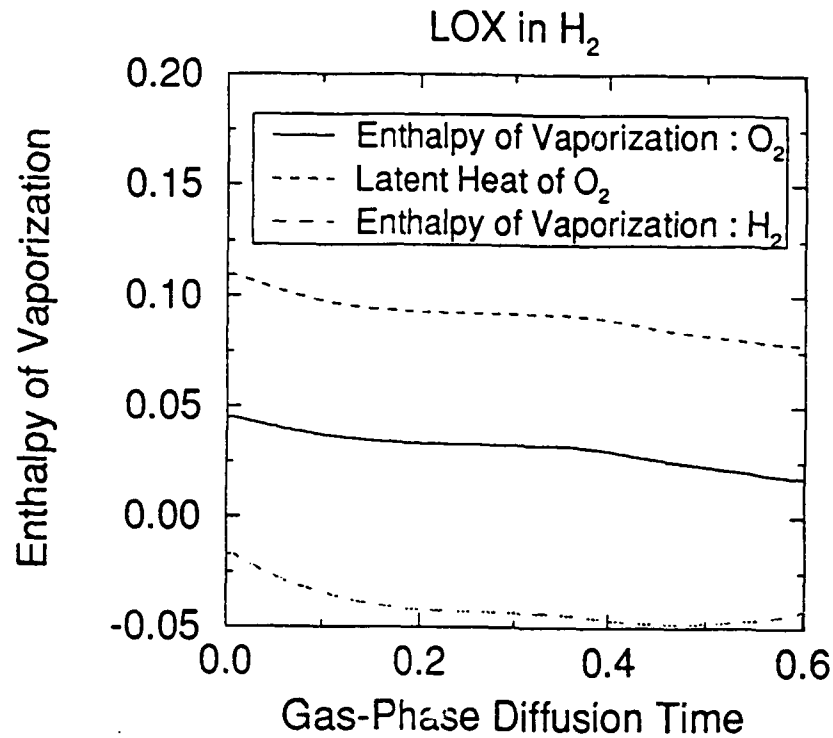


Figure 20. Time variations of enthalpy of vaporization for two components.

Compressibilities for Gas and Liquid

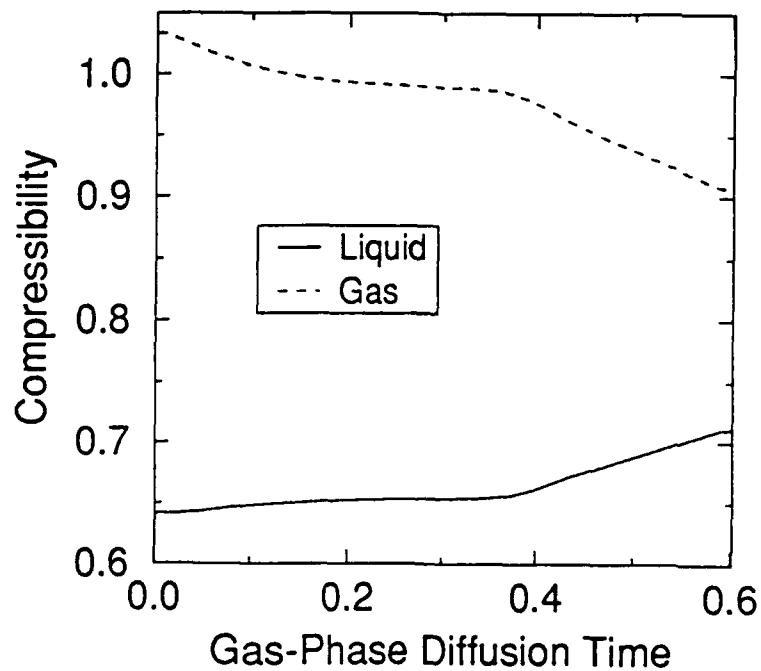


Figure 21. Time variation of compressibility of gas and liquid phases.

Critical Mixing State

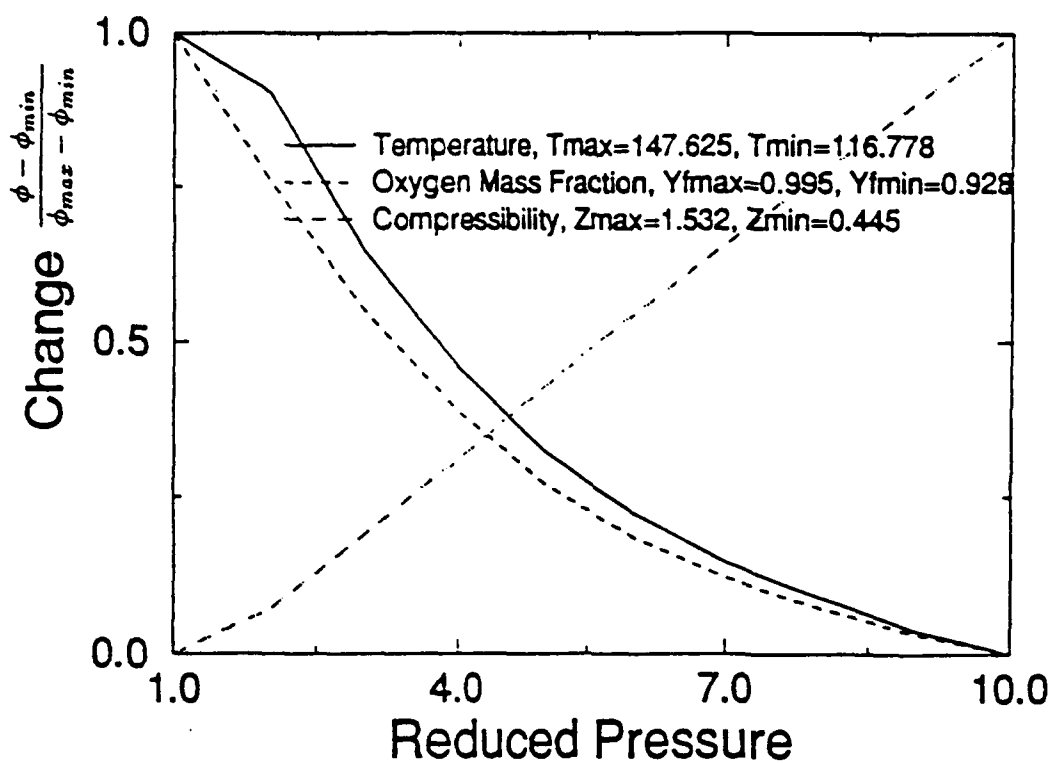


Figure 22. Variations of critical mixing temperature, oxygen mass fraction, and compressibility with respect to pressure.

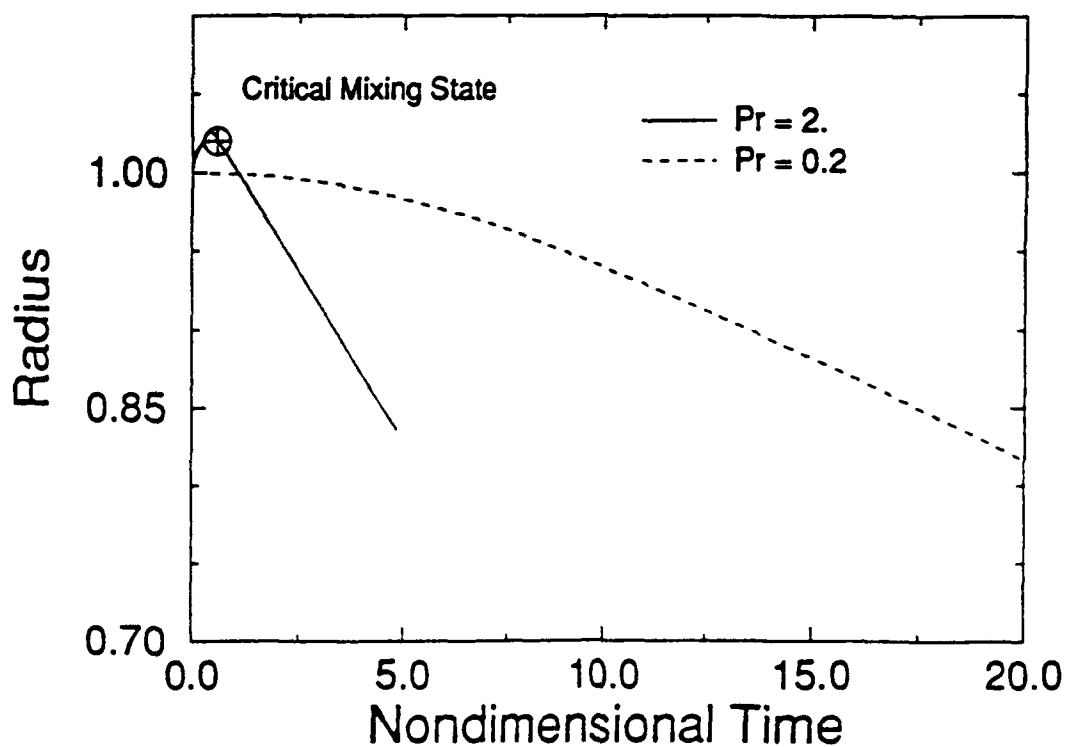


Figure 23. variations of droplet radius with respect to time for the cases of two different pressure levels.

JFM

Vol. 246

PP. 465-488

Jan. 1993

Three-dimensional flow over two spheres placed side by side

By INCHUL KIM, SAID ELGHOBASHI AND WILLIAM A. SIRIGNANO

Department of Mechanical and Aerospace Engineering, University of California at Irvine,
Irvine, CA 92717, USA

(Received 23 August 1991 and in revised form 28 July 1992)

Three-dimensional flow over two identical (solid or liquid) spheres which are held fixed relative to each other with the line connecting their centres normal to a uniform stream is investigated numerically at Reynolds numbers 50, 100, and 150. We consider the lift, moment, and drag coefficients on the spheres and investigate their dependence on the distance between the two spheres. The computations show that, for a given Reynolds number, the two spheres are repelled when the spacing is of the order of the diameter but are weakly attracted at intermediate separation distances. For small spacing, the vortical structure of the near wake is significantly different from that of the axisymmetric wake that establishes at large separations. The partially confined flow passing between the two spheres entrains the flows coming around their other sides. Our results agree with available experimental and numerical data.

1. Introduction

Flow past droplets and solid particles are important in many natural and engineering applications such as air pollution, combustion systems, and chemical processes. Many investigations have considered the interactions between droplets or particles and the surrounding fluid by analytical and numerical methods. For sufficiently low or high Reynolds numbers, a theoretical analysis can be performed using singular perturbation expansions which involve linearization or the boundary-layer approximation. For flows at intermediate Reynolds numbers, which are most common in engineering applications, it is necessary to solve the Navier-Stokes equations numerically.

The majority of the published numerical studies for intermediate Reynolds numbers have focused on flows past a single particle and are thus relevant only at low particle concentration. In regions of large concentration, the drag coefficient is significantly different from that of an isolated particle at the same Reynolds number, and the lift and moment (torque) coefficients have finite values. In order to understand the behaviour of a particle in a large-concentration region, studies of the interactions amongst particles are required. Unfortunately, in practice, the spacial arrangement of particles or droplets in a region of large concentration is quite complex and subject to uncertainty, and calculations involving the entire region are at present not feasible. In order to develop statistical approaches, information about individual droplet or particle interactions is needed.

The study of droplet or particle arrays, particularly in flows at intermediate Reynolds number, is relatively new (Patnaik 1986). A particle array as discussed by

Sirignano (1983) consists of a few particles in a well-defined geometrical arrangement or a large number of particles in a periodic configuration. These arrays, although artificial, can provide information on particle-particle interactions and their effects on the ambient conditions in the vicinity of the particle. The simplification in the geometry allows a detailed and rigorous analysis.

Tal, Lee & Sirignano (1983) studied the hydrodynamics and heat transfer in assemblages of solid spheres in a steady flow at Reynolds number 100 (based on the particle diameter and relative velocity). Their method took advantage of the periodic nature of an infinite array of spheres. They considered several spheres in tandem, and found a trend of decreasing drag coefficients in the streamwise direction. Tal, Lee & Sirignano (1984) also studied the interaction of two solid spheres in tandem in a steady uniform flow at $Re = 40$ for two different spacings using bispherical coordinates and indicated that the drag coefficient of either sphere is always less than that of a single isolated sphere and that the reduction is much greater for the downstream sphere.

Patnaik (1986) investigated the interaction of two vaporizing droplets in tandem at $Re = 50$ and 100 for interdroplet spacing equal to 4.25 diameters using the downstream solution of the lead droplet as the inflow conditions for the downstream droplet. He found that for both Reynolds numbers, the drag coefficient of the trailing droplet is lower than that of the leading droplet.

Raju & Sirignano (1990) studied the interactions between two moving vaporizing droplets in tandem at $50 \leq Re \leq 200$ for a range of spacings and droplet radii ratios. They found that the drag coefficients for both droplets are less than that of a solid sphere and, for the same Reynolds number, the trailing droplet has lower drag. Chiang & Sirignano (1991*a, b*) extended this study to include variable properties and two and three droplets. With three droplets, the difference in drag coefficients between the second and third droplets is much smaller than for the first and second droplets.

All of the above studies employed axisymmetric calculations. Recently, some numerical studies have been performed for three-dimensional flows over a single solid sphere. Dandy & Dwyer (1989) obtained three-dimensional numerical solutions for steady, uniform shear flow past a fixed, heated spherical particle over a range of Reynolds numbers ($0.1 \leq Re \leq 100$) and dimensionless shear rates ($0.005 \leq \alpha \leq 0.4$). They found that at a fixed shear rate, the lift coefficient is approximately constant over a wide range of intermediate Reynolds numbers, and the drag coefficient also remains constant when normalized by the drag for a sphere in uniform flow. Tomboulides, Orszag & Karniadakis (1991) performed a numerical study of three-dimensional flow past a sphere using a spectral element method for $30 \leq Re \leq 1000$ and discussed steady axisymmetric states and unsteady states with three-dimensional vortex shedding.

Three-dimensional flow interactions between droplets or particles at finite Reynolds number have not yet been studied. As a first step towards understanding the three-dimensional interactions in large concentration of particles, we investigate flow interactions between two identical (solid or liquid) spheres which are held fixed side by side against the uniform stream at Reynolds numbers 50, 100, and 150. We determine the effects of three-dimensional interactions on the lift, moment, and drag coefficients as a function of the dimensionless distance between the two spheres and Reynolds number. Some novel phenomena in the near wake are discovered as the gap between the two spheres decreases. Our results are also compared with available experimental and numerical data.

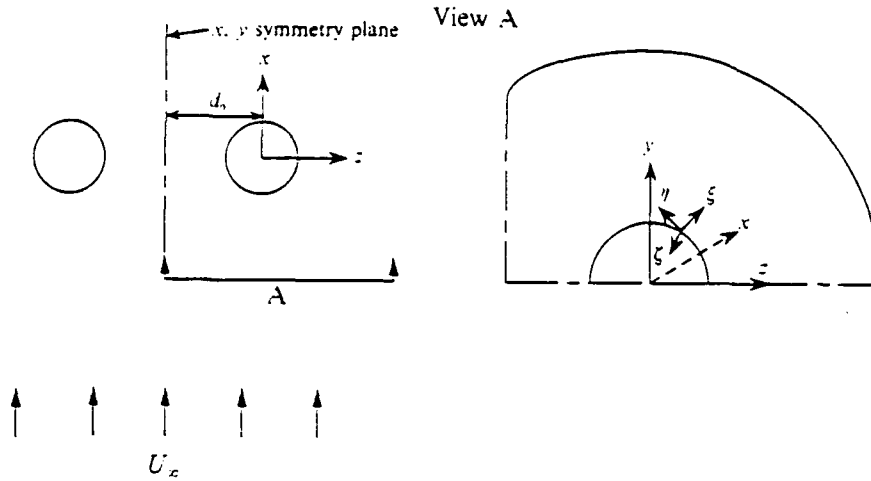


FIGURE 1. Flow geometry and coordinates.

2. Problem statement and numerical solution

We consider a steady three-dimensional incompressible laminar flow of a Newtonian fluid past two identical (solid or liquid) spheres held fixed, with the line connecting the sphere centres normal to a uniform stream, as shown in figure 1; d_0 denotes the distance, normalized by the sphere radius, from the sphere centre to the x, y symmetry plane between the two spheres. Far upstream, the flow is uniform with constant velocity U_∞ parallel to the x -axis. Two symmetry planes are noted in figure 1: the (x, z) -plane containing the centres of the two spheres and the (x, y) -plane located at $z = -d_0$ midway between the sphere centres.

We note that asymmetry of the flow past neighbouring bluff bodies might occur at lower Reynolds number than that of the first temporal instability for a single body. An example is the flow past two cylinders where flow asymmetry would occur well before the first temporal instability for a single cylinder. In contrast, we expect that, for the flow past two spheres, flow asymmetry would occur nearly simultaneously with the temporal instability since the interaction between the two halves (each containing one sphere) of the flow field should be stronger for cylinders than for spheres. That is, the flow between the two spheres is less constrained than the flow between the two side-by-side cylinders.

Two coordinate systems are used in our formulation: the Cartesian coordinates (x, y, z) and the non-orthogonal generalized coordinates (ξ, η, ζ) . The origin of the former coincides with the sphere centre; and ξ is the radial, η the angular, and ζ the azimuthal coordinate. Owing to symmetry, the physical domain is reduced to one quarter of an ellipsoid-like space.

The domain of the external flow is bounded by $1 \leq \xi \leq N_1$, $1 \leq \eta \leq N_2$, $1 \leq \zeta \leq N_3$, where $\xi = 1$ and N_1 correspond, respectively, to the sphere surface and the far-field boundary surrounding the sphere; $\eta = 1$ and N_2 denote, respectively, the positive z -axis and the negative z -axis; $\zeta = 1$ and N_3 refer, respectively, to the (x, z) -plane in the positive x -direction and the (x, z) -plane in the negative x -direction.

The domain of the internal flow is $1 \leq \xi_i \leq N_{1i}$, $1 \leq \eta_i \leq N_{2i}$, $1 \leq \zeta_i \leq N_{3i}$. $\xi_i = 1$ and N_{1i} correspond to the centre and the surface of the sphere, respectively. $\eta_i = 1$ and N_{2i} denote the positive z -axis and the negative z -axis, respectively. $\zeta_i = 1$ and N_{3i} refer to the (x, z) -plane in the positive x -direction and the (x, z) -plane in the negative

x -direction, respectively. Within the liquid sphere, $\xi_i = \text{constant}$ are a family of concentric spherical surfaces. Uniform spacing ($\delta\xi = \delta\eta = \delta\zeta = 1$) is used, for convenience, for the generalized coordinates in both flows.

The non-orthogonal generalized coordinate system of the external flow can be easily adapted to three-dimensional arbitrary geometries. We solve the continuity equation and the time-dependent Navier-Stokes equations and relax them to the steady-state solution, as will be discussed in detail in §2.2.

2.1. Governing equations and boundary conditions

Since one of our goals is to study the flow interaction with liquid spheres, we present the equations for the flows inside and outside the spheres. However, for flow interactions with solid spheres, only the external flow equations are solved. The continuity and momentum equations inside and outside a sphere and the boundary conditions are non-dimensionalized using the sphere radius a_0 as the characteristic length and U_∞ as the characteristic velocity:

external flow

$$\nabla \cdot V = 0, \quad (1)$$

$$\frac{DV}{Dt} = -\nabla p + \frac{2}{Re} \nabla^2 V; \quad (2)$$

internal flow

$$\nabla \cdot V_i = 0, \quad (3)$$

$$\frac{DV_i}{Dt} = -\nabla p_i + \frac{2}{Re_i} \nabla^2 V_i. \quad (4)$$

The governing equations are written with respect to the generalized coordinates (ξ, η, ζ) , which allows a three-dimensional body of arbitrary shape to be treated. The numerical integration is performed using a cubic computational mesh with equal spacing ($\delta\xi = \delta\eta = \delta\zeta = 1$) (Anderson, Tannehill & Pletcher 1984).

The conditions at the interface, $\xi = 1$ or $\xi_i = N_{11}$, are derived by requiring continuity of the shear stresses and tangential velocities. Because no fluid is allowed to cross the surface of the liquid sphere, the normal velocities at the interface are zero in both flows. An interface condition for the pressure is obtained from the momentum equation. Since the interface is always spherical, it is more convenient to cast these conditions in terms of spherical coordinates (r, θ, ϕ) :

$$\tau_{r\theta, s} = \tau_{l, r\theta, s}, \quad (5)$$

$$\tau_{r\phi, s} = \tau_{l, r\phi, s}, \quad (6)$$

$$V_{\theta, s} = V_{l, \theta, s}, \quad (7)$$

$$V_{\phi, s} = V_{l, \phi, s}, \quad (8)$$

$$V_{r, s} = V_{l, r, s} = 0, \quad (9)$$

$$\frac{\partial p}{\partial r_s} = V_{\theta, s}^2 + V_{\phi, s}^2 + \frac{2}{Re} \left[\frac{\partial}{\partial r} \left(r^2 \frac{\partial V_r}{\partial r} \right) - 2 \frac{\partial V_\theta}{\partial \theta} - 2 V_\theta \cot \theta - \frac{2}{\sin \theta} \frac{\partial V_\phi}{\partial \phi} \right]_s, \quad (10)$$

where the subscript s denotes the surface of the liquid sphere. For the solid-sphere case, the no-slip condition is enforced on the sphere surface.

The external flow boundary conditions are:

$$p = 0, \quad u = 1, \quad v = 0, \quad w = 0 \quad \text{at} \quad \xi = N_1 \text{ except at } z = -d_0, \quad (11)$$

$$\frac{\partial p}{\partial z} = \frac{\partial u}{\partial z} = \frac{\partial v}{\partial z} = 0, \quad w = 0 \quad \text{at} \quad z = -d_0, \quad (12)$$

$$\frac{\partial p}{\partial \eta} = \frac{\partial u}{\partial \eta} = \frac{\partial w}{\partial \eta} = 0, \quad v = 0 \quad \text{at} \quad \eta = 1 \quad \text{and} \quad N_2, \quad (13)$$

$$\frac{\partial p}{\partial \zeta} = \frac{\partial u}{\partial \zeta} = \frac{\partial w}{\partial \zeta} = 0, \quad v = 0 \quad \text{at} \quad \zeta = 1 \quad \text{and} \quad N_3, \quad (14)$$

where u , v , and w are the velocities of the external flow in the x -, y -, and z -directions, respectively. p is the pressure, and the subscript l denotes the internal flow. Equations (12) and (14) correspond, respectively, to the symmetry conditions in the x, y symmetry plane between the spheres and the x, z symmetry plane containing the centres of the spheres. Equation (13) expresses the no-flux boundary condition for p , u , and w on the axes $\eta = 1$ and $\eta = N_2$, and zero v -velocity in the x, z symmetry plane containing the two axes.

The internal flow boundary conditions are

$$\frac{\partial p_l}{\partial \xi_l} = \frac{\partial u_l}{\partial \xi_l} = \frac{\partial w_l}{\partial \xi_l} = 0, \quad v_l = 0 \quad \text{at} \quad \xi_l = 1, \quad (15)$$

$$\frac{\partial p_l}{\partial \eta_l} = \frac{\partial u_l}{\partial \eta_l} = \frac{\partial w_l}{\partial \eta_l} = 0, \quad v_l = 0 \quad \text{at} \quad \eta_l = 1 \quad \text{and} \quad N_2, \quad (16)$$

$$\frac{\partial p_l}{\partial \zeta_l} = \frac{\partial u_l}{\partial \zeta_l} = \frac{\partial w_l}{\partial \zeta_l} = 0, \quad v_l = 0 \quad \text{at} \quad \zeta_l = 1 \quad \text{and} \quad N_3, \quad (17)$$

where (15) and (16) correspond, respectively, to the no-flux boundary conditions at the centre of the droplet and on the axes $\eta_l = 1$ and N_2 , and zero v_l -velocity in the x, z symmetry plane containing the two axes. Equation (17) prescribes the symmetry condition on the x, z symmetry plane containing the centres of the spheres.

The dimensional drag, lift, and moment coefficients are evaluated from

$$F_D = \int_S -pn \cdot i dS + \int_S n \cdot \tau \cdot i dS, \quad (18)$$

$$F_L = \int_S -pn \cdot k dS + \int_S n \cdot \tau \cdot k dS, \quad (19)$$

$$M = \int_S r \times \tau dS, \quad (20)$$

where S denotes the surface of the sphere, n is the outward unit normal vector at the surface, r is the position vector from the centre of the sphere, and τ is the viscous stress tensor. Equations (18)–(20) are evaluated on the side of the external flow. The lift force is assumed positive when it is directed toward the positive z -axis. Owing to symmetry, only the y -component of the moment is non-zero and is assumed positive in the counter-clockwise direction.

Non-dimensional coefficients of drag, lift, and moment are defined respectively as

$$C_D = F_D / (\frac{1}{2} \rho U_\infty^2 \pi a_0^2), \quad (21)$$

$$C_L = F_L / (\frac{1}{2} \rho U_\infty^2 \pi a_0^2), \quad (22)$$

$$C_M = M \cdot j / (\frac{1}{2} \rho U_\infty^2 \pi a_0^3). \quad (23)$$

2.2. Numerical solution

We have developed a three-dimensional implicit finite-difference algorithm to solve simultaneously the set of discretized partial differential equations. The method is based on an Alternating-Direction-Predictor-Corrector (ADPC) scheme to solve the time-dependent Navier-Stokes equations. ADPC is a slight variation of Alternating-Direction-Implicit (ADI) method. It is first-order accurate in time but is effective and implemented easily when embedded in a large iteration scheme (Patnaik 1986). The control volume formulation is used to develop the finite-difference equations from the governing equations with respect to the generalized coordinates (ξ, η, ζ) . One of the advantages of the control volume formulation is that all dependent variables are conserved over a single control volume, and hence the whole domain regardless of the grid fineness. An important part of solving the Navier-Stokes equations in primitive variables is the calculation of the pressure field. In the present work, a pressure correction equation is employed to satisfy indirectly the continuity equation (Anderson *et al.* 1984). The pressure correction equation is of the Poisson type and is solved by the Successive-Over-Relaxation (SOR) method.

The overall solution procedure is based on a cyclic series of guess-and-correct operations. The velocity components are first calculated from the momentum equations using the ADPC method, where the pressure field at the previous time step is employed. This estimate improves as the overall iteration continues. The pressure correction is calculated from the pressure correction equation using the SOR method, and new estimates for pressure and velocities are obtained. This process continues until the solution converges at each time step. For the flow past liquid spheres, the same procedure is performed in the flow inside the sphere. The governing equations of motion in each flow are solved in an interactive sequence through the interface boundary conditions until convergence is achieved for each time step of the calculation.

The generation of the computational grid for the external multi-sphere flows is an essential part of the solution procedure. We generate the three-dimensional grid efficiently by choosing the outer boundary of the physical domain to be axisymmetric about the line connecting the centres of the two spheres and constructing an axisymmetric grid. The axisymmetric grid is generated on the (ξ, η) -plane including the line that connects the centres of the two spheres and by using a hybrid method of algebraic and differential equation methods. First, we choose the outer boundary of the computational grid as the x, y symmetry plane and an incomplete ellipse whose centre is located at the centre of the sphere, as shown in figure 1. We then generate a family of quarter-ellipses on the right side of the domain, another family of quarter-ellipses on the left side, and also a family of straight lines emanating from the centre of the sphere. Grid density is controlled by the stretching function developed by Vinokur (1983). This is followed by solving the quasi-linear elliptic system of differential equations using the SOR method with a few (not more than two) iterations in order to smooth the grid lines generated by the algebraic method. In figures 2(a-c), we present a cross-section of the three-dimensional grid at $d_0 = 21, 10$, and 3.

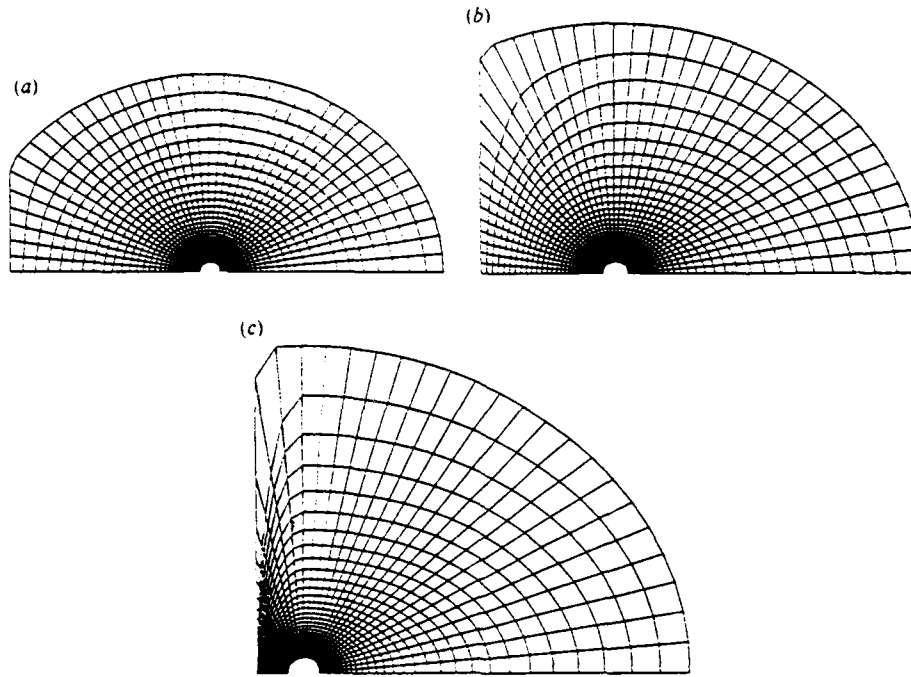


FIGURE 2. Cross-section of the three-dimensional grid system for (a) $d_0 = 21$; (b) $d_0 = 10$; (c) $d_0 = 3$.

$N_1 \times N_2 \times N_3$	C_{DP}	C_{DV}	C_D	C_D^*
$Re = 50$				
$20 \times 21 \times 21$	0.706	0.951	1.657	
$30 \times 31 \times 31$	0.683	0.934	1.617	
$40 \times 41 \times 41$	0.676	0.929	1.605	1.58
$Re = 100$				
$20 \times 21 \times 21$	0.555	0.593	1.148	
$30 \times 31 \times 31$	0.532	0.582	1.114	
$40 \times 41 \times 41$	0.524	0.581	1.105	1.09

TABLE 1. Drag coefficients as a function of grid density at $Re = 50$ and 100 where * denotes the data from Roos & Willmarth (1971) and also Clift *et al.* (1978).

3. Results and discussion

In §3.1, we test the accuracy of the full three-dimensional solution procedure by predicting the axisymmetric flow over a single (solid and liquid) sphere. In §3.2, we discuss the three-dimensional interactions between two solid spheres, and in §3.3, we examine the three-dimensional interactions between two liquid spheres.

3.1. Flow over a single sphere

We discuss the flow generated by an impulsively started solid sphere in a quiescent fluid at two Reynolds numbers: 50 and 100. The time-dependent solution converges asymptotically to a steady state, which is in excellent agreement with available experimental data and correlations as shown in tables 1 and 2. Table 1 lists the drag coefficients as a function of the computational grid density at Reynolds numbers 50

$\mathbf{r} = \mathbf{r}_1 + \mathbf{r}_2$	\mathbf{r}_1	\mathbf{r}_2	\mathbf{r}	\mathbf{r}^0
$\mathbf{R}_1 = 0$				
$20 : 20 : 20$	0.00	-0.0000	20.00	
$20 : 17 : 17$	0.0000	-0.0002	20.00	
$40 : 17 : 17$	0.0000	-0.0000	20.00	20.00
$\mathbf{R}_1 = 0.0$				
$20 : 20 : 20$	0.0000	-0.0000	20.00	
$20 : 17 : 17$	0.0000	-0.0000	20.00	
$40 : 17 : 17$	0.0000	-0.0000	20.00	20.00

TABLE 1. Pressure at the front and rear stagnation points and the separation angle measured from the front stagnation point as a function of grid density at $Re = 50$ and 100 where θ denotes the angle from the front. (Saito, 1969 and Hsu *et al.*, 1976).

and 11 respectively and compares them with the data of Jones & Willmarth (1972) and also with the correlations of Mit. Leach & Weber (1972). Table 1 shows the pressure at the front and rear stagnation points and the separation angle measured from the front stagnation point as a function of grid density at Reynolds number 30 and 60 in comparison with the data of Tanaka (1966) and also with the correlations of Mit. et al. (1972). Although the solution in these test cases are axisymmetric, none of the three velocity components in our formulation becomes identically zero. Therefore, the three-dimensional solution scheme is fully exercised here. The calculations were performed on three different grids, $128 \times 128 \times 128$, $256 \times 128 \times 128$, and $512 \times 128 \times 128$, in computational domain with an outer boundary located at 12 spheres radii from the sphere centre. The dimensionless times needed for each steady state of Reynolds number 30 and 60 are 1 and 4 respectively.

5. Before the collision procedure by varying the accident boundary condition and by changing the location of the outer boundary. In the first test, the accident surface boundary condition was changed from a free-stream condition ($T_0 = 1.0$, $u = v = w = 0$). There was a large difference in the results of the velocity field in the air wake just near the outer boundary. On almost no difference in the drag coefficient and the lift. While the acceleration along the surface of the configuration was a few percent different. And in the second test, the location of the outer boundary was changed from $x = 10$ to $x = 20$. There was almost no difference in the surface of the configuration and the velocity field. A change in the drag coefficient and the acceleration along a configuration is only a few percent different. This indicates that when the boundary is moved a given distance away from the air wake, the momentum defect in the air wake is still small and the flow field is not affected. But, the results of the

**BEST
AVAILABLE COPY**

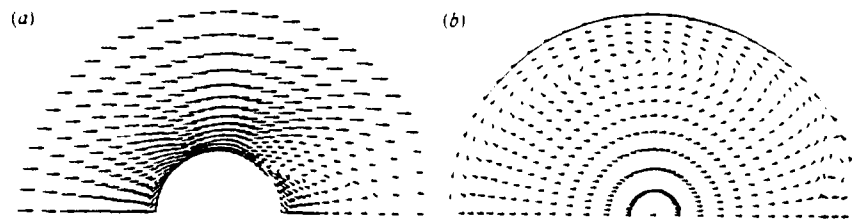


FIGURE 4. Velocity vector fields of (a) external flow; (b) internal flow for the axisymmetric flow past a liquid sphere at $Re = 100$.

The axisymmetric test-run for a solid sphere at Reynolds number 100 with the $40 \times 41 \times 41$ grid required a dimensionless time step of $\Delta t = 0.002$ and a total time of 3.75 Cray Y-MP/8-64 cpu hours. Each time step takes about 1.8 cpu seconds.

We also solved the flow generated by an impulsively started liquid sphere in a quiescent fluid, and the results were in good agreement with available numerical studies. Figure 3(a, b) shows the steady-state velocity vector distributions of the flow past a liquid sphere with viscosity ratio of 25 and density ratio of 300 (internal to external fluid) at Reynolds number 50. We observe a closed-streamline wake detached from the liquid sphere, and thus no secondary recirculating flow is found in the liquid phase (Rivkind & Ryskin 1976; Clift *et al.* 1978). In figure 4(a, b) we show the velocity vector distributions for the same parameters as above except that the Reynolds number is 100. It is interesting to note that a second circulatory flow develops in the liquid-sphere stern region. This behaviour was observed in an earlier study by Rivkind & Ryskin (1976) where a stream function-vorticity formulation was employed. Rivkind & Ryskin (1976) indicated that when the density ratio is much greater than the viscosity ratio, i.e. the Reynolds number inside the liquid sphere is much greater than the Reynolds number outside, a second circulatory flow possibly occurs in the liquid-sphere stern region. The axisymmetric test run for the liquid sphere required half the time step for the solid sphere and was about 3.4 times slower because of the numerical interaction between the internal and external flows.

For the interactions between two spheres, an ellipsoid-like domain is chosen in order to take into account the interactions when the two spheres are far away from each other. As shown in figure 1, a longer outer boundary $r_\infty = 25$ is chosen in the z -direction, and $r_\infty = 21$ is chosen in the σ -direction, where $\sigma = (x^2 + y^2)^{1/2}$. The results using the above ellipsoid outer boundary for a single sphere were identical in the steady axisymmetric flow calculations to those using the spherical outer boundary.

The results of the $30 \times 31 \times 31$ grid differ by only 0.8% in the drag coefficients and 0.4% in the separation angles from those of the $40 \times 41 \times 41$ grid as shown in tables 1 and 2. The percentage difference was calculated as follows. Let the result of the $30 \times 31 \times 31$ grid be S_1 and the result of the $40 \times 41 \times 41$ grid be S_2 . Then, the percentage difference is $(S_1 - S_2)/S_1$. Thus, we chose the medium-size grid $30 \times 31 \times 31$, and $15 \times 31 \times 31$ inside the liquid sphere, for the following of calculations. A typical run for the solid sphere with the $30 \times 31 \times 31$ grid required 0.8 cpu hours on the Cray Y-MP/8-64; the liquid sphere run with the same grid required 2.7 cpu hours. 15 runs were made for each Reynolds number to cover the range of $1.5 \leq d_0 \leq 25$.

We did not perform calculations for Reynolds number higher than 150, because it is known that the wake becomes unstable at a Reynolds number in the range of 130–220 for a single sphere (Taneda 1956; Goldburg & Florsheim 1966; Roos & Willmarth 1971; Nakamura 1976; Kim & Pearlstein 1990) and our present goal is to

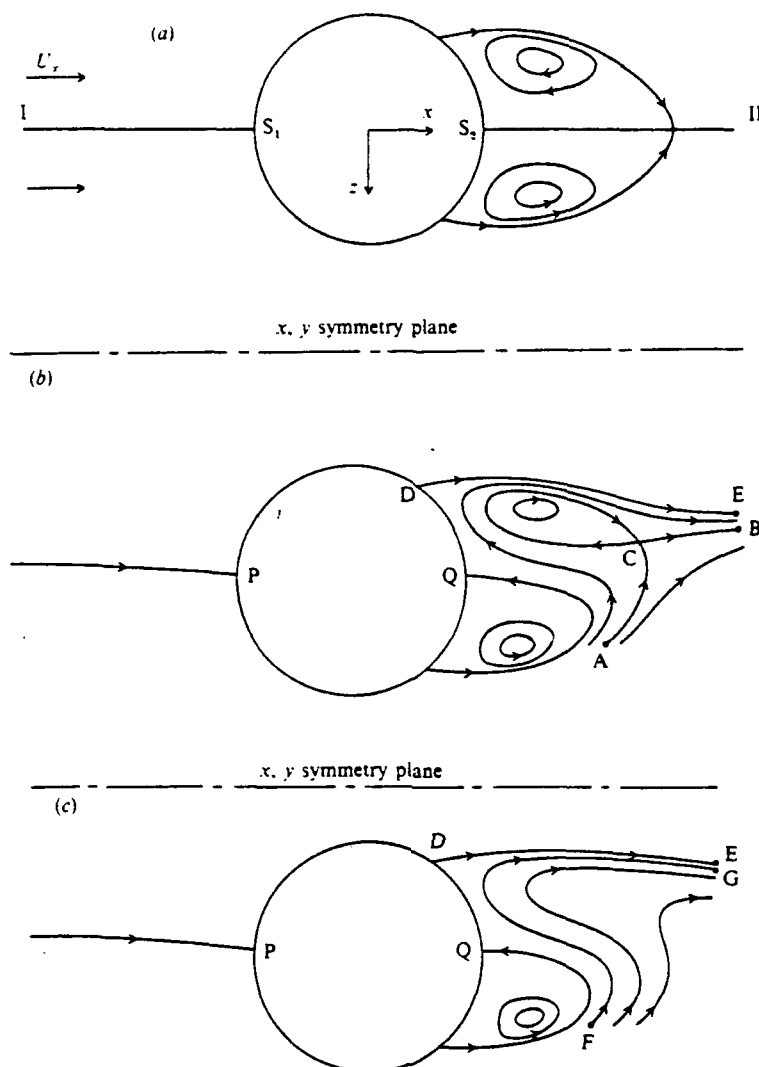


FIGURE 5. Sketch of typical streamlines over one of the two solid spheres in the principal plane (x, y -plane) at $Re = 100$ for (a) axisymmetric flow; (b) $d_0 = 2$; (c) $d_0 = 1.5$.

obtain steady-state solutions. For the solution of a flow including the three-dimensional unsteady wake, a complete computational domain (i.e. encompassing the two spheres without a symmetry plane) and periodic boundary conditions in ζ -direction will be necessary.

3.2. Interactions of two solid spheres

3.2.1. Flow structure

In order to illustrate better the fluid motion, we consider the flow field in the (x, z) -plane of symmetry, which is defined as the *principal plane*, where the narrowest path between the two spheres occurs, hence the strongest interactions between them.

Figure 5(a) displays a sketch of the actual streamlines around a single sphere in the principal plane at Reynolds number 100. As expected, two identical counter-rotating vortices (corresponding to a single vortex ring) exist in the wake, and the

downstream stagnation point is located on the axis of symmetry. Line I-II connecting the front and rear stagnation points in the standard axisymmetric flow over a single sphere will be used as a reference line: we refer to the region above this line as the 'top' or 'upper' region and that below as the 'bottom' or 'lower' region.

Figure 5(b) displays a sketch of the actual streamlines around one of the two spheres in the principal plane at Reynolds number 100. The two spheres are separated by a distance $d_0 = 2$. Owing to the blockage of the flow in the gap between the two spheres, the streamlines diverge away from the x, y symmetry plane (located at $z = -d_0$) as they approach the front stagnation region. Thus, the stagnation streamline of the single-sphere case (I-S₁ in figure 5a) no longer intersects the sphere, and another streamline closer to the symmetry plane meets the sphere to form the new front stagnation streamline at point P. As a consequence, the fluid particles move faster in the lower left region around the sphere than in the upper left region, and this causes the pressure in the lower left region to be lower than that in the upper left region. The resulting pressure difference between the upper and lower left regions is higher than that between the bottom of the sphere and the narrow path. This pressure imbalance, which will be discussed in §3.2.2, causes repulsion of the two spheres. The contribution of shear stress differences to the repulsion will also be discussed in §3.2.2.

Figure 5(b) shows an interesting streamline pattern in the wake region. Two counter-rotating eddies exist in the wake but their configuration is quite different from that for axisymmetric flow. The lower eddy is formed by the fluid separating on the lower portion of the sphere as in the case of axisymmetric flow. The upper eddy is not formed by the fluid separating on the upper portion of the sphere, but rather by the fluid turning around the lower eddy and being entrained by the upper flow. This upper eddy is detached from the sphere. A portion of the fluid moving around the bottom of the sphere passes between the detached upper eddy and the sphere. The streamline A-B encompassing the upper eddy intersects itself, and the intersection point, C, designated as the downstream stagnation point, is shifted toward the x, y symmetry plane. Both eddies are smaller than those of the axisymmetric flow. These new features can be explained as follows. The pressure above the upper wake is less than that below the lower wake owing to the increased acceleration of the fluid in the narrow path between the two spheres (as will be shown in figure 7). Thus, the fluid particles turning around the lower eddy are pushed into the upper region of the wake. The pressure distribution around the sphere will be discussed further in §3.2.2.

Figure 5(c) shows a sketch of the actual streamline pattern at Reynolds number 100 for the case $d_0 = 1.5$. The shifting of the front stagnation streamline and stagnation point toward the x, y symmetry plane are more obvious here than in the previous case of $d_0 = 2$. The significant difference is in the wake region where both the upper eddy and downstream stagnation point vanish. Fluid particles separating on the upper portion of the sphere move downstream without returning (streamline D-E). On the other hand, fluid particles turning around the lower eddy move into the upper region of the wake until they reach near the upper separation point, D, and then move downstream in an S-shaped path (streamline F-G) without returning to form an eddy. The lower eddy shrinks as the two spheres become closer, and the pressure difference between the top and bottom of the wake is larger.

It is interesting to examine the changes in the separation region at the sphere surface for the cases $d_0 = 2$ and 1.5. More specifically, we examine the behaviour of the circle of intersection of the wake and the sphere. Our results show that the circle

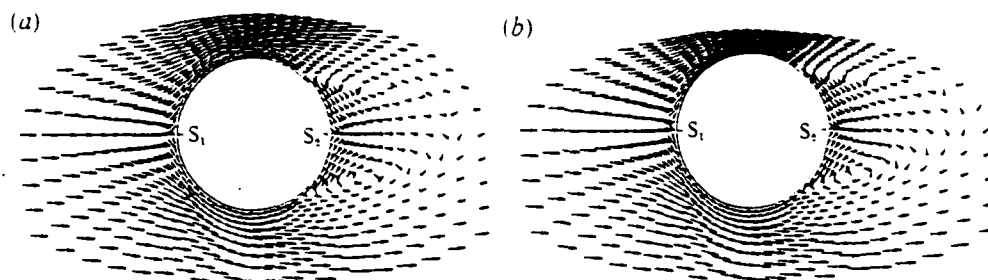


FIGURE 6. Velocity vector fields over one of the two solid spheres in the principal plane corresponding to (a) figure 5(b), $d_0 = 2$; (b) figure 5(c), $d_0 = 1.5$.

is slightly shifted toward the x, y symmetry plane due to the decreased pressure in the gap region with respect to that in the wake lower region. This shifting produces separation angles at the top, middle, and bottom of the sphere with values of 123.1° , 126.5° , and 126.2° respectively for the case $d_0 = 1.5$, where the angles are measured from the front stagnation point of the axisymmetric flow case. This is in contrast with an angle of 125.7° at all positions for a single sphere.

Figure 6(a) shows the computed velocity vector field corresponding to figure 5(b), $d_0 = 2$. The velocity vectors upstream of the front stagnation point, S_1 , for axisymmetric flow point downwards away from the x, y symmetry plane. This indicates that the front stagnation point (P in figure 5b), is shifted toward the x, y symmetry plane. Similar behaviour occurs at the rear stagnation point (Q in figure 5b). Figure 6(b) shows the computed velocity vector field corresponding to figure 5(c), $d_0 = 1.5$.

One of the advantages of the velocity vector plot is that it shows clearly the relative magnitude of velocity in the flow field, e.g. the smaller velocity in the wake region compared to that outside the wake is seen in figure 6(a, b). However, it is difficult to obtain streamlines directly from the tangents of the velocity vector plot.

A stream function ψ cannot be defined and calculated from the velocity in the principal plane owing to the existence of a divergence associated with the third component of velocity. Nevertheless, for descriptive purposes only, it is convenient to use the algorithm

$$\psi_{ps}(r, \theta_0) = \psi_{ps}(r_0, \theta_0) + \int_{r_0}^r -u_\theta dr \quad (24)$$

to present approximations to the streamline pattern. It is understood that since a true stream function does not exist, the pseudo-stream function is dependent upon the integration path. The above algorithm specifically involves only radial integration; u_θ can be recovered by differentiation of this function, but u_r cannot be recovered. The streamlines presented in figures 5(a-c) were based on this algorithm.

Phenomena in the wake similar to those described above have been found in a few previous studies. Rosfjord (1974) obtained results similar to those in figures 5(b) and 5(c) in his experimental and numerical studies of the recirculating flow region between two-dimensional parallel separated jets. He found that for velocity ratios between two jets equal to 1.11 and 1.25 (upper to lower), two eddies exist near the injector face, but the upper eddy is detached from the injector face, and a portion of the fluid originating at the lower jet is entrained by the upper jet, passing between the detached upper eddy and the injector face. He also reported that for a velocity ratio of 1.4, only the lower eddy existed and a complete entrainment of the weaker

Three-dimensional flow over two spheres

13

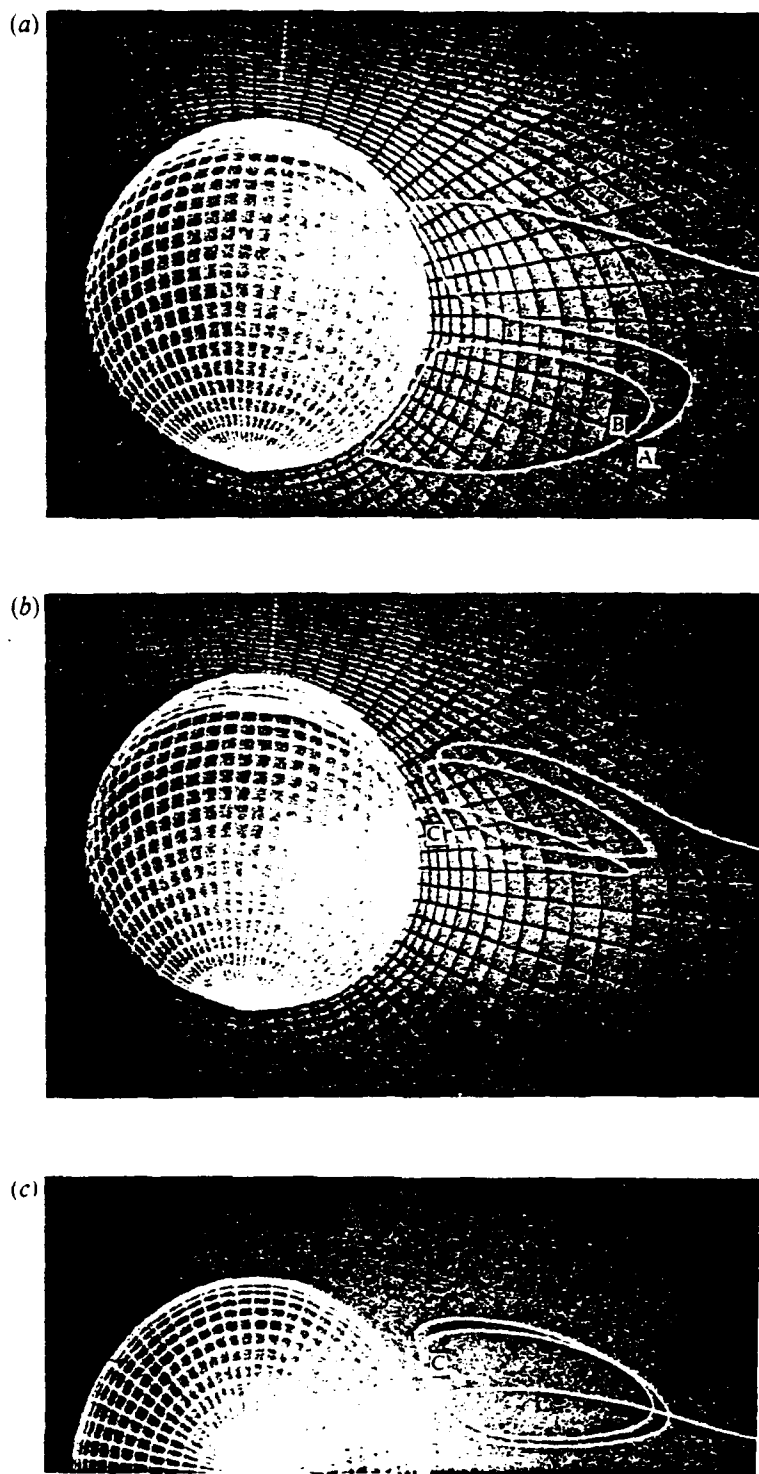


FIGURE 7. (a) Pathlines of two fluid particles (A and B) slightly above the principal plane ($y = 0.001$) of the two solid spheres. (b, c) Pathline of a fluid particle (C) whose initial position was $(x, y, z = 0.995, 0.575, 0)$: (b) a view from top of the sphere looking toward the x, y symmetry plane; (c) a side view looking normal to the x, y symmetry plane.

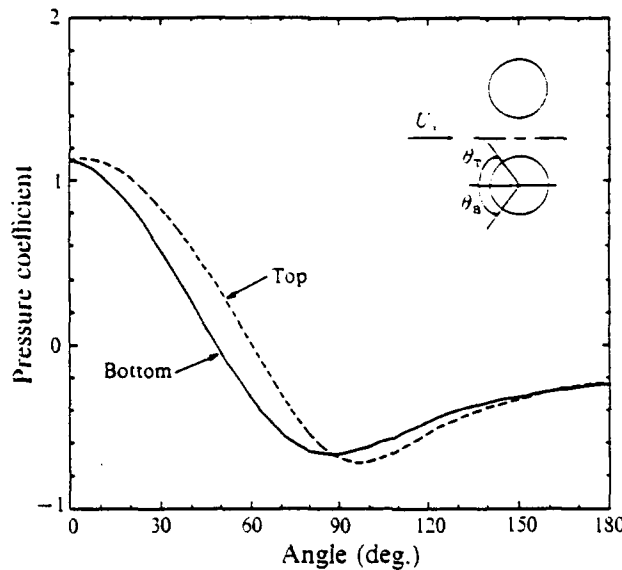


FIGURE 8. Distribution of the pressure coefficient around the solid sphere in the principal plane at $Re = 100$ for $d_0 = 1.5$.

jet was observed. In particular, the flow S-shaped loop near the stronger jet was clearly indicated. Recently, Dandy & Dwyer (1990) also found a flow pattern similar to figure 6(b) in their numerical study of steady uniform shear flow past a single solid sphere.

In order to facilitate the visualization of the three-dimensional character of the flow in the wake region discussed in detail in §3.2.1, we present the pathlines of selected fluid particles in figure 7(a–c), at Reynolds number 100 for $d_0 = 2$, where the free-stream direction is from left to right. The pathlines $x(x_0, y_0, z_0, t)$, where the subscript 0 denotes initial particle location, were obtained by solving three coupled ordinary differential equations $dx/dt = u(x)$, via a fourth-order Runge–Kutta method.

We first selected two fluid particles (A and B) slightly above the principal plane ($y = 0.001$) separated by a small distance (much smaller than the sphere radius) in the wake region. Figure 7(a) shows that particle A follows an S-shaped pathline. On the other hand, particle B follows a closed-loop pathline as was discussed in the previous section.

We then examined the pathline of a fluid particle C whose initial position $(x_0, y_0, z_0 = 0.995, 0.575, 0)$ was in the wake region but above the principal plane. Figure 7(b) (a view from top of the sphere looking toward the x, y symmetry plane) shows that the fluid particle C first follows a helical pathline as it approaches the x, y symmetry plane and then moves downstream. Figure 7(c) is a side view (looking normal to the x, y symmetry plane) of that pathline.

3.2.2. Pressure and shear stress distribution

Figure 8 shows the pressure coefficient, $2(p - p_\infty)/\rho U_\infty^2$, around one of the spheres in the principal plane at Reynolds number 100 for $d_0 = 1.5$. On average, the pressure is higher on the top, contributing to a positive lift force. The pressure on the bottom of the sphere is lower between 0° and 87.6° and also slightly lower between 159° and 180° in the wake region than that on the top of the sphere, where the angle is

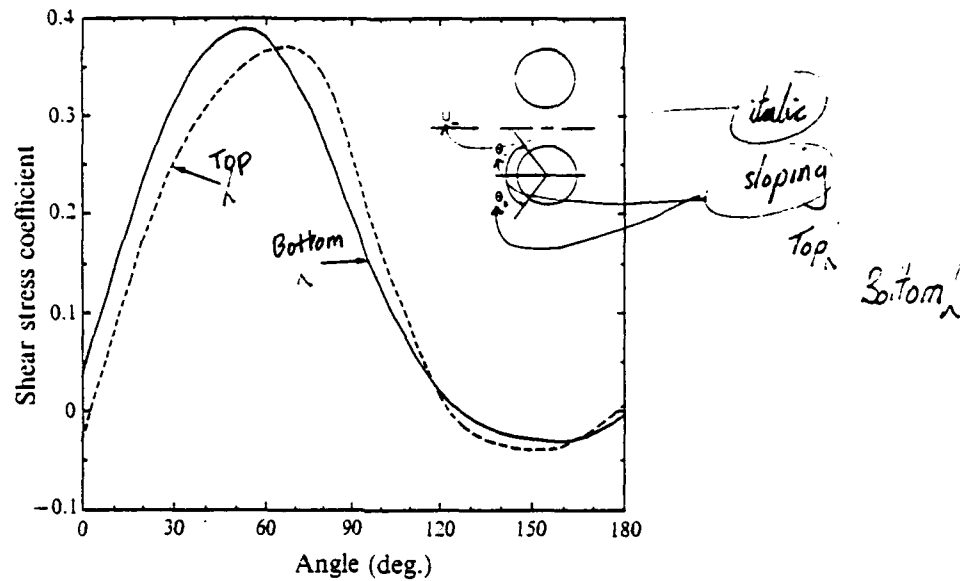


FIGURE 9. Distribution of shear stress coefficient around the solid sphere in the principal plane at $Re = 100$ for $d_0 = 1.5$.

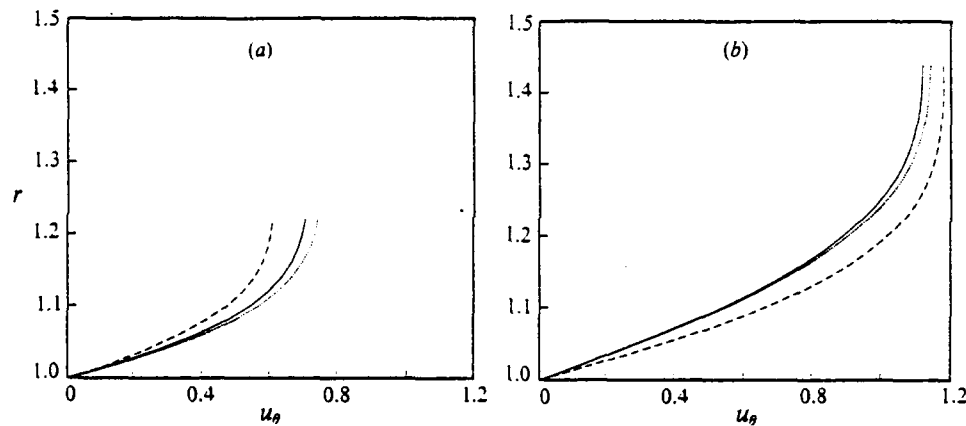


FIGURE 10. Tangential velocity profile on the bottom and top of the solid sphere in the principal plane at (a) $\theta = 36^\circ$; (b) $\theta = 84^\circ$: —, single sphere; ·····, bottom; ---, top.

measured from the front stagnation point ($\theta = 0$) of the axisymmetric flow case. On the bottom of the sphere, the minimum pressure occurs at an angle less than 90° . On the top of the sphere, the minimum pressure occurs at an angle greater than 90° and is lower than the minimum pressure on the bottom of the sphere. The maximum pressure occurs a few degrees toward the x, y symmetry plane measured from $\theta = 0$. The highest pressure in the wake region occurs a few degrees toward the x, y symmetry plane measured from $\theta = \pi$. These observations indicate that the front and rear stagnation points are shifted a few degrees toward the x, y symmetry plane.

Figure 9 shows the tangential shear stress coefficient, $2\tau_{\theta}/\rho U_\infty^2$, in the same plane used for the pressure coefficient in figure 8. Note that the clockwise direction is considered positive for the shear stress on the top of the sphere, and the counterclockwise direction is considered positive for the shear stress on the bottom.

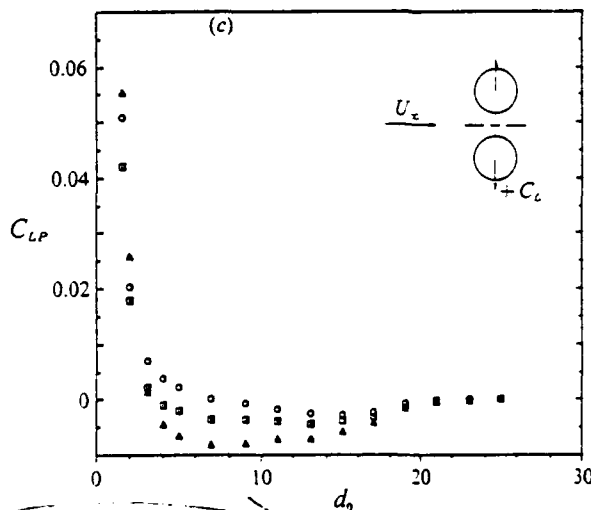
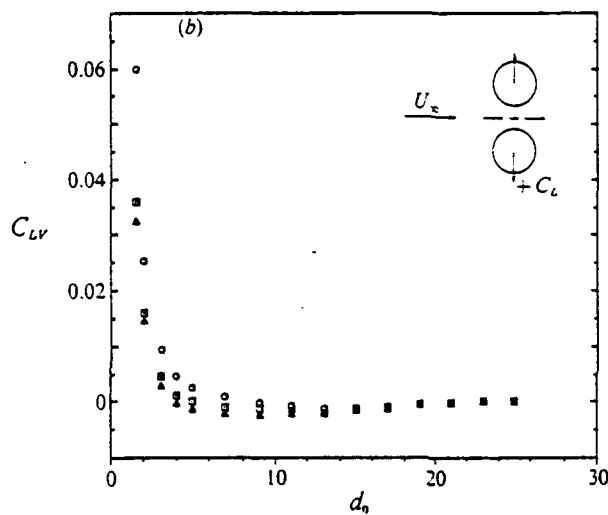
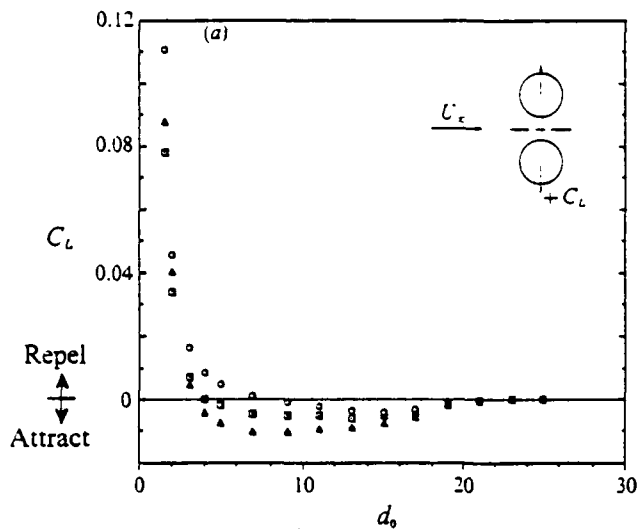


FIGURE 11. FOR LEGEND SEE OPPOSITE.

Centre / L.C.

It is seen that the shear stress, on average, is higher around the lower part of the sphere than around the top. In particular, the magnitude of the shear stress is higher in the lower regions $\theta = 0$ to 63.6 and $\theta = 165.5$ to π than on the top of the sphere. It is also important to note that, owing to their inclinations with the x -axis, the shear forces on these two lower regions contribute to both the lift (parallel to the z -axis) and drag (parallel to the x -axis), whereas the shear force at the top of the sphere contributes mainly to the drag. Thus, the shear forces in this case contribute, along with the pressure forces, to the repulsion of the two spheres. The shear stress at $\theta = 0$ is not zero but acts counterclockwise, and the shear stress at $\theta = \pi$ is not zero but acts clockwise. Therefore, the front and rear stagnation points are shifted a few degrees toward the x, y symmetry plane. Another interesting feature is that the separation angle where the shear stress vanishes on the top of the sphere is 123.1° , but that angle on the bottom is 126.2° . The computed separation angle of 125.7° for the axisymmetric flow case with the medium-size grid was shown in table 2. Thus, the reverse flow in the wake region is shifted upwards toward the x, y symmetry plane.

We examine next the tangential velocity profiles, $u_\theta(r)$, at two different θ -locations on the bottom and top of the sphere in the principal plane at Reynolds number 100 for $d_0 = 1.5$. Figure 10(a) shows the tangential velocity profiles at $\theta = 36^\circ$ on the bottom and top of one of the spheres, in addition to that for the axisymmetric case as a reference. It is seen that the maximum velocity at the bottom is higher than at the top, as mentioned earlier in the discussion of figure 5(b). It is also seen that the velocity gradient at the sphere surface is higher at the bottom than at the top, hence the higher shear stress at the bottom as explained earlier (see figure 9). Figure 10(b) shows the tangential velocity profiles at $\theta = 84^\circ$ on the bottom and top of the sphere, in addition to that for the axisymmetric case. It is seen that now the velocity gradient at the top wall is 26% higher than at the bottom although the maximum velocity at the top is only 3% higher than the maximum value at the bottom. The reason is that the boundary-layer growth at the top is limited by the interaction with the boundary layer of the other sphere.

3.2.3. Lift coefficients

In the following discussion, we classify the proximity of the two spheres into three regimes: *close*, *intermediate*, and *far separated*, depending on the values of d_0 and Reynolds number.

Figure 11(a-c) show the total lift coefficient and the lift coefficients due to viscous and pressure contributions, respectively, as a function of d_0 at Reynolds numbers 50, 100, and 150. The total lift coefficient, figure 11(a), is positive when the two spheres are close ($d_0 < 7.9$ for $Re = 50$, $d_0 < 4$ for $Re = 100$, and $d_0 < 3.4$ for $Re = 150$). That is, the two spheres repel each other, and the repulsion is stronger the closer they are. Our results show that both the viscous and pressure contributions have an important effect on the repelling force, but the pressure contribution is more dominant when $Re \geq 100$ (compare figure 11b,c). On the other hand, the total lift coefficient is negative and relatively small – that is, the two spheres attract each other weakly – at intermediate separation distances ($7.9 < d_0 < 21$ for $Re = 50$, $4 < d_0 < 21$ for $Re = 100$, and $3.4 < d_0 < 21$ for $Re = 150$). At these distances, the pressure is the main contributor to the attraction force at all Reynolds numbers. The smaller the

FIGURE 11. Lift coefficients of the solid spheres as a function of d_0 at $Re = 50, 100$, and 150 : (a) total lift coefficient; (b) viscous contribution to lift; (c) pressure contribution to lift. \circ , $Re = 50$; \square , $Re = 100$; \triangle , $Re = 150$.

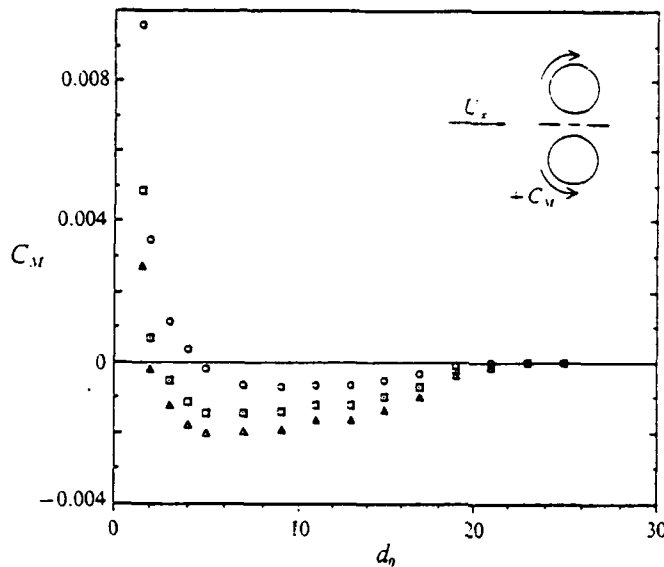


FIGURE 12. Moment coefficient of the solid spheres as a function of d_0 at $Re = 50, 100$, and 150 . Symbols as figure 11.

Reynolds number is, the smaller the pressure effect, the weaker the attraction, and the narrower the region of attraction. When $d_0 \geq 21$, however, the lift vanishes, and the two spheres have no interactions at any Reynolds numbers.

As discussed in §3.2.1, when the two spheres are in close proximity, the front stagnation point is shifted toward the x, y symmetry plane, and the fluid particles accelerate faster in the lower left region than in the upper left region of the sphere. This difference in acceleration results in a net negative pressure gradient normal to and away from the x, y symmetry plane, contributing to the repulsion between the two spheres. The shear stress is also higher in the lower left region than in the upper left as shown in figure 9. Furthermore, owing to its inclination with the x -axis, the shear force in the lower left region contributes to both the lift (parallel to the z -axis) and drag (parallel to the x -axis), whereas the shear force at the top of the sphere contributes mainly to the drag. Therefore, both the pressure and shear forces contribute to a positive lift force (i.e. the two spheres repel each other) when the two spheres are close.

On the other hand, when the two spheres are in the intermediate separation regime, the velocity vector distributions show that the front stagnation streamline is almost straight, and thus the flow in the lower left region is not affected by the presence of the other sphere. Nevertheless, the gap between the two spheres causes the flow to accelerate slightly faster on the top of the sphere than on the bottom and, as a result, the average pressure in the lower region is slightly higher than that in the narrow gap. Thus, the two spheres attract each other weakly, and the attraction force is mainly due to the pressure distribution. The shear force, nearly parallel to the x -axis at the top of the sphere, contributes mainly to the drag but not to the lift.

3.2.4. Moment and drag coefficients

Figure 12 shows the moment coefficient as a function of dimensionless distance at Reynolds numbers 50, 100, and 150. The moment coefficient is positive when the two spheres are close ($d_0 < 4.6$ for $Re = 50$, $d_0 < 2.5$ for $Re = 100$, and $d_0 < 1.96$ for $Re = 150$), that is, the two spheres experience positive torque, and the torque becomes

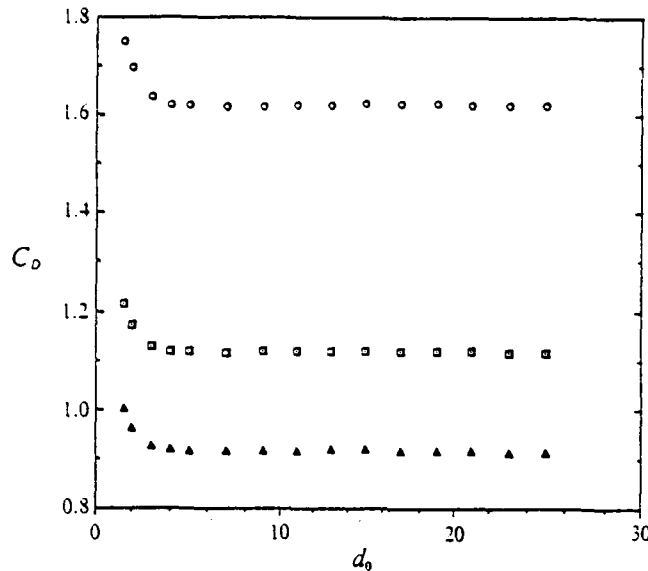


FIGURE 13. Drag coefficient of the solid spheres as a function of d_0 at $Re = 50, 100$, and 150 . Symbols as figure 11.

stronger the closer they are. On the other hand, the moment coefficient is negative at intermediate separation distances. The moment essentially vanishes, and the two spheres have negligible interactions with each other when $d_0 \geq 21$. In our calculations, the solid spheres were not allowed to rotate under the influence of the torque.

When the two spheres are close, the shear stress, on average, is higher around the lower part of the sphere than around the top, and thus they experience positive torque. On the other hand, when the spheres are at the intermediate separation distances, slightly higher velocity in the gap leads to slightly higher shear stress on the top than on the bottom of the sphere, and this causes the spheres to experience weak negative torque.

We note that the torque acting on the sphere is relatively small, and the moment coefficient is less than 1% of the drag coefficient for all the separation distances and Reynolds numbers. The main reason for this is that the torque depends only on the distribution of the shear stresses ($\tau_{r\theta}$ and $\tau_{\theta r}$) and, as shown in figure 9, the shear stress on the top of the sphere counteracts that on the left bottom of the sphere.

Figure 13 shows the drag coefficient as a function of the dimensionless distance at Reynolds numbers 50, 100, and 150. The drag increases with decreasing d_0 when d_0 is less than 4 for all Reynolds numbers. It increases slightly with increasing d_0 at intermediate separation distances, and eventually tends to that of a single sphere when $d_0 \geq 21$. The drag increases as the two spheres get close because the shear stress on the sphere is increased and the pressure distribution is changed owing to the flow acceleration on the lower left region as well as in the gap between them, as shown in figures 8 and 9.

3.3. Interactions of two liquid spheres

In the analysis of the flow field past two liquid spheres, we use a viscosity ratio (internal fluid to external fluid) of 25 and density ratio of 300. These values are typical of liquid-hydrocarbon fuel in a high-temperature high-pressure surrounding gas generally encountered in gas turbine combustors (Raju & Sirignano 1990).

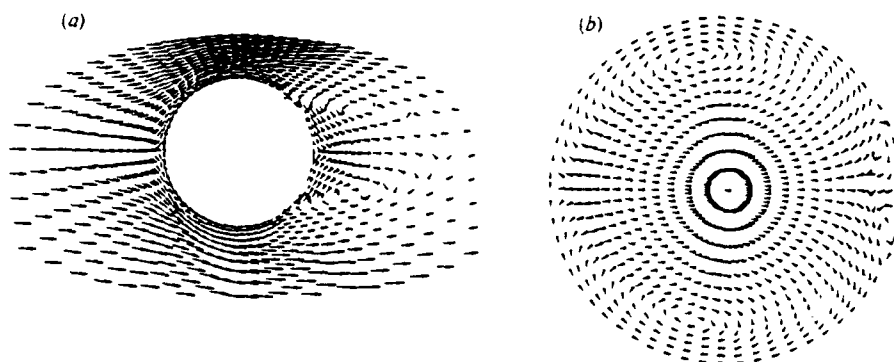


FIGURE 14. Velocity vector fields in the principal plane for a liquid sphere at $Re = 100$ for $d_0 = 2$: (a) external flow; (b) internal flow.

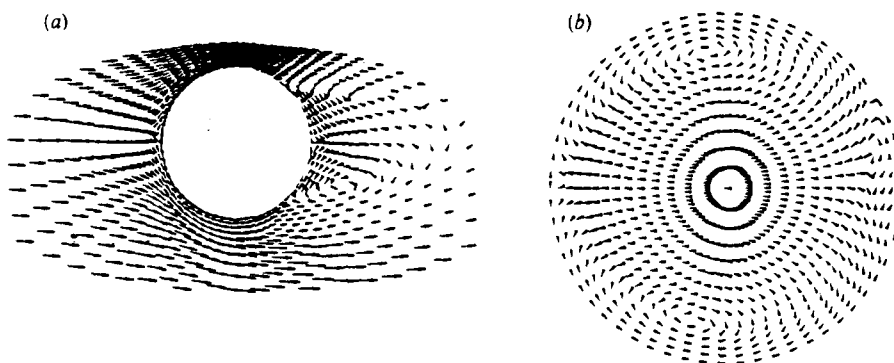


FIGURE 15. Velocity vector fields in the principal plane for a liquid sphere at $Re = 100$ for $d_0 = 1.5$: (a) external flow; (b) internal flow.

As in the solid-sphere case, we examine the flow field for two liquid spheres in the (x, z) -plane of symmetry, the *principal plane*, where the narrowest path between the liquid spheres is encountered. Figure 5(a-c) discussed in §3.2.1 can also represent typical streamlines in the external flow of liquid spheres. However, there are differences from the solid-sphere case. First, the angle, measured from $\theta = 0$, at which separation occurs on the sphere surface is much higher than that of the solid sphere. Second, a closer examination of the velocity plot (figures 14a and 15a) in the wake region indicates that the separating streamline, instead of being nearly normal to the sphere surface, now curves closer to the sphere surface, producing a 'squashed' recirculation zone. This behaviour was also seen in the velocity vector field of axisymmetric flow in figure 4(a). The length of the recirculating eddy is also slightly smaller than that of the solid sphere.

Figure 14(a, b) shows the velocity vector fields of the external and internal flows, respectively, in the principal plane at Reynolds number 100 where the two spheres are separated by a distance $d_0 = 2$. A secondary eddy in the liquid-sphere stern region is evident in both the upper and lower regions in the principal plane, but the eddy centres in both regions are asymmetrical with respect to the $z = 0$ plane. Also, these eddies are concomitant with the occurrence of the eddies in both regions in the external flow. Figure 15(a, b) shows the velocity vector fields of the external and internal flows in the principal plane at Reynolds number 100 for the case of $d_0 = 1.5$. The secondary internal eddy in the liquid-sphere stern region exists only in the lower

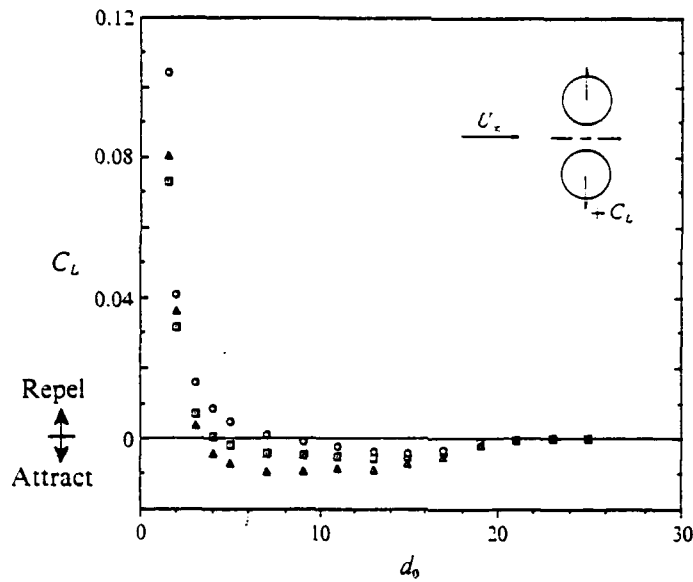


FIGURE 16. Total lift coefficient of the liquid spheres as a function of d_0 at $Re = 50$ (\circ), 100 (\square), and 150 (\triangle).

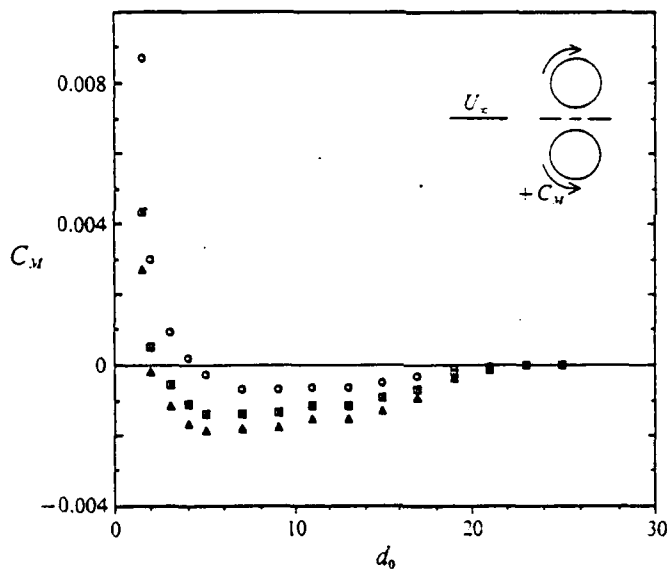


FIGURE 17. Moment coefficient of the liquid spheres as a function of d_0 at $Re = 50$, 100, and 150. Symbols as figure 16.

region, and the secondary eddy in the upper region no longer exists. The vanishing secondary internal eddy in the upper region is accompanied by the disappearance of the recirculating eddy in the upper region in the external flow.

Calculations of the lift, moment, and drag coefficients were performed for dimensionless distances from the liquid sphere centre to the symmetry plane between two liquid spheres in the range $1.5 \leq d_0 \leq 25$, for a viscosity ratio (liquid to gas) of 25 and density ratio of 300 at Reynolds numbers 50, 100, and 150. Figures 16, 17, and 18 show the coefficients of total lift, moment, and drag as a function of dimensionless

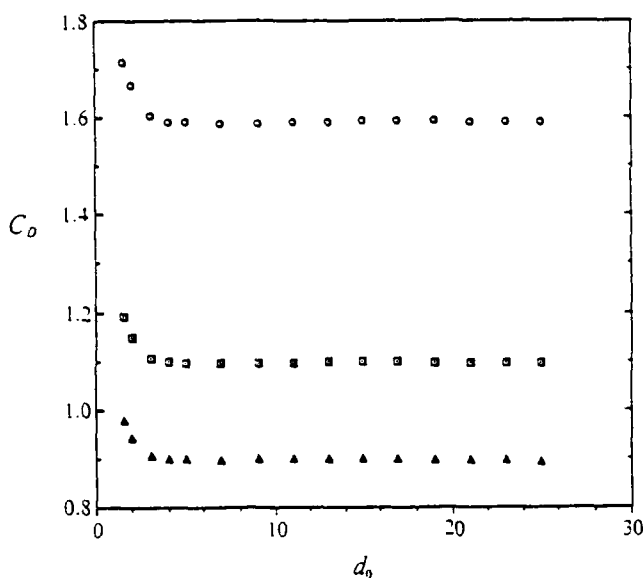


FIGURE 18. Drag coefficient of the liquid spheres as a function of d_0 at $Re = 50, 100$, and 150 . Symbols as figure 16.

distance at Reynolds numbers 50, 100, and 150. The coefficients of total lift, moment, and drag are slightly smaller in absolute value than those for the solid spheres at both the repelling and attraction separation distances and at all Reynolds numbers. The lower coefficients of the liquid sphere are attributed to the surface motion of the liquid sphere which reduces the velocity gradient and friction force. A smaller drag coefficient for the liquid sphere in axisymmetric flow has been also found in earlier calculations (Clift *et al.* 1978).

4. Conclusions

Three-dimensional flow interactions between two identical (solid or liquid) spheres which are held fixed, with the line connecting the sphere centres normal to a uniform stream, have been investigated at Reynolds numbers 50, 100, and 150 as a first step towards understanding the three-dimensional interactions with a large concentration of particles.

First, the interactions between two solid spheres have been investigated for a dimensionless distance in the range $1.5 \leq d_0 \leq 25$.

The two spheres repel each other when they are close ($d_0 < 7.9$ for $Re = 50$, $d_0 < 4$ for $Re = 100$, and $d_0 < 3.4$ for $Re = 150$), and the repulsion is stronger the closer they are. On the other hand, the two spheres attract each other weakly at intermediate separation distances ($7.9 < d_0 < 21$ for $Re = 50$, $4 < d_0 < 21$ for $Re = 100$, and $3.4 < d_0 < 21$ for $Re = 150$). For $d_0 \geq 21$, however, the lift vanishes, and the two spheres do not interact at any Reynolds numbers.

The two spheres experience positive torque when they are close ($d_0 < 4.6$ for $Re = 50$, $d_0 < 2.5$ for $Re = 100$, and $d_0 < 1.96$ for $Re = 150$), and the torque is stronger the closer they are. On the other hand, the moment coefficient is negative at intermediate separation distances. The moment vanishes, and the two spheres do not interact when $d_0 \geq 21$. The drag on the spheres increases when d_0 is less than 4 for all

Reynolds numbers. It increases slightly at intermediate separation distances, and eventually, tends to that of a single sphere when $d_0 \geq 21$.

The flow structure ahead of each sphere is such that the streamlines shift away from the x, y symmetry plane due to the flow blockage in the gap between the two spheres as they approach the front stagnation region. Also, interesting phenomena in the near wake have been discovered as the gap between the two spheres decreases. When $d_0 = 2$, the upper eddy is not formed by the fluid separating on the upper portion of the sphere, but rather by the fluid turning around the lower eddy and detached from the sphere. Furthermore, when d_0 decreases to 1.5, both the upper eddy and downstream stagnation point vanish.

The interactions between two liquid spheres have been also investigated for the dimensionless distance in the range $1.5 \leq d_0 \leq 25$ for a viscosity ratio of 25 and density ratio of 300 at Reynolds numbers 50, 100, and 150.

The magnitudes of the lift, torque, and drag on the liquid spheres are slightly smaller in absolute value than those of the solid spheres at all the separation distances and all Reynolds numbers. The flow structure in the external flow of the liquid spheres is quite similar to that of the solid spheres, except that the separation angle is much higher than that of the solid spheres and the separation streamline is bent closer to the sphere surface producing a 'squashed' recirculation zone.

This work has been supported by the Air Force Office of Scientific Research under grant No. 90-0064 with Dr Julian Tishkoff acting as the technical monitor. We would like to thank Mr Lyle Wiedeman and Dr Allen Schiano for their assistance in using a three-dimensional graphic package Application Visualization System (AVS). The support of the Pittsburgh Supercomputing Center and the San Diego Supercomputer Center under a block grant of the Office of Academic Computing of UCI are gratefully appreciated.

REFERENCES

- ANDERSON, D. A., TANNEHILL, J. C. & PLETCHER, R. H. 1984 *Computational Fluid Mechanics and Heat Transfer*. Hemisphere.
- CHIANG, C. H. & SIRIGNANO, W. A. 1991a Numerical analysis of interacting, convecting, vaporizing fuel droplets with variable properties. *Intl J. Heat Mass Transfer* (submitted). ? update
- CHIANG, C. H. & SIRIGNANO, W. A. 1991b Axisymmetric calculations of three-droplets interactions. *Atomization and Sprays* (submitted).
- CLIFT, R., GRACE, J. R. & WEBER, M. E. 1978 *Bubbles, Drops, and Particles*. Academic.
- DANDY, D. S. & DWYER, H. A. 1990 A sphere in shear flow at finite Reynolds number: effect of shear on particle lift, drag, and heat transfer. *J. Fluid Mech.* 216, 381-410.
- GOLDBURG, A. & FLORSHEIM, B. H. 1966 Transition and Strouhal number for the incompressible wake of various bodies. *Phys. Fluids* 9, 45-50.
- KIM, I. & PEARLSTEIN, A. J. 1990 Stability of the flow past a sphere. *J. Fluid Mech.* 211, 73-93.
- NAKAMURA, I. 1976 Steady wake behind a sphere. *Phys. Fluids* 19, 5-8.
- PATNAIK, G. 1986 A numerical solution of droplet vaporization with convection. Ph.D. dissertation, Carnegie-Mellon University.
- RAJU, M. S. & SIRIGNANO, W. A. 1990 Interaction between two vaporizing droplets in an intermediate-Reynolds-number flow. *Phys. Fluids A* 2, 1780-1796.
- RIVKIND, V. Y. & RYSKIN, G. 1976 Flow structure in motion of a spherical drop in a fluid medium at intermediate Reynolds numbers. *Fluid Dyn.* 11, 5-12.
- ROOS, F. W. & WILLMARTH, W. W. 1971 Some experimental results on sphere and disk drag. *AIAA J.* 9, 285-291.

- ROSFJORD, T. J. 1974 Experimental and theoretical investigations of the recirculating flow region between two-dimensional, parallel, separated jets. Ph.D. dissertation, Princeton University.
- SIRIGNANO, W. A. 1983 Fuel droplet vaporization and spray combustion. *Prog. Energy Combust. Sci.* 291-322. Vol. 9
- TAL(THAU), R., LEE, D. N. & SIRIGNANO, W. A. 1983 Hydrodynamics and heat transfer in sphere assemblages - cylindrical cell models. *Intl J. Heat Mass Transfer* 26, 1265-1273.
- TAL(THAU), R., LEE, D. N. & SIRIGNANO, W. A. 1984 Heat and momentum transfer around a pair of spheres in viscous flow. *Intl J. Heat Mass Transfer* 27, 1253-1262.
- TANEDA, S. 1956 Experimental investigation of the wake behind a sphere at low Reynolds number. *J. Phys. Soc. Japan* 11, 1104-1108.
- TOMBOULIDES, A. G., ORSZAG, S. A. & KARLADAKIS, G. E. 1991 Three-dimensional simulation of flow past a sphere. *ISOPE Proc.* Edinburgh, Scotland.
- VINOKUR, M. 1983 On one-dimensional stretching functions for finite-difference calculations. *J. Comput. Phys.* 50, 215-234.

in: vol. 9

Av: please spell out



ADDENDUM TO SECTION 3

AIAA-92-0343

**Three-Dimensional Flow Computation
for Two Interacting, Moving Droplets**

I. Kim, S. Elghobashi, and W. A. Sirignano
University of California
Irvine, CA

**30th Aerospace Sciences
Meeting & Exhibit**
January 6-9, 1992 / Reno, NV

Three-Dimensional Flow Computation for Two Interacting, Moving Droplets *

I. Kim,[†] S. Elghobashi,[‡] and W. A. Sirignano[§]

Department of Mechanical and Aerospace Engineering
University of California, Irvine

Abstract

A numerical simulation is performed for the three-dimensional interaction of two moving droplets which are injected into an initially quiescent fluid medium. The pressure and velocity fields around each of the droplet are modified due to the presence of the other droplet. Drag and lift are therefore different from the values for an axisymmetric flow around a single isolated droplet. The droplets decelerate due to the drag and changing their direction of motion due to the lift. By choosing the origin of a noninertial reference frame at the center of mass of the two droplets, the Navier-Stokes equations are solved with a noninertial term in an iterative manner. For small initial separation, the lift forces are repelling, thereby increasing the separation. For larger initial separation, a slight attraction occurs.

Nomenclature

a'_o	dimensional droplet radius
d_o	initial ratio of distance between droplet centers to droplet diameter
d_t	instantaneous dimensionless distance between droplet centers
l_t	instantaneous dimensionless position in y direction
N_1, N_2, N_3	numbers of grids in ξ, η, ζ directions
Re	initial Reynolds number based on droplet diameter, $U'_{d,o} 2a_o / \nu$
Re_t	instantaneous droplet Reynolds number, $U_{d,t} 2a_o / \nu$
$U'_{d,o}$	initial dimensional droplet velocity
$U'_{d,t}$	instantaneous dimensional droplet velocity, $\sqrt{V'^2_{\infty,t} + U'^2_{\infty,t}}$
$U'_{\infty,t}$	instantaneous dimensional droplet velocity

$V'_{\infty,t}$	in x-direction instantaneous dimensional droplet velocity
t	in y-direction time normalized by $a'_o / U'_{d,o}$
x, y, z	Cartesian coordinates

Greek symbols

ξ, η, ζ	nonorthogonal generalized coordinates
τ	viscous stress tensor

Superscript

'	dimensional quantity
---	----------------------

Subscript

o	initial quantity
---	------------------

1. Introduction

Typical dispersed two-phase flows encountered in engineering applications such as combustion systems and chemical processes have regions of large concentration of particles or droplets. In such regions, the effect of neighboring droplets modifies the ambient conditions in the flow near any given droplet. The droplet trajectory and the coefficients of drag, lift, and moment can be significantly affected by the modified flow field due to neighboring droplets.

The geometrical configurations of droplets in a real region of large concentration are complex and subject to uncertainty. Droplet arrays as discussed by Sirignano [1], although artificial, can provide information on droplets interaction and give a detailed analysis of the problem.

Several investigators [2-7] have performed research on axisymmetric configurations of interacting particles (or droplets) in the wake of another particles (or droplets).

Recently, Kim *et al.* [8] investigated three-dimensional flow interactions with two identical spherical droplets which were *held fixed relative to each other* in the transverse direction against the uniform stream at Reynolds number $O(100)$; they also studied two identical solid spheres in the same situation. They determined the effects of three-dimensional interactions

*Copyright ©1992 by the authors. Published by the American Institute of Aeronautics and Astronautics, Inc. with permission.

[†]Research Associate, Member AIAA.

[‡]Professor of Mechanical and Aerospace Engineering, member AIAA.

[§]Professor of Mechanical and Aerospace Engineering, Fellow AIAA.

on the lift, moment, and drag coefficients as a function of the dimensionless distance between the two spheres and Reynolds number and also discovered interesting near-wake flow patterns as the gap between the two spheres decreased.

In the present paper, we extend the work of Kim *et al.* [8] and study the droplets interaction in a more realistic situation where two identical droplets are injected and then move side-by-side into initially quiescent fluid medium. The droplets will be decelerating due to the drag and changing their direction of motion due to the lift. By placing the origin of a noninertial reference frame at the center of mass of the two droplets, the Navier-Stokes equations to be solved include a noninertial term, which will be evaluated from Newton's second law for the droplet motion.

2. Formulation and numerical solution

We consider an unsteady, three-dimensional, incompressible, laminar flow generated by two identical (spherical) droplets injected into initially quiescent constant property Newtonian fluid and then moving side-by-side lying in the same plane as shown in Figure 1, where d_t denotes the instantaneous distance, normalized by the droplet radius, from the droplet center to the y-z symmetry plane between the two droplets. We neglect the net gravity force acting on the droplet and also assume that the Weber number is small enough that the droplet remains of spherical shape. We choose the origin of a nonrotating noninertial reference frame at the center of mass of the two droplets and the angle of initial droplet motion $\alpha_0 = 0$. Far upstream, the flow is uniform and has an instantaneous velocity V_{∞} parallel to the y-axis. It is noted that there are two symmetry planes in Figure 1. One is the x-y plane in which the centers of the two droplets lie, and the other is the y-z plane which is midway between the droplet centers.

As shown in Figure 1, we utilize three coordinate systems in our formulation, the Cartesian coordinates (x,y,z) for the gas phase whose origin is at the center of mass of the two droplets, the Cartesian coordinates (x_l, y_l, z_l) for the liquid phase whose origin is at the droplet center, and also the nonorthogonal generalized coordinates (ξ, η, ζ). ξ is the radial, η is the angular, and ζ is the azimuthal direction. Due to symmetry of the geometry, the physical domain is chosen as one quarter of an ellipsoid-like space.

For the gas phase outside the droplet, the flow domain is bounded by $1 \leq \xi \leq N_1$, $1 \leq \eta \leq N_2$, $1 \leq \zeta \leq N_3 + 1$. $\xi = 1$ and N_1 correspond respectively to the droplet surface and the farfield boundary surrounding the droplet. $\eta = 1$ and N_2 denote respectively the positive z_l -axis and the $x_l - y_l$ plane outside the droplet. $\zeta = 1$ and $N_3 + 1$ are the same plane and refer to the $x_l - z_l$ plane outside the droplet.

For the liquid phase inside the droplet, the domain

is $1 \leq \xi_l \leq N_{1l}$, $1 \leq \eta_l \leq N_2$, $1 \leq \zeta_l \leq N_3 + 1$. $\xi_l = 1$ and N_{1l} correspond to the center and the surface of the droplet, respectively. $\eta_l = 1$ and N_2 denote the positive z_l -axis and the $x_l - y_l$ plane, respectively. $\zeta_l = 1$ and $N_3 + 1$ are the same plane and refer to the $x_l - z_l$ plane. Within the droplet, $\xi_l = \text{constant}$ are a family of concentric spherical surfaces. Uniform spacing ($\delta\xi = \delta\eta = \delta\zeta = 1$) is used for the generalized coordinates in both phases for convenience.

The nonorthogonal generalized coordinate system for the external flow can be easily adapted to three-dimensional arbitrary geometries. We solve the time-dependent equations of continuity and Navier-Stokes with all associated conditions, as will be discussed in detail in section 2.2.

2.1 Governing equations and boundary conditions

Since our goal is to study the flow interaction with the two droplets, we present the equations for the gas and liquid phases. The continuity and momentum equations in both phases, and the boundary conditions, are nondimensionalized using the droplet radius a'_0 as the characteristic length and $U'_{d,0}$ as the characteristic velocity.

Gas phase

$$\nabla \cdot \mathbf{V} = 0 \quad (1)$$

$$\frac{d\mathbf{V}_s}{dt} + \frac{D\mathbf{V}}{Dt} = -\nabla p + \frac{2}{Re} \nabla^2 \mathbf{V}, \quad (2)$$

where \mathbf{V}_s is the velocity of the center of mass of the two droplets.

Liquid phase

$$\nabla \cdot \mathbf{V}_l = 0 \quad (3)$$

$$\frac{d\mathbf{V}_d}{dt} + \frac{D\mathbf{V}_l}{Dt} = -\nabla p_l + \frac{2}{Re_l} \nabla^2 \mathbf{V}_l. \quad (4)$$

where \mathbf{V}_d is the droplet velocity. In these first calculations presented herein, the inertial correction for the liquid phase has been neglected.

The governing equations are transformed to the generalized coordinates (ξ, η, ζ), which allow for any three-dimensional body of arbitrary shape. The numerical integration of the equations is performed using a computational cubic mesh with equal spacing ($\delta\xi = \delta\eta = \delta\zeta = 1$).

Gas/liquid interface conditions

The conditions at the interface, $\xi = 1$ or $\xi_l = N_{1l}$, are based on the principle of continuity of shear stresses and tangential velocities. Since the interface in our flow

is always spherical (under the assumption of small Weber number), it is more convenient to cast these conditions in terms of spherical coordinates (r, θ, ϕ) whose origin is at the center of the droplet.

$$\tau_{r\theta,s} = \tau_{l,r\theta,s}, \quad (5)$$

$$\tau_{r\phi,s} = \tau_{l,r\phi,s}, \quad (6)$$

$$V_{\theta,s} = V_{l,\theta,s}, \quad (7)$$

$$V_{\phi,s} = V_{l,\phi,s}, \quad (8)$$

where $\tau_{r\theta,s}$ and $\tau_{r\phi,s}$ are respectively the shear stresses on a positive r -plane in the positive θ and ϕ direction, and the subscript s denotes the surface of the droplet. Because no fluid can cross the surface of the droplet, the normal velocities at the interface relative to surface are zero in both phases. The interface condition for pressure is obtained from the momentum equation.

Due to the different Cartesian coordinates used in each phase, the relation between the velocities on the interface is expressed as follows.

$$u = u_l + U_{\infty,t}, \quad (9)$$

$$v = v_l, \quad (10)$$

$$w = w_l, \quad (11)$$

where $U_{\infty,t}$ is the droplet velocity in x -direction due to the lift force acting on the droplet.

Gas-phase boundary conditions

In the following equations, u , v , and w are the gas velocities in the x , y , and z direction, respectively. p is the pressure, and the subscript l denotes liquid phase.

$$p = 0, u = 0, v = V_{\infty,t}, w = 0 \quad \text{at } \xi = N_1 \quad (12)$$

except $x = 0$.

$$\frac{\partial p}{\partial x} = \frac{\partial v}{\partial x} = \frac{\partial w}{\partial x} = 0, u = 0 \quad \text{at } x = 0. \quad (13)$$

$$\frac{\partial p}{\partial \eta} = \frac{\partial u}{\partial \eta} = \frac{\partial v}{\partial \eta} = \frac{\partial w}{\partial \eta} = 0 \quad \text{at } \eta = 1. \quad (14)$$

$$\frac{\partial p}{\partial \eta} = \frac{\partial u}{\partial \eta} = \frac{\partial v}{\partial \eta} = 0, w = 0 \quad \text{at } \eta = N_2. \quad (15)$$

The periodic condition is applied for u , v , w , and p at the two planes $\zeta = 1$ and $N_3 + 1$.

Liquid-phase boundary conditions

$$\frac{\partial p_l}{\partial \xi_l} = \frac{\partial u_l}{\partial \xi_l} = \frac{\partial v_l}{\partial \xi_l} = 0, w_l = 0 \quad \text{at } \xi_l = 1. \quad (16)$$

$$\frac{\partial p_l}{\partial \eta_l} = \frac{\partial u_l}{\partial \eta_l} = \frac{\partial v_l}{\partial \eta_l} = \frac{\partial w_l}{\partial \eta_l} = 0 \quad \text{at } \eta_l = 1. \quad (17)$$

$$\frac{\partial p_l}{\partial \eta_l} = \frac{\partial u_l}{\partial \eta_l} = \frac{\partial v_l}{\partial \eta_l} = 0, w_l = 0 \quad \text{at } \eta_l = N_2. \quad (18)$$

The periodic condition is applied for u_l , v_l , w_l , and p_l at the two planes $\zeta_l = 1$ and $N_3 + 1$.

The drag, lift, and moment coefficients are evaluated in dimensional form as follows.

$$F'_D = \int_S -p' \mathbf{n} \cdot \mathbf{e}_D dS' + \int_S \mathbf{n} \cdot \boldsymbol{\tau}' \cdot \mathbf{e}_D dS' \quad (19)$$

$$F'_L = \int_S -p' \mathbf{n} \cdot \mathbf{e}_L dS' + \int_S \mathbf{n} \cdot \boldsymbol{\tau}' \cdot \mathbf{e}_L dS' \quad (20)$$

$$\mathbf{M}' = \int_S \mathbf{r}' \times \boldsymbol{\tau}' dS', \quad (21)$$

where $\mathbf{e}_D \equiv (-\sin \alpha_i \mathbf{i} + \cos \alpha_i \mathbf{j})$, $\mathbf{e}_L \equiv (\cos \alpha_i \mathbf{i} + \sin \alpha_i \mathbf{j})$. S' denotes the surface of the droplet, \mathbf{n} is the outward unit normal vector at the surface, \mathbf{r}' is the position vector from the center of the droplet, and $\boldsymbol{\tau}'$ is the viscous stress tensor.

The repelling force is assumed positive. Due to the geometrical symmetry, only the z -component of moment exists, and counter-clockwise direction is assumed positive.

The nondimensional coefficients of drag, lift, and moment are defined respectively as

$$C_D = \frac{F'_D}{\frac{1}{2} \rho' U_{d,t}^2 \pi a_o'^2} \quad (22)$$

$$C_L = \frac{F'_L}{\frac{1}{2} \rho' U_{d,t}^2 \pi a_o'^2} \quad (23)$$

$$C_M = \frac{\mathbf{M}' \cdot \mathbf{k}}{\frac{1}{2} \rho' U_{d,t}^2 \pi a_o'^3} \quad (24)$$

2.2 Numerical solution

We solve numerically the complete set of Navier-Stokes and continuity equations in each phase, subject

to the boundary conditions discussed in the previous section. We have developed a three-dimensional implicit finite-difference algorithm to solve simultaneously the set of the discretized partial differential equations.

The governing equations are represented in generalized coordinates (ξ, η, ζ) , and the control volume formulation is used to develop the finite-difference equations from them. The method of solution employs an Alternating-Direction-Predictor-Corrector (ADPC) scheme to solve the time-dependent Navier-Stokes equations. A pressure correction equation is employed to satisfy indirectly the continuity equation.

The overall solution procedure is based on a cyclic series of estimate-and-correct operations. The velocity components are first calculated from the momentum equations using the ADPC method, where the pressure field at the previous time step is employed. This estimate improves as the overall iteration continues. The pressure correction is calculated from the pressure correction equation using the SOR successive overrelaxation method. The new estimates of pressure and velocities are then obtained.

The same procedure is performed in the liquid phase. The governing equations of motion in each phase are solved in an interactive sequence through the interface boundary conditions until convergence is achieved for each time step of the calculation. Changes in droplet velocity are also determined by resolving lift and drag forces on the droplet and applying Newton's second law. This process continues until the solution converges at each time step.

In the overall procedure, the sequential solutions of governing equations and boundary conditions with grid and relative velocity adjustment are iterated until convergence is achieved. After convergence is reached, the drag, lift, and moment coefficients are evaluated at the prescribed time interval.

Now, the moving droplets change their directions due to the interactions with the surrounding fluid. However, in order to insure its accuracy, the computational grid must satisfy the condition that the lift and torque are zero for a single droplet moving in any direction. Figures 2(a) and 2(b) show two different grid distributions on the droplet surface. The grid in Figure 2(a) for a single droplet gives at finite angle α_0 nonzero lift and torque which have the same order of magnitude as those of droplets separated by $d_0 \leq 2$. On the other hand, the grid in Figure 2(b) gives zero lift and torque at any angle. We generate this three-dimensional grid algebraically by using a set of ellipsoids, cones, and planes, where grid density is controlled by the stretching function developed by Vinokur [9]. Figure 3 presents the grid on the x-y symmetry plane with the droplet centers at dimensionless distance $d_0 = 9$. Our numerical solution scheme has been developed for arbitrary grid systems so that it is necessary only to change the subroutines of grid generation for flow geometries that

differ from ours.

3. Results and discussion

We first tested the three-dimensional code by solving the steady axisymmetric flow past a single droplet at Reynolds number 100. Since the code developed solves for three Cartesian components of velocity in the transformed grid, an axisymmetric test calculation still exercises the fully three-dimensional aspects of the code.

3.1 Flow over a single droplet

Here we discuss the flow generated by an impulsively started single droplet into an initially quiescent fluid using the three-dimensional solution procedure for viscosity ratio of 25 and a density ratio of 300 (liquid to gas) at Reynolds number 100. The time-dependent solution converges asymptotically to the steady-state results. Table 1 lists the drag coefficients (C_{DP} and C_{DV} are respectively the pressure and viscous parts of C_D) as a function of the computational grid density which are in good agreement with the correlation of Rivkind & Ryskin [10]. Table 2 shows two angles measured from the front stagnation point where θ_1 is the angle at which the surface vorticity changes its sign and θ_2 is the angle at which the surface velocity is zero.

The calculations were performed for three different grids, $(N_1 \times N_2 \times N_3 \text{ and } N_{11} \times N_{21} \times N_{31}) = (20 \times 11 \times 32 \text{ and } 10 \times 11 \times 32)$, $(30 \times 15 \times 48 \text{ and } 15 \times 15 \times 48)$, and $(40 \times 21 \times 64 \text{ and } 20 \times 21 \times 64)$, in a computational domain having an outer boundary located at 21 droplet radii from the droplet center. The solutions from the three different grids were stable and smooth, and each takes dimensionless times of 20 to reach steady state.

Tables 1 and 2 show that the results of the $30 \times 15 \times 48$ grid differ by only 0.8 % in the drag coefficient and 0.7 % in the separation angle from those of the $40 \times 21 \times 64$ grid. Thus, for computational economy (a long time period is needed for our time-dependent solution of the moving droplets), we selected the medium size grid $30 \times 15 \times 48$, and $15 \times 15 \times 48$ in the liquid phase for the remaining calculations.

3.2 Interaction of two moving droplets

Calculations were performed for initial dimensionless distance $d_0 = 2$ and 9 at initial Reynolds number 100 for the time period $0 \leq t \leq 250$. This time period is about one quarter of the lifetime for a vaporizing droplet injected into a combustor, and so major changes in transport processes and flow field would be expected to occur. The viscosity and density ratios (liquid to gas) for the droplet is 25 and 300, respectively, which are typical of liquid-hydrocarbon fuel in high-temperature, high-pressure surrounding gas generally encountered in gas turbine combustors.

Figure 4(a) shows the trajectory of one droplet for $d_0 = 2$, where the numbers on the lines denote the dimensionless time. The final location of the droplet at $t = 250$ is $(d_t, l_t) = (2.505, 212.6)$. Now, since the

final location of a single droplet at $t = 250$ in the case of no drag and lift forces acting on it would be $(d_t, l_t) = (2, 250)$, the figure indicates that the two droplets are repelling each other as well as decelerating, and the change of distance (normalized by droplet radius) is much higher (37.4 vs. 0.505) due to the drag than due to the lift force. Figure 4(b) shows the trajectory of one droplet for $d_o = 9$. The final location of the droplet at $t = 250$ is $(d_t, l_t) = (8.968, 213.1)$. The theoretical final location of a single droplet at $t = 250$ in the case of no drag and lift forces would be $(d_t, l_t) = (9, 250)$; therefore, Figure 4(b) identifies that the two droplets are weakly attracting each other as well as decelerating, and the change of distance is much higher due to the drag than due to the lift force.

Figure 5 shows the lift coefficients of the droplet for $d_o = 2$ and 9 as a function of instantaneous Reynolds number, where the repelling force is taken as positive. The lift coefficient for $d_o = 2$ is positive during the time period $0 \leq t \leq 250$, and becomes gradually smaller in time because the distance between the droplets is increasing and their directions of motion are changing due to the repelling force. On the other hand, the lift coefficient for $d_o = 9$ is negative during that time period but slowly goes towards zero. The change of the distance between the two droplets for $d_o = 9$ case is negligibly small as shown in Figure 4(b). Thus, this result also indicates that the lift coefficient slowly approaches zero when Reynolds number decreases with the fixed dimensionless distance 9. The figure also shows that rapid change occurs initially due to impulsive start of the droplets and the quasi-steady state occurs when $t \geq 30$.

Figure 6 shows the moment coefficients of the droplet for $d_o = 2$ and 9 as a function of instantaneous Reynolds number, where counter-clockwise direction is taken as positive. The moment coefficient for $d_o = 2$ is positive initially and gets gradually smaller and changes its sign from positive to negative at $t = 150$. On the other hand, the moment coefficient for $d_o = 9$ is negative during the time period $0 \leq t \leq 250$ but slowly approaches zero.

Figure 7 shows the drag coefficients of the droplet for $d_o = 2$ and 9 as a function of instantaneous Reynolds number. The drag coefficient for $d_o = 2$ is higher than that for $d_o = 9$. In earlier time, the difference is greater but becomes gradually smaller as time goes on. The reason is that the droplets for $d_o = 2$ are repelling each other and the distance between them is increasing, and so the drag becomes gradually smaller. The drag coefficient for $d_o = 9$ is almost identical to that for a single droplet (slightly higher than that for a single droplet when $t \geq 30$.) Tsuji *et al.* [10] and Kim *et al.* [8] also found that for the fixed spheres and $d_o \geq 4$, the drag coefficient is almost identical to that of a single sphere. Figure 7 also shows large drag coefficient initially which indicates that large shear stress and pressure occur ini-

tially due to impulsive start.

Figure 8 shows the speed of the droplet as a function of dimensionless time. There is a sudden drop in the speed at the moment of droplet injection and then monotonically decreases with time. The speed for $d_o = 2$ is lower than $d_o = 9$ due to the larger drag of $d_o = 2$.

Figures 9(a) and 9(b) show the velocity vector fields of gas and liquid phases at $Re_t = 96.86$, $d_t = 2.002$, and $t = 19.9$ in the x-y plane of symmetry, where the narrowest path between the two droplets is encountered. The free stream is coming from the left in the figures. The velocity vectors were first calculated in the Cartesian coordinates fixed at the center of mass of the two droplets and then converted in the Cartesian coordinates fixed at the center of the droplet. Due to the divergence of the front dividing streamline and the shift of the front stagnation point toward the y-z symmetry plane, the fluid particles accelerate more in the lower left region around the droplet than in the upper left. Furthermore, the pressure drop in the lower left region is higher than the pressure drop through the narrow path between the two droplets. Shear stresses on the lower left region are also higher and contribute to lift as well as drag due to their inclination with y-axis, whereas the shear stresses at the top of the droplet are higher due to narrow path but contribute mainly to the drag. As a consequence, the two droplets are repelling each other. These phenomena are explained in detail in the study of Kim *et al.* [8] about the flow past fixed spheres.

Figures 10(a) and 10(b) show the velocity vector fields of gas and liquid phases at $Re_t = 96.94$, $d_t = 9$, and $t = 19.9$ in the x-y plane of symmetry. The velocity vectors near the front stagnation point indicate that the front dividing streamline is similar to that of a single droplet and the front stagnation point moves very slightly away from the y-z symmetry plane. Slightly lower pressure occurred in the upper region than in the lower region due to the relatively narrow path between the two droplets. As a consequence, the two droplets are weakly attracting each other.

4. Conclusions

A numerical simulation was performed for the three-dimensional interaction of two moving droplets which are injected into an initially quiescent fluid medium. Calculations were performed for initial dimensionless distance $d_o = 2$ and 9 at initial Reynolds number 100 for the time period $0 \leq t \leq 250$.

The droplets for $d_o = 2$ repel each other as well as decelerate. Their lift coefficient is positive during the time period $0 \leq t \leq 250$ and gets gradually smaller due to the change in the distance and direction of motion.

The droplets for $d_o = 9$ weakly attract each other as well as decelerate. Their lift coefficient is negative during the time period $0 \leq t \leq 250$, but goes slowly

towards zero. This indicates that the droplets for that separation distance are tending towards weaker repulsion as the Reynolds number decreases.

The drag coefficient for $d_o = 2$ is higher than that for $d_o = 9$. In earlier time, the difference is greater but becomes gradually smaller as time goes on. The drag coefficient for $d_o = 9$ is almost identical to that for a single droplet.

Acknowledgement

This work has been supported by the Air Force Office of Scientific Research under grant No. 90-0064 with Dr. Julian Tishkoff acting as the technical monitor. The support of the San Diego Supercomputer Center under a blockgrant of the Office of Academic Computing at UCI and the support of the Pittsburgh Supercomputing Center are greatly appreciated.

References

1. Sirignano, W. A. 1983 Fuel droplet vaporization and spray combustion. *Prog. Energy and Comb. Sci.* 291-322.
2. Patnaik, G. 1986 A numerical solution of droplet vaporization with convection. Ph.D. Dissertation, Carnegie-Mellon University.
3. Tal(thau), R., Lee, D. N. & Sirignano, W. A. 1983 Hydrodynamics and heat transfer in sphere assemblages - cylindrical cell models. *Int. J. Heat Mass Transfer* 26, No. 9, 1265-1273.
4. Tal(thau), R., Lee, D. N. & Sirignano, W. A. 1984 Heat and momentum transfer around a pair of spheres in viscous flow. *Int. J. Heat Mass Transfer* 27, No. 11, 1253-1262.
5. Raju, M. S. & Sirignano, W. A. 1990 Interaction between two vaporizing droplets in an intermediate-Reynolds-number flow. *Phys. Fluids A*, 2(10), 1780-1796.
6. Chiang, C. H. & Sirignano, W. A. 1991a Numerical analysis of interacting, convecting, vaporizing fuel droplets with variable properties. submitted to *Int. J. Heat Mass Transfer*.
7. Chiang, C. H. & Sirignano, W. A. 1991b Axisymmetric calculations of three-droplet interactions. submitted to *Atomization and Sprays*.
8. Kim, I., Elghobashi S. & Sirignano, W. A. 1991 Three-dimensional flow over two spheres in parallel side-by-side motion. submitted to *J. Fluid Mech.* also see AIAA Preprint 91-0073.
9. Vinokur, M 1983 On one-dimensional stretching functions for finite-difference calculations. *J. Comput. Phys.* 50, 215-234.
10. Rivkind V. Y. & Ryskin, G. 1976 Flow structure in motion of a spherical drop in a fluid medium at intermediate Reynolds numbers. *Fluid Dyn.* 11, 5-12.
11. Tsuji, Y., Morikawa, Y. & Terashima, K. 1982 Fluid-dynamic interaction between two spheres. *Int. J. Multiphase Flow* 8, 71-82.

Gas		Liquid					
$N_1 \times N_2 \times N_3$	$N_{1l} \times N_{2l} \times N_{3l}$	C_{DP}	C_{DV}	C_D	C_D^*		
$20 \times 11 \times 32$	$10 \times 11 \times 32$	0.542	0.586	1.123			
$30 \times 15 \times 48$	$15 \times 15 \times 48$	0.520	0.573	1.092			
$40 \times 21 \times 64$	$20 \times 21 \times 64$	0.511	0.571	1.081	1.08		

Table 1. Drag coefficients as a function of grid density at $Re = 100$, where * denotes the data from the correlation of Rivkind & Ryskin (1976)

Gas		Liquid			
$N_1 \times N_2 \times N_3$	$N_{1l} \times N_{2l} \times N_{3l}$	θ_{1s}	θ_{2s}		
$20 \times 11 \times 32$	$10 \times 11 \times 32$	126.81	146.50		
$30 \times 15 \times 48$	$15 \times 15 \times 48$	127.70	150.13		
$40 \times 21 \times 64$	$20 \times 21 \times 64$	127.74	151.20		

Table 2. Angles at which the surface vorticity changes its sign and the surface velocity is zero as a function of grid density at $Re = 100$, where the angles are measured from the front stagnation point.

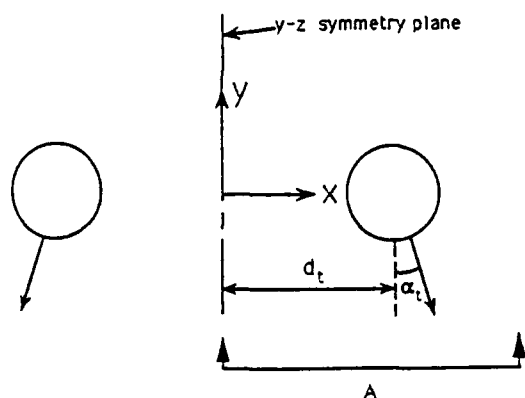


Figure 1. Flow geometry and coordinates.

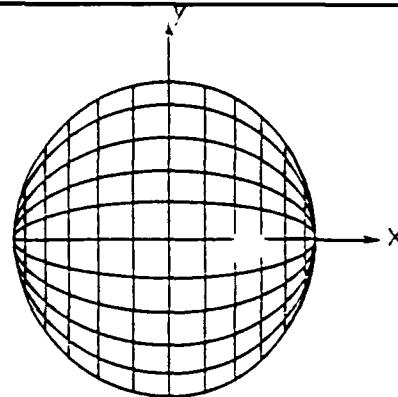


Figure 2. Two different grid distributions on the droplet surface.

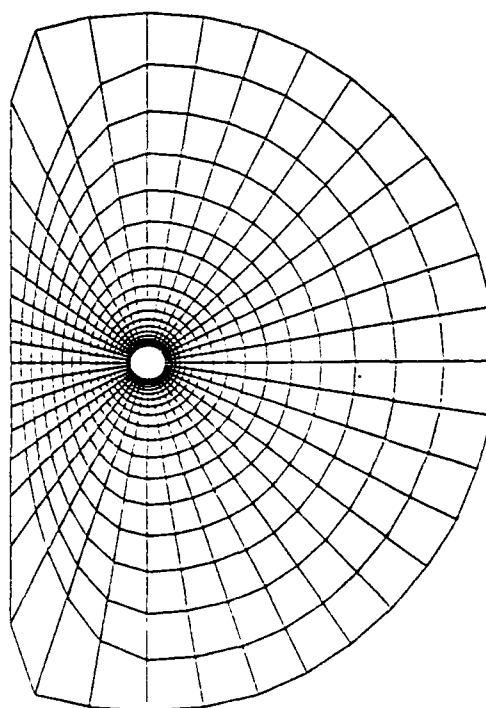


Figure 3. Grid distribution at dimensionless distance 9.

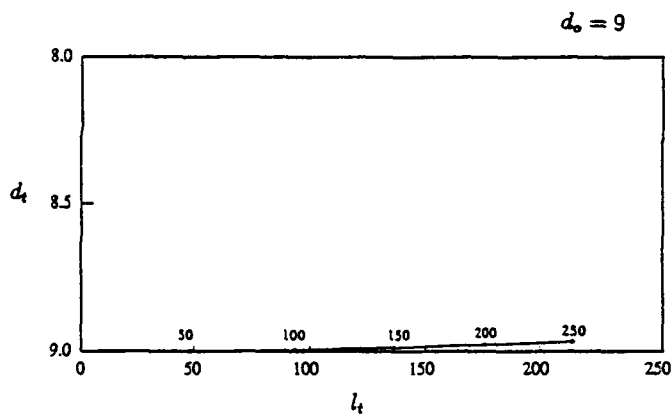
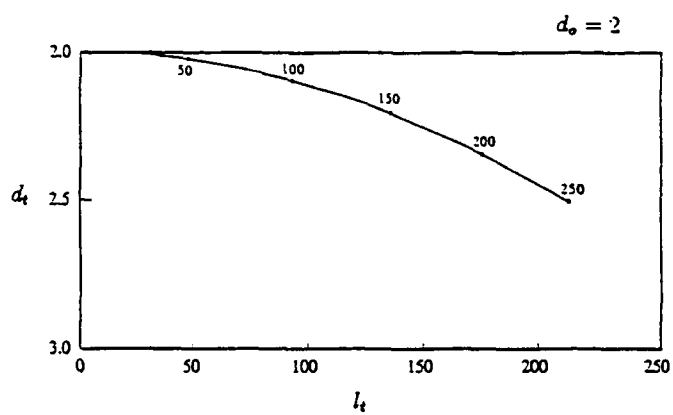


Figure 4. Trajectory of one droplet for (a) $d_o = 2$ and (b) $d_o = 9$.

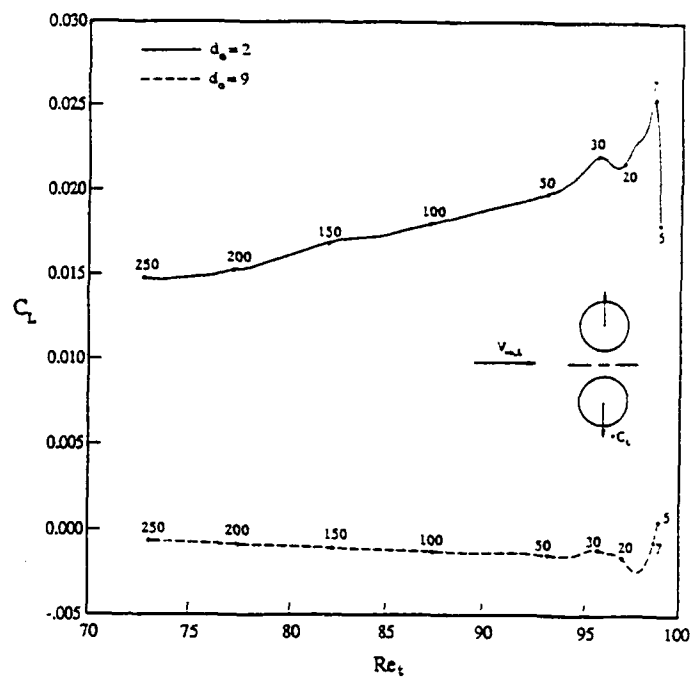


Figure 5. Lift coefficients as a function of instantaneous Reynolds number for $d_o = 2$ and 9 , where the numbers on the curves denote the dimensionless time.

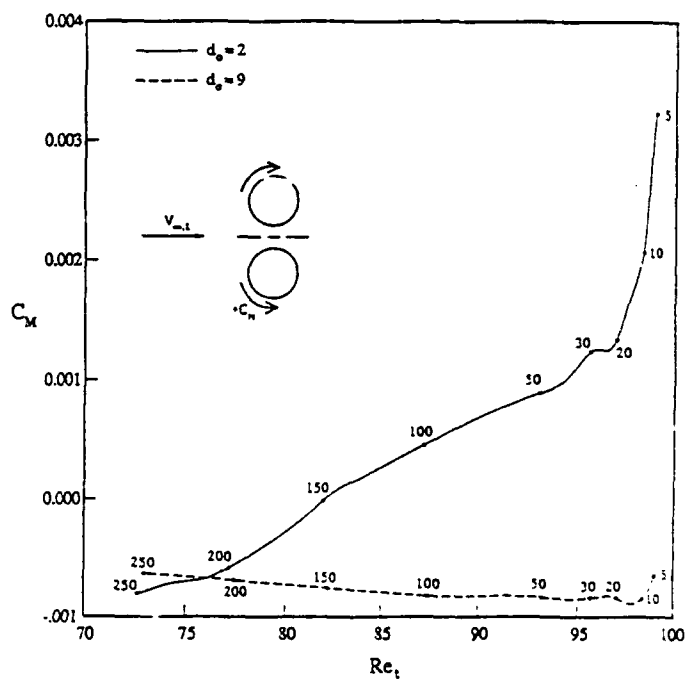


Figure 6. Moment coefficients as a function of instantaneous Reynolds number for $d_o = 2$ and 9 , where the numbers on the curves denote the dimensionless time.

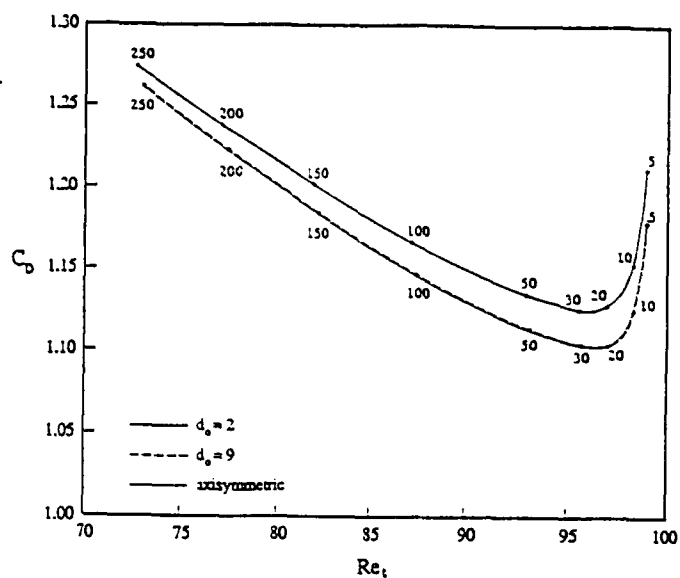


Figure 7. Drag coefficients as a function of instantaneous Reynolds number for $d_p = 2$ and 9, where the numbers on the curves denote the dimensionless time.

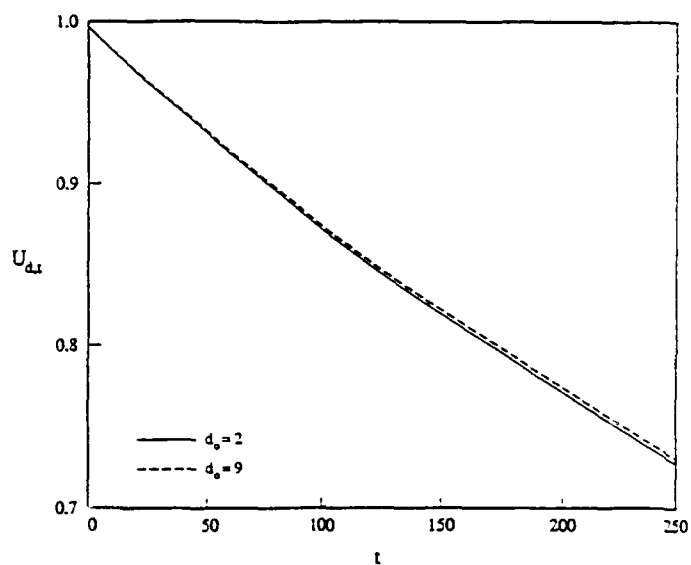


Figure 8. Speeds of the droplet as a function of dimensionless time for $d_p = 2$ and 9.

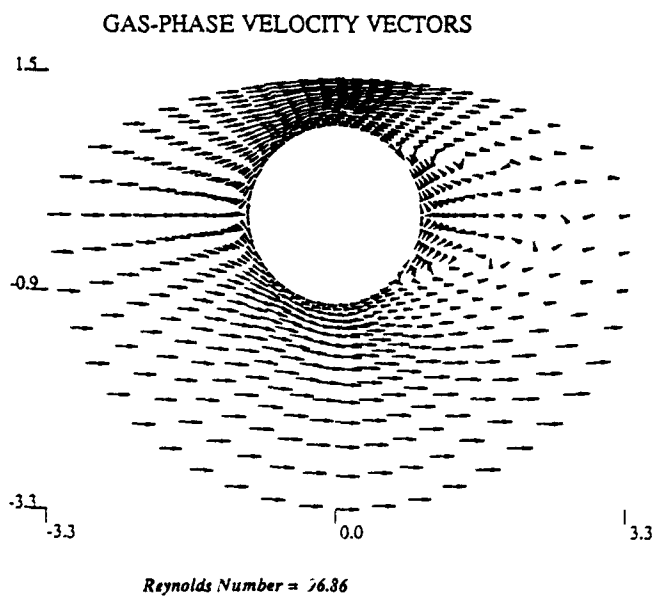


Figure 9(a) Velocity vector field of the gas phase in x-y plane at $Re_t = 96.36$, $d_t = 2.002$, and $t = 19.9$

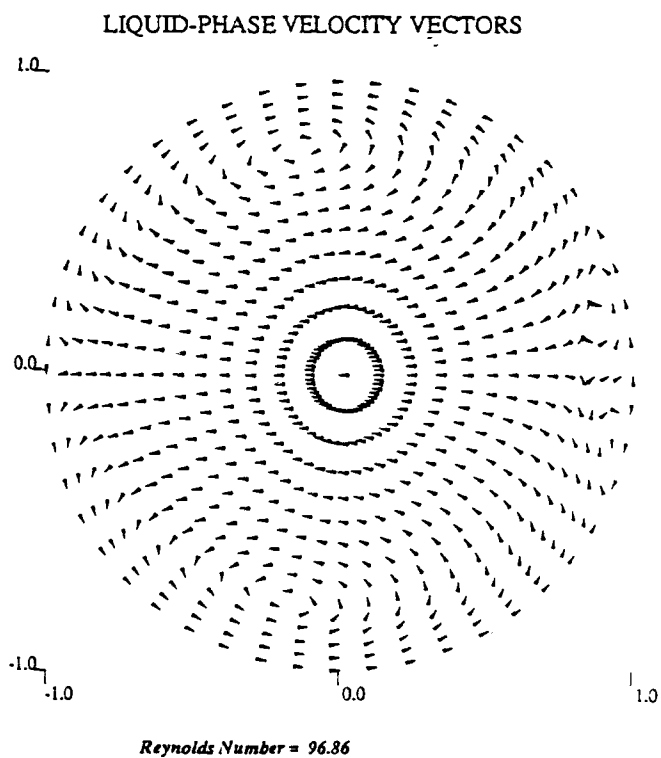


Figure 9(b) Velocity vector field of the liquid phase in x-y plane at $Re_t = 96.36$, $d_t = 2.002$, and $t = 19.9$

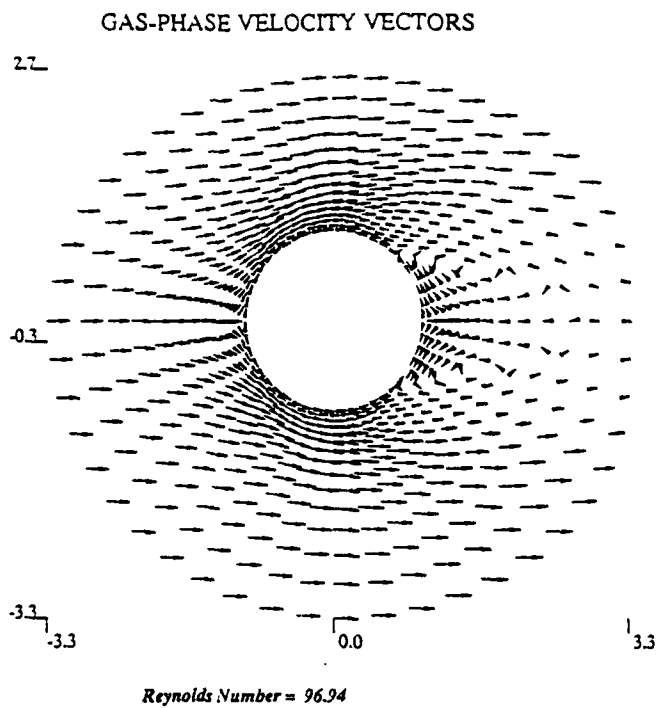


Figure 10(a) Velocity vector field of the gas phase in x-y plane
 $Re_t = 96.94$, $d_t = 9$, and $t = 19.9$

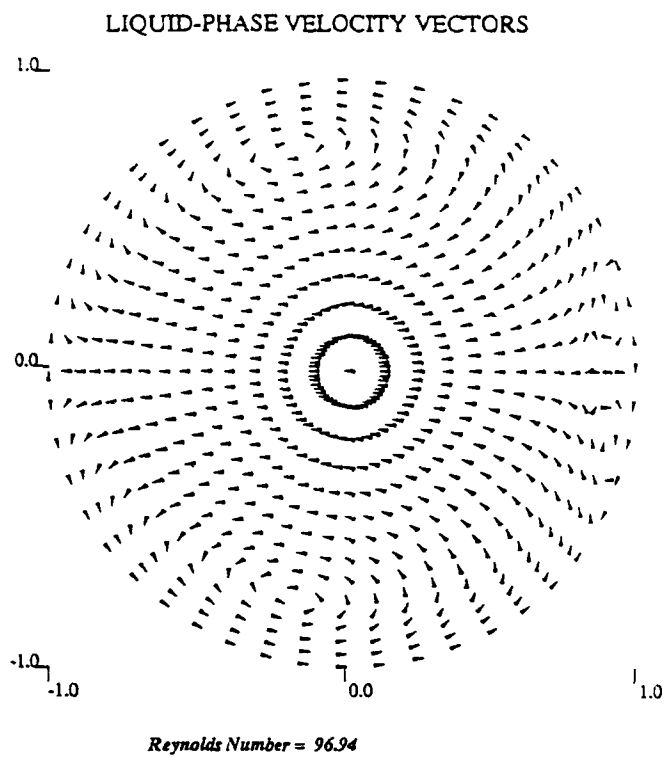


Figure 10(b) Velocity vector field of the liquid phase in x-y plane
 $Re_t = 96.94$, $d_t = 9$, and $t = 19.9$

Axisymmetric Calculations of Three-Droplet Interactions

C. H. Chiang*

W. A. Sirignano†

Department of Mechanical and Aerospace Engineering
University of California, Irvine, California

June 30, 1992

Abstract

The present study extends the previous droplet models [1, 2] to investigate numerically the system of three droplets which are moving in tandem with respect to the free flow. The purposes of this study are to study the wake effect of the lead droplet on the downstream droplets and to examine the effects of initial spacing on the total system. The effects of variable thermophysical properties, transient heating and internal circulation of liquid, deceleration of the flow due to the drag of the droplet, boundary-layer blowing, and moving interface due to surface regression as well as relative droplet motion are included. The results are compared with those of an isolated droplet [1] as well as those of the two-droplet system [2] to investigate the effect of the presence of the third droplet. The interaction effects from the downstream or upstream droplet are identified. The transport rates of droplets are reduced from the values for an isolated droplet, and values for

*research associate

†professor

the downstream droplets are profoundly less than those for the lead droplet. The difference in transport rates is large between the first two droplets; however, it becomes insignificant between the second and the third droplets. The modifications to the transfer correlations for an isolated droplet needed to account for the interaction effects are determined.

Nomenclature

B_H	$C'_{p,g,fil}(T'_\infty - T'_s)(1 - \frac{Q'_i}{Q'_g})/L'_s$, effective heat transfer number
$C_{p,g}$	$C'_{p,g}/C'_{p,g,\infty}$, specific heat of gas phase
$D12$	$D12'/R'_{1,0}$, non-dimensional droplet spacing between the first and the second droplets
$D23$	$D23'/R'_{1,0}$, non-dimensional droplet spacing between the second and the third droplets
L	$L'/(T'_\infty C'_{p1,0})$, latent heat of vaporization
Nu	$\frac{R_i \int_0^\pi \kappa_g \frac{\partial T_g}{\partial n} \sin\theta d\theta}{1 - T_s}$, Nusselt number
R	$R'/R'_{1,0}$, non-dimensional instantaneous droplet radius
Q'	heat flux
Re_g	$a'_0 U'_{\infty,0} \rho'_{g,\infty} / \mu'_{\infty}$, gas-phase Reynolds number
Sh	$\frac{R_i \int_0^\pi \rho_g D_g \frac{\partial Y_i}{\partial n} \sin\theta d\theta}{Y_{i,\infty} - Y_{i,s}}$, Sherwood number
s.p.	separation point at droplet surface (degree)
T	T'/T'_∞ , temperature
t'	time
U_∞	$U'_\infty/U'_{\infty,0}$, instantaneous free-stream velocity
Y_i	mass fraction

Greek

κ_g	$\kappa'_g/\kappa'_{g,\infty}$, conductivity of gas phase
μ_g	$\mu'_g/\mu'_{g,\infty}$, viscosity of gas phase
ρ'_g	density of gas phase
τ_{Hg}	$t' \mu'_\infty / (R'_{1,0}{}^2 \rho'_{g,\infty})$, gas hydrodynamic diffusion time

Superscript

' dimensional quantity

Subscripts

f	fuel
$film$	film conditions, average of ambient and surface conditions
g	gas phase
l	liquid phase
i	numerical index for droplets, 1=lead droplet, 2=second droplet, 3=third droplet
iso	isolated status
s	average surface condition
0	initial condition
∞	free stream condition

1 Introduction

In realistic spray situations, the fuel is usually introduced into the combustor as a stream of liquid that breaks into droplets. The droplets subsequently vaporize in the convective gas stream to form the air-fuel mixture. Typically, the fuel is of sufficiently low volatility that vaporization is an important controlling factor in the estimation of combustion rates. Usually, in the dense-spray regions such as regions near the fuel nozzle, the droplet spacing is so small that the interaction effects would modify the droplet behavior significantly. In order to obtain the qualitative modification of the transfer coefficients in the practical dense spray calculation, it is then necessary to consider the interactions among a stream of multiple moving droplets. However, a detailed and accurate simulation of hundreds of droplets will be very time consuming and very difficult to perform. In fact, the behavior of trailing droplets, which follow the first two or three droplets, can be estimated from that of the first two or three droplets on account of the periodical nature of linear droplet arrangements. This research addresses the interaction of three vaporizing droplets moving collinearly which represents a model of an injected stream of fuel droplets.

There is a lack of a detailed investigation of multiple-droplet-interactions involving variable properties, transient heating and internal circulation of droplets in the literature. Even the simplified numerical computations of three-droplet dynamics are rarely found. Tal et al. [4] used a multisphere cylindrical cell model to study hydrodynamics and heat transfer in assemblages of spheres. They found the hydrodynamic solution and Nusselt number, defined by using average bulk temperature of the cell unit inlet, to be periodic. Tong and Chen [5] have included vaporization in Tal's model to investigate the effects of droplet spacing on heat and mass transfer of droplets in a liquid droplet array. A three-droplet array in a cylindrical duct has been used to obtain correlations between Nusselt number and local ambient properties for each droplet. The cylindrical cell model is somewhat idealized and some assumptions must be imposed on the cell boundaries. Hence, their results must be verified by calculations from an advanced model. Kleinstreuer et al. [6] used a finite-element microscale analysis to find the drag coefficients of interacting spheres in a linear array and a boundary-layer analysis for vaporizing droplets to simulate coupled transfer processes for three interacting droplets in a one-dimensional trajectory. Their solution is basically the combination of three single-droplet-solutions with an "effective approach stream temperature" to account for interactions. The heat and momentum transfer of spheres in a linear array was studied by Tsai and Sterling [7] where a finite difference method combined with a body fitted grid was employed. The transient effect and mass transfer was excluded in this numerical calculation. The results of Nusselt number and drag coefficients of droplets are qualitatively in agreement with the findings of Tong and Chen [5] and Tal et al. [4].

In the present study, the momentum, heat and mass transfer of three interacting, vaporizing droplets are taken into account and the relative motion due to different drag forces that the droplets have experienced is included. We aim to understand the wake effects on the transport rates of the downstream droplets. The primary emphasis will be placed upon the interaction effects due to different initial spacings.

The schematic flow configuration is presented in Figure 1 where the flow passing over three vaporizing droplets moving in tandem is shown. The flow is laminar and axisymmetric with initially uniform ambient conditions specified by U'_{∞} , T'_{∞} , $\rho'_{g,\infty}$, p'_{∞} , and $Y_{f,\infty} = 0$. The initial droplet spacing is also prescribed. Di_j is the non-dimensional droplet spacing (with respect

to the initial radius of the first droplet) between the i^{th} droplet and the j^{th} droplet. The frame of reference is fixed to the center of the lead droplet and an account will be made for this noninertial frame by the use of a reversed pseudo force. The problem can be viewed as an impulsively-started flow over a fixed droplet and two moving downstream droplets aligned in tandem.

The full consideration of forced convection of the gas phase, transient deceleration of the flowfield due to the drag force, internal circulation and transient heating of the liquid phase, variable properties, and transport processes occurring at the vaporizing droplet interface required to solve the Navier-Stokes equations, energy equation and species equation, combined with appropriate boundary conditions simultaneously. Also, in order to consider the moving boundaries due to surface regression and relative droplet motion, a general method of generating boundary-fitted coordinate systems is required.

The axisymmetric governing-equations in cylindrical coordinates and their corresponding finite-difference equations, and numerical procedures are given in Chiang [3]. The computer codes employed in our previous research [1, 2] have been modified to deal with the present three-droplet arrangement. The modification involves the grid generation routine as well as the routines which handle the relative motion and spacings between droplets. The calling sequence and parameter transfer among subroutines have been adapted to accommodate new variables and the increase in memory size.

2 Results and Discussion

Six production runs simulating three equi-sized droplets, with the same initial droplet Reynolds number but with different initial droplet spacings, moving collinearly have been performed. The values of physical parameters employed in each case are the same as the base case of the two-interacting-droplet study [2]. The values of initial spacings in each case are given in Table 1.

The computations are performed on a CRAY Y-MP supercomputer. Figure 1 also shows the typical grid distributions at the beginning and at the final computational time for the case of droplet coalescence. It is noted that the computation is stopped when the droplet spacing is reduced below 2.6 or whenever the downstream droplet approaches the outer computational boundary, since the grid generation routine may generate an overskewed grid

system under these conditions. Often the computation terminated at a very early stage of the droplet lifetime during which most of heat flux to the droplet surface would be transferred to the interior of the droplet. Hence, the effective transfer number ($B_H = C_{p,g,fil} (T'_\infty - T'_s) (1 - \frac{Q'_s}{Q'_g}) / L'_s$) is quite small. The amount of mass evaporated is insignificant, as a result the evaporation rates of droplets are not reported here. The time scale used in the following discussion is the gas-phase hydrodynamic diffusion time scale.

The representative results to characterize the droplet behavior are summarized below.

The global contours of results from Case 1 (with $D_{12}=D_{23}=12$) and Case 4 ($D_{12}=D_{23}=6$) are compared in order to study the effect of initial spacing on the flow field. The vorticity distributions and isotherms for the gas and liquid phases are presented in the top and bottom portions of each plot of Figure 2, respectively. The results of Case 1 at two different times are portrayed in the upper two plots. At the early time, droplets experience the convective effect such that high vorticity gradients occur at the front portion of the droplet, and an asymmetric distribution is developed. The flow field surrounding each droplet resembles that surrounding an isolated droplet [1]. At five gas-phase diffusion times, the D_{12} is reduced from 12 to 2.96. The vorticity convected downstream from the first droplet has directly touched the second droplet and shifted its vortex center to the equatorial plane since less convection has acted on the downstream droplet. The second droplet is well protected by the vorticity wake of the lead droplet, while the third droplet, spaced 9.5 droplet radii away from the second droplet, behaves qualitatively as an isolated droplet.

For the case of small initial droplet spacing (Case 4), the interaction effects are expected to be strong. The velocities approaching the second and the third droplets are more or less similar but are considerably smaller than that approaching the lead droplet. As a result, the convective effect on transport is subdued. In both cases, the vorticity distribution for the lead droplet is distorted by the approaching of the second droplet.

The isotherms demonstrate thermal-transport interactions among three droplets and the gas phase. For the case with sufficient large droplet spacing, the three droplets show the same isolated-droplet-isothermal-pattern at the early time as indicated in the uppermost plot. The third trailing droplet always exhibits the same temperature contour as that of an isolated droplet,

even though the approaching temperature and velocity have decreased from the values upstream of the lead droplet. The case with small initial spacing shows quite different thermal transport mechanisms. The temperature gradients for the downstream droplets are smaller than those for the lead droplet due to the action of the thermal wake. The thermal boundary layer thickness increases in the downstream direction along the surface for the lead droplet. This behavior is opposite for the third trailing droplet in the close spacing case.

The transport properties of trailing droplets are substantially affected by the fuel vapor convected downstream. The composition of the mixture and hence the density of gas-phase surrounding each droplet will be different for each droplet depending on the droplet spacing. The mass-fraction contour of Case 1 at two different times are presented in Figure 3. An envelope of vapor wake created by the leading droplet and covering the downstream droplet is identified even though the droplet spacings are large. This envelope serves to reduce the exchanges of momentum, mass and energy between the ambience and the trailing droplets. As time progresses, the droplet spacing from the leading droplet is reduced, the change in spatial vapor distribution of downstream droplet is more profound.

The variations of Nusselt number along the gas/liquid interface of the droplets for Case 1 and Case 4 are shown in Figure 4. In Case 1, the decrease of Nusselt number at the front stagnation portions of the trailing droplets are caused by the cold fuel/air mixture convected downstream from the upstream droplets. The qualitative variations of Nusselt numbers of the second droplet and the third droplet in Case 4 are totally different from those in Case 1. The details have been discussed in Chiang[3]. The third droplet shows the same Nusselt number distribution as for the second droplet except at the separation region, where the third droplet possesses a higher value of Nusselt number due to the angular diffusion of heat flux from the free stream. Similar behavior for Sherwood numbers are observed for the three droplets.

The surface shear stress distributions are shown in Figure 5. The cascade effect of upstream wake decreases the surface stress of downstream droplets. It is well known that the momentum is dissipated along the downstream direction due to the wake action. Usually the recirculating wake from the lead droplet has dissipated a significant portion of the momentum upstream of the second droplet. As a result, the further reduction in shear stress from the second to the third droplet becomes very limited. Hence, the stress

difference between the first two droplets is much larger than that between two downstream droplets for Case 1. Note that in Case 4, the shear stress for the third droplet is higher than that for the second droplet since the second droplet interacts with both neighboring droplets. The negative shear stresses are primarily caused by the contacting wakes of close neighboring droplets.

Figures 6 and 7 present the time variations of drag coefficients and Nusselt numbers, respectively. As we expect, the transport rates of droplets are reduced from the values for an isolated droplet, and values for the downstream droplets are profoundly less than those for the lead droplet. The transport rates for the third droplet are lower than those for the second droplet, except when the lead droplet's interaction with the second droplet becomes very strong. The results of Case 4 show that the second and third droplets exhibit almost identical behaviors. The interaction between the downstream droplet and the lead droplet becomes very significant for the small initial spacing case.

The variations of trajectory with time and drag coefficients vs. instantaneous Reynolds number for the cases of different initial spacings are illustrated in Figure 8 (Cases 1, 2, and 3) and Figure 9 (Cases 4, 5, and 6), respectively. Results of Case 1 with large initial spacing ($D_{12}=D_{23}=12$) indicate that the drag coefficient is smaller for the second droplet than for the lead droplet and still smaller for the third droplet. The major decrease in drag occurs in the first two droplets. In Case 2, the drag coefficients of the lead and the second droplets are significantly reduced (comparing curves 7 and 10, and 8 and 11, respectively) due to the strong interactions when the first two droplets are spaced only two diameters away. Similar trends occur for the downstream droplet pairs of Case 3 (comparing curves 8 and 14, and 9 and 15, respectively). The third droplet in Case 2 has a higher drag coefficient than that of the second droplet since the second droplet is better shielded by the droplet before it. The D_{23} thus increases with time. Also, note that the drag coefficient of the third droplet, which is spaced far away from the second droplet, seems to be independent of D_{12} as indicated in curves 9 and 12. However, it strongly depends upon D_{23} as illustrated in curves 9, 12 and 15.

The comparison between results of Figures 8 and 9 leads to the clear conclusion that as initial spacings decrease, the transport rates decrease correspondingly. The drag coefficients for the downstream droplets are all collapsed together. However, at the final calculations when three droplets

interact extensively with neighbors, the second droplet experiences not only downstream interactions from the lead droplet but also upstream interactions from the third droplet. As a result, the second droplet possesses the lowest drag coefficient. Note the interaction from the upstream droplet is considerably larger than that from the downstream droplet. The lead droplet in Case 2 has the lowest drag coefficient (curve 10) among the lead droplets of three cases since the interaction from the second droplet is the strongest (spacing D_{12} is the smallest). The behavior of the spacing variation is qualitatively similar to that of large initial spacing case. The variation of D_{23} , for the cases of approaching droplets, is always negligible except during the final calculation period.

In order to investigate the effect of D_{23} on the first and the second droplets with a given D_{12} , the comparisons of drag coefficients for the first two droplets with variable D_{23} s are presented in Figures 10 and 11. The comparisons of results with the same D_{12} in the two-droplet-only arrangement are also presented. For the cases of small initial- D_{12} , the main droplet interactions occur between the first two droplets. The presence of the third droplet does not significantly affect the lead droplet; it reduces the Sherwood and Nusselt numbers of the lead droplet by less than 5 % in magnitude. The drag coefficients and Nusselt numbers for the second droplet decrease as the D_{23} decreases, though the percent change is small. For the cases of large initial D_{12} , the behavior of the first droplet becomes insensitive to the presence of the third droplet. An interesting observation is that the presence of the third droplet at a sufficient distance from the second droplet, with insignificant hydrodynamic interaction between the second and the third droplet, may increase the drag coefficient of the second droplet (comparing curves 4 and 5 in Figures 11). The second droplet in the two-droplet-only arrangement receives the interaction of recirculating-thermal-entrainment from the free stream; as a result, the transfer number is high. Therefore, the surface blowing is enhanced and the friction drag is reduced. The addition of the third droplet to the system moves this thermal effect to the third droplet; hence, the transport rates of the second droplet are recovered. However, for the case of a small D_{23} , the strong interaction from the third droplet reduces the transport rates of the second droplet by a large magnitude (curve 6).

A nonlinear regression model using least squares has been employed to find the correlations between the transport rates of an interacting droplet and the corresponding transport rates when droplet is isolated. The generalized

form of numerical correlations for drag coefficient and Nusselt number and Sherwood number of each droplet can be expressed as

For the lead droplet:

$$\frac{C_{D1}}{C_{D_{iso}}} = 0.759 D_{12}^{0.1} D_{23}^{0.01}$$

$$\frac{Nu_{film1}}{Nu_{film_{iso}}} = 0.752 D_{12}^{0.038} D_{23}^{0.017}$$

$$\frac{Sh_{film1}}{Sh_{film_{iso}}} = 0.231 D_{12}^{-0.285} D_{23}^{-0.203}$$

For the second droplet:

$$\frac{C_{D2}}{C_{D_{iso}}} = 0.211 D_{12}^{0.356} D_{23}^{0.171}$$

$$\frac{Nu_{film2}}{Nu_{film_{iso}}} = 0.296 D_{12}^{0.180} D_{23}^{0.195}$$

$$\frac{Sh_{film2}}{Sh_{film_{iso}}} = 4.836 D_{12}^{-0.499} D_{23}^{-0.397}$$

For the third droplet:

$$\frac{C_{D3}}{C_{D_{iso}}} = 0.434 D_{12}^{-0.103} D_{23}^{0.288}$$

$$\frac{Nu_{film3}}{Nu_{film_{iso}}} = 0.343 D_{12}^{0.102} D_{23}^{0.150}$$

$$\frac{Sh_{film3}}{Sh_{film_{iso}}} = 10.476 D_{12}^{-0.655} D_{23}^{-0.330}$$

The correlations are valid for droplet spacing ranged from 2.7 to 12 and for Reynolds number ranged from 90 to 130. Some correction factors, with different combinations of D_{12} s and D_{23} s, computed from above correlations are presented in Table 2. The correlations basically predict the right trends of interacting effects on droplet transport rates. The influence of D_{12} on the third droplet is insignificant as indicated by the small exponents of D_{12} .

3 Conclusions

The detailed behaviors of three vaporizing, interacting droplets for the cases of different initial spacings have been investigated carefully. The results indicate that the interacting effects are strongly dependent upon the initial droplet spacings. The general qualitative conclusions drawn from the two-droplet study [2] can be applied to two neighboring droplets in the three-droplet analysis.

Results for the cases of sufficiently large spacing (above approximately 6 droplet diameters) show that the flow field of each droplet is qualitatively similar to that of an isolated droplet, although the transport rates are reduced along the downstream direction due to the cascade effect of the wake. The major drops in transport rates occur in the first two droplets. For the cases of small droplet spacings (less than approximately 3 droplet diameters), the flow field of downstream droplets can be significantly altered due to the interaction effects from the upstream droplets. Usually, the second droplet has the lowest drag coefficient since it receives interactions from both neighboring droplets. However, the difference in transport rates between the second and the third droplets is not significant since both droplets are fully protected by the wake of the first droplet. The effect of D_{23} on the behavior of the first droplet is insignificant. However, depending upon the values of D_{12} as well as D_{23} , the effect of D_{23} on the behavior of the second droplet may become significant. The correlations for heat transfer and droplet dynamics have been developed and can be applied in a droplet spray calculation.

Acknowledgements

This work has been supported by the Air Force Office of Scientific Research under grant No. 90-0064 with Dr. Julian Tishkoff acting as the technical monitor. The support of the San Diego Supercomputing Center under a Block Grant of the Office of Academic Computing at UCI is greatly appreciated.

References

- [1] C. H. Chiang, M. S. Raju, and W. A. Sirignano, Numerical Analysis of Convecting, Vaporizing Fuel Droplet with Variable Properties, *Int. J. Heat Mass Transfer*, Vol 35, No. 5, pp. 1307-1324, 1992
- [2] C. H. Chiang and W. A. Sirignano, Numerical Analysis of Interacting, Convecting, Vaporizing Fuel Droplet with Variable Properties, *AIAA Aerospace Sciences Meeting*, Paper 90-0357, 1990. Also to appear in *Int. J. Heat Mass Transfer* 1992.
- [3] C. H. Chiang, Isolated And Interacting, Vaporizing Fuel Droplets: Field Calculation With Variable Properties, Ph.D. Dissertation, University of California, Irvine, Dept. of Mechanical Engineering, 1990.
- [4] R. Tal (Thau), D. N. Lee, and W. A. Sirignano, Hydrodynamics and Heat Transfer in Sphere of Particle Assemblages - Cylindrical Cell Models, *Int. J. Heat Mass Transfer*, Vol 26 , , No. 9, pp. 1265-1273, 1983.
- [5] A. Y. Tong and S. J. Chen, Heat Transfer Correlations for Vaporizing Liquid Droplet Arrays in A High-Temperature Gas at Intermediate Reynolds Number, *Int. J. Heat & Fluid Flow*, Vol 9, No. 2, pp. 118-130, 1988.
- [6] C. Kleinstreuer, H. Chiang, and Y.-Y. Wang, Mathematical Modelling of Interacting Vaporizing Fuel Droplets, HTD-Vol. 106, *Heat Transfer Phenomena in Radiation, Combustion and Fire*, pp. 469-477 (1989)
- [7] J. S. Tsai and Arthur M. Sterling, The Application of an Embedded Grid to the Solution of Heat and Momentum Transfer for Spheres in a Linear Array, *Int. J. Heat Mass Transfer*, Vol 33, No. 11. pp. 2491-2502, 1990.

Table 1: Initial Droplet Spacings Considered In Each Case of the Three-Droplet Study

Case	D12	D23
1.	12	12
2.	4	12
3.	12	4
4.	6	6
5.	4	6
6.	6	4

Table 2: Correction Factors for Cd, Nu and Sh with Different Combinations of D12 and D23

D12	D23	$\frac{C_{D1}}{C_{D100}}$	$\frac{C_{D2}}{C_{D100}}$	$\frac{C_{D3}}{C_{D100}}$	$\frac{Nu_1}{Nu_{100}}$	$\frac{Nu_2}{Nu_{100}}$	$\frac{Nu_3}{Nu_{100}}$	$\frac{Sh_1}{Sh_{100}}$	$\frac{Sh_2}{Sh_{100}}$	$\frac{Sh_3}{Sh_{100}}$
12.00	12.00	1.004	0.781	0.640	0.874	0.752	0.687	0.956	0.522	0.574
12.00	6.00	1.001	0.694	0.540	0.870	0.657	0.601	0.941	0.688	0.872
12.00	4.00	1.000	0.647	0.486	0.868	0.607	0.559	0.935	0.808	1.077
6.00	12.00	0.935	0.611	0.659	0.847	0.663	0.667	0.947	0.738	0.693
6.00	6.00	0.931	0.542	0.563	0.841	0.579	0.577	0.927	0.972	1.137
6.00	4.00	0.929	0.506	0.510	0.838	0.535	0.533	0.918	1.142	1.465
4.00	12.00	0.897	0.529	0.667	0.832	0.616	0.659	0.945	0.903	0.749
4.00	6.00	0.892	0.470	0.574	0.825	0.539	0.566	0.922	1.189	1.282
4.00	4.00	0.890	0.438	0.522	0.822	0.498	0.521	0.911	1.397	1.696
2.70	12.00	0.861	0.460	0.673	0.819	0.574	0.653	0.944	1.099	0.792
2.70	6.00	0.857	0.408	0.582	0.811	0.502	0.558	0.918	1.447	1.404
2.70	4.00	0.855	0.381	0.532	0.808	0.464	0.512	0.906	1.700	1.905

Figure 1: Flow field configuration and grid distribution at two different times.

Figure 2: Vorticity and isotherm contour plot of gas and liquid phases with different initial droplet spacings.

Figure 3: Mass-fraction contour of case 1 at two different times.

Figure 4: Local Nusselt number distribution of the three droplets with different initial droplet spacings.

- _____ 1 Lead droplet, Case 1, $Re(t) = 85.6$, s.p. at 143.2, local min. at 149.9
- 2 Lead droplet, Case 4, $Re(t) = 86.5$, s.p. at 130.3, local min. at 141.4
- _____ 3 Second droplet, Case 1, $Re(t) = 88.7$, s.p. at 145.9, local min. at 150.7
- _____ 4 Second droplet, Case 4, $Re(t) = 91.3$, s.p. at 156.6, local min. at 0.0
- _____ 5 Third droplet, Case 1, $Re(t) = 89.5$, s.p. at 150.1, local min. at 158.8
- 6 Third droplet, Case 4, $Re(t) = 91.3$, s.p. at 167.1, local min. at 0.0

Figure 5: Surface shear stress distribution of the three droplets with different initial droplet spacings.

- _____ 1 Lead droplet, Case 1, $Re(t) = 85.6$, s.p. at 143.2, local min. at 121.7
- 2 Lead droplet, Case 4, $Re(t) = 86.5$, s.p. at 130.3, local min. at 114.6
- _____ 3 Second droplet, Case 1, $Re(t) = 88.7$, s.p. at 145.9, local min. at 125.3
- _____ 4 Second droplet, Case 4, $Re(t) = 91.3$, s.p. at 156.6, local min. at 149.8
- _____ 5 Third droplet, Case 1, $Re(t) = 89.5$, s.p. at 150.1, local min. at 129.4
- 6 Third droplet, Case 4, $Re(t) = 91.3$, s.p. at 167.1, local min. at 157.7

Figure 6: Time variation of drag coefficients of the three droplets with different initial droplet spacings.

- _____ 1. Lead Droplet, (Initial $D_{12}=12$, $D_{23}=12$)
- 2. Second Droplet, (Initial $D_{12}=12$, $D_{23}=12$)
- _____ 3. Third Droplet, (Initial $D_{12}=12$, $D_{23}=12$)
- _____ 4. Lead Droplet, (Initial $D_{12}=6$, $D_{23}=6$)
- _____ 5. Second Droplet, (Initial $D_{12}=6$, $D_{23}=6$)
- 6. Third Droplet, (Initial $D_{12}=6$, $D_{23}=6$)
- 7. Isolated Droplet

Figure 7: Time variation of Nusselt numbers of the three droplets with different initial droplet spacings.

- _____ 1. Lead Droplet, (Initial $D_{12}=12$, $D_{23}=12$)
- 2. Second Droplet, (Initial $D_{12}=12$, $D_{23}=12$)
- _____ 3. Third Droplet, (Initial $D_{12}=12$, $D_{23}=12$)
- _____ 4. Lead Droplet, (Initial $D_{12}=6$, $D_{23}=6$)
- _____ 5. Second Droplet, (Initial $D_{12}=6$, $D_{23}=6$)
- 6. Third Droplet, (Initial $D_{12}=6$, $D_{23}=6$)
- 7. Isolated Droplet

Figure 8: Time variation of droplet drag coefficients and droplet spacings for the cases of large initial droplet spacings (Cases 1, 2 and 3)

- 1. D_{12} , Case 1; 2. D_{23} , Case 1; 3. D_{12} , Case 2;
- 4. D_{23} , Case 2; 5. D_{12} , Case 3; 6. D_{23} , Case 3;
- 7. C_D for the Lead Droplet, Case 1; 8. C_D for the Second Droplet, Case 1;
- 9. C_D for the Third Droplet, Case 1; 10. C_D for the Lead Droplet, Case 2;
- 11. C_D for the Second Droplet, Case 2; 12. C_D for the Third Droplet, Case 2;
- 13. C_D for the Lead Droplet, Case 3; 14. C_D for the Second Droplet, Case 3;
- 15. C_D for the Third Droplet, Case 3; 16. C_D for an Isolated Droplet;

Figure 9: Time variation of droplet drag coefficients and droplet spacings for the cases of large initial droplet spacings (Cases 4, 5 and 6)

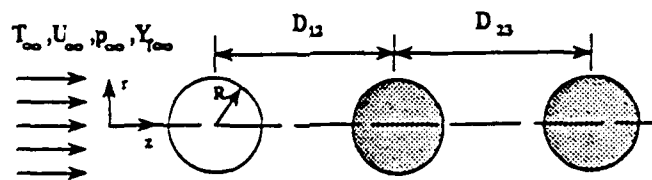
- 1. D_{12} , Case 4; 2. D_{23} , Case 4; 3. D_{12} , Case 5;
- 4. D_{23} , Case 5; 5. D_{12} , Case 6; 6. D_{23} , Case 6;
- 7. C_D for the Lead Droplet, Case 4; 8. C_D for the Second Droplet, Case 4;
- 9. C_D for the Third Droplet, Case 4; 10. C_D for the Lead Droplet, Case 5;
- 11. C_D for the Second Droplet, Case 5; 12. C_D for the Third Droplet, Case 5;
- 13. C_D for the Lead Droplet, Case 6; 14. C_D for the Second Droplet, Case 6;
- 15. C_D for the Third Droplet, Case 6; 16. C_D for an Isolated Droplet;

Figure 10: Time variation of drag coefficients of the first two droplets for $D_{12} = 4$ and variable D_{23} s

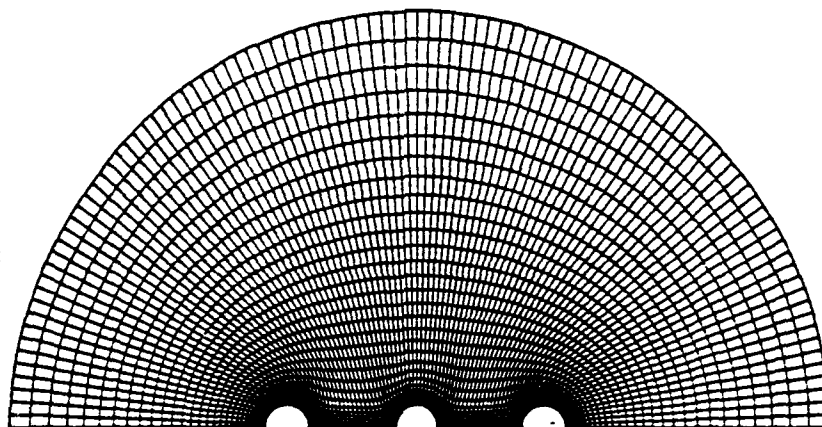
- _____ 1. The First Droplet of Two-Droplet Calculation, $D_{12}=4$
- 2. The First Droplet of Three-Droplet Calculation, $D_{12}=4$, $D_{23}=12$
- _____ 3. The First Droplet of Three-Droplet Calculation, $D_{12}=4$, $D_{23}=6$
- _____ 4. The Second Droplet of Two-Droplet Calculation, $D_{12}=4$
- _____ 5. The Second Droplet of Three-Droplet Calculation, $D_{12}=4$, $D_{23}=12$
- 6. The Second Droplet of Three-Droplet Calculation, $D_{12}=4$, $D_{23}=6$

Figure 11: Time variation of drag coefficients of the first two droplets for $D_{12} = 12$ and variable D_{23} s

- _____ 1. The First Droplet of Two-Droplet Calculation, $D_{12}=12$
- 2. The First Droplet of Three-Droplet Calculation, $D_{12}=12$, $D_{23}=12$
- _____ 3. The First Droplet of Three-Droplet Calculation, $D_{12}=12$, $D_{23}=4$
- _____ 4. The Second Droplet of Two-Droplet Calculation, $D_{12}=12$
- _____ 5. The Second Droplet of Three-Droplet Calculation, $D_{12}=12$, $D_{23}=12$
- 6. The Second Droplet of Three-Droplet Calculation, $D_{12}=12$, $D_{23}=4$



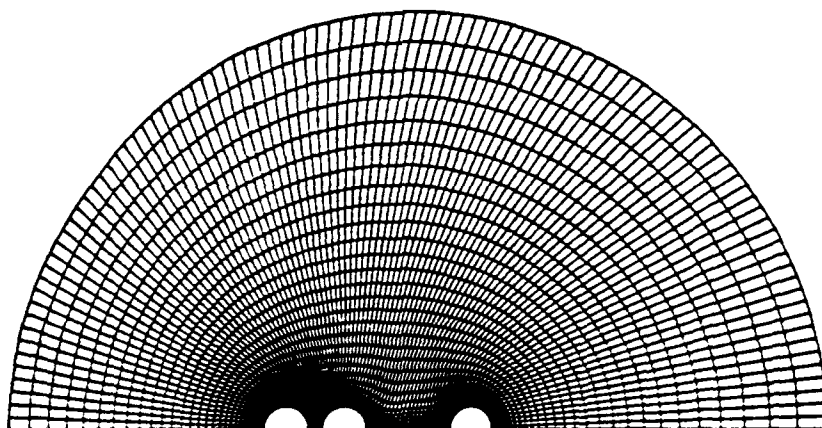
FLOW CONFIGURATION - SCHEMATIC



Time = 0.00

$R_1 = 1.000, R_2 = 1.000, R_3 = 1.000,$

$D_{12}=6.00, D_{23}=6.00, Re_1=Re_2=Re_3=100.00$

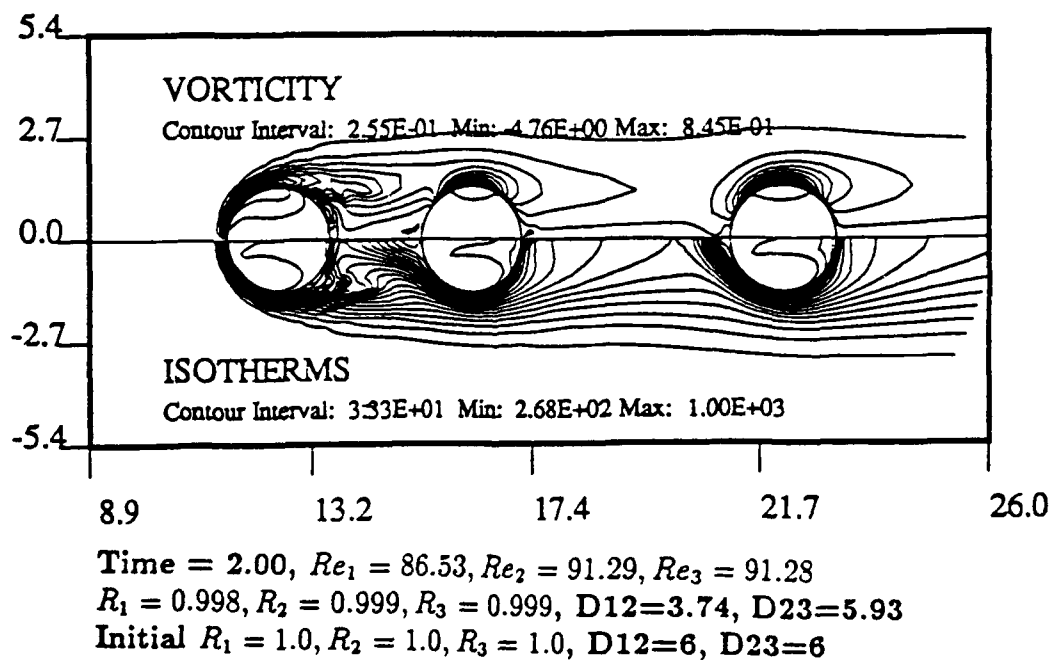
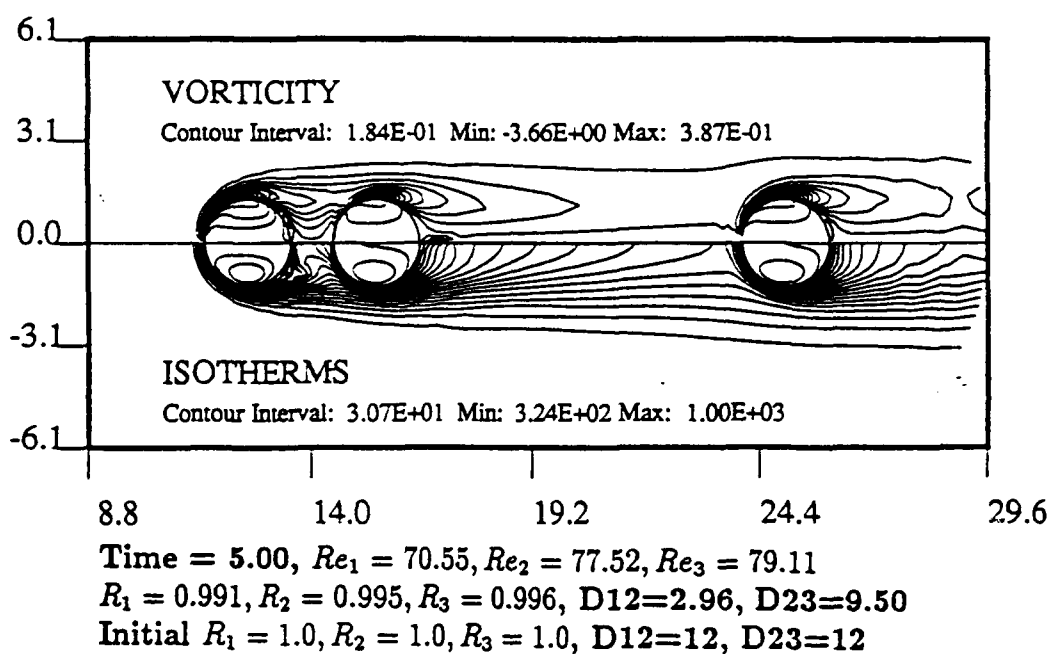
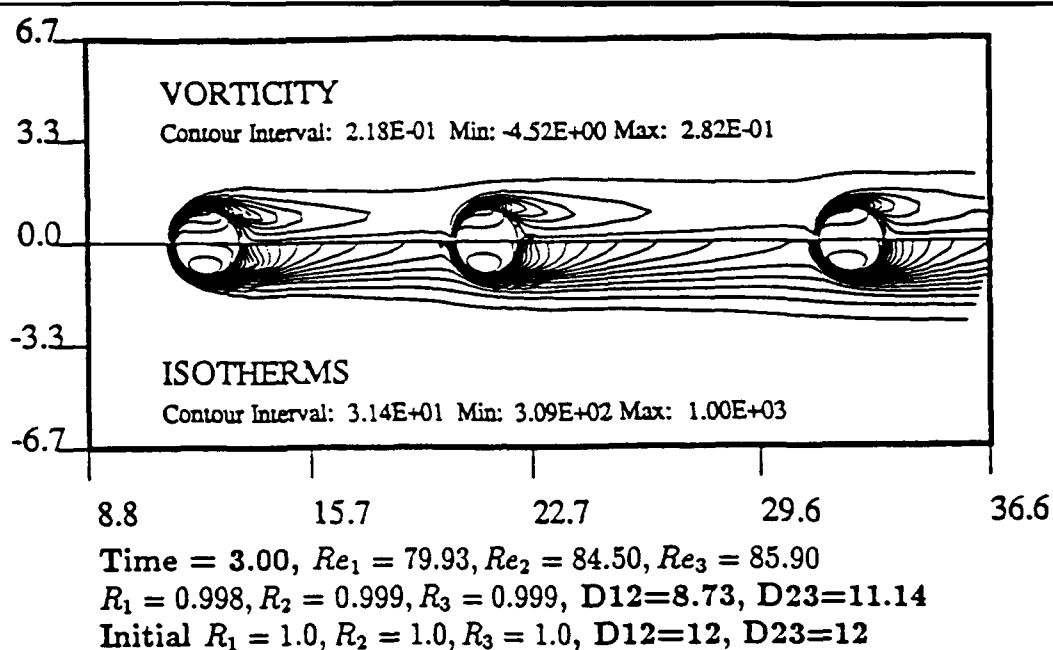


Time = 2.42

$R_1 = 0.998, R_2 = 0.999, R_3 = 0.999,$

$D_{12}=2.68, D_{23}=6.01, Re_1=84.33, Re_2=90.26, Re_3=89.67$

*Sharma &
Singh
1991*



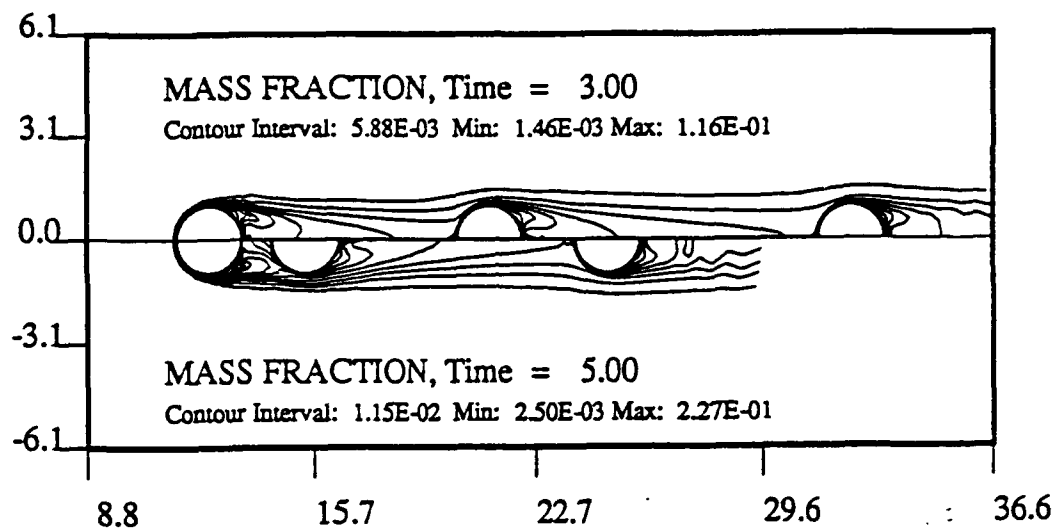


Fig 5

2007

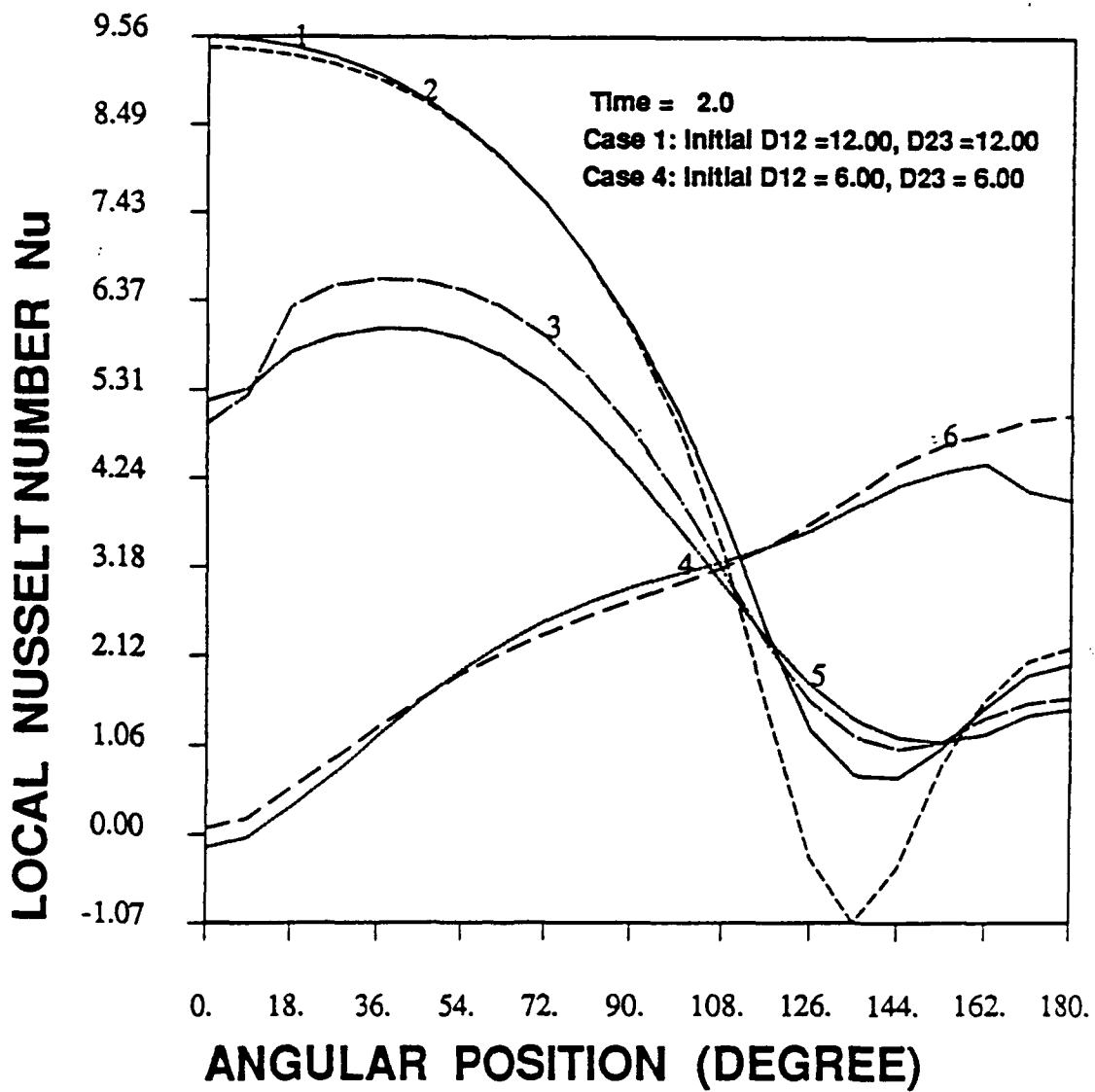
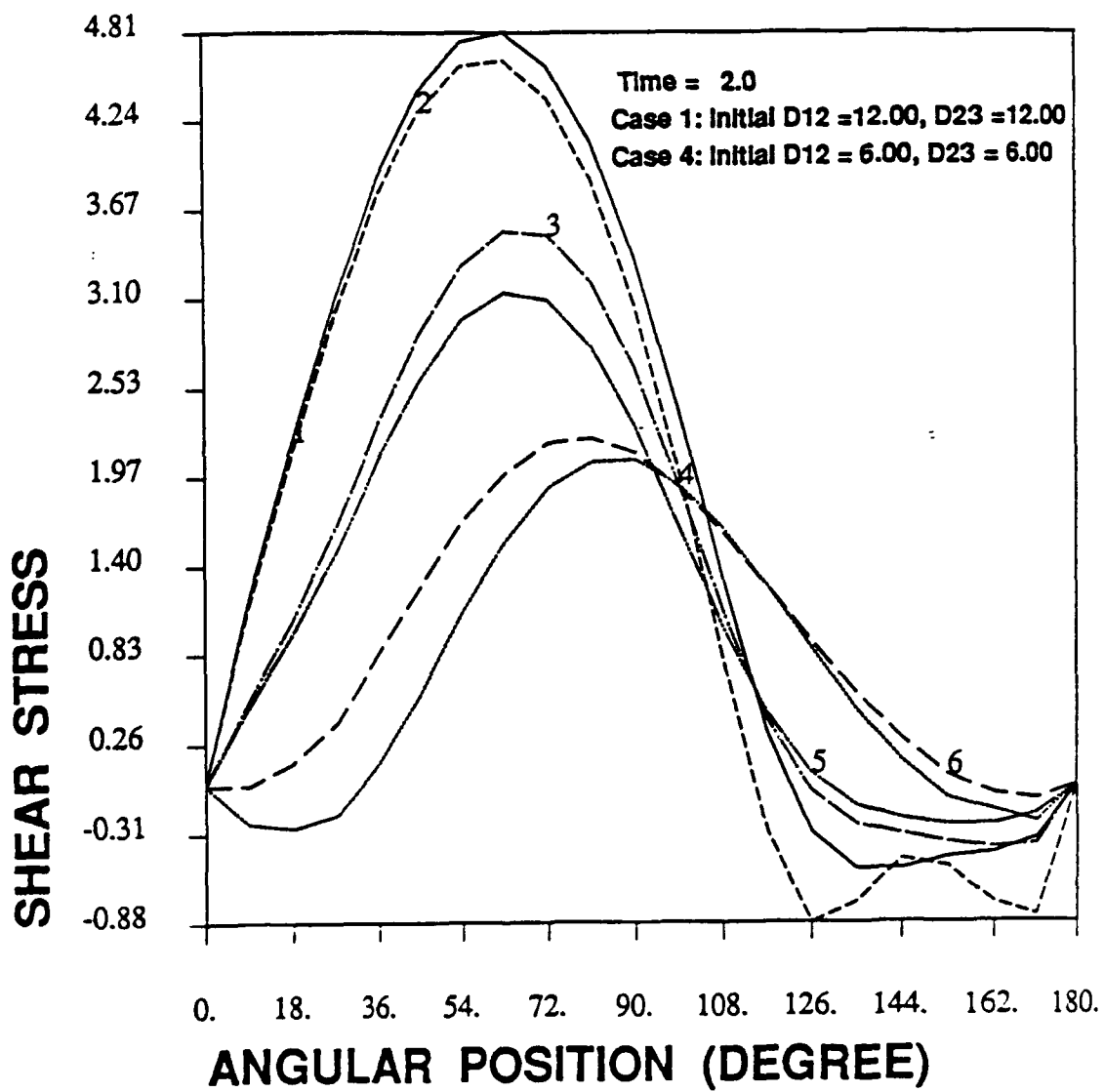


Fig 4
Change
Signature



$\tau = \frac{1}{2} \sigma$
Change
 $\sigma = \sigma_{max}$

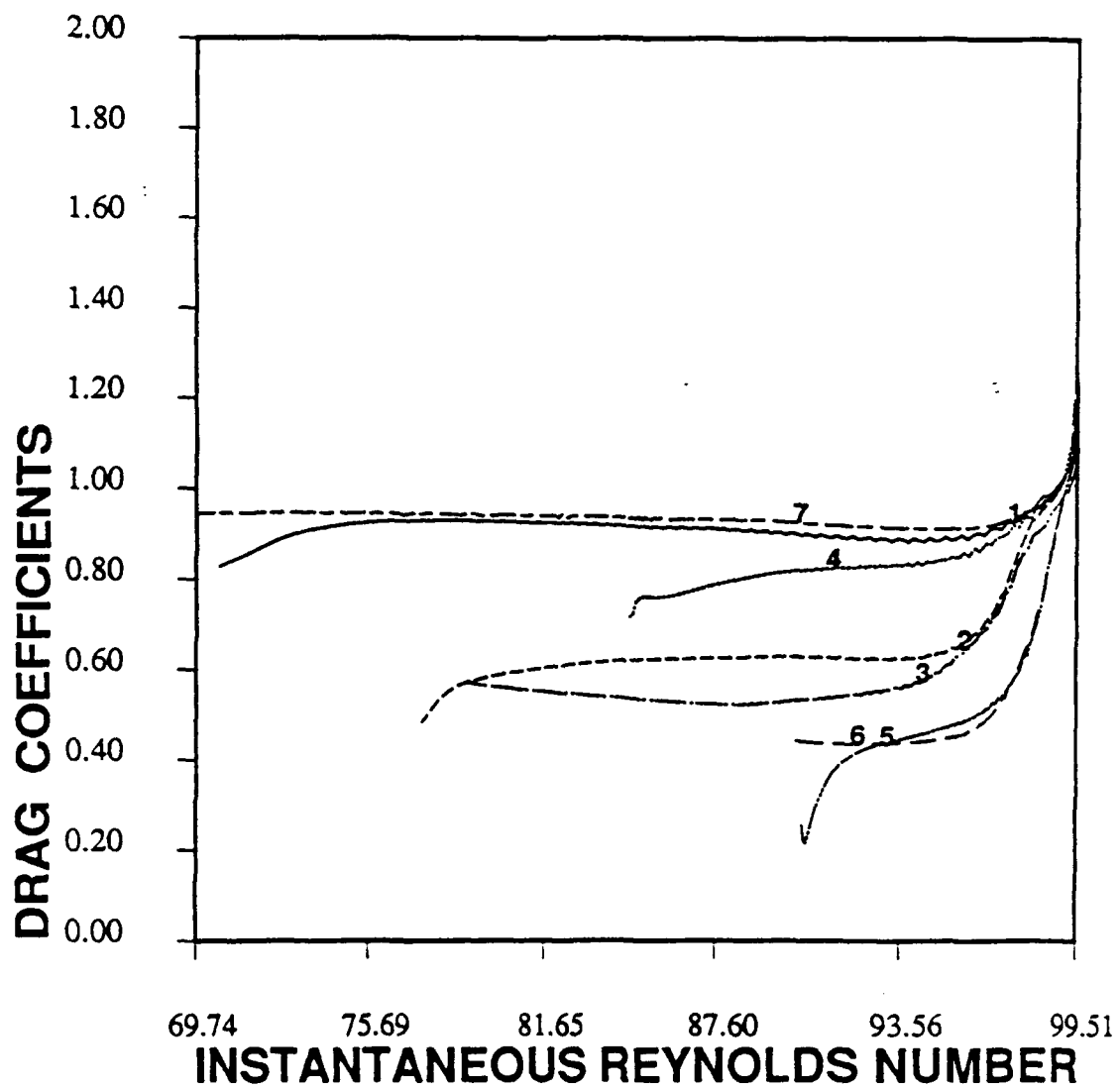


Fig 6
Change
Significant

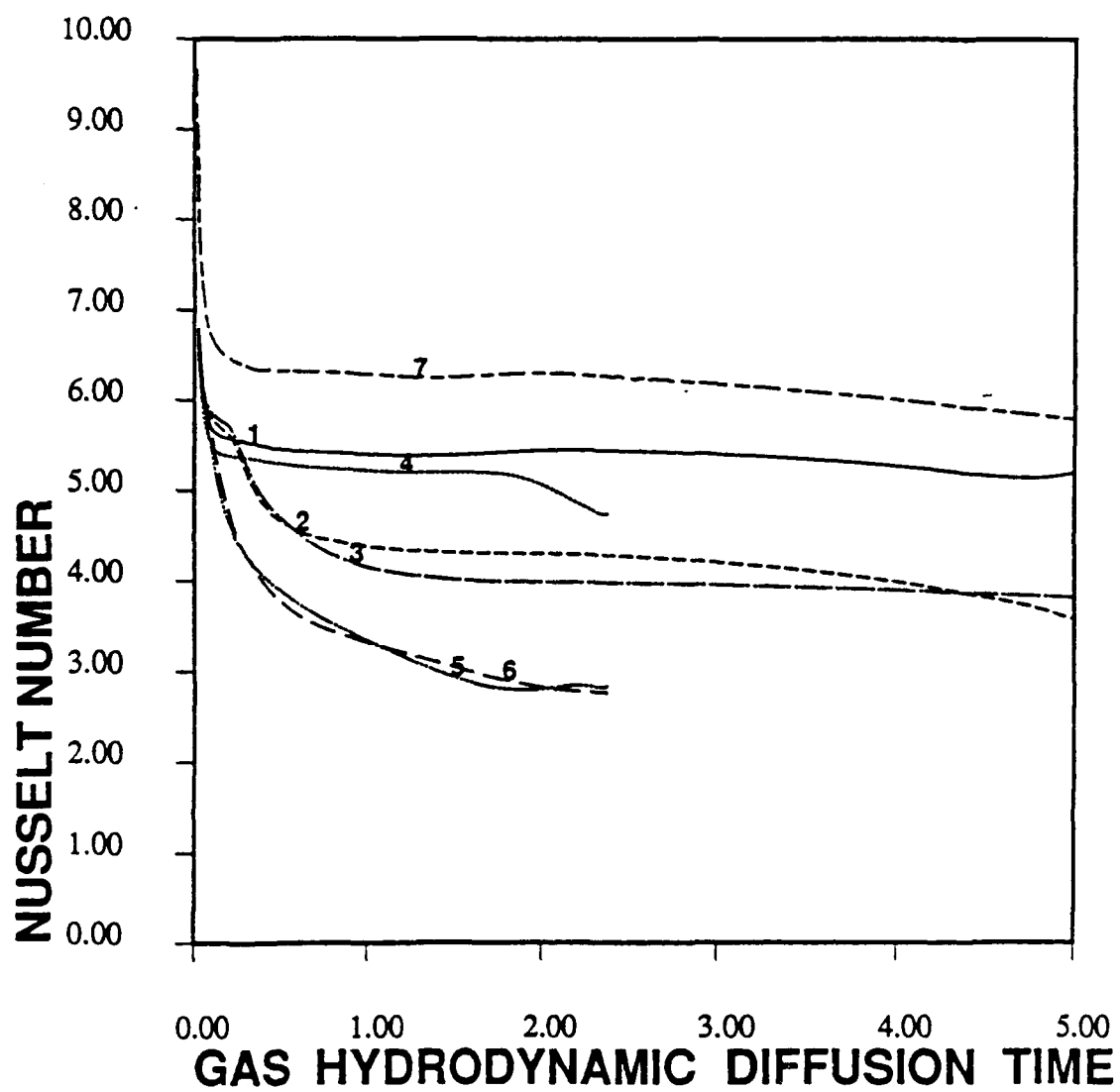
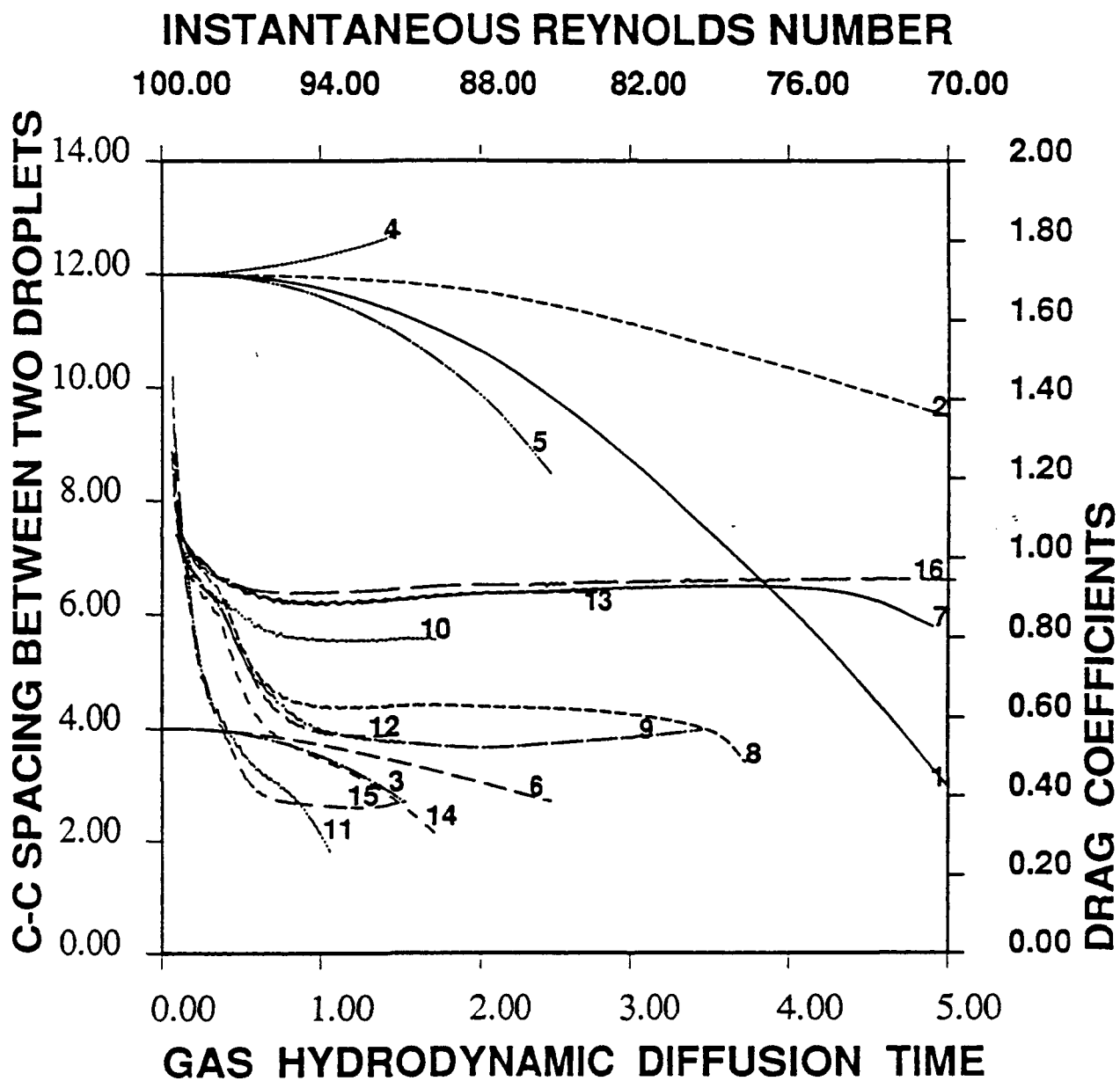


Fig 7
Change in h vs t



Handwritten notes and signatures in the bottom right corner.

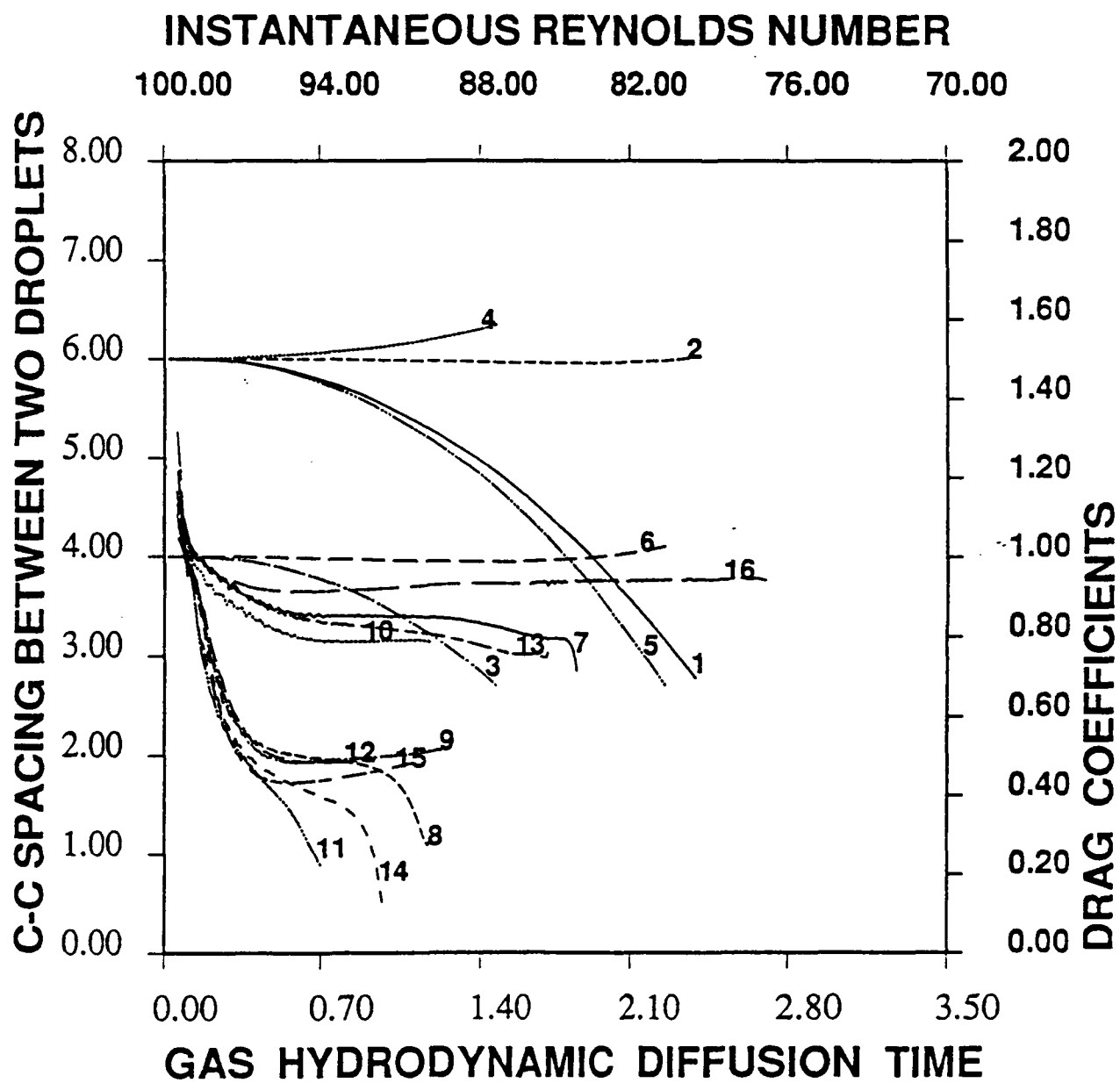


Fig 9
Chen & Sengupta

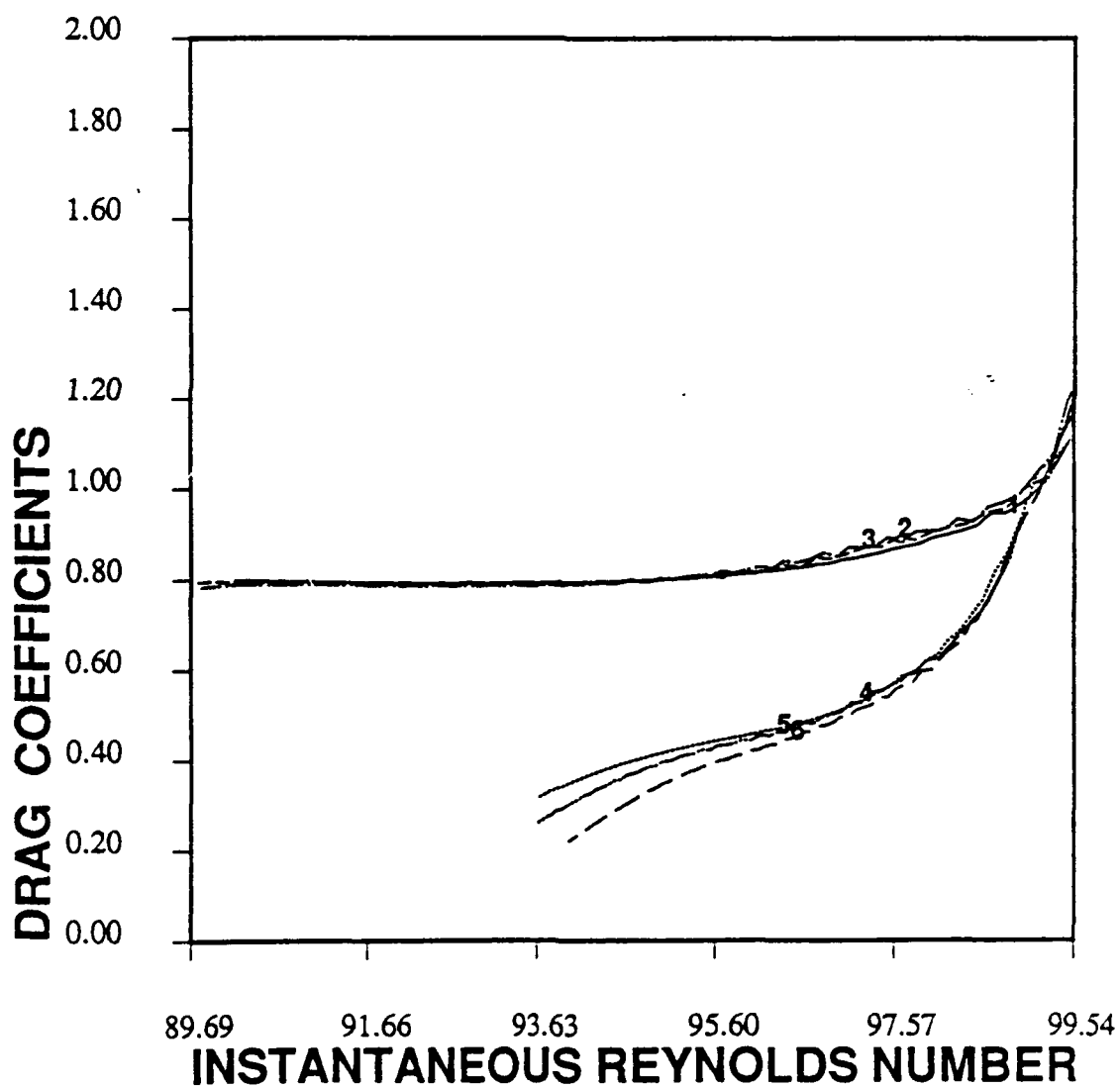


Fig 1c

Change
1.000

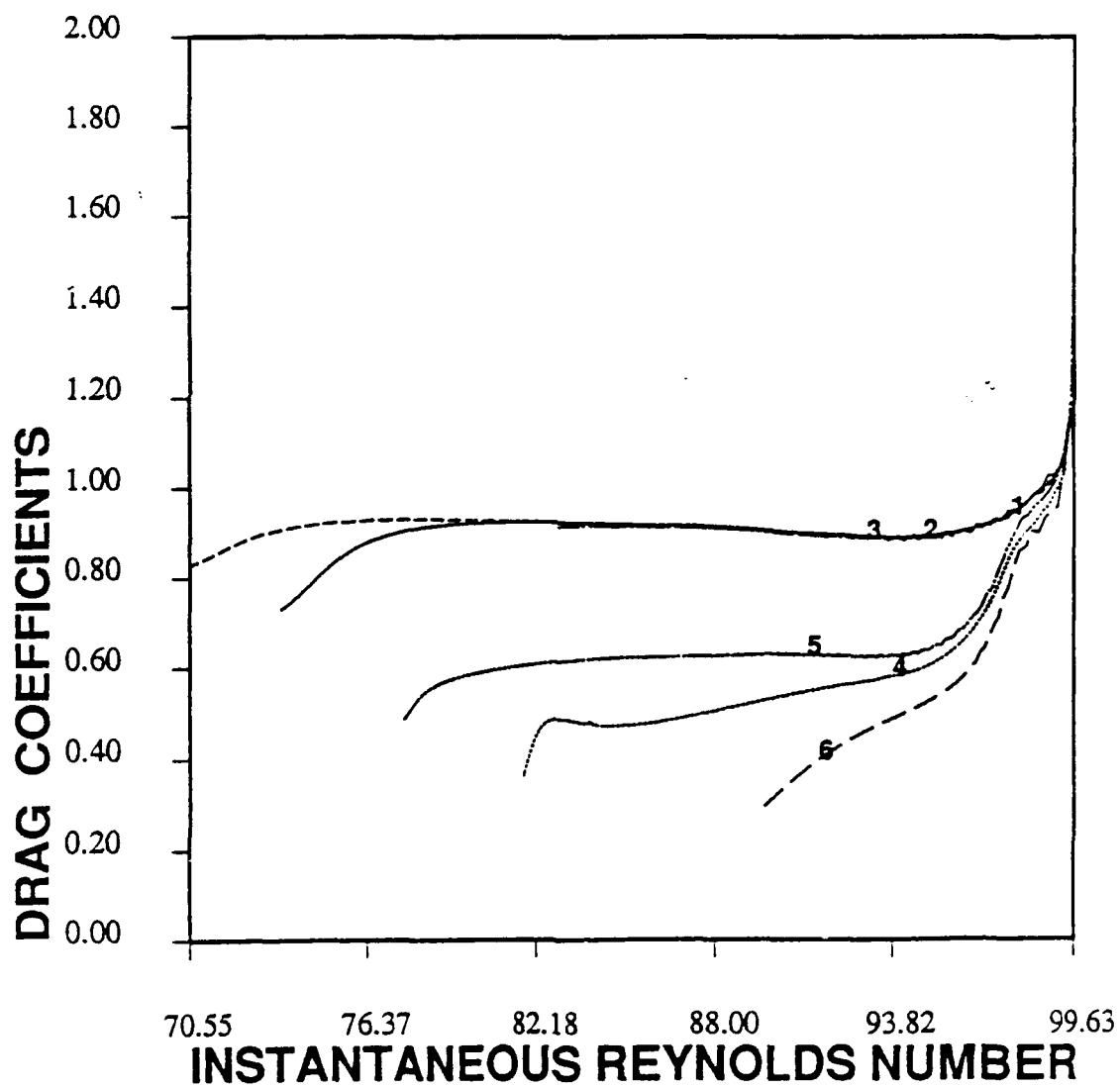


Fig 1
Change in Drag



ADDENDUM TO SECTION 6

AIAA-91-0281

Axisymmetric Vaporizing Oxygen Droplet Computations

C. H. Chiang and W. A. Sirignano
University of California
Irvine, CA

29th Aerospace Sciences Meeting

January 7-10, 1991/Reno, Nevada

Axisymmetric Vaporizing Oxygen Droplet Computations

C. H. Chiang*

W. A. Sirignano†

Department of Mechanical and Aerospace Engineering
University of California, Irvine, California

Abstract

The detailed analysis of a cold LOX droplet suddenly introduced into the hot methane fuel-vapor stream has been performed in this study. The effects of variable thermophysical properties, real gas behavior, transient heating and internal circulation of liquid, deceleration of the flow due to the drag of the droplet, boundary-layer blowing, and moving interface are included. A primitive-variable formulation with an implicit finite-difference scheme has been developed to solve the complete set of Navier-Stokes, energy, and species equations. The results are presented for the low pressure case. The interesting phenomena due to the large surface blowing and surface boiling is examined. The modifications required for the current model to treat high pressure case are discussed.

Nomenclature

C_{pg}	$C'_{pg}/C'_{pg,\infty}$, specific heat of gas phase
C_{pl}	$C'_{pl}/C'_{pl,0}$, specific heat of liquid phase
D_g	$D'_g/D'_{g,\infty}$, mass diffusivity of gas phase
F	$F'/(U'_{\infty,0}{}^2 a_0^2 \rho'_{g,\infty})$, drag force
f	fugacity
h	$h'/(C'_{pg,\infty} T'_{g,\infty})$, enthalpy
L	$L'/(C'_{pl,0} T'_{\infty})$, latent heat of vaporization
Le_g	$\rho'_{g,\infty} D'_{g,\infty} C'_{pg,\infty} / \kappa'_{g,\infty}$, gas-phase Lewis number
M	M'/M'_{∞} ; $M' = \frac{M'_f M'_{\infty}}{M'_{\infty} Y_f + (1-Y_f) M'_f}$, equivalent molecular weight
p_g	$(p'_g - p'_{g,\infty})/(\rho'_{g,\infty} U'_{\infty,0}{}^2)$, gas-phase pressure
p_l	$(p'_l - p'_{l,0})/(\rho'_{l,0} U'_{\infty,0}{}^2)$, liquid-phase pressure
Pe_g	$Re_g Pr_g$, gas-phase Peclet number
Pe_l	$Re_l Pr_l$, liquid-phase Peclet number
Pr_g	$\mu'_{g,\infty} C'_{pg,\infty} / \kappa'_{g,\infty}$, gas-phase Prandtl number
Pr_l	$\mu'_{l,0} C'_{pl,0} / \kappa'_{l,0}$, liquid-phase Prandtl number
Q'	heat flux

r	r'/a'_0 , radial coordinate
R	$R^{\circ} T'_{\infty} / (U'_{\infty,0}{}^2 M'_{\infty})$, gas constant
R°	universal gas constant
Re_g	$a'_0 U'_{\infty,0} \rho'_{g,\infty} / \mu'_{g,\infty}$, gas-phase Reynolds number
Re_l	$a'_0 U'_{\infty,0} \rho'_{l,0} / \mu'_{l,0}$, liquid-phase Reynolds number
T	T'/T'_{∞} , temperature
t'	time
V	$V'/U'_{\infty,0}$, velocity
Y_i	mass fraction
z	z'/a'_0 , axial coordinate

Greek

θ	angular coordinate
σ	$\sigma'/(U'_{\infty,0}{}^2 \rho'_{l,0} a'_0)$, surface tension
κ_g	$\kappa'_g/\kappa'_{g,\infty}$, conductivity of gas phase
κ_l	$\kappa'_l/\kappa'_{l,0}$, conductivity of liquid phase
μ_g	$\mu'_g/\mu'_{g,\infty}$, viscosity of gas phase
μ_l	$\mu'_l/\mu'_{l,0}$, viscosity of liquid phase
ρ_g	$\rho'_g/\rho'_{g,\infty}$, density of gas phase
ρ_l	$\rho'_l/\rho'_{l,0}$, density of liquid phase
τ_{Eg}	$t' \kappa'_{g,\infty} / (a_0^2 \rho'_{g,\infty} C'_{pg,\infty})$, gas-thermal-diffusion time
τ_{El}	$t' \kappa'_{l,0} / (a_0^2 \rho'_{l,0} C'_{pl,0})$, liquid-thermal-diffusion time
τ_{Hg}	$t' \mu'_{g,\infty} / (a_0^2 \rho'_{g,\infty})$, gas-hydrodynamic-diffusion time
τ_{Hl}	$t' \mu'_{l,0} / (a_0^2 \rho'_{l,0})$, liquid-hydrodynamic-diffusion time
τ_S	$t' D'_{g,\infty} / (a_0^2)$, gas-species-diffusion time
ϕ	fugacity coefficient

Subscripts

<i>ave</i>	volumetric average
<i>crit</i>	critical point
<i>f</i>	fuel
<i>g</i>	gas phase
<i>l</i>	liquid phase
<i>n</i>	normal direction
<i>o</i>	oxygen
<i>sl</i>	saturated liquid

*research associate, member AIAA

†professor, AIAA Fellow

v	vapor
0	initial conditions
θ	tangential direction
∞	free stream conditions

Superscript

0	ideal gas state
$'$	dimensional quantity

1 Introduction

The study of the liquid behavior of liquid-propellant rocket engines, where both liquid fuel and oxidizer are injected from one end of the chamber, has recently become the subject of various experimental and theoretical investigations. One of the characteristics whereby liquid-fueled rocket engines differ from air-breathing engines is that both fuel droplets and liquid oxygen (LOX) droplets are present. The use of LOX/hydrogen fuel propellant combination or LOX/methane propellant combination in an advanced launch vehicle booster engine appears extremely attractive due to high propellant bulk density and the relatively high performance characteristics of these propellant combinations. Hydrogen and methane are cryogenic fuels and would be injected in a fluid state. Usually in the practical combustor, liquid hydrogen or liquid methane vaporize faster than the oxygen droplets. As a result, oxygen droplet vaporization becomes a rate-controlling factor in determining the mixing performance of the heterogeneous fuel/oxidizer mixture.

Due to some technical difficulties in handling cryogenic fuels and LOX droplets at extremely low temperature in the regular laboratory, only very limited experimental works [1, 2] utilized LOX/ H_2 and LOX/ CH_4 propellant to study combustion performance have been constructed. Although substantial theoretical/computational results have been reported, the theoretical studies of the vaporization of LOX droplets have not reached a satisfactory status. Many assumptions employed to simplify analysis have rendered the results to become questionable when detailed transport processes of LOX vaporization occur at a high temperature, high pressure and convective environment.

Generally, the strategy of droplet research over the past decade has been to develop simplified transient vaporization models which are physically accurate but sufficiently computationally efficient so that hundreds or thousands of droplets in a spray combustor can be tracked [3, 4, 5]. During the past decade, the research of LOX vaporization has more or less followed the same trend. The existing LOX models are mainly focused on the one-dimensional calculations where quasi-steady assumption and film theory are employed for gas-phase

analysis while simplified conduction models (such as infinite conductivity, conduction limit, and effective conductivity models) are frequently used for liquid-phase analysis. No convection and variable properties effects have ever been considered in the existing LOX models. It is well known that the quasi-steady assumption becomes invalid with the high pressure environment. The internal motion of the liquid phase, induced by the gas-phase convection, may significantly change the time scales of transport processes of the droplet. Variable property effects due to the variations of temperature and species composition can also affect the computed quantities. These effects are no longer negligible in the development of a comprehensive numerical model for the LOX droplet.

In parallel with the development of simplified LOX vaporization modeling, there is a need to pursue "exact" solutions (via finite-difference calculations) of the flow and thermal fields surrounding and within vaporizing LOX droplets. These Navier-Stokes solutions serve two major purposes: 1) correlations for quantities such as droplet drag coefficients are obtained that can be used in spray combustion analyses with the simplified models (which do not independently predict drag coefficients) and 2) the exact solutions can be used as a standard for comparison of the simplified models. Also the numerical data can be provided as a benchmark for the experimental research.

The present research involves the detailed investigation of an isolated liquid oxygen droplet vaporizing in the high temperature fuel-vapor environment. The forced convection of the gas phase, the transient deceleration of the flow due to the drag force, the surface regression, the internal circulation and transient heating of the liquid phase, and variable properties are considered. The LOX vaporization at near critical conditions will be addressed since most rocket engine combustors are operated in the very high pressure domain where the state equation and thermodynamic functions are considerably different.

Our current axisymmetric models have been developed for hydrocarbon fuel droplets vaporizing under subcritical conditions [6]. Therefore, the well developed isolated-droplet-code will be utilized as the base code to facilitate the present research. The problem features very complex property calculation along with very high transfer number ($\approx O(100)$) and high density ratio. The early rapid surface heating is worthwhile to develop a new scheme to surmount the numerical difficulties. In the present research, some effort is required to adjust these transient droplet heating and vaporization models so that liquid-propellant rocket combustion can be studied.

The variation of liquid-phase density with temperature is significant. The LOX may experience the thermal expansion during the transient heating and the surface moving velocity cannot be neglected. In or-

der to carefully account for unsteadiness due to density variation, the primitive variables (V_r , V_z , p_l and ρ_l) formulation for the liquid phase is employed. Note that in previous codes [6, 7], the liquid-phase momentum equations are formulated by a streamfunction-vorticity approach. The modifications of the code to adapt the primitive variables for the liquid phase as well as to employ more accurate interface conditions have been developed. The details will be discussed in the following sections.

2 Formulation

The schematic flow configuration is presented in Figure 1 where the flow passing over a vaporizing LOX droplet moving with respect to gas stream is shown. The flow is laminar and axisymmetric with initially uniform ambient conditions specified by U'_∞ , T'_∞ , ρ'_g , p'_∞ , and $Y_{o,\infty} = 0$. The frame of reference is fixed to the center of the LOX droplet. The problem can be viewed as an impulsively-started flow over a fixed LOX droplet. Unless otherwise stated, the basic assumptions remain the same as mentioned in Chiang et al [6].

The conservation equations in both phases are written in non-dimensional forms with respect to a cylindrical coordinate system. The initial radius, upstream velocity and thermophysical properties have been used to non-dimensionalize the variables. The diffusion time has been selected as the time scale in this study. According to the non-dimensionalization given in the nomenclature, the governing equations are presented below.

2.1 Governing Equations

Gas Phase

Continuity Equation

$$\frac{\partial}{\partial \tau_{Hg}}(r\rho_g) + \frac{\partial}{\partial r}(rRe_g\rho_g V_r) + \frac{\partial}{\partial z}(rRe_g\rho_g V_z) = 0 \quad (1)$$

Momentum Equation in r-direction

$$\begin{aligned} \frac{\partial}{\partial \tau_{Hg}}(r\rho_g V_r) + \frac{\partial}{\partial r}\{rRe_g(\rho_g V_r V_r + p_g)\} + \frac{\partial}{\partial z}(rRe_g\rho_g V_r V_z) \\ = \frac{2}{3} \frac{\partial}{\partial r}\{r\mu_g[2\frac{\partial V_r}{\partial r} - \frac{V_r}{r} - \frac{\partial V_z}{\partial z}]\} + \frac{\partial}{\partial z}\{r\mu_g[\frac{\partial V_r}{\partial z} + \frac{\partial V_z}{\partial r}]\} \\ + Re_g p_g - \frac{2\mu_g}{3}(2\frac{V_r}{r} - \frac{\partial V_r}{\partial r} - \frac{\partial V_z}{\partial z}) \end{aligned} \quad (2)$$

Momentum Equation in z-direction

$$\begin{aligned} \frac{\partial}{\partial \tau_{Hg}}(r\rho_g V_z) + \frac{\partial}{\partial r}(rRe_g\rho_g V_r V_z) \\ + \frac{\partial}{\partial z}\{rRe_g(\rho_g V_z V_z + p_g)\} = \frac{\partial}{\partial r}\{r\mu_g[\frac{\partial V_r}{\partial z} + \frac{\partial V_z}{\partial r}]\} + \frac{2}{3} \frac{\partial}{\partial z} \\ \{r\mu_g[2\frac{\partial V_z}{\partial z} - \frac{V_r}{r} - \frac{\partial V_r}{\partial r}]\} + F_D \end{aligned} \quad (3)$$

where F_D is the D'Alembert force (reversed inertial force due to the drag force on the droplet) which is uniformly applied to the whole gas-phase flowfield.

Energy Equation

$$\begin{aligned} C_{p,g}\left\{\frac{\partial}{\partial \tau_{Hg}}(r\rho_g T_g) + \frac{\partial}{\partial r}(rPe_g\rho_g V_r T_g) + \frac{\partial}{\partial z}(rPe_g\rho_g V_z T_g)\right\} \\ + (h_o - h_f)\left[\frac{\partial}{\partial \tau_{Hg}}(r\rho_g Y_o) + \frac{\partial}{\partial r}(rPe_g\rho_g Y_o V_r) \right. \\ \left. + \frac{\partial}{\partial z}(rPe_g\rho_g Y_o V_z)\right] = \frac{\partial}{\partial r}(r\kappa_g \frac{\partial T_g}{\partial r}) + \frac{\partial}{\partial z}(r\kappa_g \frac{\partial T_g}{\partial z}) \\ - \frac{\partial}{\partial r}(rLe_g(C_{p,f} - C_{p,o})T_g\rho_g \mathcal{D}_g \frac{\partial Y_o}{\partial r}) \\ - \frac{\partial}{\partial z}(rLe_g(C_{p,f} - C_{p,o})T_g\rho_g \mathcal{D}_g \frac{\partial Y_o}{\partial z}) \end{aligned} \quad (4)$$

where $h = \int_{T_o}^T C_{p,g} dT$

Species Equation

$$\begin{aligned} \frac{\partial}{\partial \tau_g}(r\rho_g Y_i) + \frac{\partial}{\partial r}(r\frac{Pe_g}{Le_g}\rho_g V_r Y_i) + \frac{\partial}{\partial z}(r\frac{Pe_g}{Le_g}\rho_g V_z Y_i) \\ = \frac{\partial}{\partial r}(r\rho_g \mathcal{D}_g \frac{\partial Y_i}{\partial r}) + \frac{\partial}{\partial z}(r\rho_g \mathcal{D}_g \frac{\partial Y_i}{\partial z}) \end{aligned} \quad (5)$$

Equation of State

$$p_g = \frac{R}{M}(\rho_g T_g - M) \quad (6)$$

We assume that the mixture behaves as an ideal gas. This is a good assumption for the low pressure case. The assumption may become impractical for pressure near the critical point. The other alternative to relate p_g , ρ_g , T_g and Y_i is to employ the two-parameter Redlich-Kwong equation [8] with the mixing rule of Chueh and Prausnitz [9]. Our test runs indicated that the computational time will increase tremendously since it is necessary to solve the real root of a third-order polynomial equation which is a very time-consuming task within an iterative Poisson equation solver. For the time being, in order to prevent exhausting our precious supercomputer allocation, we employ this assumption for the pressure below 40 atms.

Liquid Phase

Continuity Equation

$$\frac{\partial}{\partial r}(r\rho_l) + \frac{\partial}{\partial r}(rRe_l\rho_l V_r) + \frac{\partial}{\partial z}(rRe_l\rho_l V_z) = 0 \quad (7)$$

Momentum Equation in r-direction

$$\begin{aligned} \frac{\partial}{\partial r}(r\rho_l V_r) + \frac{\partial}{\partial r}\{rRe_l(\rho_l V_r V_r + p_l)\} + \frac{\partial}{\partial z}(rRe_l\rho_l V_r V_z) \\ = \frac{2}{3} \frac{\partial}{\partial r}\{r\mu_l[2\frac{\partial V_r}{\partial r} - \frac{V_r}{r} - \frac{\partial V_z}{\partial z}]\} + \frac{\partial}{\partial z}\{r\mu_l[\frac{\partial V_r}{\partial z} + \frac{\partial V_z}{\partial r}]\} \\ + Re_l p_l - \frac{2\mu_l}{3}(2\frac{V_r}{r} - \frac{\partial V_r}{\partial r} - \frac{\partial V_z}{\partial z}) \end{aligned} \quad (8)$$

Momentum Equation in z-direction

$$\begin{aligned} \frac{\partial}{\partial r}(r\rho_l V_z) + \frac{\partial}{\partial r}(rRe_l\rho_l V_r V_z) + \frac{\partial}{\partial z}\{rRe_l(\rho_l V_z V_z + p_l)\} \\ = \frac{\partial}{\partial r}\{r\mu_l[\frac{\partial V_r}{\partial z} + \frac{\partial V_z}{\partial r}]\} + \frac{2}{3} \frac{\partial}{\partial z}\{r\mu_l[2\frac{\partial V_z}{\partial z} - \frac{V_r}{r} - \frac{\partial V_r}{\partial r}]\} \end{aligned} \quad (9)$$

Energy Equation

$$\begin{aligned} C_{p_l}\{\frac{\partial}{\partial r}(r\rho_l T_l) + \frac{\partial}{\partial r}(rPe_l\rho_l V_r T_l) + \frac{\partial}{\partial z}(rPe_l\rho_l V_z T_l)\} \\ = \frac{\partial}{\partial r}(r\kappa_l \frac{\partial T_l}{\partial r}) + \frac{\partial}{\partial z}(r\kappa_l \frac{\partial T_l}{\partial z}) \end{aligned} \quad (10)$$

Pressure-Density-Temperature Relation

The Hankinson-Brost-Thomson technique is used to predict the compressed liquid density.

$$\frac{1}{\rho'_l} = \frac{1}{\rho'_{l,sat}} \left[1 - c \ln \left(\frac{\beta + p'_l}{\beta + p'_{vp}} \right) \right] \quad (11)$$

where $\rho'_{l,sat}$, the saturated liquid density at the vapor pressure, p'_{vp} . β is obtained from

$$\beta/p'_{crit} = -1 + a(1 - T_r)^{1/3} + b(1 - T_r)^{2/3} + d(1 - T_r) + e(1 - T_r)^{4/3} \quad (12)$$

where $T_r = \frac{T}{T_{crit}}$. Values of constants are available in Reid et al [10]. We assume that there is no absorption of fuel-vapor into the liquid phase; as a result, there is no need to solve species equations for the liquid phase.

2.2 Initial and Boundary Conditions

2.2.1 Initial Conditions

Gas Phase: $V_r = p_g = Y_o = 0$, $V_z = T_g = \rho_g = 1$

Liquid Phase: $V_r = p_l = V_z = 0$, $\rho_l = 1$, $T_l = T_{l,0}$

Gas/Liquid Interface: $V_r = V_z = Y_o = p_g = p_l = 0$, $T_g = T_l = T_{l,0}$, $\rho_g = 1/T_{l,0}$, $\rho_l = 1$

2.2.2 Gas/Liquid Interface Boundary Conditions

Tangential Stress Condition:

$$\tau'_{n\theta,g} - \tau'_{n\theta,l} = \nabla_s \sigma'$$

where $\sigma' = \sigma'_0 + \frac{d\sigma'_l}{dT'_l} T'_l$; Usually $\frac{d\sigma'_l}{dT'_l}$ is assumed to be a constant. The nondimensional form becomes

$$\begin{aligned} \frac{\mu_l}{Re_l} \left(\frac{\partial V_{l,\theta}}{\partial n} - \frac{V_{l,\theta}}{a} + \frac{1}{a} \frac{\partial V_{l,n}}{\partial \theta} \right) \\ - \frac{\rho'_{g,\infty}}{\rho'_{l,0}} \frac{\mu_g}{Re_g} \left(\frac{\partial V_{g,\theta}}{\partial n} - \frac{V_{g,\theta}}{a} + \frac{1}{a} \frac{\partial V_{g,n}}{\partial \theta} \right) = \frac{1}{a} \frac{d\sigma}{dT_l} \frac{dT_l}{d\theta} \end{aligned} \quad (13)$$

Normal Stress Condition:

$$p'_l + \tau'_{nn,l} - p'_g - \tau'_{nn,g} = 2\sigma'/a'$$

The corresponding nondimensional-form of the above equation is

$$\begin{aligned} p_l - \frac{\rho'_{g,\infty}}{\rho'_{l,0}} p_g - 2 \frac{\mu_l}{Re_l} \frac{\partial V_{l,n}}{\partial n} + 2 \frac{\rho'_{g,\infty}}{\rho'_{l,0}} \frac{\mu_g}{Re_g} \frac{\partial V_{g,n}}{\partial n} \\ = 2 \frac{\sigma}{a} + \frac{p'_{g,\infty} - p'_{l,0}}{U'^2_{\infty,0} \rho'_{l,0}} \end{aligned} \quad (14)$$

Continuity of Tangential Velocity:

$$V_{g,\theta,s} = V_{l,\theta,s} \quad (15)$$

Conservation of Mass Flux:

By assuming no accumulation of mass at surface, the integral form of the continuity equation can be written as

$$Re_g V_{g,n} - \frac{d a}{d\tau_{Hg}} = \frac{\rho'_{l,s}}{\rho'_{g,s}} \left(Re_g V_{l,n} - \frac{d a}{d\tau_{Hg}} \right) \quad (16)$$

where the droplet regression rate is give

$$\begin{aligned} \frac{d a}{d\tau_{Hg}} = \frac{-1}{\rho_{l,ave}} \left\{ \frac{1}{2} \left(\frac{\rho'_{\infty}}{\rho'_{l,0}} \right) Re_g \int_0^\pi [\rho_g(V_{g,n} \right. \\ \left. - \frac{d a}{d\tau_{Hg}} \frac{1}{Re_g})] \sin\theta d\theta + \frac{a}{3} \frac{d\rho_{l,ave}}{d\tau_{Hg}} \right\} \end{aligned} \quad (17)$$

Note that this equation is employed to calculate the instantaneous radius.

Continuity of Temperature:

$$T_{g,s} = T_{l,s} \quad (18)$$

Conservation of Energy:

$$\left(\frac{\kappa'_g}{\kappa'_l} \right) \frac{\partial T_g}{\partial n} \Big|_s = \frac{\partial T_l}{\partial n} \Big|_s$$

$$+ Pe_l \left[\frac{\rho_g L}{\kappa_l} \left(V_{g,n} - \frac{d}{d\tau_{Hg}} \frac{1}{Re_g} \right) \right] \left(\frac{\rho'_\infty}{\rho'_{l,0}} \right) \quad (19)$$

Conservation of Species:

$$\left(\mathcal{D}_g \frac{\partial Y_o}{\partial n} \right)_s = Re_g Sc_g \left[\left(V_{g,n} - \frac{d}{d\tau_{Hg}} \frac{1}{Re_g} \right) (Y_o - 1) \right], \quad (20)$$

$Y_o - T_s$ Relation for Phase Equilibrium:

The vapor pressure is usually estimated as function of surface temperature. The correlation taken from Reid et al. [10] is employed in the current study.

$$\ln(p'_{v,o}/p'_{crit}) = (1-x)^{-1} [Ax + Bx^{1.5} + Cx^3 + Dx^6] \quad (21)$$

where $x = 1 - T'_s/T'_{crit}$

This kind of correlation have been particularly successful in computational programing.

The mass fraction at the interface can be determined by

$$Y_o = \frac{\chi_o M'_o}{\chi_o M'_o + (1 - \chi_o) M'_\infty} \quad (22)$$

At low pressure case, the ideal-solution assumption is valid and the Lewis fugacity rule leads to the Raoult' law which simply says that

$$\chi_o = \frac{p'_{v,o}}{p'_g} \quad (23)$$

However, the ideal behavior of gas mixture no longer occurs under the high pressure situation. The vapor/liquid equilibrium requires that fugacity of each species component must be equal in both phases at the surface; that is $f_{i,g} = f_{i,l}$, where subscript i stands for species. Hence, it is necessary to compute fugacity of oxygen in both phases. The mole fraction of oxygen vapor can be determined once fugacity is available. Since the fugacity has a dependency on mole fraction (through the mixing rule), the procedure for the calculation of χ_o requires the iteration of χ_o until a convergence criteria is satisfied. The equations for iteration are given in the following two equations.

$$\chi_o = \frac{p'_{v,o}}{p'_g} \frac{\phi_{s,l,o}}{\phi_{v,o}} \exp \left(\frac{\int_{p'_{v,o}}^{p'_g} \bar{V}_l dp}{R^o T} \right) \quad (24)$$

where \bar{V}_l is the molar density of the liquid phase.

Vapor-phase fugacity coefficient of oxygen, $\phi_{v,o}$, is given by

$$\ln \phi_{v,o} = \frac{\int_0^{p'_g} (\bar{V}_{v,o} - R^o T/p) dp}{RT} \quad (25)$$

In order to integrate this equation, the Redlich-Kwong equation of state combined with the mixing rules of Chueh and Prausnitz must be employed. χ_o is implicitly involved in the above equation.

The enthalpy of vaporization for oxygen can be calculated from the thermodynamic relationship

$$\frac{h^0_{v,o} - h_{v,o}}{R^o T^2} = \frac{\partial \ln \phi_{v,o}}{\partial T} \quad (26)$$

$$L = h_{v,o} - h_{l,o} \quad (27)$$

The enthalpy of vaporization at high pressure case is expected to be different from the conventional latent heat which is a function of temperature only.

The detailed computations of droplet thermophysical properties for the high pressure case can be found in Reference [12, 13, 14, 15, 16, 17]

2.2.3 Outflow ($r = r_\infty, \pi/2 \leq \theta \leq \pi$) Boundary Conditions:

$$\frac{D}{Dt}(V_r) = \frac{D}{Dt}(V_z) = \frac{D}{Dt}(T) = \frac{D}{Dt}(p_g) = \frac{D}{Dt}(Y_o) = 0 \quad (28)$$

2.2.4 Inflow ($r = r_\infty, 0 \leq \theta \leq \pi/2$) Boundary Conditions:

$$p_g = Y_o = V_r = 0, T = p_g = V_z = 1 \quad (29)$$

2.2.5 Axis of Symmetry ($0 \leq r \leq r_\infty, \theta = 0, \pi$) Boundary Conditions

Gas Phase:

$$V_r = \frac{\partial V_\theta}{\partial \theta} = \frac{\partial p_g}{\partial \theta} = \frac{\partial T}{\partial \theta} = \frac{\partial \rho_g}{\partial \theta} = \frac{\partial Y_o}{\partial \theta} = 0 \quad (30)$$

Liquid Phase:

$$V_r = \frac{\partial V_\theta}{\partial \theta} = \frac{\partial p_l}{\partial \theta} = \frac{\partial T}{\partial \theta} = \frac{\partial \rho_l}{\partial \theta} = 0 \quad (31)$$

2.2.6 Boundary Conditions for Governing Equations of Liquid Phase

At Droplet Surface

Solutions obtained from the boundary-conditions-solver are regarded as the Dirichlet conditions for the liquid-phase solver.

At Droplet Center

$$\frac{\partial T_l}{\partial n} = \frac{\partial V_z}{\partial n} = \frac{\partial V_r}{\partial n} = \frac{\partial p_l}{\partial n} = 0 \quad (32)$$

3 Solution Procedure

A brief description of the computational methodologies is given here. The finite-difference equations, and detailed numerical procedures are given in Chiang [11].

Since we have considered internal circulation and transient heating of the liquid phase, forced convection of the gas phase, transient deceleration of the flow and

variable properties, it is then necessary to solve simultaneously the complete set of unsteady Navier-Stokes equations, energy and species equations, combined with the appropriate boundary conditions. The nonlinear and highly coupled equations make the analytical solution almost impossible. We have to resort to an implicit finite-difference numerical algorithm.

The governing equations are represented in generalized coordinates which conform to changing boundaries due to decreasing droplet radii associated with liquid component evaporation. Pressure correction equations are employed to satisfy indirectly the continuity equations in both phases. The pressure correction equations, which are Poisson type of equations, are solved by the successive-over-relaxation (SOR) method. Note that the equation of state is incorporated with the Poisson equation to relate pressure and density of gas phase. The density is immediately updated when the new estimate of pressure becomes available during the iterations. In the pressure correction equation of liquid phase, we temporarily decouple the relationship between density and pressure to avoid the undesired acoustic pressure wave. Actually the liquid density is a very weak function of pressure. Hence, the variation of pressure in the liquid phase is assumed to be caused by the fluid motion only. The density is updated until the iterations of pressure correction equation are done. The momentum, energy and species equations are solved by an alternating-direction-predictor-corrector (ADPC) method. The non-linear gas/liquid interface boundary equations are treated by a quasilinearization technique and solved directly by the inversion of tridiagonal block matrices. The governing equations of motion as well as the interface boundary conditions are solved sequentially in an interactive sequence until convergence is achieved for each time-step of the calculation.

Since the reference frame is fixed to the liquid droplet, the evaluation of the drag force and its associated velocity correction for the gas phase are incorporated in the iterative process. In order to maintain a dense grid distribution at the droplet interface, the grid locations have to be adjusted at each time step to accommodate droplet surface regression. Obviously, the metrics of the transformation have to be updated whenever the grid system is moved.

In the overall procedure, the sequential solutions of governing equations and boundary conditions with grid and relative velocity adjustment are iterated until convergence is achieved. After convergence is reached, the drag coefficients, average Nusselt and Sherwood numbers are evaluated at prescribed time intervals.

The actual property computation is extremely time-consuming since most of the thermo properties are strongly coupled together through the set of thermodynamics equations. An iterative approach has to be employed. We have compiled the available property in-

formation from [10, 18, 19, 20] and constructed the property correlations based on the ambient pressure and an extensive range of temperature before starting droplet computation. We learned that some of the involved material properties change abruptly near the interface where the temperature gradient is large.

The major numerical difficulties occur at a very early time. The large gradients at interface seem to create inappropriate initial profiles used to start iterations. Since the initial conditions are physically meaningless before a residence time, it is safe to employ any suitable profile for variables in order to form a converged solution. We have designed a "ramp temperature profile," where the ambient temperature increases slowly with time, to smooth the transient gradient of temperature variation. Also, we have developed a control-volume scheme to solve conservation equations at the interface sequentially to decouple temporarily variables at the beginning of computation. After a near converged solution is obtained, we switch to the tri-diagonal block solver. The danger of solving interface conditions sequentially is that the temperature may shoot above the boiling temperature dramatically when the LOX droplet temperature approaches the boiling point.

4 Results and Discussion

The numerical simulations of an isolated LOX droplet suddenly injected into a methane-fuel-vapor flow are studied in the present research. The ambient temperature and initial droplet temperature, are selected to be 1,000 K and 100 K, separately. The initial droplet Reynolds number is 100. The critical pressure and temperature for the LOX droplet are 154.58 K and 50.43 atm, respectively. In order to handle the surface blowing at the interface, we have to employ a very small time step which render the whole computation become very time-consuming. For this reason, only very limited production runs with pressure ranging from 10 to 50 atm are made in order to study the pressure effects. Unfortunately, our code fails when the ambient pressure exceeds 40 atm. The detailed reasons will be discussed later. We only present results from the low pressure calculations.

In general, the flowfield structure is similar to that of a fuel droplet vaporizing in an air/fuel mixture. The detail discussion of the global flowfield is given in Chiang et al [6]. It is worthy to note that LOX vaporization features highly surface blowing and highly transient heating which leads to surface boiling at very early lifetime. The gas flowfield near the droplet interface is expected to be significantly influenced by the vaporization. The transport rates are also expected to be significantly reduced due to the surface blowing.

Several snap shots of the flowfield are presented in Figure 2 to Figure 6. Figure 2 shows the instan-

taneous velocity vectors at 5 hydrodynamic diffusion times when 20% of mass has been vaporized. The outward velocity vectors are observed at the 4 grid points next to the surface of the front stagnant region. Actually, the surface blowing has pushed the velocity stagnant point away from the droplet surface.

The large surface blowing also cause the flow separation to occur early since the vertical interaction of mass flux momentum with the boundary-layer flow makes the pressure gradient more favorable for flow separation. The predicted separation angle is 108° , measured from the front stagnation point, while the rigid sphere predicts 129° [21]. A recirculation wake, detached to the surface, is clearly shown. The wake moves backward in downstream direction as the vaporization increases. As a result, the increase in wake length will be also appreciable. The current calculation predicts the wake length is about 1.25 droplet diameter. For the same Reynolds number, the sphere without surface blowing has a wake length that is about 0.8 droplet diameter [21].

We have learned in all calculations that the LOX droplet surface reaches the boiling temperature, which is about 120 K for the case of 10 atm ambient pressure, very quickly. However, the droplet core remains cold since the conductivity is low and at early time, the circulation strength is not strong enough to convect much energy. All the available heat transfer from the gas phase is used to heat the surface and also utilized for latent heat of vaporization. The surface boiling persists throughout the droplet lifetime. The very rich and cold oxygen vapor surrounding the droplet is depicted in Figures 3 and 4. The large gradient occurs at the front stagnant region as we expect.

The internal circulation of the droplet is evidenced in Figure 5. Since a stream function is not available in this unsteady, compressible problem, we have to construct the "quasi-steady stream function", which strictly speaking does not satisfy the continuity equation by definition, in order to demonstrate the circulation. Note that since the droplet surface moves as the vaporization persists, the liquid normal velocity at surface is not identically zero. Hence, the droplet surface is not necessarily a streamline. Due to the large viscosity ratio, the time needed to develop a spherical vortex is much longer than for the hydrocarbon-fuel droplet case.

The isotherms of droplet at two different times are shown in Figure 6. The heat conduction mode dominates a significant portion of the early droplet lifetime. The convection mode then takes over after 3 hydrodynamic diffusion times.

The pressure distribution along azimuthal direction is displayed in Figure 7. Due to the momentum dissipation caused by the surface blowing, the pressure recovery at the rear portion of droplet is poor. The shear stress distribution is illustrated in Figure 8. The large

recirculation wake induced by the early separation of the flow has pushed the maximum shear stress point to forward of the equator. The asymmetric distribution of shear stress is attributed to the high surface blowing.

Figure 9 presents the surface Nusselt number distribution. By a pure diffusion analysis, it can be shown that the Nusselt number for a stagnant sphere is 2. The results indicate that the Nusselt numbers in the present study are well below the stagnant value even the Reynolds number is intermediate high. Similar trends for the Sherwood numbers are also identified. Due to the continuous surface boiling, the high blowing velocity has significantly impeded the heat and mass transport processes of the LOX droplet.

The normal velocity is mainly determined by the surface mass fraction and mass-fraction gradient which are associated with the surface temperature, Nusselt number and Sherwood number distributions. Hence, the distribution of normal velocity shown in Figure 10 resembles those of surface temperature and Nusselt numbers; it progressively decreases along the downstream direction, then slightly increases after flow separation. In fact, the oxygen vapor at the recirculating zone is relatively lean due to the shape effect of the droplet. As a result, the blowing velocity increases in this region.

The time variations of total drag and its three components, pressure, friction and thrust drag, are illustrated in Figure 11. The friction drag contributes less than 20% of the total drag. Also, the friction drag remains almost constant throughout our calculation since no change of surface condition occurs after the LOX droplet-surface reaches the boiling point. The slight increase in pressure drag is offset by the increase in thrust drag; as a result, the total drag almost levels off even though the reduction in Reynolds number continues.

The transient variation of Nusselt number is demonstrated in Figure 12. Care must be taken when the convective effect is taken into account for the nonconvective Nusselt or Sherwood numbers in a simplified film-theory model. The conventional Frossling correlation, which is a function of Reynolds number and Prandtl (or Schmidt) number, may yield a significant error. Our results indicate that the Nusselt and Sherwood numbers are much less than their stagnant values(2).

Figure 13 presents the changes of droplet heating rate, averaged surface mass fraction, temperature, and averaged volumetric temperature (nondimensionalized by the boiling temperature). Due to the persisting surface boiling, the energy distributed to the droplet heating is moderately low. Most of the available energy for LOX droplet has been used for enthalpy of vaporization. The surface temperature peaks very quickly. The volumetric temperature increases slowly with time.

A case with $p'_\infty = 20$ atm is also performed. The qualitative behavior is similar to that of case of $p'_\infty = 10$. Since our supercomputer resource is very limited,

we decide to terminate the calculation when 30% of the mass has vaporized. Our results indicate that the LOX droplet vaporizes much faster in the high pressure case as shown in Figure 14. The diffusion time scales in the high pressure environment are shorter than in the low pressure environment. The period for transient droplet heating and development of the internal circulation decreases as pressure (and density) increases and thus the droplet lifetime reduces. The preliminary results also indicate that the drag coefficients is relatively insensitive to the variation of pressure. However, the Nusselt and Sherwood numbers increase as pressure increases.

We have experienced numerical difficulties with the high pressure cases ($p'_\infty \geq 40$ atms). The surface temperature shoots above the critical temperature at the very early time of the computation. The liquid phase pressure solver fails when the interface solutions become disarranged due to the overshoot of surface temperature. In our first analysis, two assumptions of our model turn out to be critical in the high pressure case. In the present model, there is an inconsistency of equation of state employed at the gas/liquid interface. We use the Redlich-Kwong equation with mixing rules to determine the mole fraction and then the density, while in the gas-phase pressure equation, we employed the ideal-gas law to predict the density. The inconsistency grows as the pressure increases. The second bad assumption is that the solubility of fuel-vapor in the LOX droplet is neglected. Usually, the consideration of real gas effects will predict higher mole fraction than Raoult's law predicts. When the droplet approaches the near critical state, our fugacity and mole fraction iteration procedure predicts a mole fraction greater than unity and destroys the balanced conditions at interface. The omission of absorption of fuel-vapor into LOX droplet also drastically affects the estimation of enthalpy of evaporation.

5 Concluding Remarks and Future Work

We have conducted a very detailed study of a LOX droplet vaporizing in a convective environment. The primitive-variable approach has been employed to solve the complete set of Navier-stokes, energy, and species equations. The preliminary results for low pressure case have provided us a clear picture of the transport processes. The high surface blowing velocity has a significant effect to the flow structure and modifies the flow separation angle and wake length etc. The drag coefficient, Nusselt and Sherwood numbers are reduced to below their corresponding stagnant values. The surface boiling occurs immediately after the LOX droplet is injected to combustor and persists throughout the droplet lifetime. The LOX droplet would spend a large portion of energy in providing the heat of vaporization

rather than heating the internal fluid. As a result, the transient droplet heating is responsible for the unsteady thermal behavior of the LOX droplet.

This research by no means is completed. The current model apparently is insufficient to handle the LOX droplet at the high pressure environment. The ideal gas assumption is questionable when the pressure is near the critical condition where the interaction of other species is important. There is a lack of a computationally efficient equation of state which is applicable for a wide range of pressure in two dimensional calculations. The Redlich-Kwong equation is accurate but is too time-consuming to incorporate with a pressure correction equation. The new method to linearize the nonlinear equation of state is currently underway. A very restrictive assumption that ignores the solubility of the fuel-vapor in the liquid phase should be released in our future computation. There is also a need to review more advanced numerical techniques at the present high transfer number and high density-ratio two-phase flow. The ADI originated methods currently employed converges slowly at the early computation.

Acknowledgement

This work has been supported by the Air Force Office of Scientific Research under grant No. 90-0064 with Dr. Julian Tishkoff and Dr. Mitat Birkan acting as the technical monitors. The discussion with Mr. J.-P. Delplanque about the thermophysical properties is very helpful to the present research. The support of the San Diego Supercomputing Center under a Block Grant of the Office of Academic Computing at UCI is greatly appreciated.

References

- [1] Barsotti, R.J., et al, *Development of Liquid Oxygen/Liquid Hydrogen Thrust Chamber for the M-1 Engine*, NASA CR-54813, NASA Contract NAS3-2555, 1968
- [2] Jensen, R.J., et al, *Oxygen/Methane Combustion Stability Investigation*, 1988 Earth to Orbit Conference, MsFc, May 1988.
- [3] Prakash, S. and Sirignano, W. A., "Theory of Convective Droplet Vaporization with Unsteady Heat Transfer in the Circulating Liquid Phase. *Int. J. Heat Mass Transfer*, **23**, 253-268 (1980).
- [4] Tong, A. Y. and Sirignano, W. A., "Analytical Solution for Diffusion and Circulation in a Vaporizing Droplet", *Nineteenth Symposium (International) on Combustion*, pp. 1007-1020. Combustion Institute (1982).

- [5] Abramzon, B. and Sirignano, W. A., "Droplet Vaporization Model for Spray Combustion Calculations", *Int. J. Heat Mass Transfer*, **32**, 1605-1618 (1989).
- [6] Chiang, C. H., Raju, M. S. and Sirignano, W. A., "Numerical Analysis of Convecting, Vaporizing Fuel Droplet with Variable Properties", *AIAA Aerospace Sciences Meeting*, Paper 89-0834. (1989). Also to appear in *Int. J. Heat Mass Transfer* (1990).
- [7] Chiang, C. H. and Sirignano, W. A., "Numerical Analysis of Interacting, Convecting, Vaporizing Fuel Droplet with Variable Properties", *AIAA Aerospace Sciences Meeting*, Paper 90-0357 (1990). Also to be submitted to *Int. J. Heat Mass Transfer*.
- [8] Redlich, O. and Kwong, J.N.S. "On the Thermodynamics of Solutions," *Chem. Rev.* **44**:233, 1949.
- [9] Chueh, P.L. and Prausnitz, J.M. "Vapor-Liquid Equilibrium at High Pressures. Vapor-Phase Fugacity Coefficients in Nonpolar and Quantum-Gas Mixtures." *I & EC Fundamentals*, **6**(4):493-498, Nov. 1967.
- [10] Reid, R.C., Prausnitz J.M. and Poling B.E., *The Properties of Gases and Liquids* 4th Ed., McGraw-Hill, inc. 1987
- [11] C. H. Chiang, *Isolated And Interacting, Vaporizing Fuel Droplets: Field Calculation With Variable Properties*, Ph.D. Dissertation, University of California, Irvine, Dept. of Mechanical Engineering (1990).
- [12] Matlosz, R.L., Leipziger, S. and Torda, T.P. "Investigation of a Liquid Drop Evaporation in a High Temperature and High Pressure Environment" *Int. J. Heat and Mass Transfer*, **15**:831-852, 1972
- [13] Manrique, J.A. and Borman, G.L. "Calculation of Steady State Droplet Vaporization at High Ambient Pressures" *Int. J. Heat Mass Transfer*, **12**:1081-1095, 1969.
- [14] Curtis, E.W. and Farrell, P.V. "Droplet Vaporization in a Supercritical Microgravity Environment", *Astronautica Acta* **17**, 11/12:1189-1193, 1988.
- [15] Hsieh, K.C., Shuen, J.S. and Yang, V. "Analysis of Multicomponent Droplet Vaporization at Near-Critical Conditions," *AIAA 26th Aerospace Sciences Meeting*, January 11-14, 1988/Reno, NV.
- [16] Litchford, R.J. and Jeng, S.-M. "LOX Vaporization in High-Pressure Hydrogen-Rich Gas", presented at the *AIAA/SAE/ASSME/ASEE, 26th Joint Propulsion Conference*, Orlando, FL, 1990.
- [17] Umemura, A. "Supercritical Liquid Fuel Combustion", *Twenty-First Symposium (International) on Combustion/The Combustion Institute* pp.463-471, 1986
- [18] Vargaftik, N.B., *Tables on the Thermophysical Properties of Liquids and Gases*. Hemisphere - 1975.
- [19] Prausnitz, J.M., Lichtenthalek, R.N. and de Avezedo, E.G. *Molecular Thermodynamics of Fluid-Phase Equilibria*, Prentice-Hall Co., Inc., 1986.
- [20] Delplanque, J.-P., and Sirignano, W.A. "Transient Vaporization and Burning for an Oxygen Droplet at Sub- and Near-Critical Conditions". Presented at the *AIAA 29th Aerospace Sciences Meeting and Exhibit*, Reno, NV - 1991.
- [21] Clift, R., J. R. Grace, J. R. and Weber, M.E. *Bubbles, Drops, and Particles*, Academic Press, New York (1978).

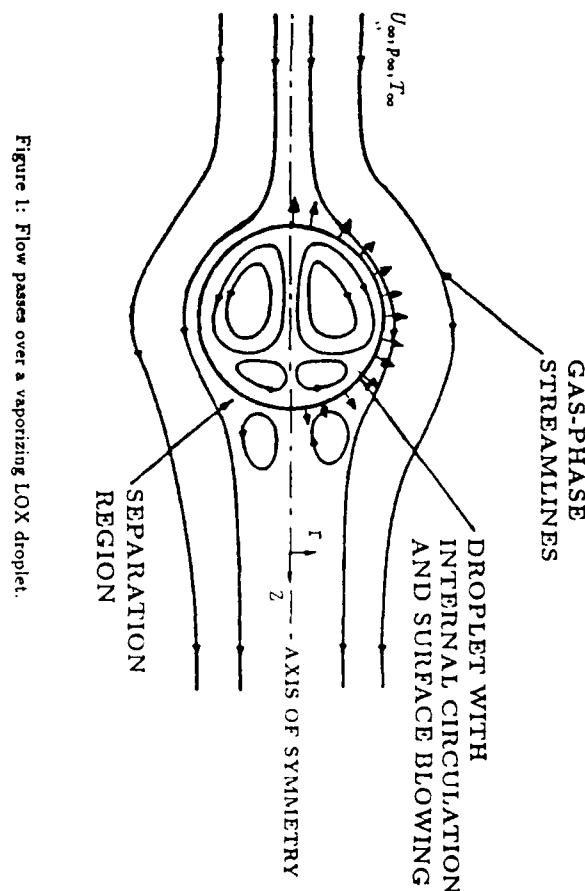


Figure 1: Flow passes over a vaporizing LOX droplet.

GAS-PHASE VELOCITY VECTORS

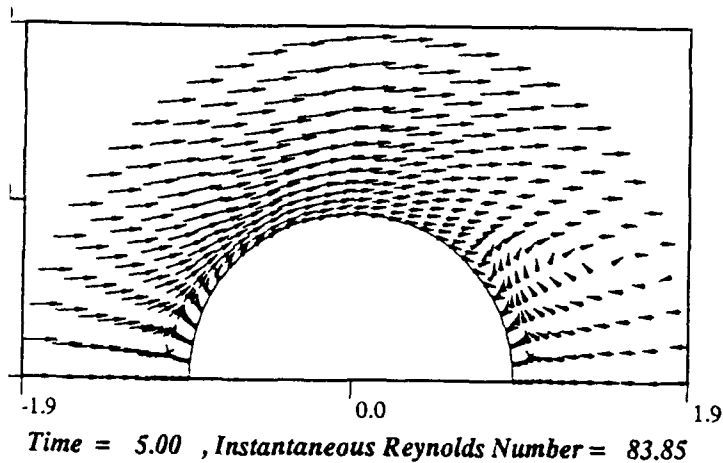


Figure 2: Instantaneous velocity of gas phase at time = 5.

GAS-PHASE ISOTHERMS

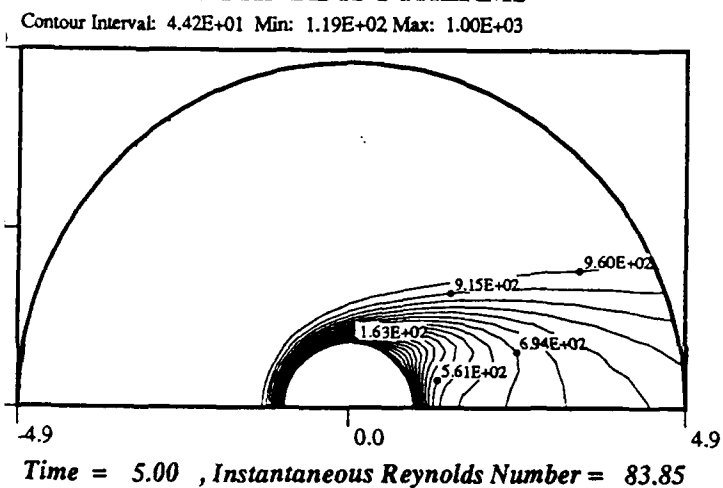


Figure 3: Temperature contour plot at time = 5.

OXYGEN MASS FRACTION

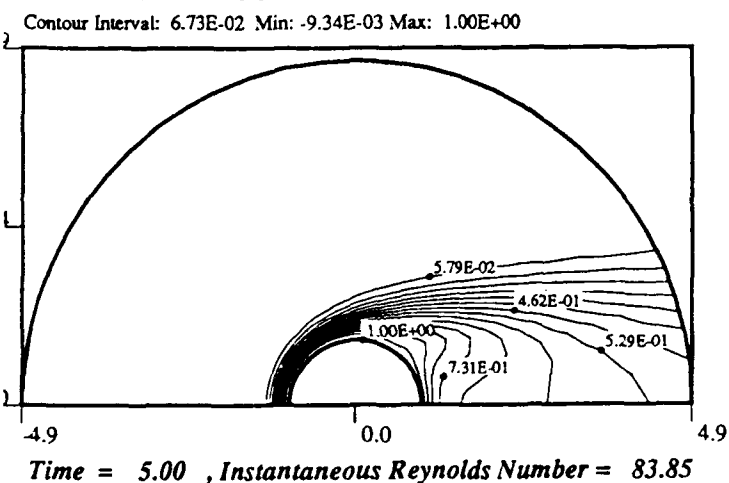


Figure 4: Mass fraction contour plot at time = 5.

LIQUID-PHASE STREAM FUNCTION

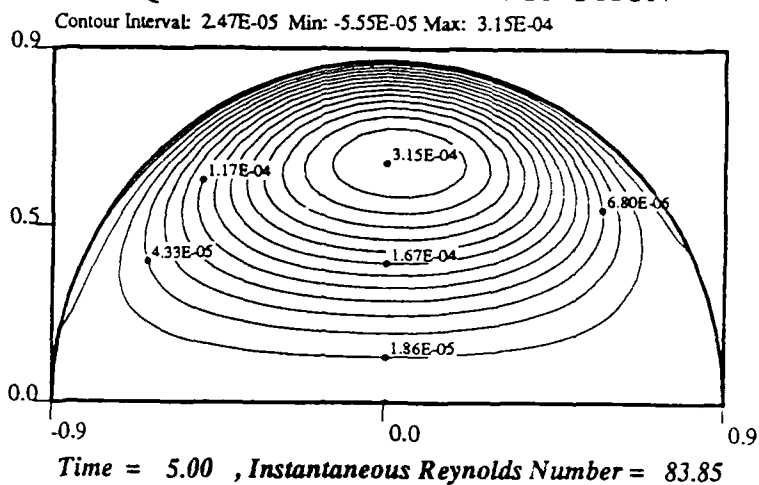
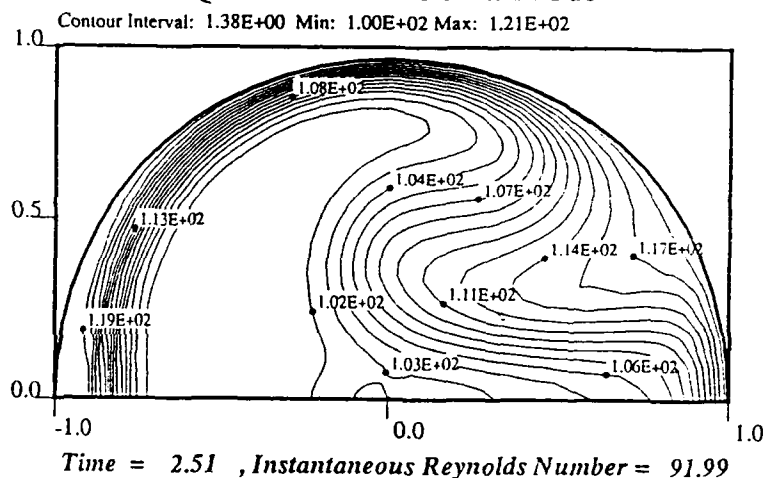


Figure 5: Stream function of liquid phase at time = 5.

LIQUID-PHASE ISOTHERMS



LIQUID-PHASE ISOTHERMS

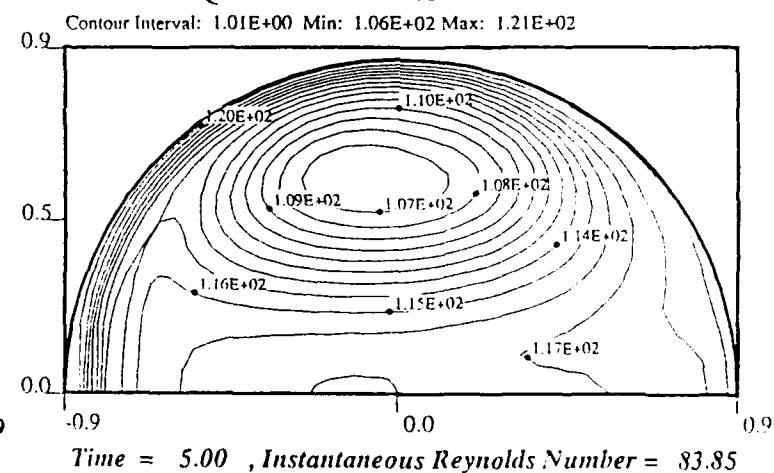


Figure 6: Transient history of LOX droplet heating at two different times.

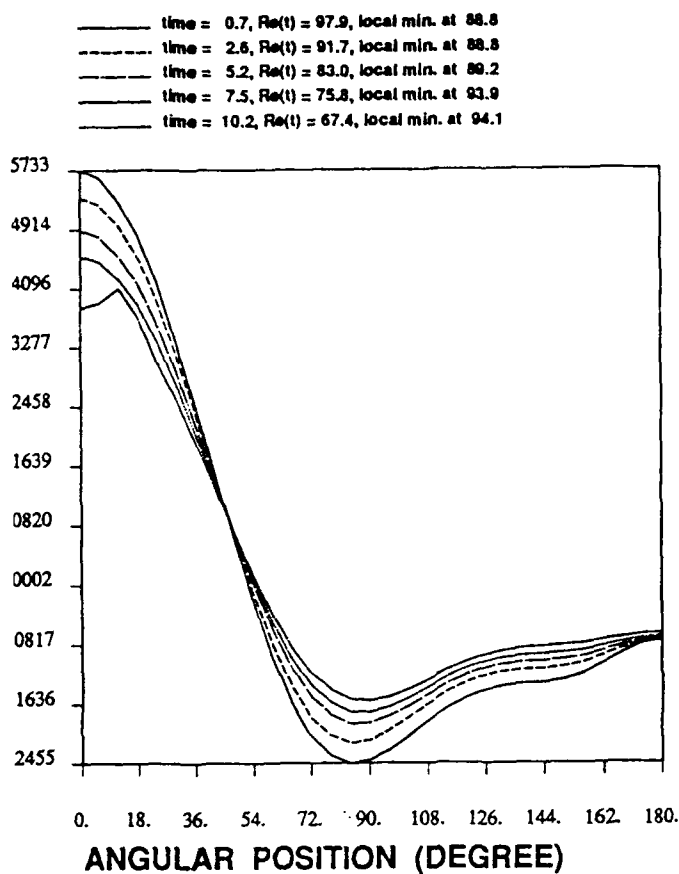


Fig. 7 Surface pressure distribution at different times.

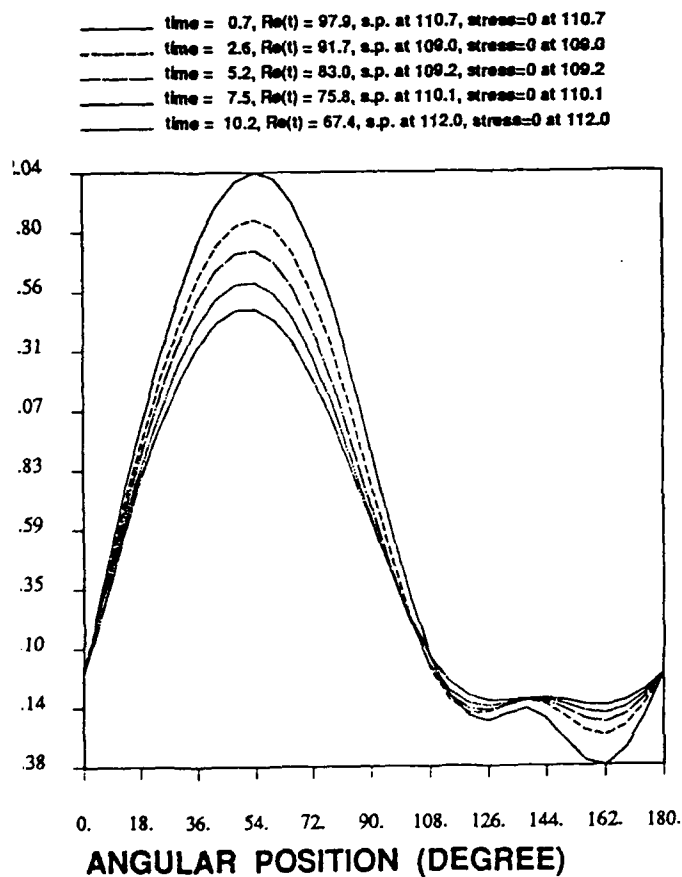


Fig. 8 Surface shear stress distribution at different times.

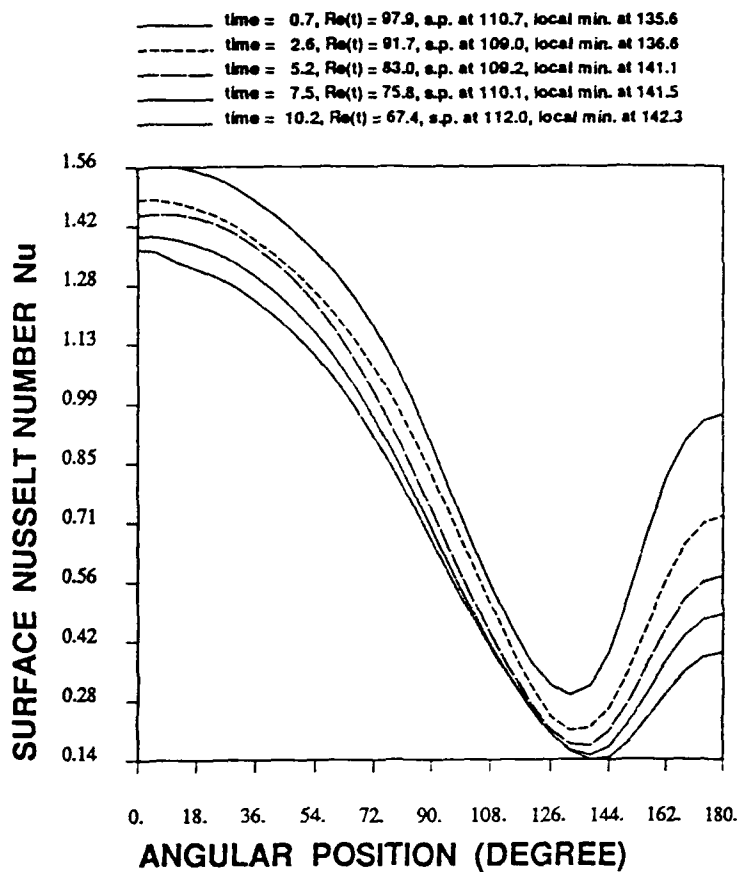


Fig. 9 Surface Nusselt number distribution at different times.

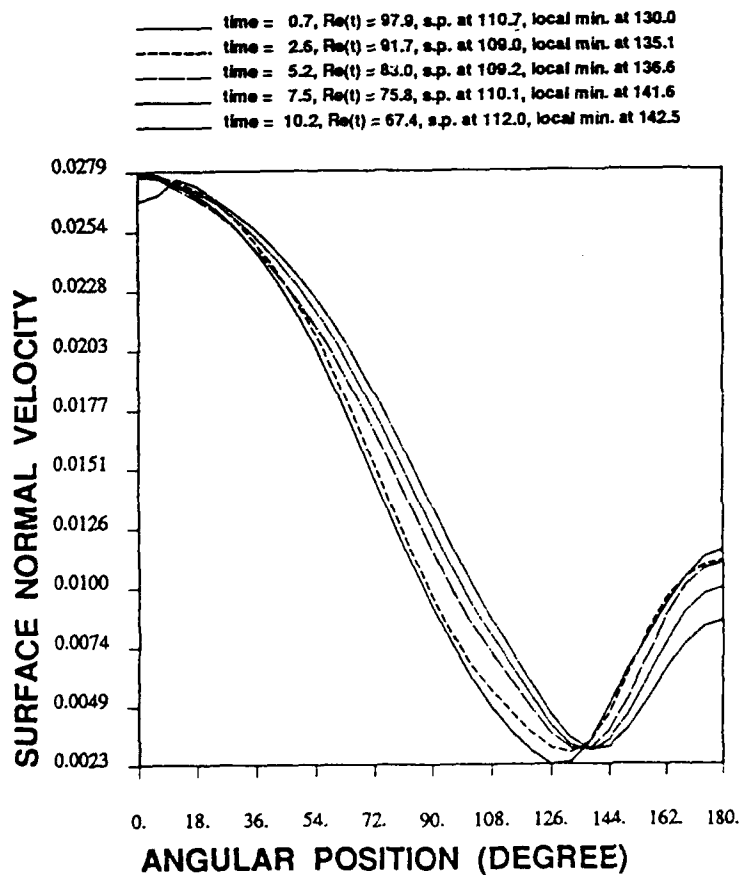


Fig. 10 Surface normal velocity distribution at different times.

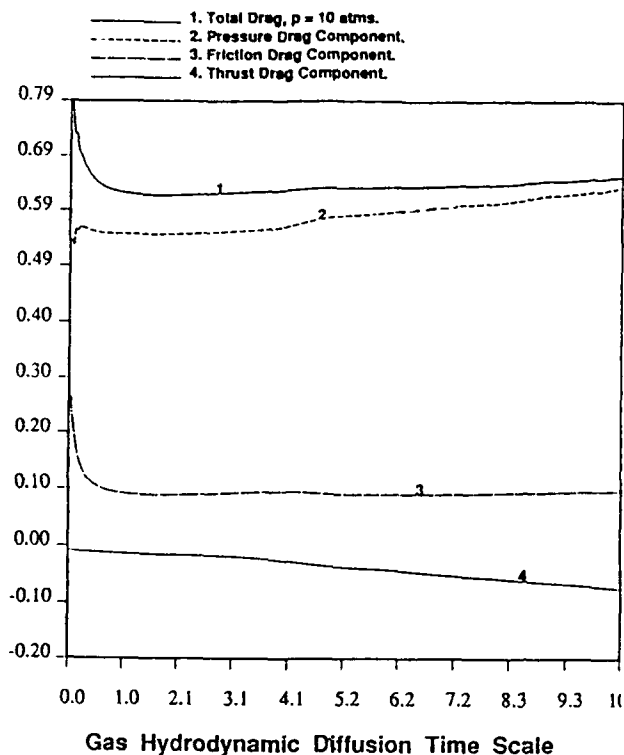


Figure 11: Time variations of total drag and three drag components.

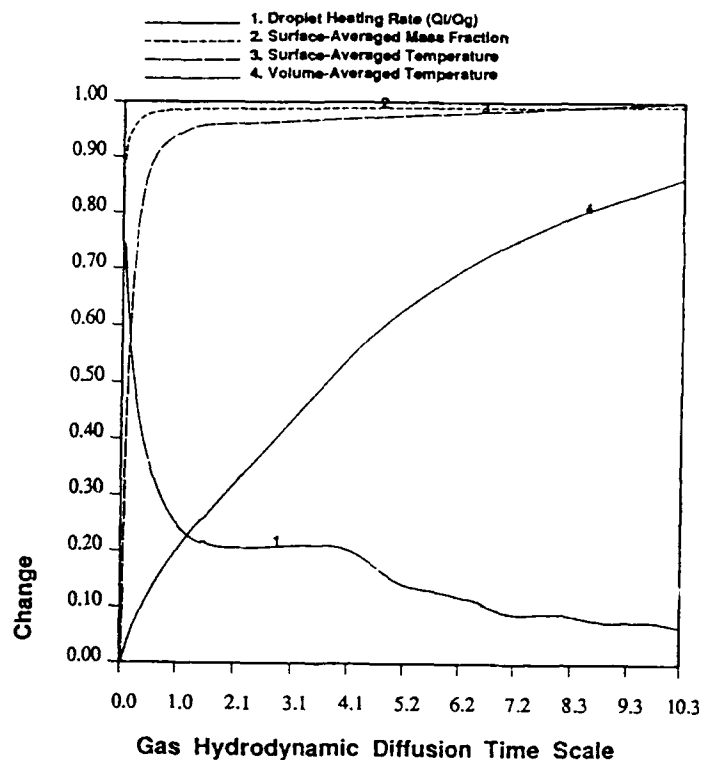


Figure 13: Time variations of droplet heating rate, averaged surface mass fraction, temperature, and averaged volumetric temperature.

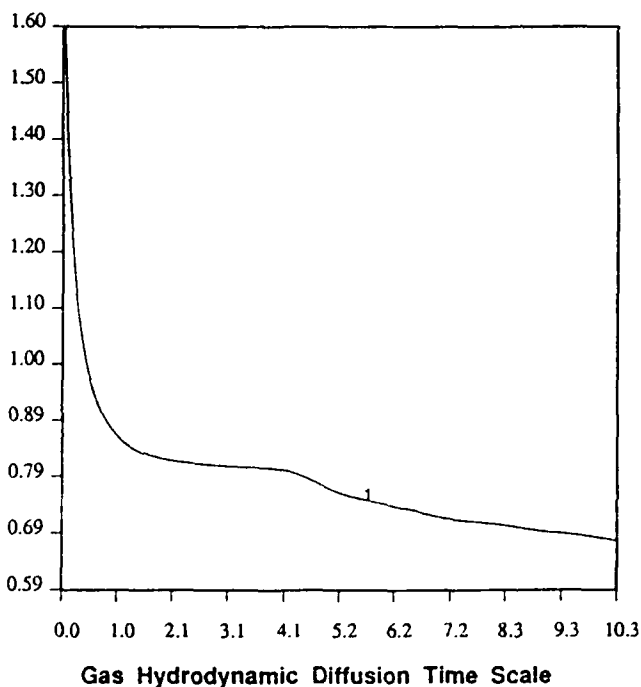


Figure 12: Time variations of averaged surface Nusselt number.

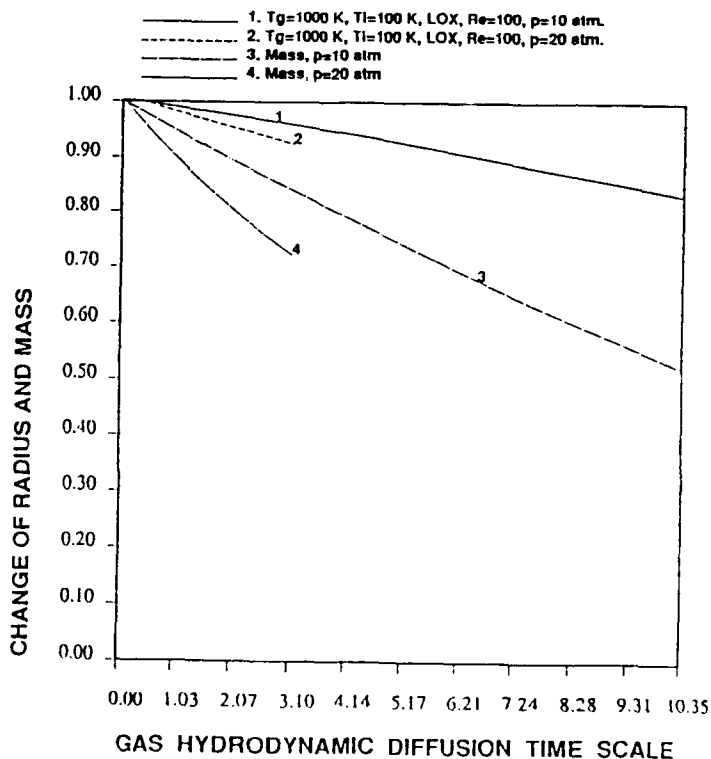


Figure 14: Time variations of radius and mass for the cases of different ambient pressures.